Current-Driven Magnetization Dynamics: Analytical Modeling and Numerical Simulation

D i s s e r t a t i o n

zur Erlangung des Doktorgrades
des Fachbereichs Physik
der Universität Hamburg

vorgelegt von

Benjamin Krüger
aus Hamburg

Hamburg
2011

Gutachterin / Gutachter der Dissertation:	Prof. Dr. Daniela Pfannkuche Prof. Dr. Ulrich Merkt Prof. Dr. Rembert Duine
Gutachterin / Gutachter der Disputation:	Prof. Dr. Daniela Pfannkuche Prof. Dr. Wolfgang Hansen
Datum der Disputation:	16.11.2011
Vorsitzender des Prüfungsausschusses:	PD Dr. Alexander Chudnovskiy
Vorsitzender des Promotionsausschusses:	Prof. Dr. Peter Hauschildt
Dekan der Fakultät für Mathematik, Informatik und Naturwissenschaften:	Prof. Dr. Heinrich Graener

Abstract

In this thesis the magnetization dynamics, driven by spin-polarized currents or magnetic fields, in nanostructured thin films is investigated by means of analytical and numerical calculations. These calculations are based on the micromagnetic model. The dynamics is given by an extended version of the Landau-Lifshitz-Gilbert equation that takes the action of spin-polarized currents into account. The investigations focus on a magnetic vortex or a magnetic antivortex in a thin-film element and on a magnetic domain wall in a thin nanowire. From a collective coordinate approach analytical models are derived which are then compared with numerical simulations to test the applicability of the models. The analytical models are especially valuable since they can be used to explain how a change of the material parameters, the geometry of the sample, or the temporal shape of the excitation may alter the behavior of the magnetization.

For a harmonic confining potential analytical expressions for the current- and field-driven trajectories of a vortex or antivortex are derived. For harmonic excitations the analytically predicted trajectories are compared with the results of the numerical simulations. Here special attention is put on the amplitude of the gyration and its phase with respect to the excitation. The comparison yields good accordance between the analytical and numerical results.

The current can excite the magnetization via the adiabatic and the non-adiabatic spin-transfer torque. The strength of the latter is still under debate. A scheme is derived that enables the numerical calculation of the Oersted field for arbitrary current densities. It is found that for an inhomogeneous current flow the Oersted field is also able to excite the vortex or antivortex. The analytical model allows for the development of a precise measurement scheme of the excitations due to the non-adiabatic spin-transfer torque, the adiabatic spin-transfer torque, and the Oersted field.

It is shown that the analytical model can be used to design new magnetic memory devices. In a vortex or antivortex random access memory a bit is stored using a thin-film element that contains a vortex or antivortex whose orientation can be switched back and forth using excitations with magnetic fields or electric currents. When the vortex or antivortex is excited by a collinear or perpendicular alignment of current and field, respectively, their combined action on the vortex or antivortex depends strongly on the momentary state. For one state the system exhibits a strong excitation while for the other state the actions are opposing each other and the excitation may be completely quenched. This can be used for a state-dependent switching of the orientation of the vortex or antivortex core. No reading operation would be needed before writing. This combined excitation can also be used to read out the current state of the memory.

From the analytical model for a transverse domain wall one finds an expression that connects the properties of the domain-wall quasiparticle, that are the mass and the damping time of the wall, with the microscopic parameters that enter the micromagnetic model. It is shown that the equation of motion can be conveniently extended to Bloch and Néel walls. The equation of motion is also valid for vortex walls using effective parameters. Numerical simulations yield that this equation delivers a good description of the field- and current-driven dynamics of the wall.

A comparison of the analytically calculated domain-wall dynamics with experiments showed that the equation of motion also precisely describes oscillations of the wall in a restoring potential. From the analytical calculations a strong reduction of the critical current density, that is needed to depin the domain wall from a pinning center, is predicted for currents with risetimes that are smaller than the characteristic damping time of the wall. This is of special importance as it should allow for efficient displacements of domain walls by fast varying currents. A comparison with experiments revealed that the predicted reduction is indeed observed.

When the domain walls are close together their interaction becomes important. Their interaction energy is calculated making use of a multipole expansion of the interaction energy up to third order. The interaction energy of two domain walls in parallel wires is compared with micromagnetic simulations and shows a good agreement.

Kurzfassung

In dieser Arbeit wird die Magnetisierungsdynamik, getrieben durch spinpolarisierte Ströme oder Magnetfelder, in nanostrukturierten Filmen mittels analytischer und numerischer Rechnungen untersucht. Diese Rechnungen basieren auf dem mikromagnetischen Modell. Die Dynamik ist dabei gegeben durch eine erweiterte Version der Landau-Lifshitz-Gilbert-Gleichung, die die Auswirkung spinpolarisierter Ströme berücksichtigt. Die Untersuchung konzentriert sich auf einen magnetischen Vortex oder Antivortex in einem dünnen Filmelement und auf magnetische Domänenwände in dünnen Nanodrähten. Basierend auf einem Ansatz mit kollektiven Koordinaten werden analytische Modelle hergeleitet, welche anschließend mit numerischen Simulationen verglichen werden, um die Anwendbarkeit der Modelle zu testen. Die analytischen Modelle sind besonders nützlich, da sie es erlauben, zu verstehen, wie sich eine Änderung der Materialparameter, der Geometrie der Probe oder der zeitlichen Form der Anregungen auf die Dynamik der Magnetisierung auswirken.

Für ein harmonisches einschließendes Potential wird ein analytischer Ausdruck für die strom- und feldgetriebene Bahn des Vortex oder Antivortex hergeleitet. Für harmonische Anregungen werden die analytisch berechneten Bahnen mit den Resultaten numerischer Simulationen verglichen. Dabei werden speziell die Amplitude und die Phase bezüglich der Anregung berücksichtigt. Der Vergleich zeigt eine gute Übereinstimmung zwischen den analytischen und numerischen Resultaten.

Der Strom kann die Magnetisierung über das adiabatische oder nichtadiabatische Spintransferdrehmoment anregen. Die Stärke des letzteren wird zur Zeit noch kontrovers diskutiert. Es wird ein Schema hergeleitet, das die numerische Berechnung des Oerstedfeldes für eine beliebige Stromdichteverteilung ermöglicht. Es wurde festgestellt, dass für einen inhomogenen Stromfluss der Vortex oder Antivortex auch durch das Oerstedfeld angeregt werden kann. Das analytische Modell gibt Hinweise für eine präzise Messung der Anregungen durch das nichtadiabatische Spintransferdrehmoment, das adiabatische Spintransferdrehmoment und das Oerstedfeld.

Es wird gezeigt, dass das analytische Modell auch die Konstruktion neuer Speicherzellen ermöglicht. In einem Vortex- oder Antivortexspeicher wird ein Bit durch die Orientierung eines Vortex oder Antivortex repräsentiert. Diese Orientierung kann durch Anregungen mit Magnetfeldern oder elektrischen Strömen hin- und hergeschaltet werden. Wenn der Vortex durch kollinear oder der Antivortex durch senkrecht zueinander ausgerichtete Ströme und Felder angeregt wird, hängt deren kombinierter Einfluss stark von dem momentanen Zustand ab. Für den einen Zustand zeigt das System eine starke Reaktion, während sich für den anderen Zustand die Einflüsse gegenseitig aufheben. So ist kein Leseprozess vor dem Schalten nötig. Die Anregung mit kollinearen oder senkrechten Strömen und Feldern kann auch für das Auslesen des Speichers benutzt werden.

Über das analytische Modell für eine transverse Domänenwand findet man einen Ausdruck, der die Eigenschaften des Domänenwandquasiteilchens, also seine Masse und seine Dämpfungszeit, mit den mikroskopischen Parametern, die in das mikromagnetische Modell eingehen, in Verbindung setzt. Es wird gezeigt, dass die Bewegungsgleichung auch auf Bloch- und Néelwände erweitert werden kann. Unter der Benutzung effektiver Parameter ist diese Gleichung auch für Vortexwände gültig. Ein Vergleich mit numerischen Simulationen zeigt, dass die Bewegungsgleichung eine gute Beschreibung der feld- und stromgetriebenen Dynamik liefert.

Ein Vergleich der analytisch berechneten Domänenwanddynamik mit Experimenten zeigt, dass die Bewegungsgleichung auch die Oszillationen der Wand in einem einschließenden Potenzial präzise beschreibt. Die analytischen Rechnungen sagen vorher, dass die kritische Stromdichte, welche zum Ablösen der Wand von einem Haftzentrum benötigt wird, stark verringert wird, wenn die Anstiegszeit des Stromes kürzer ist als die Dämpfungszeit der Wand. Dieses ist besonders interessant, da es ein effizientes Verschieben von Domänenwänden mit Hilfe von schnell variierenden Strömen erlauben sollte. In Experimenten wird die Reduzierung tatsächlich beobachtet.

Die Wechselwirkungsenergie benachbarter Domänenwände wird durch eine Multipolentwicklung berechnet. Die Wechselwirkungsenergie von zwei Wänden in parallelen Drähten wird mit mikromagnetischen Simulationen verglichen und zeigt gute Übereinstimmung.

Contents

Introduction

In today's computer applications we are faced with a strong boost in memory requirements. This is especially caused by the storage of photos, music, and videos. But, this increase can also be seen in the size of computer programs. Twenty years ago a commonly known operating system was delivered on a small number of discs with a capacity of 1.44 MB each while its current version is shipped on a DVD with a capacity of 4.7 GB. This leads to the necessity of memory devices with large capacity.

Magnetization has a long history in data storage. For more than seven decades the orientation of the magnetization in a magnetic sample is used to represent a single bit in computer memories. Prime examples for such magnetic memories are the core memory and the hard disk drive.

A core memory,[1,2] that was invented in the early fifties of the last century, is depicted in figure I.1(a). It consists of a grid of wires with magnetic rings that are placed around the intersections of the wires. The orientation of the magnetization of these magnetic rings is changed by the Oersted field that is generated by the wires. The bit of a certain ring is written by the Oersted field generated by the wires in the so-called cross point architecture. One horizontal and one vertical wire are traversed by a current that generates an Oersted field of 71% of the field that is needed to change the magnetization in the ring. The rings that are situated around one of these wires do not switch their magnetization since the field is not strong enough. For the ring that is placed at the intersection of both wires the fields of both wires add up to the field that is needed for the switching of the magnetization. For the read process the ring is set to a logical zero and a switching occurs in dependence of the initial state of the ring. This switching induces a current pulse in the wire that is detected by the memory controller. The presence or absence of this pulse allows for a determination of the value of the stored bit. This type of memory is nowadays replaced by semiconductor memories.

In contrast the hard disk drive,[1,2] that was also invented in the early fifties of the last century, is still used to store large amounts of data. There was a strong development from the first hard disk drive, which had a capacity of 5 megabytes, to modern drives with a capacity of several terabytes. A hard disk drive consists of a disc that is coated with a magnetic material and a read and write head which floats over the disc. While the disc rotates the read and write head is able to move in radial direction. The head is thus able to reach every position on the disc. In former times the head consisted of a coil that magnetized the magnetic coating, situated below the head, parallel to the disc's surface. The orientation of the magnetization then depends on the value of the according bit. A change of the orientation of the magnetization leads to a stray field that induces a voltage in the coil of the read head. This voltage allows for a read out of the stored bit. For a long time the capacity of hard disk drives was increased only by reducing of the size of the components and the magnetic bits. This reduction met some constraints that made the introduction of new technologies necessary. Some of these technologies are described in the following.

When the size of the magnetic bits is decreased their accompanying magnetic field reduces. At a certain size the field becomes so small that it cannot be detected by the coil in the read head. The discovery of the giant magneto resistance (GMR) effect[3,4] and tunnel magneto resistance (TMR) effect[5] allows one to overcome this problem. When two magnetic layers with a non-magnetic spacer in between are traversed by a current, their resistance depends on the relative alignment of the magnetization in the two magnetic layers. The resistance has a maximum for an antiparallel alignment and a minimum for a parallel alignment. In the first samples the change of the resistivity was rather small, but it has been found that with magnesium oxide tunnel barriers the difference between the low and the high resistance states can be more than a factor of seven.[6–8] This effect is called giant magneto resistance effect or tunnel magneto resistance effect for a spacer that is a conductor or an insulator, respectively. The read head can now be constructed of such a layered system. One layer, called free layer, is designed so that it changes its magnetization depending on the field that is produced by the magnetic bits. The second layer, called fixed layer, retains its

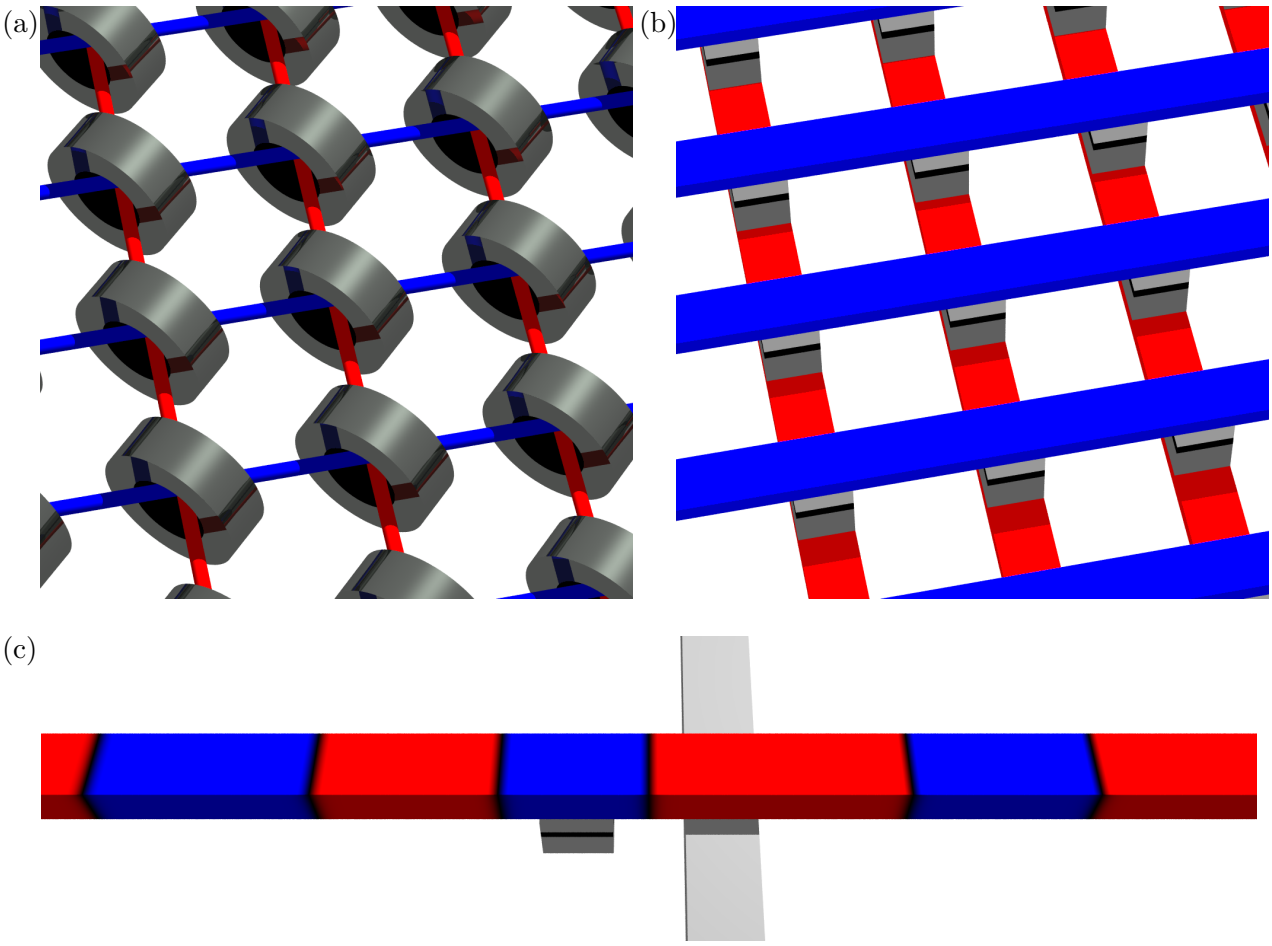

Figure I.1: (a) Scheme of a magnetic core memory. The memory consists of a grid of electric wires (red and blue). The magnetization of the ferromagnetic rings at the crosspoints of the wires can be switched by the magnetic field that is generated by a current that flows through the wires. (b) Like for the core memory the magnetic random access memory consists of a grid of electric wires (red and blue). The memory cells in between these wires consist of a free ferromagnetic layer (light gray), a fixed ferromagnetic layer (dark gray), and a spacer (black). The orientation of the free layer can be changed by a magnetic field generated by the wires. The orientation can be read out by sending a current through the cell (see text). (c) Scheme of a planar racetrack memory. The magnetization in the direction of the wire is given by the color gradient (red to blue). A current that flows along the wire allows for a shift of the magnetic bits to the reading and writing devices. The reading device can for example be a GMR or TMR stack (see text). A possible writing device is a strip line. Both devices are depicted in gray.

magnetization. The measurement of the resistance allows for a determination of the bit's magnetic orientation even for very small bit sizes.

The size of a bit in a state-of-the-art hard disk drive is so small that one approaches the regime of the super-paramagnetic effect where the energy barrier between the two orientations of the bit shrinks to the order of the thermal energy. Then thermal excitations are able to overcome the energy barrier and the orientation of one magnetic bit switches randomly under the influence of temperature. This led to the development of hard disk drives using perpendicular recording. In such drives the magnetic bits are not aligned parallel to the disc's surface but perpendicular. This allows for a reduction of the areal storage density while keeping the bit's size constant. However, this method can be applied only once and is not suitable for a further increase of the areal storage density.

A possibility to beard the super-paramagnetic limes for a while is heat-assisted magnetic recording. Here the magnetic material is heated at the position where the bit should be written. The heating reduces the coercivity of the material temporally and locally. In systems with heat-assisted magnetic recording it is possible to use magnetic materials with a higher coercivity which show the super-paramagnetic effect at smaller bit sizes. Due to the heating these materials can be written with magnetic fields that are small enough to have no influence on the neighboring bits.

Another possibility is the utilization of discrete track recording or bit patterned media. In discrete track recording the spacing between two tracks is equipped with groovings that minimize the interaction between the bits in neighboring tracks. The bit patterned media is a further step in this direction.[9–13] Here, sequent bits on the same track are also separated. Furthermore the shape of each bit is chosen to get further advantages like a higher stability of the magnetization. In bit patterned media one is faced with problems that do not occur in recording on a homogeneous disc. These problems are for example keeping the head on the track and the synchronization between the field pulses of the write head and the bit pattern on the disc.[14,15]

It has also been discussed to use composite materials that are especially adapted for perpendicular recording[16] or heat-assisted magnetic recording.[17] However, all these technologies will not allow for an indefinite increase of the areal storage density of a hard disk drive. Thus, to keep pace with the increasing memory requirements new types of memories have to be developed.

While the hard disk is able to store large amounts of data, it cannot keep up with the speed of the processor. Thus in a computer the data that is currently processed is stored in the random access memory (RAM) and cache memory. This memory is much faster than the hard disk but its capacity is limited. Furthermore the information that is stored in many types of RAMs is volatile in the manner that it is lost when the computer is switched off. In any case the information has to be copied between the hard disk and the faster memory. Thus, one would prefer a memory that combines the capacity and non-volatility of a hard disk with the speed of a RAM.

One possible candidate for such a universal memory is the magnetic random access memory (MRAM).[18] A scheme of an MRAM is depicted in figure I.1(b). Each MRAM cell consists of a free and a fixed ferromagnetic layer and combines two principles that are described above. The information is written by a magnetic field in the cross point architecture that was mentioned for the core memory. This field switches the free layer. The information is read out by passing a current through a distinct MRAM cell making use of the GMR or TMR effect. For high storage densities the long range magnetic field may also affect neighboring cells.

The observation that a current that is traversing a magnetic sample may alter the magnetic configuration[19–24] paves the road for new types of memory devices like the spin-transfer torque random access memory (STTRAM). This type of memory cell works similar to the MRAM but the orientation of the free ferromagnetic layer is changed by passing a current trough the cell.[25–27] For this changing the current has to be larger than a distinct threshold which is system dependent. A small current is used to read out the state of the memory while a larger current is used for writing. The current flows only through a distinct memory cell and does not influence neighboring cells as it may be the case for the writing fields of MRAMs.

In MRAMs or STTRAMs the magnetization in the magnetic layers is homogeneous with a current flowing perpendicular to the plane. In addition to a magnetic field or an out-of-plane current, an inhomogeneous magnetization can be excited by an in-plane current. Inhomogeneous magnetization patterns in thin-film elements and their excitations have been intensively studied.[28–76] There are also possible applications to memory devices. Examples are a vortex random access memory[77] (VRAM) or an antivortex random access memory[78] (AVRAM). These types of memory as well as their theoretical foundation are discussed in this work.

Finally, there is an approach that is more comparable with a hard disk. In the racetrack memory[79] the magnetic bits are beaded along a nanowire. The bits are shifted through the wire by a current that flows in the wire. During this motion the bits pass a reading and a writing device. In contrast to a hard disc, this memory has no moving parts. Figure I.1(c) shows a planar racetrack memory, but it should also be possible to introduce curvatures in the wire. This would extend the memory into the third dimension and thus drastically increase the storage density compared to a hard disk where only the surface is used to store informations. It has also been proposed to use the magnetization that is shifted along a nanowire for logic devices.[80,81]

Due to its possible applications there is currently a large effort in the investigation on the magnetization in nanowires.[82–126] This work deals with analytical and numerical investigations on this topic. In this work the dynamics of the magnetic moments is described within the micromagnetic model. The theory of micromagnetism is based upon a semiclassical description of the dynamics of the magnetization of ferromagnetic bodies. It is used to describe the magnetization on a length-scale which extends from hundreds of nanometers up to several micrometers and is too large for a quantum mechanical description. The magnetization is supposed to be a continuous vector field which changes under the influence of external as well as effective magnetic fields. The latter have their origin in internal interactions. The time evolution of the magnetization is described by an equation that was introduced by L. D. Landau and E. M. Lifshitz.[127,128] Its area of applicability lies between tens of nanometers and hundreds of micrometers. The lower boundary is due to the non-continuity of real materials and the quantum nature of elementary spins. The upper boundary is a result of the calculation time and memory requirements.

A spin-polarized current flowing through a ferromagnetic sample interacts with the magnetization and exerts a torque on the local magnetic moments. For conduction electron spins that follow the local magnetization adiabatically it has been shown that the interaction via spin transfer can be described by adding a current-dependent term to the Landau-Lifshitz-Gilbert equation.[23] This equation has been extended by an additional term that takes the non-adiabatic influence of the itinerant spins into account.[24] In most cases the resulting equations are too complex for an exact analytical solution. However, it is possible to perform analytical calculations using some approximations or numerical calculations.

There are several programs that can be used for micromagnetic simulations including the action of a spin-polarized current.[129–138] The numerical simulations that are presented in this work where performed using the Object Oriented MicroMagnetic Framework (OOMMF).[139] This program has been extended by the author of this work to include the action of a spin-polarized current.[129]

This work is organized as follows. The first part introduces the fundamentals that are needed in the subsequent sections. This includes the micromagnetic model, the influence of a spin-polarized current on the magnetization, magnetic vortices, magnetic antivortices, and magnetic domain walls. In the second part analytical and numerical calculations that describe the dynamics of magnetic vortices and antivortices are presented. The dynamics can be due to an external magnetic field, a spin-polarized current traversing the sample, and the Oersted field generated by this current. This part ends with a section that describes memory devices that base on vortices and antivortices like the aforementioned VRAM and AVRAM. The dynamics of domain walls is discussed in the third part. First the free domain wall is investigated by analytical and numerical calculations. This investigation is then extended to the interaction of a domain wall with pinning centers and other walls. A conclusion and an outlook is given in the fourth part. The appendices contain calculations

that base on standard techniques like solving of differential equations and evaluation of integrals and derivatives.

Part I
Fundamentals

In this part we introduce the fundamentals that are needed for the calculations in the subsequent parts. In the first section the Landau-Lifshitz equation is derived from quantum mechanics by the aid of a semiclassical continuum limit. Then the different energies that influences the magnetization dynamics are introduced. With this knowledge we will discuss how magnetic vortices, antivortices, and domain walls emerge. The third section describes the extension of the Landau-Lifshitz equation to include the spin-transfer torque. Finally the constraints of the micromagnetic model are discussed.

1 Landau-Lifshitz Equation

L. D. Landau and E. M. Lifshitz proposed an equation that describes the dynamics of the magnetization in a ferromagnetic body.[127,128] In this section we will discuss a quantum mechanical derivation of this equation.

We start with the quantum mechanical Heisenberg equation of a single spin $\vec{S}$. The dynamic behavior of $\vec{S}$ is written as

$$\frac{dS_j}{dt} = \frac{i}{\hbar}[\hat{H}, S_j] = \frac{i}{\hbar}\left(\sum_k \frac{\partial \hat{H}}{\partial S_k}[S_k, S_j] + O(\hbar^2)\right) \tag{1.1}$$

with the Hamiltonian $\hat{H}$ of the system. $O(\hbar^2)$ denotes a function that is at least of quadratic order in $\hbar$. The commutation relation for two components of the spin yields $[S_k, S_j] = -i\hbar\sum_l \epsilon_{jkl} S_l$. Inserting this in equation (1.1) we get

$$\frac{dS_j}{dt} = \sum_{k,l} \frac{\partial \hat{H}}{\partial S_k}\epsilon_{jkl} S_l + O(\hbar) \tag{1.2}$$

for the j-th component of $\vec{S}$. In vector notation this is

$$\frac{d\vec{S}}{dt} = -\vec{S} \times \frac{\partial \hat{H}}{\partial \vec{S}} + O(\hbar) \tag{1.3}$$

with $\partial/\partial\vec{S}$ defined as $\partial/\partial\vec{S} = (\partial/\partial S_x, \partial/\partial S_y, \partial/\partial S_z)$.

In a semi-classical approximation we replace the spins $\vec{S}$ that are discrete in space and orientation by the continuous vector field of the magnetization $\vec{M}$ and use the limit $\hbar \to 0$. This approximation is valid when the characteristic length scale on which the magnetization changes its direction is large compared to the distance of the spins. The time derivative of the magnetization is thus given by

$$\frac{d\vec{M}}{dt} = -\gamma \vec{M} \times \vec{H}_{\text{eff}} \tag{1.4}$$

with the gyromagnetic ratio $\gamma = g\mu_0\mu_B/\hbar$ and an effective field

$$\vec{H}_{\text{eff}} = \frac{1}{\gamma}\left\langle \frac{\partial \hat{H}}{\partial \vec{S}} \right\rangle = -\frac{1}{\mu_0}\frac{dE}{d\vec{m}_s} \tag{1.5}$$

that depends on the current state of the system with energy E. $\vec{m}_s = -g\mu_B\vec{S}/\hbar$ denotes the magnetic moment of the spin at the point of the magnetic field. In the continuum limit the effective field is

$$\vec{H}_{\text{eff}} = -\frac{1}{\mu_0}\frac{\delta E}{\delta \vec{M}} \tag{1.6}$$

where δ denotes the variational derivative defined as

$$\frac{\delta E[\vec{M}(\vec{r})]}{\delta \vec{M}(\vec{r}_0)} = \lim_{\epsilon \to 0} \frac{1}{\epsilon} \begin{pmatrix} E[\vec{M}(\vec{r}) + \epsilon \vec{e}_x \delta^3(\vec{r} - \vec{r}_0)] - E[\vec{M}(\vec{r})] \\ E[\vec{M}(\vec{r}) + \epsilon \vec{e}_y \delta^3(\vec{r} - \vec{r}_0)] - E[\vec{M}(\vec{r})] \\ E[\vec{M}(\vec{r}) + \epsilon \vec{e}_z \delta^3(\vec{r} - \vec{r}_0)] - E[\vec{M}(\vec{r})] \end{pmatrix}. \tag{1.7}$$

Equation (1.4) describes the precession of the magnetization around the effective field. This precession keeps the energy constant since

$$\frac{dE}{dt} = \int dV \, \frac{\delta E}{\delta \vec{M}} \frac{d\vec{M}}{dt} = \int dV \, \left(-\mu_0 \vec{H}_{\text{eff}}\right) \left(-\gamma \vec{M} \times \vec{H}_{\text{eff}}\right) = 0. \tag{1.8}$$

To account for some dissipative force, which is present at a macroscopic level, a phenomenological damping term can be added to equation (1.4). L. D. Landau and E. M. Lifshitz introduced the term $-(\lambda_{\text{LL}}/M_S^2)\vec{M} \times (\vec{M} \times \vec{H}_{\text{eff}})$ with $\lambda_{\text{LL}} \ll \gamma M_s$. For $\lambda_{\text{LL}} = 1$ this is the part of the magnetic field that is perpendicular to the magnetization.[127] The new term thus rotates the magnetization towards the direction of the field. The time derivative of the magnetization is then given by

$$\frac{d\vec{M}}{dt} = -\gamma \vec{M} \times \vec{H}_{\text{eff}} - \frac{\lambda_{\text{LL}}}{M_S^2} \vec{M} \times \left(\vec{M} \times \vec{H}_{\text{eff}}\right). \tag{1.9}$$

T. L. Gilbert proposed the term $(\alpha/M_s)\vec{M} \times d\vec{M}/dt$ with $\alpha \ll 1$. This yields[140]

$$\frac{d\vec{M}}{dt} = -\gamma \vec{M} \times \vec{H}_{\text{eff}} + \frac{\alpha}{M_s} \vec{M} \times \frac{d\vec{M}}{dt}. \tag{1.10}$$

We will see that both terms lead to similar results. Both equations do not change the saturation magnetization $M_s = |\vec{M}|$ as the time derivatives

$$\frac{d}{dt} M_s^2 = \frac{d}{dt} \left(\vec{M}\right)^2 = 2\vec{M} \frac{d\vec{M}}{dt} = 2\vec{M} \left[-\gamma \vec{M} \times \vec{H}_{\text{eff}} - \frac{\lambda_{\text{LL}}}{M_S^2} \vec{M} \times \left(\vec{M} \times \vec{H}_{\text{eff}}\right)\right] = 0 \tag{1.11}$$

and

$$\frac{d}{dt} M_s^2 = \frac{d}{dt} \left(\vec{M}\right)^2 = 2\vec{M} \frac{d\vec{M}}{dt} = 2\vec{M} \left[-\gamma \vec{M} \times \vec{H}_{\text{eff}} + \frac{\alpha}{M_s} \vec{M} \times \frac{d\vec{M}}{dt}\right] = 0 \tag{1.12}$$

vanish.

Equation (1.10) is implicit in the time derivative of the magnetization. To get an explicit differential equation we take the vector product with $\vec{M}$ on both sides and get

$$\vec{M} \times \frac{d\vec{M}}{dt} = -\gamma \vec{M} \times \left(\vec{M} \times \vec{H}_{\text{eff}}\right) + \frac{\alpha}{M_s} \left[\underbrace{\left(\vec{M} \frac{d\vec{M}}{dt}\right)}_{=\frac{1}{2}\frac{d}{dt}M_s^2 = 0} \vec{M} - \underbrace{\left(\vec{M}\vec{M}\right)}_{=M_s^2} \frac{d\vec{M}}{dt} \right] \tag{1.13}$$

where the Grassmann identity

$$\vec{a} \times (\vec{b} \times \vec{c}) = (\vec{a}\vec{c})\vec{b} - (\vec{a}\vec{b})\vec{c} \tag{1.14}$$

has been used to simplify the second term on the right-hand side. Inserting equation (1.13) into equation (1.10) we get

$$\frac{d\vec{M}}{dt} = -\gamma \vec{M} \times \vec{H}_{\text{eff}} + \frac{\alpha}{M_s} \left(-\gamma \vec{M} \times \left(\vec{M} \times \vec{H}_{\text{eff}}\right) - \alpha M_s \frac{d\vec{M}}{dt}\right). \tag{1.15}$$

Moving the last term on the right-hand side to the left-hand side and dividing by $(1+\alpha^2)$ yields

$$\frac{d\vec{M}}{dt} = -\frac{\gamma}{1+\alpha^2}\vec{M}\times\vec{H}_{\text{eff}} - \frac{\gamma}{1+\alpha^2}\frac{\alpha}{M_S}\vec{M}\times\left(\vec{M}\times\vec{H}_{\text{eff}}\right). \tag{1.16}$$

The motion of the magnetization consists of a non-dissipative precession around the effective magnetic field and a damping that changes the direction of the magnetization in the direction of the field. Introducing the effective gyromagnetic ration $\gamma' = \gamma/(1+\alpha^2)$ this equation becomes

$$\frac{d\vec{M}}{dt} = -\gamma'\vec{M}\times\vec{H}_{\text{eff}} - \frac{\gamma'\alpha}{M_S}\vec{M}\times\left(\vec{M}\times\vec{H}_{\text{eff}}\right). \tag{1.17}$$

With $\lambda_{\text{LL}} = \gamma\alpha M_S$ equations (1.17) and (1.9) differ only by a factor of $1+\alpha^2$ that leads to a renormalization of the gyromagnetic ratio γ for the case of Gilbert damping. This renormalization does not affect a static magnetization pattern. It is important for the dynamics only. Experimental investigations at permalloy samples found that α is about 0.01.[141–143] Since $\alpha^2 \ll 1$ in many materials, it is hard to experimentally distinguish between both damping terms. In this work the damping term of T. L. Gilbert will be used.

To calculate the rate at which energy is dissipated we take the cross product of equation (1.10) with the magnetization and apply the vector expression in equation (1.14) on both terms on the right-hand side. This yields

$$\vec{M}\times\frac{d\vec{M}}{dt} = -\gamma\left[\left(\vec{M}\vec{H}_{\text{eff}}\right)\vec{M} - M_s^2\vec{H}_{\text{eff}}\right] - \alpha M_s\frac{d\vec{M}}{dt} \tag{1.18}$$

which can be written as

$$\vec{H}_{\text{eff}} = \frac{1}{\gamma M_s^2}\vec{M}\times\frac{d\vec{M}}{dt} + \frac{1}{M_s^2}\left(\vec{M}\vec{H}_{\text{eff}}\right)\vec{M} + \frac{\alpha}{\gamma M_s}\frac{d\vec{M}}{dt}. \tag{1.19}$$

This expression allows for a calculation of the rate of energy dissipation similar as in equation (1.8). We find the time derivative of the energy as[144]

$$\begin{aligned}\frac{dE}{dt} &= \int dV\,\frac{\delta E}{\delta\vec{M}}\frac{d\vec{M}}{dt} = -\mu_0\int dV\,\vec{H}_{\text{eff}}\frac{d\vec{M}}{dt}\\ &= -\mu_0\int dV\,\left(\frac{1}{\gamma M_s^2}\vec{M}\times\frac{d\vec{M}}{dt} + \frac{1}{M_s^2}\left(\vec{M}\vec{H}_{\text{eff}}\right)\vec{M} + \frac{\alpha}{\gamma M_s}\frac{d\vec{M}}{dt}\right)\frac{d\vec{M}}{dt}\\ &= -\frac{\mu_0\alpha}{\gamma M_s}\int dV\,\left(\frac{d\vec{M}}{dt}\right)^2.\end{aligned} \tag{1.20}$$

This expression vanishes for a static magnetization and is negative for a dynamic system. Thus in a dynamic system the energy is dissipated.

2 Effective Fields

Equation (1.17) allows for a calculation of the evolution of the magnetization in time. For this calculation the knowledge of the effective magnetic field is needed. This field is calculated from the energy of the system that can have several contributions like the Zeeman energy, the exchange energy, the demagnetization energy, and the anisotropy energy. In this section we will discuss these energy contributions and calculate the respective effective fields.

2.1 Zeeman Energy

The Zeeman energy is the energy of the magnetization in an external magnetic field. This energy is given as

$$E_Z = -\int dV \mu_0 \vec{H}\vec{M}. \tag{2.1}$$

Its effective magnetic field is given by

$$\vec{H}_Z = \vec{H}. \tag{2.2}$$

2.2 Exchange Energy

The exchange energy is of quantum origin. For the calculation of the exchange energy we restrict ourselves to the interaction between neighboring spins. Then the exchange energy is given by a Heisenberg type interaction between neighboring spins in the crystal lattice

$$E_E = -J\sum_{\langle i,j\rangle} \vec{S}_i\vec{S}_j \tag{2.3}$$

where the sum is taken over all neighboring spins and J is the exchange integral. This expression can be rewritten as

$$E_E = -J\sum_i\sum_{nn} \vec{S}_i\vec{S}_{nn} = -JS^2\sum_i\sum_{nn} \cos(\phi_{i,nn}) \tag{2.4}$$

where nn denotes the nearest neighbors of the i-th spin and $\phi_{i,nn}$ is the angle between the i-th spin and the accordant next neighbor.

With the aid of the magnetization and the law of cosines we can write

$$\left(\vec{M}(\vec{r}_i + \vec{r}_{nn}) - \vec{M}(\vec{r}_i)\right)^2 = 2M_s^2 - 2M_s^2\cos(\phi_{i,nn}) \tag{2.5}$$

where $\vec{r}_{nn}$ is the distance between a spin and its next neighbors. This expression yields an energy of

$$E_E = \frac{JS^2}{2M_s^2}\sum_i\sum_{nn} \left(\vec{M}(\vec{r}_i + \vec{r}_{nn}) - \vec{M}(\vec{r}_i)\right)^2 \tag{2.6}$$

where the term that is constant in the magnetization is neglected. As discussed in section 1 the continuum limit is valid only if the characteristic length scale on which the orientation of the magnetization changes is large compared to the distance between two spins. Thus the angles between two neighboring spins have to be small and the magnetization can be expanded in a Taylor series up to the first order. The energy is thus given by

$$E_E = \frac{JS^2}{2M_s^2}\sum_i\sum_{nn} \left((\vec{r}_{nn}\vec{\nabla})\vec{M}(\vec{r}_i)\right)^2. \tag{2.7}$$

For a cubic lattice with lattice constant a each spin has six next neighbors with the distances $\vec{r}_{c,1} = (a,0,0)$, $\vec{r}_{c,2} = (-a,0,0)$, $\vec{r}_{c,3} = (0,a,0)$, $\vec{r}_{c,4} = (0,-a,0)$, $\vec{r}_{c,5} = (0,0,a)$, and $\vec{r}_{c,6} = (0,0,-a)$. For a body-centered cubic lattice each spin has eight next neighbors with the distances $\vec{r}_{bcc,1} = (a/2,a/2,a/2)$, $\vec{r}_{bcc,2} = (-a/2,a/2,a/2)$, $\vec{r}_{bcc,3} = (a/2,-a/2,a/2)$, $\vec{r}_{bcc,4} = (-a/2,-a/2,a/2)$, $\vec{r}_{bcc,5} = (a/2,a/2,-a/2)$, $\vec{r}_{bcc,6} = (-a/2,a/2,-a/2)$, $\vec{r}_{bcc,7} = (a/2,-a/2,-a/2)$, and $\vec{r}_{bcc,8} = (-a/2,-a/2,-a/2)$. For a face-centered cubic lattice each spin has twelve next neighbors with the distances $\vec{r}_{fcc,1} = (0,a/2,a/2)$, $\vec{r}_{fcc,2} = (0,-a/2,a/2)$, $\vec{r}_{fcc,3} = (0,a/2,-a/2)$, $\vec{r}_{fcc,4} = (0,-a/2,-a/2)$, $\vec{r}_{fcc,5} = (a/2,0,a/2)$, $\vec{r}_{fcc,6} = (-a/2,0,a/2)$, $\vec{r}_{fcc,7} = (a/2,0,-a/2)$, $\vec{r}_{fcc,8} = (-a/2,0,-a/2)$, $\vec{r}_{fcc,9} = (a/2,a/2,0)$, $\vec{r}_{fcc,10} = (-a/2,a/2,0)$, $\vec{r}_{fcc,11} = (a/2,-a/2,0)$, and $\vec{r}_{fcc,12} = (-a/2,-a/2,0)$. For all three lattice types we get the energy

$$E_E = \frac{JS^2}{2M_s^2}\sum_i \left(2a^2\left(\frac{\partial\vec{M}}{\partial x}\right)^2 + 2a^2\left(\frac{\partial\vec{M}}{\partial y}\right)^2 + 2a^2\left(\frac{\partial\vec{M}}{\partial z}\right)^2\right). \tag{2.8}$$

Using the density c_s/a^3 of the spins where c_s is then number of spins per unit cell we get

$$E_E = \frac{Ja^2S^2}{M_s^2}\int dV\ \frac{c_s}{a^3}\left(\left(\frac{\partial\vec{M}}{\partial x}\right)^2+\left(\frac{\partial\vec{M}}{\partial y}\right)^2+\left(\frac{\partial\vec{M}}{\partial z}\right)^2\right) \tag{2.9}$$

with $c_s = 1$ for a cubic lattice, $c_s = 2$ for a body centered cubic lattice and $c_s = 4$ for a face centered cubic lattice. This is usually written as

$$E_E = \frac{A}{M_s^2}\int dV\ \left(\left(\frac{\partial\vec{M}}{\partial x}\right)^2+\left(\frac{\partial\vec{M}}{\partial y}\right)^2+\left(\frac{\partial\vec{M}}{\partial z}\right)^2\right) \tag{2.10}$$

where $A = Jc_sS^2/a$ is the so called exchange constant.

From this the effective exchange field evolves as

$$\begin{aligned}\vec{H}_E(\vec{r}) &= -\frac{1}{\mu_0}\frac{\delta E_E}{\delta\vec{M}(\vec{r})}\\ &= -\frac{2A}{\mu_0 M_s^2}\int dV'\left(\frac{\partial\vec{M}(\vec{r}')}{\partial x'}\frac{\partial\delta^3(r'-r)}{\partial x'}+\frac{\partial\vec{M}(\vec{r}')}{\partial y'}\frac{\partial\delta^3(r'-r)}{\partial y'}+\frac{\partial\vec{M}(\vec{r}')}{\partial z'}\frac{\partial\delta^3(r'-r)}{\partial z'}\right)\end{aligned} \tag{2.11}$$

Integration by parts leads to

$$\begin{aligned}\vec{H}_E(\vec{r}) &= \frac{2A}{\mu_0 M_s^2}\int dV'\left(\frac{\partial^2\vec{M}(\vec{r}')}{\partial x'^2}\delta^3(r'-r)+\frac{\partial^2\vec{M}(\vec{r}')}{\partial y'^2}\delta^3(r'-r)+\frac{\partial^2\vec{M}(\vec{r}')}{\partial z'^2}\delta^3(r'-r)\right)\\ &= \frac{2A}{\mu_0 M_s^2}\left(\frac{\partial^2\vec{M}}{\partial x^2}+\frac{\partial^2\vec{M}}{\partial y^2}+\frac{\partial^2\vec{M}}{\partial z^2}\right)\\ &= \frac{2A}{\mu_0 M_s^2}\nabla^2\vec{M}.\end{aligned} \tag{2.12}$$

In the integration by parts the boundary terms vanish because of the delta function that is localized at $\vec{r}$.

2.3 Demagnetization Energy

The magnetization at two different points of the sample interacts via the long range dipolar interaction. In the absence of currents and electric fields Ampère's law

$$\vec{\nabla}\times\vec{H} = 0 \tag{2.13}$$

yields that the magnetic field $\vec{H}$ is conservative. Thus the magnetic field can be written as the gradient of a potential Φ_M. The magnetic field is then given by

$$\vec{H} = -\vec{\nabla}\Phi_M. \tag{2.14}$$

From Gauss's law for magnetism

$$\vec{\nabla}\cdot\vec{B} = 0 \tag{2.15}$$

we find that the magnetic flux density $\vec{B}$ is solenoidal. The relation

$$\vec{B} = \mu_0(\vec{H}+\vec{M}) \tag{2.16}$$

between the magnetic flux density, the magnetic field, and the magnetization yields that the divergence of the magnetic field is given by the negative divergence of the magnetization. Then, the potential Φ_M fulfills the Poisson equation

$$\vec{\nabla}^2\Phi_M = -\vec{\nabla}\vec{H} = \vec{\nabla}\vec{M}. \tag{2.17}$$

The magnetic potential can thus be written as[145]

$$\Phi_M(\vec{r}) = \frac{1}{4\pi}\int dV' \frac{1}{|\vec{r}-\vec{r'}|}\left(-\vec{\nabla}'\vec{M}(\vec{r'})\right) + \frac{1}{4\pi}\int d\vec{A'}\frac{1}{|\vec{r}-\vec{r'}|}\vec{M}(\vec{r'}) \tag{2.18}$$

where $\vec{A'} = A'\vec{n}(\vec{r'})$. V' is the volume and A' is the surface of the sample. $\vec{n}(\vec{r'})$ is the normal component of the surface at position $\vec{r'}$. The first term in equation (2.18) is the solution of the Poisson equation and the second term accounts for the boundary conditions. From the potential the magnetic field can be calculated as

$$\vec{H}(\vec{r}) = -\vec{\nabla}\frac{1}{4\pi}\left(\int dV' \frac{1}{|\vec{r}-\vec{r'}|}\left(-\vec{\nabla}'\vec{M}(\vec{r'})\right) + \int d\vec{A'}\frac{1}{|\vec{r}-\vec{r'}|}\vec{M}(\vec{r'})\right). \tag{2.19}$$

The magnetostatic energy can be derived from the product of the magnetization and the magnetic field. It yields

$$\begin{aligned} E_D &= -\frac{\mu_0}{2}\int dV\ \vec{M}(\vec{r})H(\vec{r}) \\ &= \frac{\mu_0}{8\pi}\int dV\ \vec{M}(\vec{r})\vec{\nabla}\left(\int dV' \frac{1}{|\vec{r}-\vec{r'}|}\left(-\vec{\nabla}'\vec{M}(\vec{r'})\right) + \int d\vec{A'}\frac{1}{|\vec{r}-\vec{r'}|}\vec{M}(\vec{r'})\right). \end{aligned} \tag{2.20}$$

The factor 1/2 stems from the fact that we integrate over the volume twice. Exchanging the order of integrals, the energy can also be written as

$$E_D = \frac{\mu_0}{8\pi}\int \left(dV'\ \left(-\vec{\nabla}'\vec{M}(\vec{r'})\right) + d\vec{A'}\ \vec{M}(\vec{r'})\right)\int dV\ \vec{M}(\vec{r})\vec{\nabla}\frac{1}{|\vec{r}-\vec{r'}|}. \tag{2.21}$$

Using the divergence theorem we find

$$\begin{aligned} \int d\vec{A}\frac{1}{|\vec{r}-\vec{r'}|}\vec{M}(\vec{r}) &= \int dV\vec{\nabla}\left(\frac{1}{|\vec{r}-\vec{r'}|}\vec{M}(\vec{r})\right) \\ &= \int dV\frac{1}{|\vec{r}-\vec{r'}|}\vec{\nabla}\vec{M}(\vec{r}) + \int dV\vec{M}(\vec{r})\vec{\nabla}\frac{1}{|\vec{r}-\vec{r'}|}. \end{aligned} \tag{2.22}$$

Rewriting the last integral in equation (2.21) by means of equation (2.22) yields

$$E_D = \frac{\mu_0}{8\pi}\int \left(dV\ \left(-\vec{\nabla}\vec{M}(\vec{r})\right) + d\vec{A}\,\vec{M}(\vec{r})\right)\int \left(dV'\ \left(-\vec{\nabla}'\vec{M}(\vec{r'})\right) + d\vec{A'}\ \vec{M}(\vec{r'})\right)\frac{1}{|\vec{r}-\vec{r'}|}. \tag{2.23}$$

This can be brought in the usual form

$$E_D = \frac{\mu_0}{8\pi}\int \left(dV\ \rho_v(\vec{r}) + dA\,\sigma_s(\vec{r})\right)\int dV'\left(dV'\ \rho_v(\vec{r'}) + dA'\,\sigma_s(\vec{r'})\right)\frac{1}{|\vec{r}-\vec{r'}|} \tag{2.24}$$

with the so called volume charges

$$\rho_v(\vec{r}) = -\vec{\nabla}\vec{M}(\vec{r}) \tag{2.25}$$

and surface charges

$$\sigma_s(\vec{r}) = \vec{M}(\vec{r})\vec{n}(\vec{r}). \tag{2.26}$$

One can see that these charges are minimized by a flux-closure magnetization pattern where the flux of the magnetization has no source or drain.[146,147]

With the aid of equation (2.22) it is also possible to rewrite equation (2.20) as

$$\begin{aligned} E_D &= \frac{\mu_0}{8\pi} \int dV \int dV' \, \vec{M}(\vec{r}) \vec{\nabla} \left(\vec{M}(\vec{r}') \vec{\nabla}' \frac{1}{\sqrt{(\vec{r}-\vec{r}')^2}} \right) \\ &= \frac{\mu_0}{8\pi} \int dV \int dV' \, \vec{M}(\vec{r}) \vec{\nabla} \frac{\vec{M}(\vec{r}')(\vec{r}-\vec{r}')}{\sqrt{(\vec{r}-\vec{r}')^2}^3} \\ &= \frac{\mu_0}{8\pi} \int dV \int dV' \left(\frac{\vec{M}(\vec{r})\vec{M}(\vec{r}')}{\sqrt{(\vec{r}-\vec{r}')^2}^3} - 3 \frac{(\vec{M}(\vec{r})(\vec{r}-\vec{r}'))(\vec{M}(\vec{r}')(\vec{r}-\vec{r}'))}{\sqrt{(\vec{r}-\vec{r}')^2}^5} \right). \end{aligned} \tag{2.27}$$

This is the energy of a field of dipoles with the dipole density $\vec{M}(\vec{r})$ at position $\vec{r}$.

2.4 Anisotropy Energy

Some materials exhibit an intrinsic anisotropy that is also present in bulk materials. The most common examples are the uniaxial anisotropy and the cubic anisotropy. Both are described in the following.

Uniaxial Anisotropy Energy

In the case of materials with hexagonal lattices like cobalt, gadolinium, or dysprosium, there is a principal axis that points out of the hexagonal plane. This leads to an uniaxial anisotropy. This type of anisotropy can be also caused by a layered structure of the sample where the principal axis is perpendicular to the layers. Here we assume for simplicity the principal axis to be parallel to the z-axis. The uniaxial anisotropy energy should be even in M_z to show the same mirroring symmetry as the lattice or layer. This can lead to[148]

$$E_U = -\int dV \left(K_{u1} \frac{M_z^2}{M_s^2} + K_{u2} \frac{M_z^4}{M_s^4} \right) \tag{2.28}$$

where higher orders in M_z have been neglected. The corresponding anisotropy field is given by

$$\vec{H}_U = -\frac{1}{\mu_0} \frac{\delta E_U}{\delta \vec{M}} = \frac{2K_{u1}}{\mu_0 M_s^2} \begin{pmatrix} 0 \\ 0 \\ M_z \end{pmatrix} + \frac{4K_{u2}}{\mu_0 M_s^4} \begin{pmatrix} 0 \\ 0 \\ M_z^3 \end{pmatrix}. \tag{2.29}$$

Cubic Anisotropy Energy

Some ferromagnetic materials like iron (body-centered cubic) or nickel (face-centered cubic) have lattices with cubic symmetry. Because the rotational symmetry of such materials is broken it is likely that some kind of anisotropy occurs. The energy of the cubic anisotropy is determined by the following phenomenological ansatz. The energy is a function of the three components of the magnetization M_x, M_y and M_z. We use a series expansion of powers of all three components up to sixth order. The function has to be even in all three components because mirroring should not change the anisotropy energy. Due to the symmetry of rotation by 90 degrees we find that all terms have to be invariant under the exchange of two components, for example M_x^2 is replaced by M_y^2 and vice versa. Utilizing these criteria we are left with six linearly independent terms, namely M_s^2, M_s^4, M_s^6, $M_x^2 M_y^2 M_z^2$, $M_x^2 M_y^2 + M_x^2 M_z^2 + M_y^2 M_z^2$, and $(M_x^2 M_y^2 + M_x^2 M_z^2 + M_y^2 M_z^2) M_s^2$. Since M_s is constant, the first three terms do not depend on the magnetization and can be neglected. The last two terms differ by a constant factor. Thus we need to take into account $M_x^2 M_y^2 + M_x^2 M_z^2 + M_y^2 M_z^2$ and $M_x^2 M_y^2 M_z^2$ only. The energy for the cubic anisotropy then yields[148]

$$E_C = \int dV \left(K_{c1} \frac{M_x^2 M_y^2 + M_x^2 M_z^2 + M_y^2 M_z^2}{M_s^4} + K_{c2} \frac{M_x^2 M_y^2 M_z^2}{M_s^6} \right) \tag{2.30}$$

and the corresponding anisotropy field is

$$\vec{H}_C = -\frac{1}{\mu_0}\frac{\delta E_C}{\delta \vec{M}} = -\frac{2K_{c1}}{\mu_0 M_s^4}\begin{pmatrix} M_x M_y^2 + M_x M_z^2 \\ M_x^2 M_y + M_y M_z^2 \\ M_x^2 M_z + M_y^2 M_z \end{pmatrix} - \frac{2K_{c2}}{\mu_0 M_s^6}\begin{pmatrix} M_x M_y^2 M_z^2 \\ M_x^2 M_y M_z^2 \\ M_x^2 M_y^2 M_z \end{pmatrix}. \tag{2.31}$$

3 Current-Induced Spin-Torque

Beside a magnetic field there is another possibility to excite or influence a ferromagnetic system. This is the spin-transfer torque. The spin-transfer torque can be explained by means of the sd-model that is usually used for the description of 3d transition metals like iron, cobalt, and nickel.[19–23] In this model the magnetization is mainly contributed by the 3d electrons. Because of their high effective mass these electrons can be seen as localized. The current flow is due to itinerant 4s electrons. Due to the exchange interaction between the 3d and the 4s electrons, called sd-interaction, the spins of the 4s electrons align in the same direction as the spins of the local 3d electrons.

The adiabatic spin-transfer torque can now be explained as follows. In a part of the sample where the magnetization varies in space the spins of the 3d electrons have to vary as well. When a 4s electron passes this part its spin is assumed to follow the local spins adiabatically. Due to the conservation of angular momentum the spin from the itinerant electron has to be transfered to one or more local electrons. This leads to a change in the magnetization. Y. B. Bazaliy et *al.* showed that the influence of this adiabatic spin-transfer torque on the magnetization can be described by an additional term in equation (1.10). They found[23]

$$\frac{d\vec{M}}{dt} = -\gamma\vec{M}\times\vec{H}_{\text{eff}} + \frac{\alpha}{M_s}\vec{M}\times\frac{d\vec{M}}{dt} - \frac{b_j}{M_s^2}\vec{M}\times(\vec{M}\times(\vec{j}\vec{\nabla})\vec{M}) \tag{3.1}$$

with the current density $\vec{j}$ and the coupling constant $b_j = \mu_B P/(eM_s)$ between the current and the magnetization. Here μ_B is the Bohr magneton and e is the elementary charge. P is the polarization of the current.

In this picture the dynamics of the localized electrons experiences an energy dissipation that is described by the second term on the right-hand side of equation (3.1). In contrast the spin of the itinerant electrons is fully transferred to the localized electrons, that is, the itinerant electrons do not experience any damping. S. Zhang and Z. Li calculated the dynamics of the magnetization for a system in which the electrons do not follow the magnetization adiabatically.[24] Their calculations base upon the spin continuity equation of the itinerant electrons. For more informations see appendix A. In this equation they introduce a phenomenological damping term within a relaxation-time approximation. The strength of the damping is described by the parameter $\xi = \tau_{\text{ex}}/\tau_{\text{sf}}$. Here τ_{ex} and τ_{sf} are the relaxation times of the itinerant spins due to the sd-interaction and spin flips, respectively. Currently there is a large endeavor to describe the source of this damping theoretically.[24, 149–152]

The result of S. Zhang and Z. Li is a second current dependent term that describes effects which occur due to the non-adiabatic spin torque. Equation (1.10) then yields

$$\frac{d\vec{M}}{dt} = -\gamma\vec{M}\times\vec{H}_{\text{eff}} + \frac{\alpha}{M_s}\vec{M}\times\frac{d\vec{M}}{dt} \underbrace{-\frac{b_j}{M_s^2}\vec{M}\times(\vec{M}\times(\vec{j}\vec{\nabla})\vec{M})}_{\text{adiabatic spin torque}} \underbrace{-\frac{\xi b_j}{M_s}\vec{M}\times(\vec{j}\vec{\nabla})\vec{M}}_{\substack{\text{non-adiabatic} \\ \text{spin torque}}}. \tag{3.2}$$

The non-adiabatic spin torque also affects the coupling constant between the current and the magnetization. This constant now yields $b_j = \mu_B P/[eM_s(1+\xi^2)]$.

A. Thiaville et *al.* found the same expression but without the additional factor $1+\xi^2$ in b_j. In their theory b_j remains the same as for the adiabatic case.[153] Since ξ is assumed to be smaller

than one this difference is comparable with the factor $1+\alpha^2$ that is the difference between the two theories in section 1.

Equation (3.2) can be brought to an explicit equation in a similar way as equation (1.10). The result is

$$\begin{aligned}\frac{d\vec{M}}{dt} =& -\gamma'\vec{M}\times\vec{H}_{\text{eff}} - \frac{\gamma'\alpha}{M_S}\vec{M}\times\left(\vec{M}\times\vec{H}_{\text{eff}}\right) \\ & \underbrace{-(1+\xi\alpha)\frac{b'_j}{M_s^2}\vec{M}\times\left(\vec{M}\times(\vec{j}\vec{\nabla})\vec{M}\right)}_{\text{motion term}} \underbrace{-(\xi-\alpha)\frac{b'_j}{M_s}\vec{M}\times(\vec{j}\vec{\nabla})\vec{M}}_{\text{distortion term}}\end{aligned} \tag{3.3}$$

where $b'_j = b_j/(1+\alpha^2)$. The two current-dependent terms in equation (3.3) that are labeled as motion term and distortion term both consist of adiabatic and non-adiabatic spin-torque contributions. The labeling is due to the following considerations. In a homogeneous material the saturation magnetization is constant and thus independent of the position. Then the spatial derivative of the magnetization is perpendicular to the magnetization since

$$\vec{M}(\vec{\nabla}\vec{M}) = \vec{\nabla}(\vec{M})^2/2 = \vec{\nabla}M_s^2/2 = 0. \tag{3.4}$$

In this case we can use equation (1.14) to rewrite the motion term. For $\xi=\alpha$ the distortion term vanishes. This leads to the equation

$$\frac{d\vec{M}}{dt} = -\gamma'\vec{M}\times\vec{H}_{\text{eff}} - \frac{\gamma'\alpha}{M_S}\vec{M}\times\left(\vec{M}\times\vec{H}_{\text{eff}}\right) - (\vec{u}\vec{\nabla})\vec{M} \tag{3.5}$$

with the speed $\vec{u} = -b_j\vec{j}$ of the magnetization pattern. It becomes obvious that for $\xi=\alpha$ the current leads to a motion of the magnetization pattern in the direction of the electron flow. For $\xi\neq\alpha$ the distortion term becomes non-zero and the pattern is not only shifted but also distorted.

Equations (3.2) and (3.3) are the central equations which we will exploit in the rest of this work.

4 Magnetic Vortices and Antivortices

Vortices and antivortices are formed in nanostructured thin-film elements due to the interplay of the exchange and the demagnetization energy. The demagnetization energy forces the magnetization in the film plane to reduce the surface charges. For a range of lateral sizes of the element the in-plane magnetization curls around a center region[39,146,154,155] as shown in figures 4.1(a) and (b). For a magnetization that is fully in-plane the exchange energy in the center would become infinite as two regions with opposite magnetization are close together. To lower the exchange energy[31] the magnetization is thus forced to turn out-of-plane in a few-nanometer-large center region[34] as shown in figure 4.1(c). This region is called the vortex or antivortex core. The actual shape of the core is given by the minimization of the total energy. An increasing exchange energy would broaden the core while an increasing demagnetization energy would shrink it. In general thin-film elements it is possible to obtain magnetization pattern with several vortices and antivortices.[146] Figure 4.1 shows four examples of structures where a single vortex or antivortex can be stable.

The out-of-plane magnetization in the core can have two possible orientations that are labeled by the polarization p which can assume the values $p=+1$ and $p=-1$ depending on whether the magnetization in the core points parallel or antiparallel to the out-of-plane axis, that is the z axis in figure 4.1(c). A parallel alignment is denoted by $p=+1$ while an antiparallel alignment is denoted by $p=-1$.

The in-plane magnetization of a vortex or an antivortex is described by the parameterization

$$\phi = n\beta + \frac{\pi c}{2}, \tag{4.1}$$

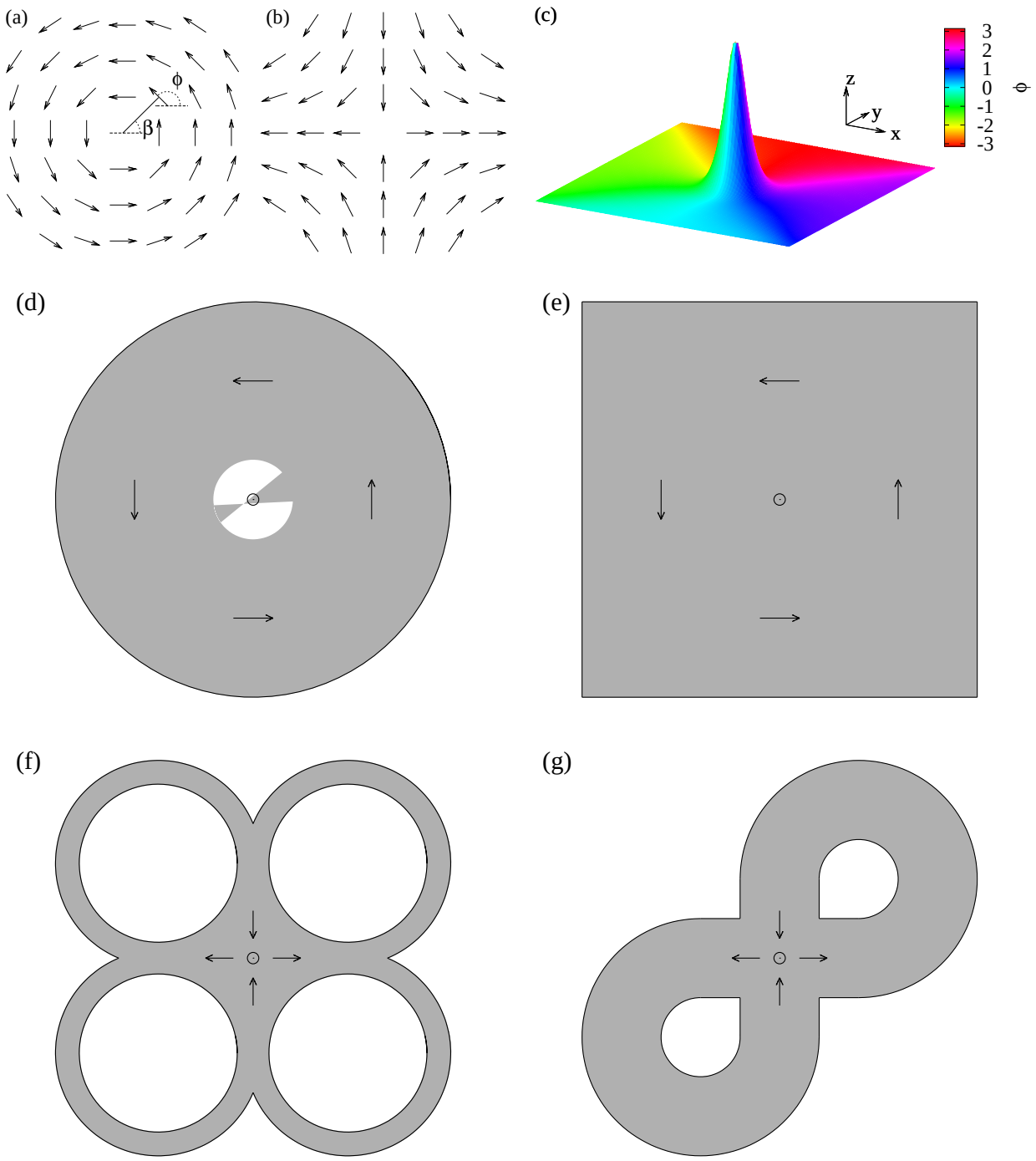

Figure 4.1: Scheme of the in-plane magnetization of (a) a vortex ($n = 1$) with chirality $c = 1$ and (b) an antivortex ($n = -1$) with chirality $c = 0$ determined from Eq. (4.1). (c) Numerically calculated magnetization in a permalloy square thin-film element with 200 nm edge length and 20 nm thickness. The vortex has chirality $c = 1$ and polarization $p = 1$. The height describes the value of the out-of-plane magnetization and the color denotes the angle ϕ of the in-plane magnetization. (d)-(g) Scheme of possible samples in which (d) and (e) a single vortex or (f) and (g) a single antivortex can be realized. The grey area depicts the magnetic material. The direction of the magnetization is denoted by the arrows. The vortex or antivortex core is denoted by the circle. (Subfigures (a) and (b) are reprints from reference [156].)

where ϕ is the angle of the magnetization and β is the angle that describes the position with respect to the core as shown in figure 4.1(a). While the winding number n can theoretically assume every integer value we will focus on the special cases of a vortex ($n = 1$) and an antivortex ($n = -1$). The difference between a vortex and an antivortex is the sense of rotation of the in-plane magnetization that occurs when moving around the core. The offset between the two angles ϕ and β is parameterized by the chirality c. For a vortex a chirality of $c = 1$ denotes a counterclockwise curling of the in-plane magnetization while $c = -1$ denotes a clockwise curling. Since a rotation of the sample affects both angles, that are ϕ and β, in the same manner the chirality $c = 2(\phi - \beta)/\pi$ does not change. For an antivortex the expression $c = 2(\phi + \beta)/\pi$ depends on the orientation of the sample. Thus the chirality is not an intrinsic property of the antivortex and one has to choose a distinct axis from which the angles are measured. To meet these concerns, for an antivortex c is sometimes called the c value instead of chirality.[157] Here we will use the term chirality for both vortex and antivortex. It is worth noting that in some publications about magnetic vortices the term chirality is used to describe the relation between in-plane and out-of-plane magnetization that is given by pc. Here the product pc will be called handedness.

For thin films where the magnetization is forced in the film plane A. A. Belavin and A. M. Polyakov introduced a topological charge

$$q = \frac{1}{8\pi M_s^3} \int d^2r \sum_{k,l,m,p,q} \epsilon_{pqz}\epsilon_{klm} M_k \frac{\partial M_l}{\partial r_p} \frac{\partial M_m}{\partial r_q} = \frac{1}{4\pi M_s^3} \int d^2r \; \vec{M} \left(\frac{\partial \vec{M}}{\partial x} \times \frac{\partial \vec{M}}{\partial y} \right) \tag{4.2}$$

where the z direction is the out-of-plane direction. This charge is called the skyrmion charge.[158] For vortices and antivortices this quantity is a half integer that is given by $q = np/2$.[159,160] For a continuously varying magnetization, as assumed in the micromagnetic model, the skyrmion charge is conserved as long as no vortices or antivortices enter or leave the system at the boundaries.

It is known that vortices are displaced from their equilibrium position when excited by spin-polarized electric currents that flow in the film plane.[50] For excitations with magnetic field pulses or alternating fields vortices and antivortices precess around their equilibrium position[40,47] and it was shown that spin-polarized electric currents can cause the same precession.[50,161]

For an excitation with large magnetic fields or currents the vortex or antivortex core eventually switches its polarization, that is after the switching process a vortex or antivortex with the opposite orientation of the out-of-plane magnetization remains.[47] The switching of a vortex core by an alternating in-plane field or current proceeds as follows. When the excitation increases a dip is formed on the inside of the core's orbit close to the core. In this dip the magnetization points out-of-plane but in a different direction compared to the vortex core. When this dip reaches a critical size it decouples to a vortex core and an antivortex core. The antivortex core moves towards the original vortex core and both annihilate. The new vortex core, which has opposite polarization compared to the original one, remains. For an antivortex the switching proceeds the same way but with vortex core and antivortex core exchanged. In micromagnetic calculations this switching of a vortex or antivortex is not allowed as it changes the skyrmion charge. However, it can be simulated on a lattice of discrete spins. This is discussed in section 6.

As we will see in this work, due to its high symmetry and spatial confinement a vortex or an antivortex in a micro- or nanostructured magnetic thin-film element are promising systems for the investigation of the spin-torque effect. The high symmetry of the magnetization leads to an analytically feasible system while the spatial confinement of the vortex core within the film element and its periodic motion around its ground state yields an especially accessible system for measurements with scanning probe techniques, such as soft x-ray microscopy, x-ray photoemission electron microscopy, or scanning electron microscopy with polarization analysis.[40,47,49,74,162–164] Furthermore a vortex or an antivortex is an ideal candidate for the development of new memory devices.

5 Magnetic Domain Walls

In ferromagnetic materials the short range exchange energy tries to align the magnetic moments in the same direction while the long range demagnetization energy is lower for a flux-closure magnetization pattern. The sum of both energies is minimized by forming local regions with uniform magnetization to favor the exchange energy. The angle between the magnetization in neighboring regions can be arbitrary. This allows for a minimization of the demagnetization energy. These local regions are called domains and the boundaries between them are called domain walls.

There are many possible types of domain walls. The simplest domain walls are the 180° Néel and Bloch walls. When moving through the wall the magnetization rotates from one direction to the other. The difference between a Néel wall and Bloch wall is that the magnetization in a Bloch wall rotates in the plane that is given by the domain wall while the magnetization in a Néel can be oriented perpendicular to the wall plane. Both wall types are depicted in figure 5.1.

The energy of a Néel or Bloch wall is given by

$$E_{\mathrm{NB}} = \int dV \left(A \left(\frac{\partial \theta}{\partial x} \right)^2 + A \sin^2(\theta) \left(\frac{\partial \phi}{\partial x} \right)^2 + K \sin^2(\theta) + K_\perp \sin^2(\theta) \sin^2(\phi) \right) \tag{5.1}$$

where $A\left(\partial\theta/\partial x\right)^2 + A\sin^2(\theta)\left(\partial\phi/\partial x\right)^2$ is the energy density of the exchange coupling and $K\sin^2(\theta) + K_\perp \sin^2(\theta)\sin^2(\phi)$ describes the anisotropy of the system. This anisotropy can be due to a crystalline anisotropy, a layered sample, or due to the shape of the sample. θ is the angle between the magnetization and the easy axis, ϕ is the angle around the easy axis, and x is the position perpendicular to the wall. The second term is minimized by a constant value of ϕ and the fourth term is minimized if this constant value of ϕ is zero. The magnetization configuration with the minimal energy is derived from the variation

$$\frac{\delta E_{\mathrm{NB}}}{\delta \theta} = -2A \frac{\partial^2 \theta}{\partial x^2} + 2K \sin(\theta)\cos(\theta) = 0 \tag{5.2}$$

of the energy and the solution is given by the angle

$$\theta = 2 \operatorname{atan}\left(e^{\pm \frac{x-X}{\lambda}} \right). \tag{5.3}$$

Here X is the position of the wall and $\lambda = \sqrt{A/K}$ is the width of the wall. For further calculations it is helpful to derive expressions for $M_\parallel/M_s = \cos(\theta)$ and $M_\perp/M_s = \sin(\theta)$ which denotes the fraction of the magnetization that is parallel and perpendicular to the easy axis, respectively. From equation (5.3) we derive

$$e^{\pm \frac{x-X}{\lambda}} = \tan\left(\frac{\theta}{2}\right) = \sqrt{\frac{1-\cos(\theta)}{1+\cos(\theta)}} \tag{5.4}$$

which leads to the expression for the cosine

$$\cos(\theta) = \frac{1 - e^{\pm 2\frac{x-X}{\lambda}}}{1 + e^{\pm 2\frac{x-X}{\lambda}}} = \mp \tanh\left(\frac{x-X}{\lambda}\right). \tag{5.5}$$

Now we can easily calculate

$$\sin(\theta) = \sqrt{1-\cos^2(\theta)} = \sqrt{\frac{\cosh^2\left(\frac{x-X}{\lambda}\right) - \sinh^2\left(\frac{x-X}{\lambda}\right)}{\cosh^2\left(\frac{x-X}{\lambda}\right)}} = \pm \frac{1}{\cosh\left(\frac{x-X}{\lambda}\right)}. \tag{5.6}$$

We thus get $|M_\parallel| = M_s \left|\tanh\left(\frac{x-X}{\lambda}\right)\right|$ and $|M_\perp| = M_s/\cosh\left(\frac{x-X}{\lambda}\right)$ as shown in figure 5.1. These results for $M_\parallel$ and $M_\perp$ only determine the absolute value of the parallel and the perpendicular

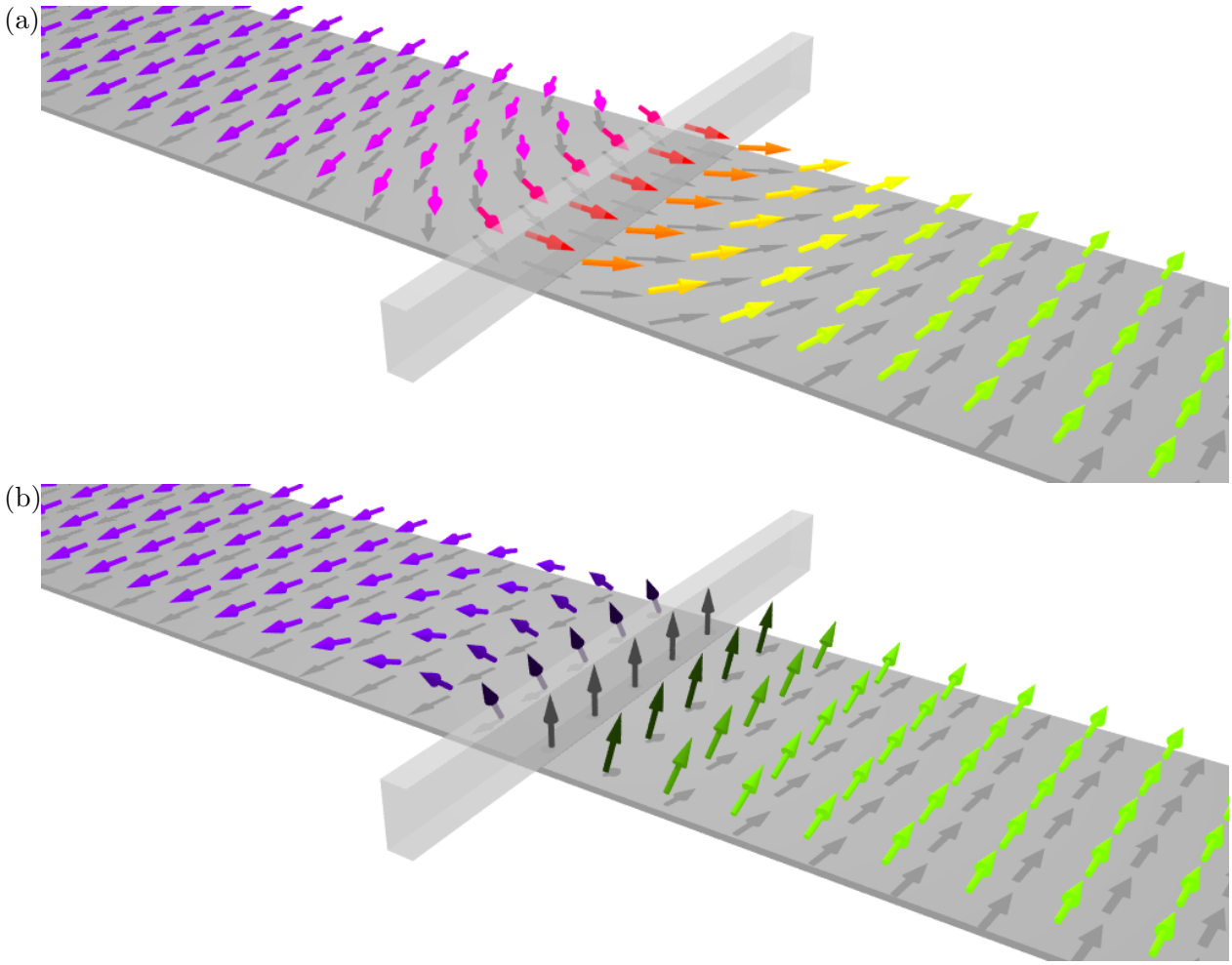

Figure 5.1: Scheme of the magnetization in (a) a 180° Néel wall and (b) a 180° Bloch wall. The in-plane magnetization is given by the color of the magnetization arrows. A black arrow indicates a magnetization that points out-of-plane. The semi transparent box denotes the plane of the domain wall.

magnetization. Thus both the Néel and the Bloch domain wall are fourfold degenerate according to the different signs of the parallel and the perpendicular magnetization.

While the magnetization in the Néel and Bloch domain walls does not depend on the position along the wall there are types of domain walls in which the magnetization also depends on this position. These more complex composite wall types can also contain vortices and antivortices that determine the dynamics of the domain wall. This underlines the importance of the dynamics of vortices and antivortices.

One system that allows for a study of the increasing complexity of domain walls is a small magnetic nanowire. In magnetic nanowires the minimization of the surface charges leads to a magnetization which is nearly everywhere parallel to the wire. Two domains with opposite magnetization direction are separated by a domain wall. These walls are called head-to-head walls if the magnetization in the neighboring domains point towards each other. For the opposite orientation of the magnetization they are called tail-to-tail walls.

The type of this domain wall strongly depends on the width w and thickness d of the wire and on the initial magnetization.[90,165,166] With increasing cross section of the wire one finds an increasing complexity of the domain wall that constitutes the groundstate. Figure 5.2 shows the numerically calculated groundstates of four different types of domain walls in a permalloy nanowire.

The most simple wall is the transverse wall that exists for small cross sections $S = wd$. Similar to a Néel and a Bloch wall the magnetization performs a continuous rotation from one orientation to the other. The transverse wall is commonly described by a one dimensional model where the magnetization depends only on the position along the wire axis. The energy is approximated by

$$E_{\mathrm{T}} = \int dV \left(A \left(\frac{\partial \theta}{\partial x} \right)^2 + A \sin^2(\theta) \left(\frac{\partial \phi}{\partial x} \right)^2 + K \sin^2(\theta) + K_{\perp} \sin^2(\theta) \sin^2(\phi) \right) \tag{5.7}$$

where θ is the angle between the magnetization and the wire axis while ϕ describes a rotation of the magnetization around the wire. The first two terms in equation (5.7) represent the exchange energy. The demagnetization energy is accounted for by the approximation with a so called shape anisotropy. The third term in equation (5.7), that is an easy axis anisotropy along the wire, describes the tendency of the magnetization to align in the wire direction. For wires with an aspect ratio $d/w \neq 1$, that is a non-quadratic cross section, the last energy term describes a preferred orientation of the perpendicular magnetization.

When the cross sections $S = wd$ of the wire exceeds a critical value a vortex wall becomes the energetic groundstate.[165,166] R. D. McMichael and M. J. Donahue determined a critical cross section of 64 l_{ex}^2 and Y. Nakatani et *al.* found a similar value of 61.3 l_{ex}^2. The exchange length l_{ex} is given by $\sqrt{2A/(\mu_0 M_s^2)}$. In a vortex wall the alignment of the magnetization changes over the cross section. The vortex can have the two polarizations $p = \pm 1$ and the two chiralities $c = \pm 1$. In analytic calculations this type of domain wall has been approximated by two transverse walls which point in different directions and a vortex between those two walls.[102]

Experiments and simulations with permalloy rings of different sizes showed a strong dependence of the wall type on the initial magnetization.[90] In these investigations the initial state of the ring is a magnetization that is saturated along a certain direction by a magnetic field. After the field is switched off the rings exhibit two domain walls. Due to the symmetric initial magnetization the symmetric transverse wall is preferred. For large cross sections the transverse wall switches to a vortex wall. There is an intermediate regime where the vortex wall is the energetic groundstate but the transverse wall constitutes a local energy minimum and no switching to a vortex wall occurs.

An asymmetric transverse wall as shown in figure 5.2(b) is similar to the common transverse wall but it does not exhibit the mirroring symmetry with respect to the center of the wall. In wires with extremely non-quadratic cross section this type of wall appears in the transition region between the transverse wall and the vortex wall.[115,166] A double vortex wall contains two vortices with opposite chirality as shown in figure 5.2(d). A further increase of the wire cross section leads to a couple of additional wall types that contain more vortices and antivortices.[103,116,119,167]

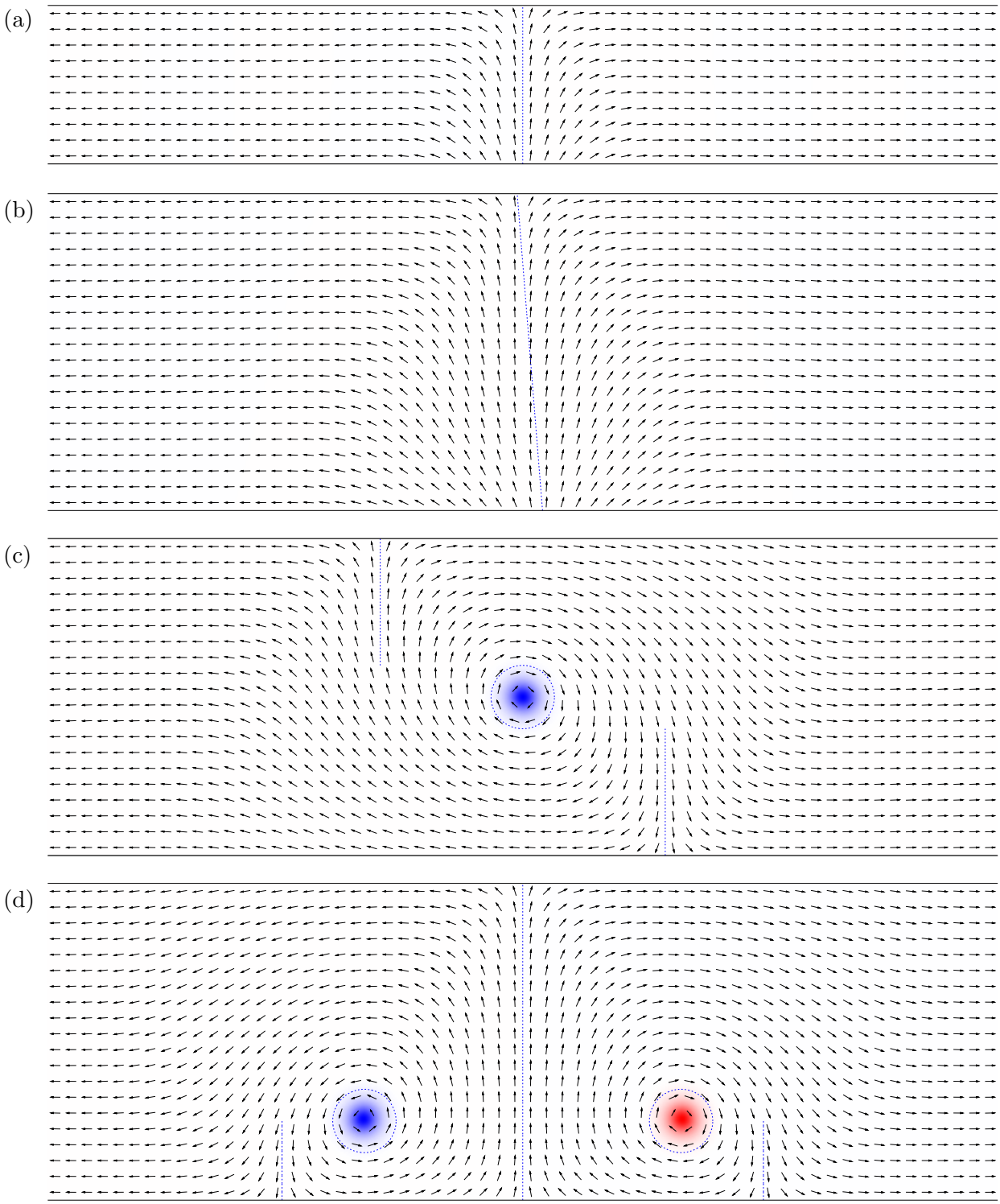

Figure 5.2: Numerically calculated magnetization of (a) a transverse, (b) an asymmetric transverse, (c) a vortex, and (d) a double-vortex domain wall in a permalloy nanowire. The width of the wire is (a) 100 nm and (b) - (d) 200 nm. The thickness is (a), (c), and (d) 10 nm and (b) 8 nm. Each arrow denotes the average of the in-plane magnetization of a square film element with 10 nm edge length. The color denotes the out-of-plane magnetization and ranges from a full out-of-plane magnetization pointing towards the reader (blue) to a full out-of-plane magnetization pointing in the opposite direction (red). White denotes a magnetization that points in-plane. The vortex cores and the Néel wall like structures are highlighted by the dashed blue lines. All simulations are performed with a simulation-cell size of 1 nm in lateral direction and one cell in the thickness.

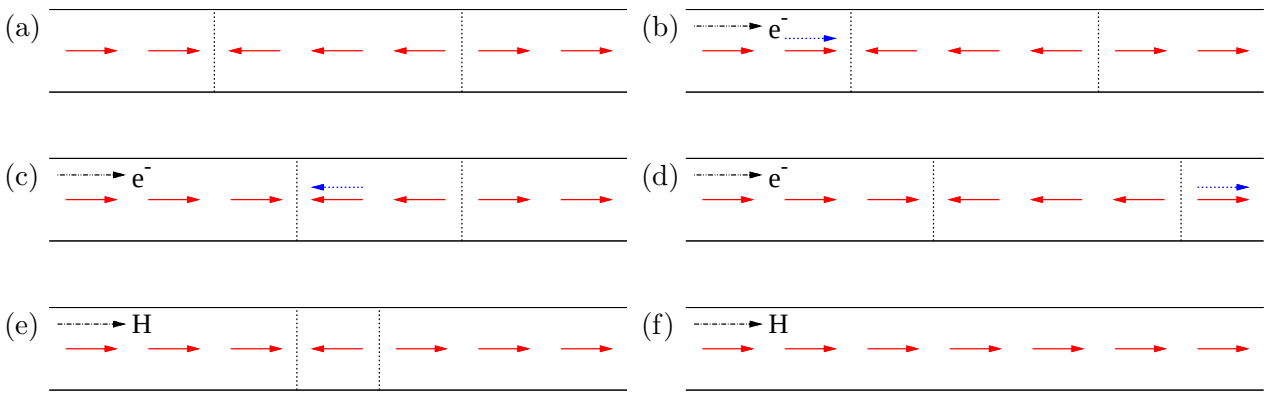

Figure 5.3: Scheme of (a)-(d) current and (e)-(f) field-driven motion of domain walls in a nanowire. For the sake of simplicity we neglect the internal structure of the two domain walls that are denoted by the dashed lines and assume a full polarization of the conduction electrons. (a) In our initial state the magnetization (red solid arrows) exhibits two domain walls a head-to-head (left) and a tail-to-tail domain wall (right). (b) The magnetic moment of the conduction electron (dashed blue arrow) that enters from the left is aligned parallel to the local magnetization. (c) and (d) When the conduction electron passes the domain walls it has to flip its spin. Due to the conservation of angular momentum one localized electron has to flip its spin as well. Thus both walls are shifted in the direction of the electron flow. (e) A magnetic field (dashed-dotted arrow) that is applied in the direction of the wire increases the energy of the domain that is pointing left. Consequently this domain decreases and both walls move in opposite direction. (f) Finally both domain walls annihilate.

In a magnetic nanowire the domain walls can be moved along the wire by an external magnetic field or by a spin polarized current that flows in the wire.[129,168–170] This motion can be used in novel high-density memory devices like the racetrack memory.[79] In this kind of memory the information is stored in the orientation of the magnetization at different positions in the wire. Applying an external magnetic field or a spin polarized current allows for a shifting of these bits along the wire passing a writing and a reading device.

For a reliable operation of this device it is essential that all domain walls in the wire move in the same direction and with the same speed. Otherwise two neighboring domain walls can collide and annihilate each other yielding an inevitable loss of information.[171] A magnetic field in the direction of the wire is not suitable because it forces head-to-head and tail-to-tail domain walls to move in opposite directions. A current is more appropriate since all domain walls would move in the direction of the electron flow. Figure 5.3 shows a scheme of the current and the field-driven motion of a domain wall.

A drawback is that the motion of a domain wall is highly affected by pinning centers like grain boundaries or surface roughness. This leads to a highly stochastic motion.[172,173] This problem can be overcome by introducing artificial pinning sites like notches that are stronger than the randomly distributed pinning centers. Then the wall can be moved deterministically from one artificial pinning site to the next. Thus it becomes important to understand the pinning and depinning processes of current-driven domain walls.

The probability that a domain wall is depinned by a current pulse does not only depend on the amplitude of the pulse but also on its temporal shape. In experiments, it was shown that a current with a special temporal shape can reduce the critical current density that is needed to depin the domain wall.[105,111,113,174] These experiments aim at resonant excitations of the wall. The resonant behavior depends on the pulse length, on a series of properly timed current pulses, or on a resonantly alternating current that is applied to the wire.

It was found theoretically that domain-wall motion driven by temporally varying spin-polarized

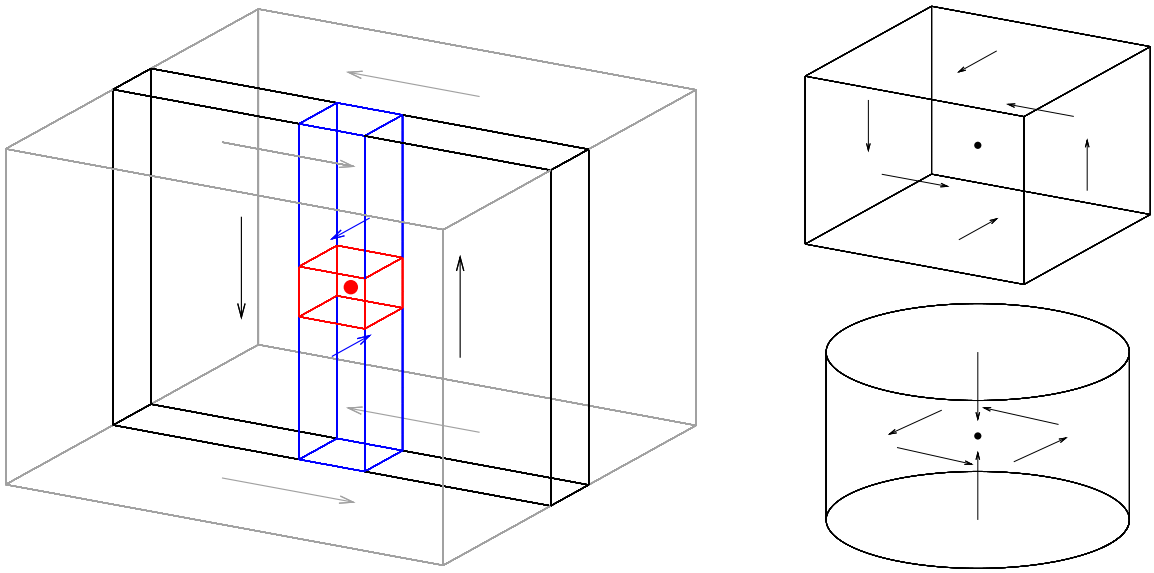

Figure 6.1: (a) Scheme of a magnetization configuration with a micromagnetic singularity. The two domains (grey) are separated by two Bloch domain walls (black). The Bloch walls have different senses of rotation and are divided by two Néel/Bloch lines (blue). Between the two Néel/Bloch lines with different orientations a micromagnetic singularity (red) is formed. This singularity is called a Bloch point. A magnification of the red square is shown in (b). It can be seen that in the vicinity of the singularity the magnetization points in different directions. This leads to a singularity in the exchange energy. (c) A micromagnetic singularity also exists during the switching of a magnetic vortex core in a thin film. The singularity moves through the film along the core. Shown is the magnetization when the singularity (dot) is at the midpoint of the core. (The subfigures (a) and (b) are adopted from reference [176].)

currents depends not only on the current density but also on its time derivative.[129,175] In this work we will see that this leads to the fact that the critical current density can be reduced by shortening the risetime of the current pulse.

6 Constraints of the Micromagnetic Model

In the micromagnetic model the magnetization is described by a continuous vector field with a constant magnitude. This approximation is valid only if the magnetization changes on a length scale that is large compared to the distance of two magnetic moments, that is the distance of two atoms.

For the calculation of the angle between two spins we have a closer look at the three topological defects that are depicted in figure 6.1(a).

For a Néel or Bloch wall the angle between two neighboring spins can be expressed by

$$\Delta\theta = \theta(x + d_a) - \theta(x) \approx \frac{\partial\theta}{\partial x}(x) d_a = \frac{d_a}{\cosh\left(\frac{x-X}{\lambda}\right)\lambda} \leq \frac{d_a}{\lambda} \ll 1 \tag{6.1}$$

assuming that the atomic distance d_a is small compared to the wall width λ. Thus the maximum angle between two spins is given by d_a/λ. The minimum value for the domain-wall width is given by

$$\lambda_{\min} = \sqrt{\frac{A}{\frac{1}{2}\mu_0 M_s^2 + K_{u1}}} \tag{6.2}$$

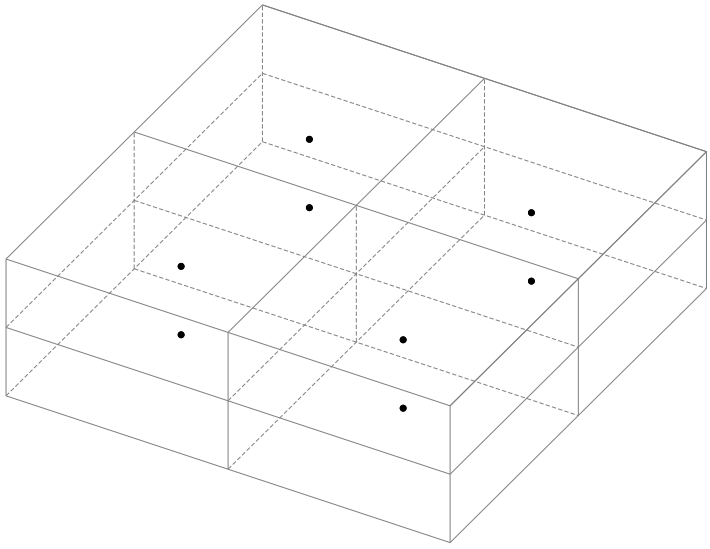

Figure 6.2: One possible spatial discretization of the magnetization for numerical calculations. The space is subdivided in cuboidic cells. The magnetization is stored at the midpoints of these cells that are denoted by the dots.

where $(1/2)\mu_0 M_s^2$ is the maximum anisotropy due to the shape of the sample and K_{u1} is the intrinsic uniaxial anisotropy. Here we neglected cubic anisotropy and higher orders of the uniaxial anisotropy. In materials with no intrinsic anisotropy, for example permalloy, the magnetization changes on a length scale that is given by the exchange length

$$l_{\mathrm{ex}} = \sqrt{\frac{2A}{\mu_0 M_s^2}}. \tag{6.3}$$

For permalloy with $A = 1.3 \cdot 10^{-11}$ J/m and $M_s = 8 \cdot 10^5$ A/m this length is about $l_{\mathrm{ex}} = 5.7$ nm which is more than one order of magnitude larger than the atomic distance of $d_a = 0.25$ nm that can be calculated from the lattice constants of $a_{\mathrm{Ni}} = 0.352$ nm for nickel and $a_{\mathrm{Fe}} = 0.287$ nm for iron, bearing in mind that nickel has a face-centered cubic lattice and iron has a body-centered cubic lattice. The maximum angle between two neighboring spins is thus 2.5° and the magnetization in a domain wall changes slowly enough for a micromagnetic description.

Two domain walls with different orientations are separated by a Néel/Bloch line. In this work such lines occur only in vortices or antivortices where they constitute the vortex or antivortex core as depicted in figure 6.1(c). Numerical simulations of a vortex in a permalloy film element showed that the maximum spatial derivative of the magnetization angle, that can be found in films with a thickness of $d = 10$ nm, is about 0.17 nm^{-1} which is close to the value $l_{\mathrm{ex}}^{-1} = 0.18$ nm^{-1} that was found for the domain wall.

Bloch points occur especially during reversal processes of the magnetization.[38,159,176,177] In the vicinity of these points the magnetization points in all three spatial directions as depicted in figure 6.1(b). Thus a continuous rotation of the magnetization is not possible. Such a discontinuity leads to a singularity in the exchange energy because two positions with opposite magnetization direction are infinitely close to each other. A second problem that arises is that in the vicinity of the Bloch point the magnetization vanishes since the magnetic moments point in all possible directions. This is not compatible with the micromagnetic assumption that the length of the magnetization vector is constant. Thus a Bloch point cannot be described by the micromagnetic model.

In numerical micromagnetic calculations the magnetization has to be spatially discretized as shown in figure 6.2. The derivatives of the magnetization are then expressed by the difference of the magnetization in neighboring grid points divided by the distance of the points. Since the grid points have a finite distance the exchange energy is prevented from becoming infinite although it obtains very large numbers. But the approximation of the derivative by finite differences becomes certainly incorrect in the vicinity of the Bloch point. This can especially be seen when the energy of a Bloch point, and thus the results of the simulations, show a strong mesh dependence.[177] Thus

physical values can depend on the non-physical value of the mesh size. This makes numerical micromagnetic calculations of systems that contain Bloch points unreliable.

During the switching of a vortex or an antivortex core a Bloch point is generated in the sample as shown in figure 6.1(c).[176] Thus the switching process is not suitable for an investigation with the micromagnetic model even though in numerical calculations a switching can be observed. Due to these apparent problems the switching of vortices and antivortices will not be investigated in this work.

Part II
Dynamics of Vortices and Antivortices

A magnetic vortex or a magnetic antivortex can be excited by applying a magnetic field or a spin-polarized current. In this part the dynamics of a vortex or an antivortex are discussed. Firstly, analytical calculations within the micromagnetic framework using some approximations are presented. Secondly, the results of these calculations are compared with numerical simulations that base upon the micromagnetic model. The comparison between the analytical and numerical results allows us to test the applicability of the approximations that are used in the analytical calculations. In a third section the action of the Oersted field accompanying the current on a vortex and an antivortex is investigated. The final three sections deal with applications of vortex and antivortex dynamics. These sections include the distinction between spin-torque and Oersted-field driven dynamics, measurement of the non-adiabatic spin-torque parameter ξ, and an application of a vortex or antivortex in memory devices.

7 Analytical Calculations

In this section the dynamics of vortices and antivortices is discussed analytically. The results that are presented in this section have been published slightly modified in references [156,157,178–180].

7.1 The Thiele Equation

In micromagnetism the LLG equation describes the temporal change of the magnetization at each position of a magnetization pattern. Since the magnetization is a continuous vector field an arbitrary magnetization pattern is described by an infinite number of parameters. To reduce the number of parameters one can use the approach of collective coordinates. In this approach the magnetization at each point within the sample is given by an expression that depends on the position of this point and a number of parameters, called collective coordinates, that evolve in time.

A simple approach was found by Thiele in 1973.[181–183] He recognized that for a magnetization pattern that performs a rigid motion without deformations the current state of the whole magnetization can be described by the current position of one characteristic feature of the pattern. In this case the magnetization at the position $\vec{r} = (x, y, z)$ is given by $\vec{M}(\vec{r} - \vec{R}(t))$ where $\vec{R} = (X, Y, Z)$ is the position of the characteristic feature. He derived an equation of motion by expressing the time derivative at each point by the according spatial derivative and the velocity of the whole pattern. In 2005 Thiaville et *al.* expanded this equation by the action of a spin-polarized current.[153] This equation is derived in the following.

According to Thiele we write

$$\begin{aligned}\frac{d\vec{M}(\vec{r}-\vec{R}(t))}{dt} &= \dot{X}\frac{\partial\vec{M}(\vec{r}-\vec{R}(t))}{\partial X} + \dot{Y}\frac{\partial\vec{M}(\vec{r}-\vec{R}(t))}{\partial Y} + \dot{Z}\frac{\partial\vec{M}(\vec{r}-\vec{R}(t))}{\partial Z} \\ &= -\dot{X}\frac{\partial\vec{M}(\vec{r}-\vec{R}(t))}{\partial x} - \dot{Y}\frac{\partial\vec{M}(\vec{r}-\vec{R}(t))}{\partial y} - \dot{Z}\frac{\partial\vec{M}(\vec{r}-\vec{R}(t))}{\partial z} \\ &= -\left(\vec{v}\cdot\vec{\nabla}\right)\vec{M}(\vec{r}-\vec{R}(t)),\end{aligned} \tag{7.1}$$

where $\vec{v} = (\dot{X}, \dot{Y}, \dot{Z})$ is the velocity of the magnetization pattern. With this expression we can simplify the LLG. The implicit LLG with the spin torque terms

$$\frac{d\vec{M}}{dt} = -\gamma\vec{M}\times\vec{H} + \frac{\alpha}{M_s}\vec{M}\times\frac{d\vec{M}}{dt} - \frac{b_j}{M_s^2}\vec{M}\times\left(\vec{M}\times\left(\vec{j}\cdot\vec{\nabla}\right)\vec{M}\right) - \frac{\xi b_j}{M_s}\vec{M}\times\left(\vec{j}\cdot\vec{\nabla}\right)\vec{M} \tag{7.2}$$

can be written as

$$-\left(\vec{v}\cdot\vec{\nabla}\right)\vec{M} = -\gamma\vec{M}\times\vec{H} - \frac{\alpha}{M_s}\vec{M}\times\left(\vec{v}\cdot\vec{\nabla}\right)\vec{M} - \frac{b_j}{M_s^2}\vec{M}\times\left(\vec{M}\times\left(\vec{j}\cdot\vec{\nabla}\right)\vec{M}\right) - \frac{\xi b_j}{M_s}\vec{M}\times\left(\vec{j}\cdot\vec{\nabla}\right)\vec{M} \tag{7.3}$$

using the expression in equation (7.1). With equation (3.4) the left hand side of equation (7.3) can be rewritten as

$$-\left(\vec{v}\cdot\vec{\nabla}\right)\vec{M} = \frac{1}{M_s^2}\vec{M}\cdot\underbrace{\left(\vec{M}\cdot\left(\vec{v}\cdot\vec{\nabla}\right)\vec{M}\right)}_{=0} - \underbrace{\frac{1}{M_s^2}\left(\vec{M}\cdot\vec{M}\right)}_{=1}\cdot\left(\vec{v}\cdot\vec{\nabla}\right)\vec{M} = \frac{1}{M_s^2}\vec{M}\times\left(\vec{M}\times\left(\vec{v}\cdot\vec{\nabla}\right)\vec{M}\right), \tag{7.4}$$

where we applied equation (1.14). Equation (7.4) can now be inserted in equation (7.3). Grouping terms with similar dependence on $\vec{M}$ we get the expression

$$0 = -\gamma\vec{M}\times\vec{H} - \frac{1}{M_s^2}\vec{M}\times\left(\vec{M}\times\left(\left(\vec{v}+b_j\vec{j}\right)\cdot\vec{\nabla}\right)\vec{M}\right) - \frac{1}{M_s}\vec{M}\times\left(\left(\alpha\vec{v}+\xi b_j\vec{j}\right)\cdot\vec{\nabla}\right)\vec{M}. \tag{7.5}$$

The equation

$$0 = \vec{H} + \frac{1}{\gamma M_s^2}\vec{M}\times\left(\left(\vec{v}+b_j\vec{j}\right)\cdot\vec{\nabla}\right)\vec{M} + \frac{1}{\gamma M_s}\left(\left(\alpha\vec{v}+\xi b_j\vec{j}\right)\cdot\vec{\nabla}\right)\vec{M} + \rho\vec{M} \tag{7.6}$$

reproduces equation (7.5) after multiplication with $-\gamma$ and application of the cross product with $\vec{M}$ from the left. Here $\rho\vec{M}$ is a magnetic field in the direction of the magnetization. This term is arbitrary since the torque on the magnetization depends only on the cross product between the field and the magnetization. Thus the field component in the direction of the magnetization has no effect.

The i-th component of the force on the magnetization pattern can be calculated as

$$\begin{aligned}\vec{F}_i &= -\frac{\partial E}{\partial\vec{R}_i} = -\int dV\sum_k \frac{\delta E}{\delta\vec{M}_k(\vec{r})}\frac{\partial}{\partial\vec{R}_i}\vec{M}_k(\vec{r}) \\ &= \int dV\sum_k[-\mu_0\vec{H}_k(\vec{r})]\vec{\nabla}_i\vec{M}_k(\vec{r}) = -\mu_0\int dV\sum_k[\vec{\nabla}_i\vec{M}_k(\vec{r})]\vec{H}_k(\vec{r}).\end{aligned} \tag{7.7}$$

This yields the force density

$$\vec{f} = -\mu_0\sum_k(\vec{\nabla}\vec{M}_k)\vec{H}_k. \tag{7.8}$$

Multiplying the field equation (7.6) with $-\mu_0\sum_k(\vec{\nabla}\vec{M}_k)$ yields the i-th component of the force density

$$\begin{aligned}0 = &\sum_k(-1)\mu_0\left(\vec{\nabla}_i\vec{M}_k\right)\vec{H}_k \\ &+\sum_{k,l,m,n}(-1)\frac{\mu_0\epsilon_{klm}}{\gamma M_s^2}\left(\vec{\nabla}_i\vec{M}_k\right)\vec{M}_l\left(\vec{\nabla}_n\vec{M}_m\right)\left(\vec{v}+b_j\vec{j}\right)_n \\ &+\sum_{k,n}(-1)\frac{\mu_0}{\gamma M_s}\left(\vec{\nabla}_i\vec{M}_k\right)\left(\vec{\nabla}_n\vec{M}_k\right)\left(\alpha\vec{v}+\xi b_j\vec{j}\right)_n \\ &+\underbrace{\sum_k(-1)\mu_0\left(\vec{\nabla}_i\vec{M}_k\right)\rho\vec{M}_k.}_{=0}\end{aligned} \tag{7.9}$$

The last term vanishes due to the relation in equation (3.4). For the calculation of the steady state motion of the whole magnetization pattern the force density is integrated over the volume to determine the equation of forces

$$\begin{aligned} 0 = & \int dV \sum_k (-1)\mu_0 \left(\vec{\nabla}_i \vec{M}_k\right) \vec{H}_k \\ & + \int dV \sum_{k,l,m,n} (-1) \frac{\mu_0 \epsilon_{klm}}{\gamma M_s^2} \left(\vec{\nabla}_i \vec{M}_k\right) \vec{M}_l \left(\vec{\nabla}_n \vec{M}_m\right) \left(\vec{v} + b_j \vec{j}\right)_n \\ & + \int dV \sum_{k,n} (-1) \frac{\mu_0}{\gamma M_s} \left(\vec{\nabla}_i \vec{M}_k\right) \left(\vec{\nabla}_n \vec{M}_k\right) \left(\alpha \vec{v} + \xi b_j \vec{j}\right)_n . \end{aligned} \tag{7.10}$$

If the velocity of the magnetization is independent of the position, that is the magnetization pattern does not deform during the motion, the velocity can be taken outside the integration. For a spatially homogeneous current flow the current density is also independent of the position and can be taken outside the integral. The equation of forces can then be written as

$$\begin{aligned} 0 = & \underbrace{\int dV \sum_k (-1)\mu_0 \left(\vec{\nabla}_i \vec{M}_k\right) \vec{H}_k}_{\text{force}} \\ & + \sum_n \underbrace{\left(\int dV \, (-1) \sum_{k,l,m} \frac{\mu_0 \epsilon_{klm}}{\gamma M_s^2} \left(\vec{\nabla}_i \vec{M}_k\right) \vec{M}_l \left(\vec{\nabla}_n \vec{M}_m\right) \right)}_{\text{gyro tensor}} \left(\vec{v} + b_j \vec{j}\right)_n \\ & + \sum_n \underbrace{\left(\int dV \, (-1) \sum_k \frac{\mu_0}{\gamma M_s} \left(\vec{\nabla}_i \vec{M}_k\right) \left(\vec{\nabla}_n \vec{M}_k\right) \right)}_{\text{dissipation tensor}} \left(\alpha \vec{v} + \xi b_j \vec{j}\right)_n . \end{aligned} \tag{7.11}$$

The gyro tensor is an antisymmetric tensor. In three dimensions the product of an antisymmetric tensor and a vector can always be written as a cross product between two vectors. This is archived by inserting two additional Levi-Civita symbols and summing over the new variables. With the cross product equation (7.11) reads

$$\begin{aligned} 0 = & \underbrace{\int dV \sum_k (-1)\mu_0 \left(\vec{\nabla}_i \vec{M}_k\right) \vec{H}_k}_{\text{force}} \\ & + \sum_{n,o} \epsilon_{ion} \underbrace{\left(\int dV \, (-1) \sum_{k,l,m,p,q} \frac{\mu_0 \epsilon_{klm} \epsilon_{poq}}{2\gamma M_s^2} \left(\vec{\nabla}_p \vec{M}_k\right) \vec{M}_l \left(\vec{\nabla}_q \vec{M}_m\right) \right)}_{\text{gyrovector}} \left(\vec{v} + b_j \vec{j}\right)_n \\ & + \sum_n \underbrace{\left(\int dV \, (-1) \sum_k \frac{\mu_0}{\gamma M_s} \left(\vec{\nabla}_i \vec{M}_k\right) \left(\vec{\nabla}_n \vec{M}_k\right) \right)}_{\text{dissipation tensor}} \left(\alpha \vec{v} + \xi b_j \vec{j}\right)_n . \end{aligned} \tag{7.12}$$

Expressed in vector notation this yields

$$0 = \vec{F} + \vec{G} \times \left(\vec{v} + b_j \vec{j}\right) + D \left(\alpha \vec{v} + \xi b_j \vec{j}\right) . \tag{7.13}$$

For calculating the densities of the force $\vec{F}$, the gyrovector $\vec{G}$, and the dissipation tensor D at a distinct position $\vec{r}_0$ we introduce a coordinate system given by the unit vectors

$$\vec{e}_r = \begin{pmatrix} \sin(\theta(\vec{r}_0))\cos(\phi(\vec{r}_0)) \\ \sin(\theta(\vec{r}_0))\sin(\phi(\vec{r}_0)) \\ \cos(\theta(\vec{r}_0)) \end{pmatrix}, \quad \vec{e}_\theta = \begin{pmatrix} \cos(\theta(\vec{r}_0))\cos(\phi(\vec{r}_0)) \\ \cos(\theta(\vec{r}_0))\sin(\phi(\vec{r}_0)) \\ -\sin(\theta(\vec{r}_0)) \end{pmatrix}, \quad \text{and} \quad \vec{e}_\phi = \begin{pmatrix} -\sin(\phi(\vec{r}_0)) \\ \cos(\phi(\vec{r}_0)) \\ 0 \end{pmatrix}, \tag{7.14}$$

where θ and ϕ are the polar and the azimuthal angle of the magnetization, respectively. It is worth noting that this coordinate system is not equal to spherical coordinates. This coordinate system is independent of the position $\vec{r}$ since its unit vectors depend on the magnetization at position $\vec{r}_0$ only. This selection of the coordinate system allows us to calculate the spacial derivatives at position $\vec{r}_0$ without the difficulties that one would be faced with in a rotating coordinate system. From equation (7.14) we find that at position $\vec{r}_0$ the magnetization is given by

$$\vec{M}(\vec{r}_0) = M_s \vec{e}_r(\vec{r}_0). \tag{7.15}$$

For small deviations $d\vec{r}$ from this position the magnetization is given by

$$\vec{M}(\vec{r}_0 + d\vec{r}) = M_s \vec{e}_r(\vec{r}_0) + \left(d\vec{r}\,(\vec{\nabla}\theta)(\vec{r}_0)\right) M_s \vec{e}_\theta(\vec{r}_0) + \left(d\vec{r}\,(\vec{\nabla}\phi)(\vec{r}_0)\right) M_s \sin(\theta)\vec{e}_\phi(\vec{r}_0). \tag{7.16}$$

Moving from position $\vec{r}$ to $\vec{r} + d\vec{r}$ the angles θ and ϕ of the magnetization change since the magnetization rotates. In contrast the vectors $\vec{e}_r(\vec{r}_0)$, $\vec{e}_\theta(\vec{r}_0)$, and $\vec{e}_\phi(\vec{r}_0)$ remain constant. The gradient of the magnetization can be expressed by θ and ϕ as

$$\vec{\nabla}\vec{M} = (\vec{\nabla}\theta)\frac{\partial \vec{M}}{\partial \theta} + (\vec{\nabla}\phi)\frac{\partial \vec{M}}{\partial \phi}. \tag{7.17}$$

With these definitions the force in equation (7.12) can be written as

$$\vec{F} = \int dV \sum_k (-1)\mu_0 \left(\vec{\nabla}\vec{M}_k\right)\vec{H}_k = -\mu_0 \int dV \left[(\vec{\nabla}\theta)\frac{\partial}{\partial\theta} + (\vec{\nabla}\phi)\frac{\partial}{\partial\phi}\right](\vec{H}\cdot\vec{M}). \tag{7.18}$$

From equation (7.12) we get the o-th component of the gyrovector

$$G_o = -\int dV \sum_{k,l,m,p,q} \frac{\mu_0 \epsilon_{klm}\epsilon_{poq}}{2\gamma M_s^2}\left(\vec{\nabla}_p\vec{M}_k\right)\vec{M}_l\left(\vec{\nabla}_q\vec{M}_m\right). \tag{7.19}$$

For a magnetization that does not change in z direction it becomes obvious that the z component of the gyrovector is proportional to the topological skyrmion charge defined in equation (4.2). From equation (7.15) we can see that $M_l = 0$ if $l \neq r$, where M_r denotes the component of the magnetization that points in the direction of the unit vector defined in equation (7.14). This yields

$$\begin{aligned} G_o &= -\int dV \sum_{k,m,p,q} \frac{\mu_0 \epsilon_{rkm}\epsilon_{opq}}{2\gamma M_s^2}\left(\vec{\nabla}_p\vec{M}_k\right) M_s \left(\vec{\nabla}_q\vec{M}_m\right) \\ &= -\int dV \sum_{p,q} \frac{\mu_0 \epsilon_{opq}}{2\gamma M_s}\left(\left(\vec{\nabla}_p\vec{M}_\theta\right)\left(\vec{\nabla}_q\vec{M}_\phi\right) - \left(\vec{\nabla}_p\vec{M}_\phi\right)\left(\vec{\nabla}_q\vec{M}_\theta\right)\right) \\ &= -\int dV \sum_{p,q} \frac{M_s \mu_0 \epsilon_{opq}}{2\gamma}\left(\left(\vec{\nabla}_p\theta\right)\left(\sin(\theta)\vec{\nabla}_q\phi\right) - \left(\sin(\theta)\vec{\nabla}_p\phi\right)\left(\vec{\nabla}_q\theta\right)\right). \end{aligned} \tag{7.20}$$

Renaming the indices p and q in the second term leads to

$$\begin{aligned} G_o &= -\int dV \sum_{p,q} \frac{M_s \mu_0 \epsilon_{opq}}{2\gamma}\left(\left(\vec{\nabla}_p\theta\right)\left(\sin(\theta)\vec{\nabla}_q\phi\right) + \left(\sin(\theta)\vec{\nabla}_q\phi\right)\left(\vec{\nabla}_p\theta\right)\right) \\ &= -\int dV \sum_{p,q} \frac{M_s \mu_0 \epsilon_{opq}}{\gamma}\sin(\theta)\left(\vec{\nabla}_p\theta\right)\left(\vec{\nabla}_q\phi\right). \end{aligned} \tag{7.21}$$

In vector notation the gyrovector reads

$$\vec{G} = -\frac{M_s \mu_0}{\gamma} \int dV \, \sin(\theta) (\vec{\nabla}\theta \times \vec{\nabla}\phi). \tag{7.22}$$

In component notation the dissipation tensor in equation (7.12) reads

$$\begin{aligned} D_{i,n} &= -\int dV \sum_k \frac{\mu_0}{\gamma M_s} \left(\vec{\nabla}_i \vec{M}_k\right) \left(\vec{\nabla}_n \vec{M}_k\right) \\ &= -\int dV \, \frac{\mu_0}{\gamma M_s} \left(\left(\vec{\nabla}_i \vec{M}_\theta\right) \left(\vec{\nabla}_n \vec{M}_\theta\right) + \left(\vec{\nabla}_i \vec{M}_\phi\right) \left(\vec{\nabla}_n \vec{M}_\phi\right)\right) \\ &= -\int dV \, \frac{M_s \mu_0}{\gamma} \left(\left(\vec{\nabla}_i \theta\right) \left(\vec{\nabla}_n \theta\right) + \left(\sin(\theta) \vec{\nabla}_i \phi\right) \left(\sin(\theta) \vec{\nabla}_n \phi\right)\right) \end{aligned} \tag{7.23}$$

which can be translated to the vector notation

$$D = -\frac{M_s \mu_0}{\gamma} \int dV \, (\vec{\nabla}\theta \vec{\nabla}\theta + \sin^2(\theta) \vec{\nabla}\phi \vec{\nabla}\phi). \tag{7.24}$$

The force in equation (7.18), the gyrovector in equation (7.22), and the dissipation tensor in equation (7.24) can now be inserted into the Thiele equation (7.13) to get an equation of motion of the magnetization pattern. Like the LLG equation the Thiele equation is a differential equation of first order in time. As a consequence the magnetization pattern has no inertia but reacts instantaneously to fields and currents. Since the velocity occurs in a cross product given by $\vec{G} \times \vec{v}$, the velocity of the magnetization pattern points not only in the direction of the force but also perpendicular to it.

7.2 The Gyrovector

We will now calculate the gyrovector for a vortex or an antivortex. For this calculation we will use cylindrical coordinates where ρ is the distance from the center of the core. The angle β is the angle that is introduced in section 4. The expression of the gyrovector in equation (7.22) contains gradients of the in-plane angle ϕ and of the out-of-plane angle θ. Due to the rotational symmetry of the vortex or antivortex the angle θ changes in ρ direction only. The angle ϕ depends only on the angle β. Thus we can write

$$\vec{G} = -\frac{M_s \mu_0}{\gamma} \int_0^d dz \int_0^\infty d\rho \, \rho \int_0^{2\pi} d\beta \, \sin(\theta) \frac{\partial \theta}{\partial \rho} (\vec{e}_\rho \times \vec{e}_\beta) \frac{1}{\rho} \frac{\partial \phi}{\partial \beta} = -\frac{M_s \mu_0}{\gamma} \int_0^d dz \int_{\theta(\rho=0)}^{\theta(\rho=\infty)} d\theta \sin(\theta) \int_0^{2\pi} d\beta \, \frac{\partial \phi}{\partial \beta} \vec{e}_z \tag{7.25}$$

where d is the thickness of the film. The gyrovector depends on the out-of-plane angles at the vortex core and far away from the core that are given by $\theta(\rho = 0) = (1 - p)\pi/2$ and $\theta(\rho = \infty) = \pi/2$, respectively. From the expression of the in-plane magnetization in equation (4.1) we can calculate $\partial\phi/\partial\beta = n$ and obtain

$$\vec{G} = -\frac{M_s \mu_0}{\gamma} \int_0^d dz \int_{(1-p)\pi/2}^{\pi/2} d\theta \sin(\theta) \int_0^{2\pi} d\beta \, n \vec{e}_z = -\frac{M_s \mu_0 d}{\gamma} p 2\pi n \vec{e}_z = -\frac{2\pi M_s \mu_0 d p n}{\gamma} \vec{e}_z = G_0 \vec{e}_z. \tag{7.26}$$

The gyrovector is parallel or antiparallel to the z-axis.

7.3 The Dissipation Tensor

While the gyrovector of a vortex or an antivortex turns out to be a topological charge that depends only on the out-of-plane magnetization at the center of the core and far away from the core, the calculation of the dissipation tensor requires the exact knowledge of the magnetization in the core. N. A. Usov and S. E. Peschany calculated the magnetization using a variational approach. They first calculated the expression[184]

$$\sin\theta = \begin{cases} \frac{2R_0\rho}{R_0^2+\rho^2}, & \rho \leq R_0 \\ 1, & \rho > R_0 \end{cases} \tag{7.27}$$

for the out-of-plane angle θ of the magnetization, taking only the exchange energy into account. The variational parameter R_0, that represents the radius of the core, is then varied to minimize the total energy of the system. In this minimization also the demagnetization energy is included. This expression is valid for thick systems. However, for thin films that this work focuses on we adopt this model insofar as the out-of-plane magnetization vanishes outside the small core.

As for the gyrovector cylindrical coordinates are used for the integration. The integral then reads

$$D = -\frac{M_s\mu_0}{\gamma}\int_0^d dz \int_0^{R_{\max}} d\rho\,\rho \int_0^{2\pi} d\beta\,(\vec{\nabla}\theta\vec{\nabla}\theta + \sin^2(\theta)\vec{\nabla}\phi\vec{\nabla}\phi) \tag{7.28}$$

where $R_{\max}$ is the size of the sample. This can be split up in two integrals

$$\begin{aligned} D = &-\frac{M_s\mu_0}{\gamma}\int_0^d dz \int_0^{R_0} d\rho\,\rho \int_0^{2\pi} d\beta\,(\vec{\nabla}\theta\vec{\nabla}\theta + \sin^2(\theta)\vec{\nabla}\phi\vec{\nabla}\phi) \\ &-\frac{M_s\mu_0}{\gamma}\int_0^d dz \int_{R_0}^{R_{\max}} d\rho\,\rho \int_0^{2\pi} d\beta\,(\vec{\nabla}\theta\vec{\nabla}\theta + \sin^2(\theta)\vec{\nabla}\phi\vec{\nabla}\phi). \end{aligned} \tag{7.29}$$

The first term is integrated over the vortex core while the second integral covers the region outside the core. According to the aforementioned model the out-of-plane magnetization is zero outside the core. Then $\sin^2(\theta)$ is equal to one and $\vec{\nabla}\theta\vec{\nabla}\theta$ vanishes. Since we deal with thin films, we assume that the magnetization is independent of the z coordinate and get

$$D = -\frac{M_s\mu_0 d}{\gamma}\int_0^{R_0} d\rho\,\rho \int_0^{2\pi} d\beta\,(\vec{\nabla}\theta\vec{\nabla}\theta + \sin^2(\theta)\vec{\nabla}\phi\vec{\nabla}\phi) - \frac{M_s\mu_0 d}{\gamma}\int_{R_0}^{R_{\max}} d\rho\,\rho \int_0^{2\pi} d\beta\,\vec{\nabla}\phi\vec{\nabla}\phi, \tag{7.30}$$

The gradients of the angles θ and ϕ have been derived in section 7.2. With these results one gets

$$\begin{aligned} D = &-\frac{M_s\mu_0 d}{\gamma}\int_0^{R_0} d\rho\,\rho \int_0^{2\pi} d\beta\,\left(\left(\frac{\partial\theta}{\partial\rho}\right)^2 \vec{e}_\rho\otimes\vec{e}_\rho + \sin^2(\theta)\frac{1}{\rho^2}\left(\frac{\partial\phi}{\partial\beta}\right)^2 \vec{e}_\beta\otimes\vec{e}_\beta\right) \\ &-\frac{M_s\mu_0 d}{\gamma}\int_{R_0}^{R_{\max}} d\rho\,\rho \int_0^{2\pi} d\beta\,\frac{1}{\rho^2}\left(\frac{\partial\phi}{\partial\beta}\right)^2 \vec{e}_\beta\otimes\vec{e}_\beta. \end{aligned} \tag{7.31}$$

The unit vectors of the cylindrical coordinates can be expressed by the unit vectors of the Cartesian

coordinates. This yields

$$\begin{aligned} D = &- \frac{M_s\mu_0 d}{\gamma}\int_0^{R_0} d\rho\,\rho\left(\frac{\partial\theta}{\partial\rho}\right)^2\int_0^{2\pi} d\beta\ (\cos(\beta)\vec{e}_x+\sin(\beta)\vec{e}_y)\otimes(\cos(\beta)\vec{e}_x+\sin(\beta)\vec{e}_y) \\ &- \frac{M_s\mu_0 d}{\gamma}\int_0^{R_0} d\rho\,\frac{1}{\rho}\sin^2(\theta)\int_0^{2\pi} d\beta\, n^2\,(\cos(\beta)\vec{e}_y-\sin(\beta)\vec{e}_x)\otimes(\cos(\beta)\vec{e}_y-\sin(\beta)\vec{e}_x) \\ &- \frac{M_s\mu_0 d}{\gamma}\int_{R_0}^{R_{\max}} d\rho\,\frac{1}{\rho}\int_0^{2\pi} d\beta\, n^2\,(\cos(\beta)\vec{e}_y-\sin(\beta)\vec{e}_x)\otimes(\cos(\beta)\vec{e}_y-\sin(\beta)\vec{e}_x)\,. \end{aligned} \tag{7.32}$$

After the integration over β this reduces to

$$\begin{aligned} D = &- \frac{\pi M_s\mu_0 d}{\gamma}\int_0^{R_0} d\rho\,\left(\rho\left(\frac{\partial\theta}{\partial\rho}\right)^2+n^2\frac{1}{\rho}\sin^2(\theta)\right)(\vec{e}_x\otimes\vec{e}_x+\vec{e}_y\otimes\vec{e}_y) \\ &- \frac{\pi M_s\mu_0 d n^2}{\gamma}\int_{R_0}^{R_{\max}} d\rho\,\frac{1}{\rho}\,(\vec{e}_x\otimes\vec{e}_x+\vec{e}_y\otimes\vec{e}_y)\,. \end{aligned} \tag{7.33}$$

The dissipation tensor has the same value for a vortex ($n=1$) or an antivortex ($n=-1$). It is

$$D = -\frac{\pi M_s\mu_0 d}{\gamma}\ln\left(\frac{R_{\max}}{R_0 e^{-C_D}}\right)(\vec{e}_x\otimes\vec{e}_x+\vec{e}_y\otimes\vec{e}_y) = -\frac{|G_0|}{2}\ln\left(\frac{R_{\max}}{R_0 e^{-C_D}}\right)(\vec{e}_x\otimes\vec{e}_x+\vec{e}_y\otimes\vec{e}_y) \tag{7.34}$$

with the parameter

$$C_D = \int_0^{R_0} d\rho\,\left(\rho\left(\frac{\partial\theta}{\partial\rho}\right)^2+\frac{1}{\rho}\sin^2(\theta)\right) \tag{7.35}$$

that depends on the magnetization in the core.

Since the integrand in equation (7.35) is a positive function C_D is always positive and thus $e^{-C_D}<1$. From the model of N. A. Usov and S. E. Peschany one obtains $C_D=2$ irrespective of the size of the vortex core. The value of $R_0e^{-C_D}$ depends on the thickness of the film. It can be determined from numerical calculations (see section 8.2). Equation (7.34) shows that the dissipation tensor is diagonal with $D_{xx}=D_{yy}=D_0$ and $D_{zz}=0$. From $R_0<R_{\max}$ and $e^{-C_D}<1$ we find that $D_0<0$. Equation (7.34) also shows that the dissipation tensor depends logarithmically on the sample size.

7.4 Energy

For the calculation of the force on the vortex core we will now calculate the different energies that contribute to the total energy of the core.

Confining Energy

For the confining energy we restrict ourselves to a potential that is symmetric under rotations by $\pi/2$ and mirroring with respect to the coordinate axes, for example the confining potential in a disc or square film element. The core of the vortex or antivortex is confined by the potential of the stray-field energy E_s and the exchange energy E_e. For small displacements of the vortex core from its equilibrium position this potential can be expanded up to second order in the coordinates X and Y that denote the displacement in x and y direction, respectively. Since the confining potential has

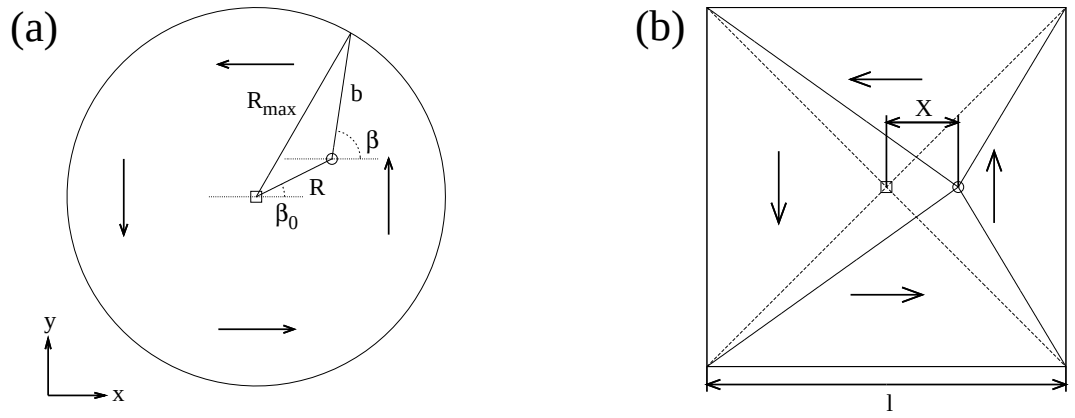

Figure 7.1: Scheme of a skyrmion core (circle) situated in (a) a disc with radius $R_{\max}$ or (b) a square with edge length l. The core is displaced from its equilibrium position (square) by a distance $R = \sqrt{X^2 + Y^2}$. In both figures the in-plane magnetization for a vortex with chirality $c = 1$ is depicted by the arrows. For the square the domain walls are depicted by the dashed and solid lines for a vortex core that is at its equilibrium position or displaced from this position, respectively. (The subfigures (a) and (b) are reprints from referenceces [156] and [178], respectively.)

mirroring symmetry all terms that are linear in X or Y vanish. The rotational symmetry ensures that the prefactors of X^2 and Y^2 are the same. The confining energy reads

$$E_c = \frac{1}{2} m\omega_r^2 (X^2 + Y^2), \tag{7.36}$$

where the term $m\omega_r^2$ parameterizes the strength of the potential.

Zeeman Energy of a Skyrmion in a Disc

Using cylindrical coordinates the position of the skyrmion is given by $X = R\cos(\beta_0)$ in x-direction and $Y = R\sin(\beta_0)$ in y-direction as shown in figure 7.1. The magnetization is given by equation (4.1). For the integration we use cylindrical coordinates with the origin at the skyrmion core. From figure 7.1 the relation $R_{\max}^2 = R^2 + b^2 - 2bR\,\cos(180° - \beta + \beta_0)$ can be obtained using the law of cosines. Thus the Zeeman energy for a magnetic field in y direction is given by

$$E_z = -\mu_0 M_s H d \int_0^{2\pi} d\beta\ \sin(\phi) \int_0^b dr' r' = -\mu_0 M_s H d \int_0^{2\pi} d\beta\ \sin(\phi) \frac{b^2}{2} \tag{7.37}$$

with $b = -R\cos(\beta - \beta_0) + \sqrt{R^2\cos^2(\beta - \beta_0) - R^2 + R_{\max}^2}$. For small displacements R, that is $R^2 \ll R_{\max}^2$, one finds $b^2 \approx R_{\max}^2 - 2R_{\max}R\cos(\beta - \beta_0)$ and the Zeeman energy can be written as

$$\begin{aligned} E_z =& \mu_0 M_s H R R_{\max} d \int_0^{2\pi} d\beta\ \sin\left(n\beta + \frac{\pi c}{2}\right) \cos(\beta - \beta_0) \\ =& \mu_0 M_s H R R_{\max} d \int_0^{2\pi} d\beta\ \left[\sin(n\beta)\cos\left(\frac{\pi c}{2}\right) + \cos(n\beta)\sin\left(\frac{\pi c}{2}\right)\right] \\ & \left[\cos(\beta)\cos(\beta_0) + \sin(\beta)\sin(\beta_0)\right]. \end{aligned} \tag{7.38}$$

Here we neglected the term proportional to $R_{\max}^2$ which does not depend on the position of the skyrmion.

Due to the orthogonality of the $\sin(nx)$ and $\cos(nx)$ functions the integral is non-zero only if $|n| = 1$. Thus in first order only skyrmions with winding numbers $n = \pm 1$ move in an external

Zeeman field. Therefore, in the following we focus on the winding numbers $n = 1$ and $n = -1$ which denote a vortex and an antivortex, respectively. The Zeeman energy is then given by

$$E_z = \mu_0 M_s H R_{\max} \pi d \left[\sin\left(\frac{\pi c}{2}\right) X + n \cos\left(\frac{\pi c}{2}\right) Y \right]. \tag{7.39}$$

In this model it is assumed that the magnetization pattern moves with the vortex or antivortex core but undergoes no deformation. Guslienko et *al.* calculated the Zeeman energy using a surface charge free model where the magnetization at the boundaries of the disk is always parallel to the surface. Thus except inside the small vortex core no surface charges emerge. Their Result differ by a factor of 2/3 compared to the result that is presented here.[48,65]

Zeeman Energy of a Skyrmion in a Square

In squared magnetic thin-film element as depicted in figure 7.1 the Zeeman energy of a magnetic field in y-direction can be calculated from the Zeeman energy of the four triangular domains. Depending on the chirality and the winding number the domains contribute with different signs. For $n = \pm 1$ the Zeeman energy is

$$\begin{aligned} E_z = \mu_0 M_s H d \frac{l}{2} \Bigg[& \underbrace{\left(\frac{l}{2} + X\right) \sin\left(\frac{\pi c}{2}\right)}_{\text{left domain}} - \underbrace{\left(\frac{l}{2} - X\right) \sin\left(\frac{\pi c}{2}\right)}_{\text{right domain}} \\ & - \underbrace{\left(\frac{l}{2} - Y\right) n \cos\left(\frac{\pi c}{2}\right)}_{\text{top domain}} + \underbrace{\left(\frac{l}{2} + Y\right) n \cos\left(\frac{\pi c}{2}\right)}_{\text{bottom domain}} \Bigg] \\ = \mu_0 M_s H l d & \left[\sin\left(\frac{\pi c}{2}\right) X + n \cos\left(\frac{\pi c}{2}\right) Y \right]. \end{aligned} \tag{7.40}$$

The expressions for the disc and for the square have the same form. Thus we can write

$$E_z = \mu_0 M_s H l d \left[\sin\left(\frac{\pi c}{2}\right) X + n \cos\left(\frac{\pi c}{2}\right) Y \right], \tag{7.41}$$

with the characteristic length l, where $l = R_{\max}\pi$ for the circular sample and l is the edge length for the quadratic sample.

7.5 Modified Thiele Equation

For an analytical investigation the motion of the vortex is commonly described employing the Thiele equation (7.13) that is derived in the last sections. This equation is exact for the steady state motion of a non-deformable magnetization pattern. However, this assumption holds true only for the small vortex core. Due to the spacial restriction the vortex has to deform while the core is moving. This yields a small modification of the Thiele equation that is especially important for current-driven vortex motion in view of the non-adiabatic spin torque.

Here we derive a modified Thiele equation that takes a deformation of the outer part of the vortex into account.

With the magnetization $\vec{M}$ and the magnetic field $\vec{H}$ a generalized version of the Thiele equation

reads[181]

$$\begin{aligned} 0 = &- \mu_0 \int dV \left[(\vec{\nabla}\theta)\frac{\partial}{\partial\theta} + (\vec{\nabla}\phi)\frac{\partial}{\partial\phi} \right] (\vec{H}\cdot\vec{M}) \\ &- \frac{M_s\mu_0}{\gamma} \int dV \, \sin(\theta)(\vec{\nabla}\theta \times \vec{\nabla}\phi) \times (\vec{v} + b_j\vec{j}) \\ &- \frac{M_s\mu_0}{\gamma} \int dV \, (\vec{\nabla}\theta\vec{\nabla}\theta + \sin^2(\theta)\vec{\nabla}\phi\vec{\nabla}\phi)(\alpha\vec{v} + \xi b_j\vec{j}) \end{aligned} \tag{7.42}$$

with the saturation magnetization M_S, the gyromagnetic ratio γ, the current density $\vec{j}$, the Gilbert damping α, the non-adiabaticity parameter ξ, and the coupling constant b_j between current and magnetization. θ and ϕ are the out-of-plane and in-plane angle of the magnetization, respectively. The velocity $\vec{v} = \vec{v}(r)$ of the magnetization pattern may depend on the position in the pattern. Assuming that the magnetization pattern does not deform the velocity is independent of the position. Then equation (7.42) can be written in the form

$$\vec{F} + \vec{G} \times (\vec{v}_c + b_j\vec{j}) + D(\alpha\vec{v}_c + \xi b_j\vec{j}) = 0 \tag{7.43}$$

with the velocity $\vec{v}_c$ of the vortex core.

The integrand in the gyrovector is non-zero only in the small vortex core where the out-of-plane angle θ varies while the integrand in the dissipation tensor is also non-zero outside the core. By comparing the distances between the domain walls in figure 7.1, it can be seen that close to the boundaries of the sample the magnetization pattern moves slower compared to the center. Thus the velocity in the third term of equation (7.42) depends on position. Aiming at a similar form as in equation (7.43) we replace the spatially dependent velocity $\vec{v}$ in the third term of equation (7.42) by an effective value $\vec{v}_e$ which is independent of position. This effective velocity occurs only in the third term as the second term is located at the vortex core. For a homogeneous current flow $b_j\vec{j}$ is constant over the sample. Thus we do not replace the current by an effective value. The equation then reads

$$\vec{F} + \vec{G} \times (\vec{v}_c + b_j\vec{j}) + D_0\alpha\vec{v}_e + D_0\xi b_j\vec{j} = 0. \tag{7.44}$$

The effective velocity $\vec{v}_e$ depends on the core position $\vec{R} = (X, Y)$ and the core velocity $\vec{v}_c$. For small deflections of the vortex core, that is small deformations of the vortex, $\vec{v}_e$ can be expanded in $\vec{R}$ and $\vec{v}_c$. For $\vec{v}_c = 0$ the magnetization is static and $\vec{v}_e = 0$. Thus the first non-vanishing term in the expansion is proportional to $\vec{v}_c$. Here and hereafter we write

$$\vec{v}_e = \frac{D_\Gamma}{D_0}\vec{v}_c. \tag{7.45}$$

Since the effective velocity $\vec{v}_e$ is always smaller than the velocity $\vec{v}_c$ of the vortex core $D_\Gamma/D_0 < 1$. Inserting equation (7.45) in equation (7.44) yields a modified Thiele equation

$$\vec{F} + \vec{G} \times (\vec{v}_c + b_j\vec{j}) + D_\Gamma\alpha\vec{v}_c + D_0\xi b_j\vec{j} = 0. \tag{7.46}$$

7.6 Equation of Motion

Equation (7.46) contains the velocity $\vec{v}_c$ of the vortex core in a cross product and a scalar product. We can transform this equation to an equation of motion that is explicit in $\vec{v}_c$. By multiplying equation (7.46) with $-D_\Gamma\alpha$ we get

$$-D_\Gamma\alpha\vec{F} - D_\Gamma\alpha\vec{G} \times \vec{v}_c - D_\Gamma\alpha\vec{G} \times b_j\vec{j} - D_\Gamma^2\alpha^2\vec{v}_c - D_\Gamma\alpha D_0\xi b_j\vec{j} = 0. \tag{7.47}$$

Taking the cross product of equation (7.46) with $\vec{G}$ leads to

$$\vec{G} \times \vec{F} - G_0^2\vec{v}_c - G_0^2 b_j\vec{j} + \vec{G} \times D_\Gamma\alpha\vec{v}_c + \vec{G} \times D_0\xi b_j\vec{j} = 0. \tag{7.48}$$

Here we used equation (1.14) and the orthogonality of $\vec{G}$ and $\vec{v}_c$. The sum of equation (7.47) and equation (7.48)

$$(G_0^2 + D_\Gamma^2\alpha^2)\vec{v}_c = -D_\Gamma\alpha\vec{F} + \vec{G}\times\vec{F} - D_\Gamma\alpha b_j\vec{G}\times\vec{j} + D_0\xi b_j\vec{G}\times\vec{j} - D_\Gamma\alpha D_0\xi b_j\vec{j} - G_0^2 b_j\vec{j} \quad (7.49)$$

leads to the sought equation

$$\vec{v}_c = \frac{-D_\Gamma\alpha\vec{F} + G_0\vec{e}_z\times\vec{F} - D_\Gamma\alpha b_j G_0\vec{e}_z\times\vec{j} + D_0\xi b_j G_0\vec{e}_z\times\vec{j} - D_\Gamma\alpha D_0\xi b_j\vec{j} - G_0^2 b_j\vec{j}}{G_0^2 + D_\Gamma^2\alpha^2} \quad (7.50)$$

for the velocity $\vec{v}_c$ of the vortex core. The force

$$\vec{F} = -\frac{d(E_s+E_z)}{d\vec{R}} = -\mu_0 M_s H l d\left[\sin\left(\frac{\pi c}{2}\right)\vec{e}_x + n\cos\left(\frac{\pi c}{2}\right)\vec{e}_y\right] - m\omega_r^2 X\vec{e}_x - m\omega_r^2 Y\vec{e}_y \quad (7.51)$$

can be calculated from the energies in equations (7.36) and (7.41). With this we can also calculate the expression

$$\vec{e}_z\times\vec{F} = -\mu_0 M_s H l d\left[\sin\left(\frac{\pi c}{2}\right)\vec{e}_y - n\cos\left(\frac{\pi c}{2}\right)\vec{e}_x\right] - m\omega_r^2 X\vec{e}_y + m\omega_r^2 Y\vec{e}_x. \quad (7.52)$$

We restrict ourselves to a current in x direction that is given by

$$\vec{j} = j\vec{e}_x \quad (7.53)$$

and its cross product with the z direction is given by

$$\vec{e}_z\times\vec{j} = j\vec{e}_y. \quad (7.54)$$

Inserting the force and the current in equation (7.50) we get

$$\begin{aligned}\begin{pmatrix}\dot{X}\\ \dot{Y}\end{pmatrix} = &-\frac{m\omega_r^2}{G_0^2+D_\Gamma^2\alpha^2}\begin{pmatrix}-D_\Gamma\alpha X - G_0 Y\\ -D_\Gamma\alpha Y + G_0 X\end{pmatrix} - \frac{\mu_0 M_s H l d}{G_0^2+D_\Gamma^2\alpha^2}\begin{pmatrix}-D_\Gamma\alpha\sin\left(\frac{\pi c}{2}\right) - G_0 n\cos\left(\frac{\pi c}{2}\right)\\ -D_\Gamma\alpha n\cos\left(\frac{\pi c}{2}\right) + G_0\sin\left(\frac{\pi c}{2}\right)\end{pmatrix}\\ &- \frac{G_0 b_j j}{G_0^2+D_\Gamma^2\alpha^2}\begin{pmatrix}G_0\\ D_\Gamma\alpha\end{pmatrix} - \frac{D_0\xi b_j j}{G_0^2+D_\Gamma^2\alpha^2}\begin{pmatrix}D_\Gamma\alpha\\ -G_0\end{pmatrix}.\end{aligned} \quad (7.55)$$

Here and hereafter we discard the z component since the core does not move in this direction.

In the absence of current and field the equation becomes homogeneous. The excited core performs an exponentially damped spiral rotation around its equilibrium position. This rotation is given by

$$\begin{pmatrix}X\\ Y\end{pmatrix} = C_1\begin{pmatrix}i\\ np\end{pmatrix}e^{-\Gamma t + i\omega t} + C_2\begin{pmatrix}-i\\ np\end{pmatrix}e^{-\Gamma t - i\omega t} \quad (7.56)$$

with the free frequency

$$\omega = -\frac{npG_0 m\omega_r^2}{G_0^2+D_\Gamma^2\alpha^2} \quad (7.57)$$

and the damping constant

$$\Gamma = -\frac{D_\Gamma\alpha m\omega_r^2}{G_0^2+D_\Gamma^2\alpha^2}. \quad (7.58)$$

C_1 and C_2 are constants that have to be chosen so that the displacement for $t = 0$ fulfills the starting conditions.

With the aid of the free frequency and the damping constant the equation of motion can be written as

$$\begin{aligned}\begin{pmatrix}\dot{X}\\ \dot{Y}\end{pmatrix} = &\begin{pmatrix}-\Gamma & -np\omega\\ np\omega & -\Gamma\end{pmatrix}\begin{pmatrix}X\\ Y\end{pmatrix} - \frac{\mu_0 M_s H l d np\omega G_0^{-1}}{\omega^2+\Gamma^2}\begin{pmatrix}-\Gamma\sin\left(\frac{\pi c}{2}\right) - p\omega\cos\left(\frac{\pi c}{2}\right)\\ -\Gamma n\cos\left(\frac{\pi c}{2}\right) + np\omega\sin\left(\frac{\pi c}{2}\right)\end{pmatrix}\\ &- \frac{np\omega b_j j}{\omega^2+\Gamma^2}\begin{pmatrix}np\omega\\ \Gamma\end{pmatrix} - \frac{D_0 np\omega G_0^{-1}\xi b_j j}{\omega^2+\Gamma^2}\begin{pmatrix}\Gamma\\ -np\omega\end{pmatrix}.\end{aligned} \quad (7.59)$$

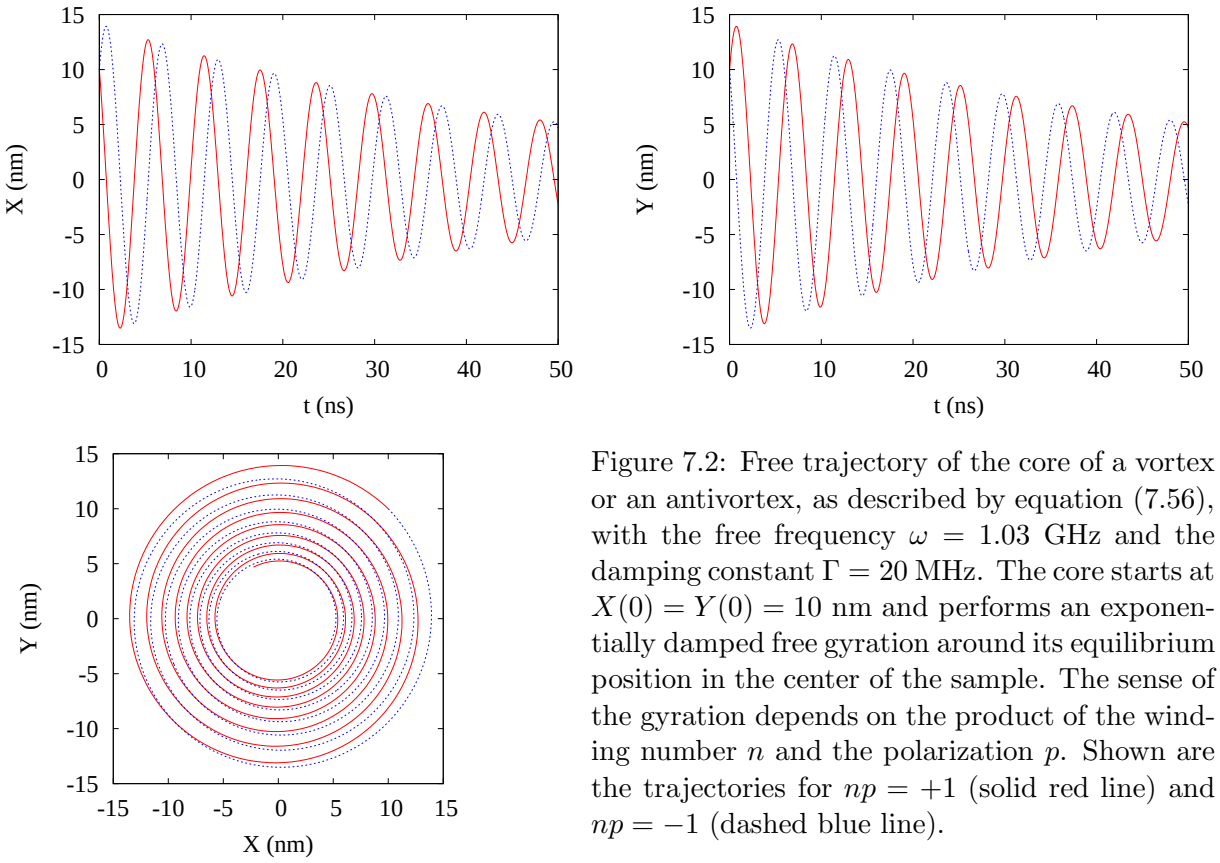

Figure 7.2: Free trajectory of the core of a vortex or an antivortex, as described by equation (7.56), with the free frequency $\omega = 1.03$ GHz and the damping constant $\Gamma = 20$ MHz. The core starts at $X(0) = Y(0) = 10$ nm and performs an exponentially damped free gyration around its equilibrium position in the center of the sample. The sense of the gyration depends on the product of the winding number n and the polarization p. Shown are the trajectories for $np = +1$ (solid red line) and $np = -1$ (dashed blue line).

By rearranging the terms we get

$$\begin{aligned}\begin{pmatrix}\dot{X}\\ \dot{Y}\end{pmatrix} = \begin{pmatrix}-\Gamma & -np\omega\\ np\omega & -\Gamma\end{pmatrix}\begin{pmatrix}X\\ Y\end{pmatrix} + \frac{\mu_0 M_s H l d p\omega G_0^{-1}\cos\left(\frac{\pi c}{2}\right)}{\omega^2+\Gamma^2}\begin{pmatrix}np\omega\\ \Gamma\end{pmatrix} - \frac{np\omega b_j j}{\omega^2+\Gamma^2}\begin{pmatrix}np\omega\\ \Gamma\end{pmatrix}\\ + \frac{\mu_0 M_s H l d np\omega G_0^{-1}\sin\left(\frac{\pi c}{2}\right)}{\omega^2+\Gamma^2}\begin{pmatrix}\Gamma\\ -np\omega\end{pmatrix} - \frac{D_0 np\omega G_0^{-1}\xi b_j j}{\omega^2+\Gamma^2}\begin{pmatrix}\Gamma\\ -np\omega\end{pmatrix}.\end{aligned} \tag{7.60}$$

Inserting the value of the gyrovector that is given in equation (7.26) yields

$$\begin{aligned}\begin{pmatrix}\dot{X}\\ \dot{Y}\end{pmatrix} = \begin{pmatrix}-\Gamma & -np\omega\\ np\omega & -\Gamma\end{pmatrix}\begin{pmatrix}X\\ Y\end{pmatrix} - \left(b_j j + \frac{\gamma H l p}{2\pi}\cos\left(\frac{\pi c}{2}\right)\right)\begin{pmatrix}\frac{\omega^2}{\omega^2+\Gamma^2}\\ \frac{np\Gamma\omega}{\omega^2+\Gamma^2}\end{pmatrix}\\ - \left(\left|\frac{D_0}{G_0}\right|\xi b_j j np + \frac{\gamma H l np}{2\pi}\sin\left(\frac{\pi c}{2}\right)\right)\begin{pmatrix}\frac{np\Gamma\omega}{\omega^2+\Gamma^2}\\ -\frac{\omega^2}{\omega^2+\Gamma^2}\end{pmatrix}.\end{aligned} \tag{7.61}$$

Harmonic Excitations

In the following we will focus on harmonic excitations, that are $j = j_0 e^{i\Omega t}$ and $H = H_0 e^{i\Omega t}$. The current and the magnetic field are assumed to be in phase. We introduce two abbreviations. In the following we express the current as

$$\tilde{j}_x = b_j j_0 \tag{7.62}$$

and the field as

$$\tilde{H}_y = \frac{\gamma H_0 l}{2\pi}. \tag{7.63}$$

Both values have the dimension of a velocity and allow us to compare the field and the current. The equation of motion is then given by

$$\begin{aligned}\begin{pmatrix}\dot{X}\\ \dot{Y}\end{pmatrix} &= \begin{pmatrix}-\Gamma & -np\omega\\ np\omega & -\Gamma\end{pmatrix}\begin{pmatrix}X\\ Y\end{pmatrix}\\ &- \begin{pmatrix}\tilde{j}_x + \tilde{H}_y p\cos\left(\frac{\pi c}{2}\right) & \left|\frac{D_0}{G_0}\right|\xi\tilde{j}_x np + \tilde{H}_y np\sin\left(\frac{\pi c}{2}\right)\\ -\left|\frac{D_0}{G_0}\right|\xi\tilde{j}_x np - \tilde{H}_y np\sin\left(\frac{\pi c}{2}\right) & \tilde{j}_x + \tilde{H}_y p\cos\left(\frac{\pi c}{2}\right)\end{pmatrix}\begin{pmatrix}\frac{\omega^2}{\omega^2+\Gamma^2}\\ \frac{np\Gamma\omega}{\omega^2+\Gamma^2}\end{pmatrix}e^{i\Omega t}.\end{aligned} \tag{7.64}$$

In this equation both matrices commute. In the trivial case where $\tilde{j}_x + \tilde{H}_y p\cos(\pi c/2) = 0$ and $|D_0/G_0|\,\xi\tilde{j}_x np + \tilde{H}_y np\sin(\pi c/2) = 0$ there is no dynamics of the vortex or antivortex. In all other cases the matrix

$$\begin{pmatrix}\tilde{j}_x + \tilde{H}_y p\cos\left(\frac{\pi c}{2}\right) & \left|\frac{D_0}{G_0}\right|\xi\tilde{j}_x np + \tilde{H}_y np\sin\left(\frac{\pi c}{2}\right)\\ -\left|\frac{D_0}{G_0}\right|\xi\tilde{j}_x np - \tilde{H}_y np\sin\left(\frac{\pi c}{2}\right) & \tilde{j}_x + \tilde{H}_y p\cos\left(\frac{\pi c}{2}\right)\end{pmatrix} \tag{7.65}$$

is invertible. For these cases we can introduce a new coordinate system $(\tilde{X}, \tilde{Y})$ that is given by

$$\begin{pmatrix}X\\ Y\end{pmatrix} = \begin{pmatrix}\tilde{j}_x + \tilde{H}_y p\cos\left(\frac{\pi c}{2}\right) & \left|\frac{D_0}{G_0}\right|\xi\tilde{j}_x np + \tilde{H}_y np\sin\left(\frac{\pi c}{2}\right)\\ -\left|\frac{D_0}{G_0}\right|\xi\tilde{j}_x np - \tilde{H}_y np\sin\left(\frac{\pi c}{2}\right) & \tilde{j}_x + \tilde{H}_y p\cos\left(\frac{\pi c}{2}\right)\end{pmatrix}\begin{pmatrix}\tilde{X}\\ \tilde{Y}\end{pmatrix}. \tag{7.66}$$

Both coordinate systems can be transformed into each other by a rotation and a subsequent scaling. By inserting equation (7.66) in equation (7.64) and a multiplication with the inverse matrix of equation (7.65) one finds that in the new coordinate system the equation of motion is given by

$$\begin{pmatrix}\dot{\tilde{X}}\\ \dot{\tilde{Y}}\end{pmatrix} = \begin{pmatrix}-\Gamma & -np\omega\\ np\omega & -\Gamma\end{pmatrix}\begin{pmatrix}\tilde{X}\\ \tilde{Y}\end{pmatrix} - \begin{pmatrix}\frac{\omega^2}{\omega^2+\Gamma^2}\\ \frac{np\Gamma\omega}{\omega^2+\Gamma^2}\end{pmatrix}e^{i\Omega t}. \tag{7.67}$$

This equation can also be written as

$$\begin{pmatrix}\dot{\tilde{X}}\\ \dot{\tilde{Y}}\end{pmatrix} = \begin{pmatrix}-\Gamma & -np\omega\\ np\omega & -\Gamma\end{pmatrix}\begin{pmatrix}\tilde{X}\\ \tilde{Y} + \frac{np\omega}{\omega^2+\Gamma^2}e^{i\Omega t}\end{pmatrix}. \tag{7.68}$$

Thus in the new coordinate system the equilibrium position of the vortex or antivortex is shifted along the $\tilde{Y}$ axis.

Equation (7.67) is of the form

$$\begin{pmatrix}\dot{\tilde{X}}\\ \dot{\tilde{Y}}\end{pmatrix} = \begin{pmatrix}-\Gamma & -np\omega\\ np\omega & -\Gamma\end{pmatrix}\begin{pmatrix}\tilde{X}\\ \tilde{Y}\end{pmatrix} + \begin{pmatrix}A\\ B\end{pmatrix}e^{i\Omega t}. \tag{7.69}$$

The solution of this equation is calculated in appendix B and is given by

$$\begin{pmatrix}\tilde{X}\\ \tilde{Y}\end{pmatrix} = \frac{e^{i\Omega t}}{\omega^2 + (i\Omega+\Gamma)^2}\begin{pmatrix}A(i\Omega+\Gamma) - Bnp\omega\\ Anp\omega + B(i\Omega+\Gamma)\end{pmatrix}. \tag{7.70}$$

This yields the solution

$$\begin{pmatrix}\tilde{X}\\ \tilde{Y}\end{pmatrix} = -\frac{e^{i\Omega t}}{\omega^2 + (i\Omega+\Gamma)^2}\begin{pmatrix}\frac{\omega^2(i\Omega+\Gamma)}{\omega^2+\Gamma^2} - \frac{\Gamma\omega^2}{\omega^2+\Gamma^2}\\ \frac{\omega^3 np}{\omega^2+\Gamma^2} + \frac{np\Gamma\omega(i\Omega+\Gamma)}{\omega^2+\Gamma^2}\end{pmatrix} = -\frac{e^{i\Omega t}}{\omega^2 + (i\Omega+\Gamma)^2}\begin{pmatrix}\frac{\omega^2 i\Omega}{\omega^2+\Gamma^2}\\ \omega np + \frac{np\Gamma\omega i\Omega}{\omega^2+\Gamma^2}\end{pmatrix} \tag{7.71}$$

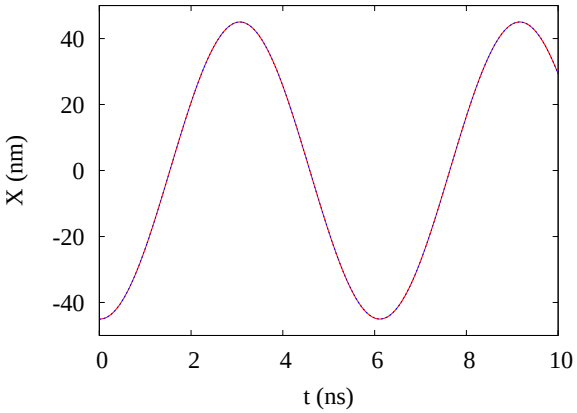

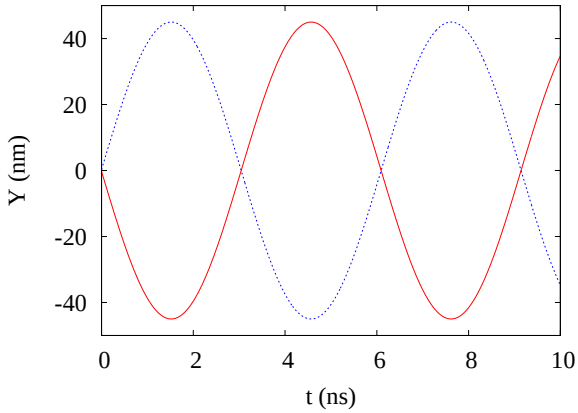

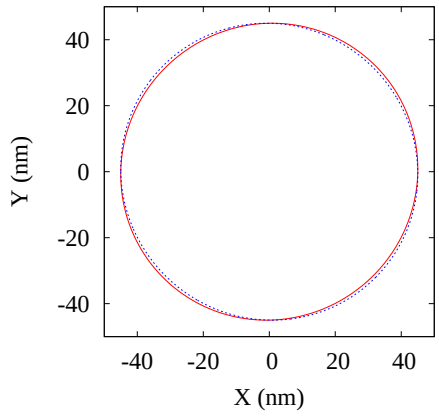

Figure 7.3: Trajectory of the core of a vortex or an antivortex that is excited by an alternating spin-polarized current in x direction at resonance. The dynamics is described by equation (7.72) with $\tilde{j} = 1.8$ m/s, the free frequency $\omega = 1.03$ GHz, the damping constant $\Gamma = 20$ MHz, the non-adiabaticity parameter $\xi = 0.01$, and $|D_0/G_0| = 2.26$. The sense of the gyration depends on the product of the winding number n and the polarization p. Shown are the trajectories for $np = +1$ (solid red line) and $np = -1$ (dashed blue line).

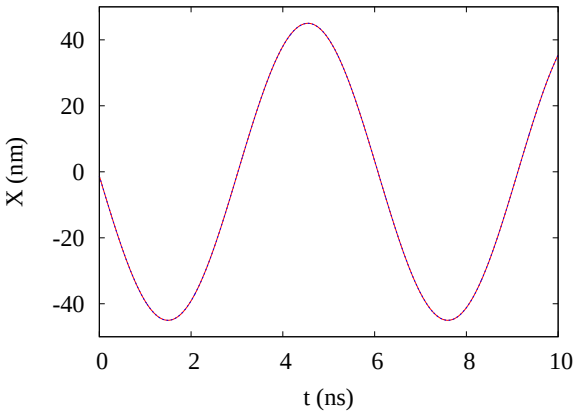

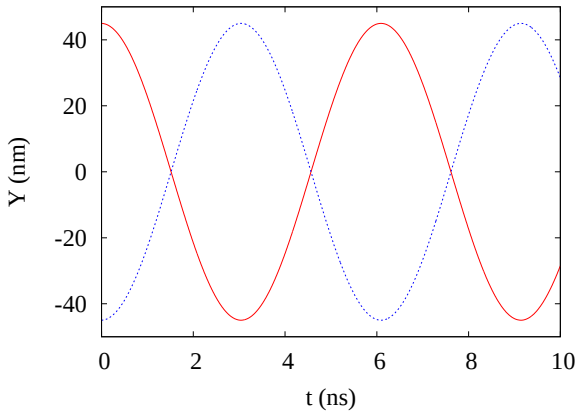

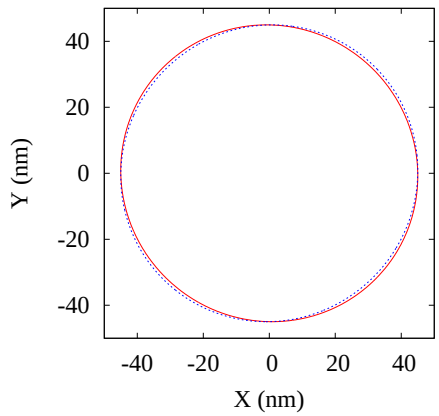

Figure 7.4: Trajectory of the core of a vortex or an antivortex that is excited by an alternating magnetic field in y direction at resonance. The chirality is $c = 1$. The dynamics is described by equation (7.72) with $\tilde{H} = 1.8$ m/s, the free frequency $\omega = 1.03$ GHz, and the damping constant $\Gamma = 20$ MHz. The sense of the gyration depends on the product of the winding number n and the polarization p. Shown are the trajectories for $np = +1$ (solid red line) and $np = -1$ (dashed blue line)

that can be transformed back to the original coordinate system to get the sought solution

$$\begin{pmatrix} X \\ Y \end{pmatrix} = -\frac{e^{i\Omega t}}{\omega^2 + (i\Omega + \Gamma)^2} \begin{pmatrix} \tilde{j}_x + \tilde{H}_y p \cos\left(\frac{\pi c}{2}\right) & \left|\frac{D_0}{G_0}\right| \xi \tilde{j}_x np + \tilde{H}_y np \sin\left(\frac{\pi c}{2}\right) \\ -\left|\frac{D_0}{G_0}\right| \xi \tilde{j}_x np - \tilde{H}_y np \sin\left(\frac{\pi c}{2}\right) & \tilde{j}_x + \tilde{H}_y p \cos\left(\frac{\pi c}{2}\right) \end{pmatrix} \begin{pmatrix} \frac{\omega^2 i\Omega}{\omega^2+\Gamma^2} \\ \omega np + \frac{np\Gamma\omega i\Omega}{\omega^2+\Gamma^2} \end{pmatrix}. \tag{7.72}$$

Examples for the dynamics of a harmonically-excited vortex or antivortex are shown in figures 7.3 (current) and 7.4 (field). The solution for a current in y direction and a magnetic field in x direction can be found from a rotation of the coordinate system by $-\pi/2$, that is a rotation of the above solution by $\pi/2$, and the replacements of $\tilde{j}_x \to \tilde{j}_y$ and $\tilde{H}_y \to -\tilde{H}_x$. For the case of the antivortex it is important to keep in mind that the rotation also affects the chirality. The chirality can be derived from equation (4.1) that yields $c = (\phi - n\beta)2/\pi$. A rotation by $-\pi/2$ increases the angles ϕ and β by $\pi/2$. This leads to

$$c' = (\phi' - n\beta')\frac{2}{\pi} = \left(\phi + \frac{\pi}{2} - n\beta - n\frac{\pi}{2}\right)\frac{2}{\pi} = (\phi - n\beta)\frac{2}{\pi} + (1 - n). \tag{7.73}$$

In general the rotation by $-\pi/2$ increases the chirality by $1 - n$. This leads to the additional replacement $c \to c - 1 + n$ so that after the rotation the system assumes the desired chirality. The result then reads

$$\begin{pmatrix} X \\ Y \end{pmatrix} = -\frac{e^{i\Omega t}}{\omega^2 + (i\Omega + \Gamma)^2} \begin{pmatrix} \left|\frac{D_0}{G_0}\right| \xi \tilde{j}_y np - \tilde{H}_x p \sin\left(\frac{\pi c}{2}\right) & -\tilde{j}_y + \tilde{H}_x np \cos\left(\frac{\pi c}{2}\right) \\ \tilde{j}_y - \tilde{H}_x np \cos\left(\frac{\pi c}{2}\right) & \left|\frac{D_0}{G_0}\right| \xi \tilde{j}_y np - \tilde{H}_x p \sin\left(\frac{\pi c}{2}\right) \end{pmatrix} \begin{pmatrix} \frac{\omega^2 i\Omega}{\omega^2+\Gamma^2} \\ \omega np + \frac{np\Gamma\omega i\Omega}{\omega^2+\Gamma^2} \end{pmatrix}. \tag{7.74}$$

With equations (7.56), (7.72), and (7.74) we have an analytical description of the dynamics of magnetic vortices and antivortices under harmonic excitations with currents and fields. After the transient states have been damped out the core of the vortex or antivortex gyrates on an elliptical trajectory around its equilibrium position. The sense of gyration depends only on the product of the core polarization p and the winding number n. For $pn = 1$ the core gyrates counter clockwise and for $pn = -1$ the core gyrates clockwise. The field-driven dynamics depend on the chirality while for the current-driven dynamics the trajectory is independent of the chirality.

Pulsed Excitations

In the following we will discuss the excitation of a vortex or an antivortex with a current or field pulse of the form $\vec{j}(t) = \Theta(t - t_0)\vec{j}_0$ or $\vec{H}(t) = \Theta(t - t_0)\vec{H}_0$, respectively. Here $\Theta(t)$ is the Heaviside step function that is given by

$$\Theta(t) = \begin{cases} 0, & t \leq 0 \\ 1, & t > 0. \end{cases} \tag{7.75}$$

Thus there is no field or current prior to time $t = t_0$. After this time the current and field have a constant value. A long time after the current or field has been changed, that is all transient states are damped out, the position of the core can be determined from equations (7.72) and (7.74) by setting $\Omega = 0$. This position is given by

$$\begin{pmatrix} X_\infty \\ Y_\infty \end{pmatrix} = -\frac{\omega}{\omega^2 + \Gamma^2} \begin{pmatrix} \left|\frac{D_0}{G_0}\right| \xi \tilde{j}_x - \tilde{j}_y np + \tilde{H}_x \cos\left(\frac{\pi c}{2}\right) + \tilde{H}_y \sin\left(\frac{\pi c}{2}\right) \\ \tilde{j}_x np + \left|\frac{D_0}{G_0}\right| \xi \tilde{j}_y - \tilde{H}_x n \sin\left(\frac{\pi c}{2}\right) + \tilde{H}_y n \cos\left(\frac{\pi c}{2}\right) \end{pmatrix}. \tag{7.76}$$

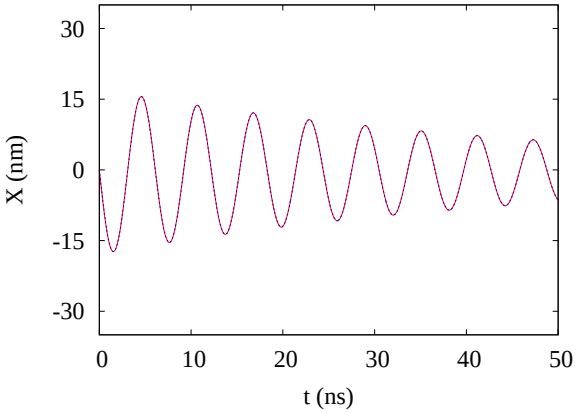

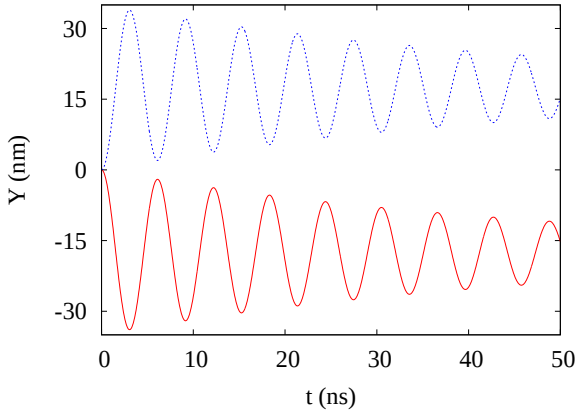

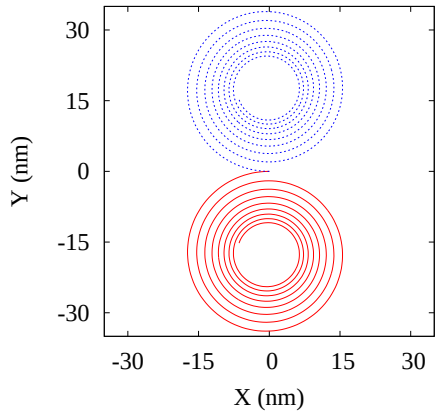

Figure 7.5: Trajectory of the core of a vortex or an antivortex that is excited by spin-polarized current in x direction. For $t < 0$ the current is zero and the core is at its equilibrium position at the middle of the sample. For $t > 0$ a constant current of $\tilde{j} = 18$ m/s is applied and the core starts to gyrate around a new equilibrium position. The dynamics is described by equation (7.79) with the free frequency $\omega = 1.03$ GHz, the damping constant $\Gamma = 20$ MHz, the non-adiabaticity parameter $\xi = 0.01$, and $|D_0/G_0| = 2.26$. The new equilibrium position depends on the product of the winding number n and the polarization p. Shown are the trajectories for $np = +1$ (solid red line) and $np = -1$ (dashed blue line).

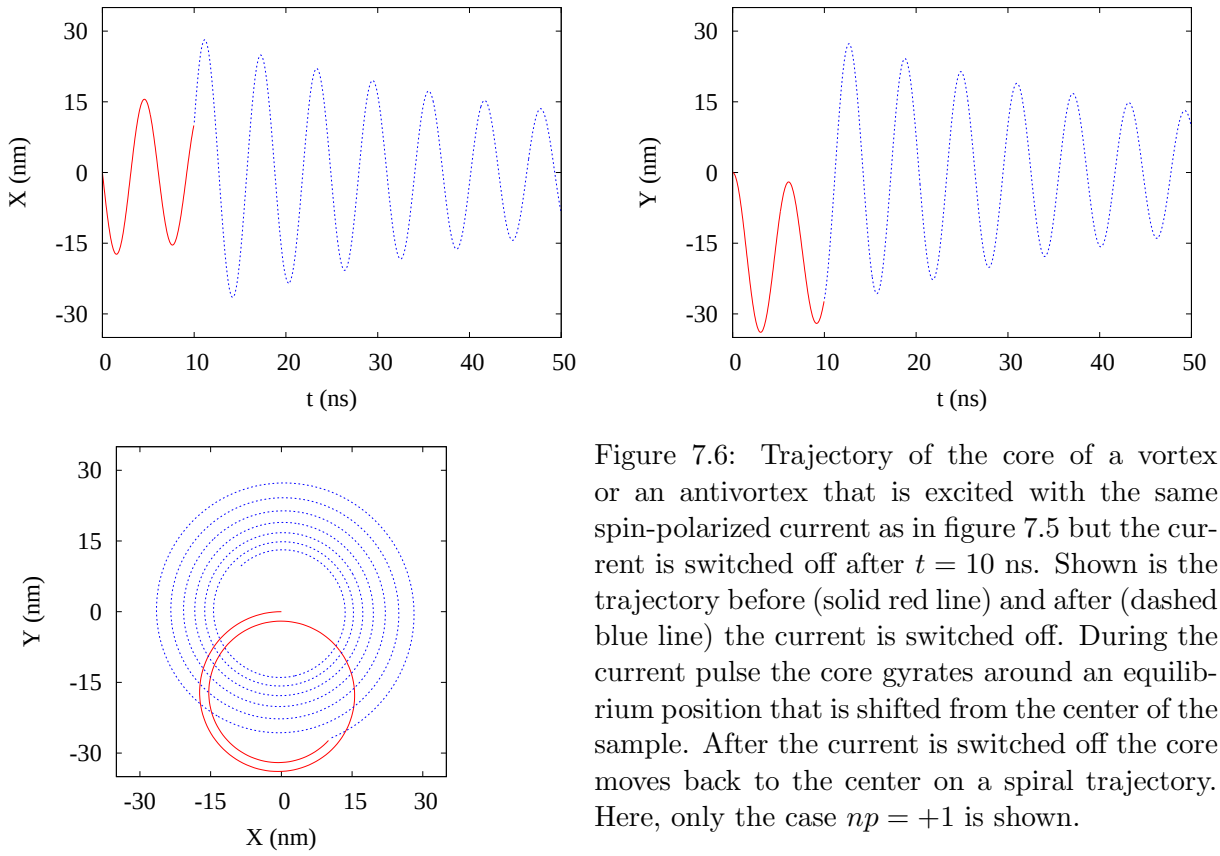

Figure 7.6: Trajectory of the core of a vortex or an antivortex that is excited with the same spin-polarized current as in figure 7.5 but the current is switched off after $t = 10$ ns. Shown is the trajectory before (solid red line) and after (dashed blue line) the current is switched off. During the current pulse the core gyrates around an equilibrium position that is shifted from the center of the sample. After the current is switched off the core moves back to the center on a spiral trajectory. Here, only the case $np = +1$ is shown.

With the aid of equation (7.56) the position including the transient states is written as

$$\begin{pmatrix} X \\ Y \end{pmatrix} = C_1 \begin{pmatrix} i \\ np \end{pmatrix} e^{-\Gamma(t-t_0)+i\omega(t-t_0)} + C_2 \begin{pmatrix} -i \\ np \end{pmatrix} e^{-\Gamma(t-t_0)-i\omega(t-t_0)} + \begin{pmatrix} X_\infty \\ Y_\infty \end{pmatrix} \tag{7.77}$$

where C_1 and C_2 are given by

$$\begin{pmatrix} X_0 \\ Y_0 \end{pmatrix} = C_1 \begin{pmatrix} i \\ np \end{pmatrix} + C_2 \begin{pmatrix} -i \\ np \end{pmatrix} + \begin{pmatrix} X_\infty \\ Y_\infty \end{pmatrix}. \tag{7.78}$$

Here (X_0, Y_0) is the core position at time $t = t_0$. The solution is given by

$$\begin{aligned} \begin{pmatrix} X \\ Y \end{pmatrix} = {} & \frac{np(Y_0 - Y_\infty) - i(X_0 - X_\infty)}{2} \begin{pmatrix} i \\ np \end{pmatrix} e^{-\Gamma(t-t_0)+i\omega(t-t_0)} \\ & + \frac{np(Y_0 - Y_\infty) + i(X_0 - X_\infty)}{2} \begin{pmatrix} -i \\ np \end{pmatrix} e^{-\Gamma(t-t_0)-i\omega(t-t_0)} + \begin{pmatrix} X_\infty \\ Y_\infty \end{pmatrix}. \end{aligned} \tag{7.79}$$

For a current-driven excitation an example for a trajectory can be found in figure 7.5. Pulses of finite length can be expressed by a successive application of equation (7.79) where the initial positions for each step are the final positions from the preceding step. An example is shown in figure 7.6.

8 Numerical Calculations

The applicability of the approximations leading to the analytical result in equations (7.56), (7.72), (7.74), and (7.79) are tested by micromagnetic simulations. In this section we will discuss the

results of micromagnetic simulations for magnetic thin-film elements of different sizes containing vortices and antivortices with different polarizations and chiralities.

The results are compared with the analytical predictions. The analytical calculations yield the position of the vortex core. In the numerical simulations the position of the vortex is defined by the maximum amplitude of the out-of-plane magnetization. To determine this maximum, the simulation cell with maximum out-of-plane magnetization and its next neighbors are interpolated with a polynomial of second order (see appendix C for details). For the simulations the material parameters of permalloy are used, that are an exchange constant of $A = 13 \cdot 10^{-12}$ J/m and a saturation magnetization of $M_s = 8 \cdot 10^5$ A/m. Numerical calculations are performed for vortices in square film elements with edge lengths l from 200 nm to 1000 nm and film thicknesses d from 10 nm to 30 nm. The magnetization dynamics is investigated mainly for square shaped magnetic film elements with length $l = 200$ nm and thickness $d = 20$ nm and with length $l = 500$ nm and thickness $d = 10$ nm. This system sizes allow for reasonable computing time. The results that are presented in this section have been published in references [157, 178, 179].

8.1 Calculation of the Groundstate

For the simulations the magnetization configuration of a vortex in the groundstate for all lateral sizes l and thicknesses d is needed. As one can see from equation (7.2) the Gilbert damping parameter α occurs only in a term that is proportional to the time derivative of the magnetization. When the simulation reaches its groundstate this time derivative becomes zero. Thus the groundstate is not affected by the choice of the parameter α. For calculations of the groundstate it is convenient to use a high Gilbert damping that speeds up the calculation since there is a faster dissipation of energy. Here a value of $\alpha = 0.5$ is used. Since the LLG equation provides only the time derivative of the magnetization it is inevitable to supply an initial magnetization for the simulations. The final state depends strongly on this initial magnetization. For instance the polarization and chirality of the final state are affected by the initial magnetization. There are even initial magnetizations that do not relax to a vortex state. In the calculations that are presented here the groundstate for $l = 200$ nm and $d = 20$ nm is calculated using the initial magnetization that is given by the pattern

$$\frac{\vec{M}}{M_s} = \begin{cases} (0,0,p), & x^2+y^2 \leq 100 \text{ nm}^2 \\ (0,c,0), & x^2+y^2 > 100 \text{ nm}^2,\ y \leq x, \text{ and } y > -x \\ (c,0,0), & x^2+y^2 > 100 \text{ nm}^2,\ y \leq x, \text{ and } y \leq -x \\ (0,-c,0), & x^2+y^2 > 100 \text{ nm}^2,\ y > x, \text{ and } y \leq -x \\ (-c,0,0), & x^2+y^2 > 100 \text{ nm}^2,\ y > x, \text{ and } y > -x \end{cases} \tag{8.1}$$

that is depicted in figure 8.1 for polarization $p = 1$ and chirality $c = 1$. Subsequently, the groundstate obtained for $l = 200$ nm and $d = 20$ nm is scaled and serves as an initial state for the remaining samples.

8.2 The Free Parameters of the Analytical Calculations

In the analytical calculations we have three free parameters, the strength $m\omega_r^2$ of the confining potential, the ratio D_Γ/G_0, and the ration D_0/G_0. The first two parameters are needed to calculate the free frequency ω and the damping constant Γ while the third one is important for the strength of the non-adiabatic spin torque. Here, these free parameters are determined from numerical calculations for vortices in square film elements with edge lengths l from 200 nm up to 1000 nm and film thicknesses d from 10 nm up to 30 nm.

For the determination of $m\omega_r^2$ and D_Γ/G_0 the vortex is excited by a short field pulse. Due to this field pulse the vortex core is displaced from its equilibrium position. After the field is switched off the core performs a damped spiral gyration around its equilibrium position, that is the midpoint of the sample. This gyration can be fitted with the expression in equation (7.56). This yields the

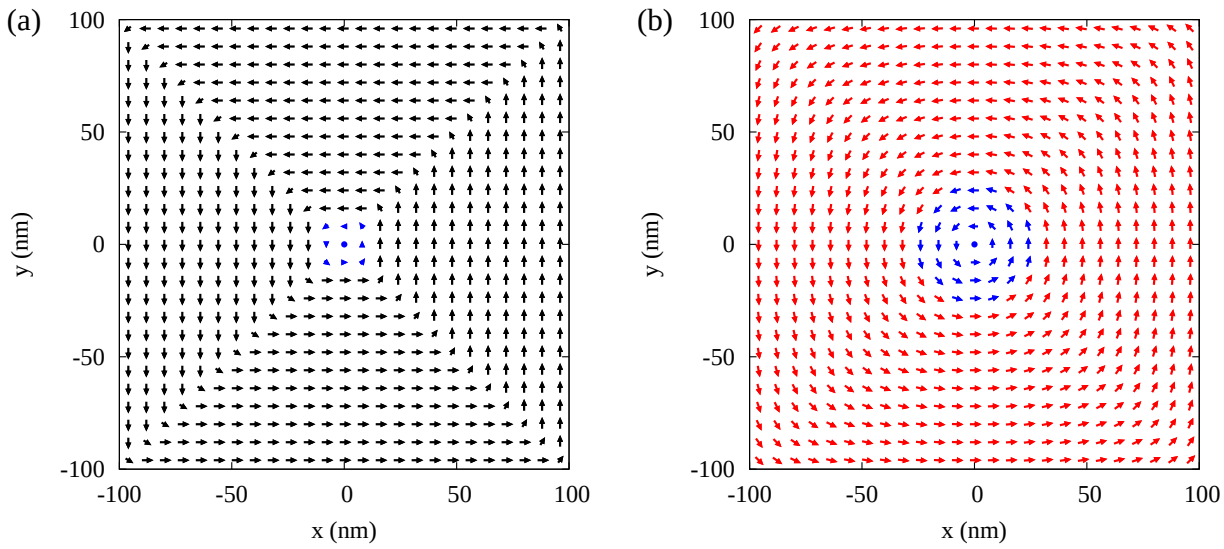

Figure 8.1: (a) Scheme of the initial magnetization as defined in equation (8.1) for the calculation of the groundstate in a permalloy thin-film element with $l = 200$ nm and $d = 20$ nm. In a simulation with $\alpha = 0.5$ this pattern relaxes to the vortex state shown in (b). (b) One of the four energetically degenerate vortex groundstates in a permalloy thin-film element with $l = 200$ nm and $d = 20$ nm. Shown is the groundstate with polarization $p = 1$ and chirality $c = 1$. The grid for the simulation has one cell in the perpendicular direction and a cell size of 2 nm in lateral direction. In both plots the color denotes the sign of the out-of-plane magnetization. Blue is a positive and red is a negative out-of-plane magnetization. A black arrow denotes a vanishing out-of-plane magnetization. One arrow represents the average magnetization of 4×4 simulation cells.

values of the free frequency ω and the damping constant Γ. From these values it is possible to calculate $m\omega_r^2$ and D_Γ/G_0 with the aid of equations (7.57) and (7.58).

Since the ratio D_0/G_0 occurs only in the term that describes the non-adiabatic spin torque we need an excitation with a current to determine its value. One possibility is to excite the sample with a direct current that displaces the core to a new equilibrium position. From equation (7.72) one finds that this new equilibrium position is given by

$$\begin{pmatrix} X_{\mathrm{dc}} \\ Y_{\mathrm{dc}} \end{pmatrix} = -\frac{\omega}{\omega^2 + \Gamma^2} \begin{pmatrix} \left|\frac{D_0}{G_0}\right| \xi \tilde{j}_x \\ \tilde{j}_x np \end{pmatrix}. \tag{8.2}$$

The factor $\omega\tilde{j}_x/(\omega^2 + \Gamma^2)$ can be eliminated by using the ratio between the x component and the y component of the position. The value of $|D_0/G_0|$ is now given by

$$\left|\frac{D_0}{G_0}\right| = \frac{npX_{\mathrm{dc}}}{\xi Y_{\mathrm{dc}}}. \tag{8.3}$$

The results of the three parameters for all values of l and d can be found in figure 8.2.

8.3 Amplitude and Phase of a Harmonically Excited Vortex

The analytical result for a harmonically excited vortex in equation (7.72) can be compared with results obtained from numerical simulations. Since the free parameters of the analytical calculations have been obtained in section 8.2 from pulsed excitations we can compare the analytical and numerical data for harmonic excitations without any free parameter. The numerical simulations are performed with a Gilbert damping parameter of $\alpha = 0.01$ that is in the regime that has been found experimentally for permalloy.[141–143] The value of the non-adiabatic spin-torque parameter

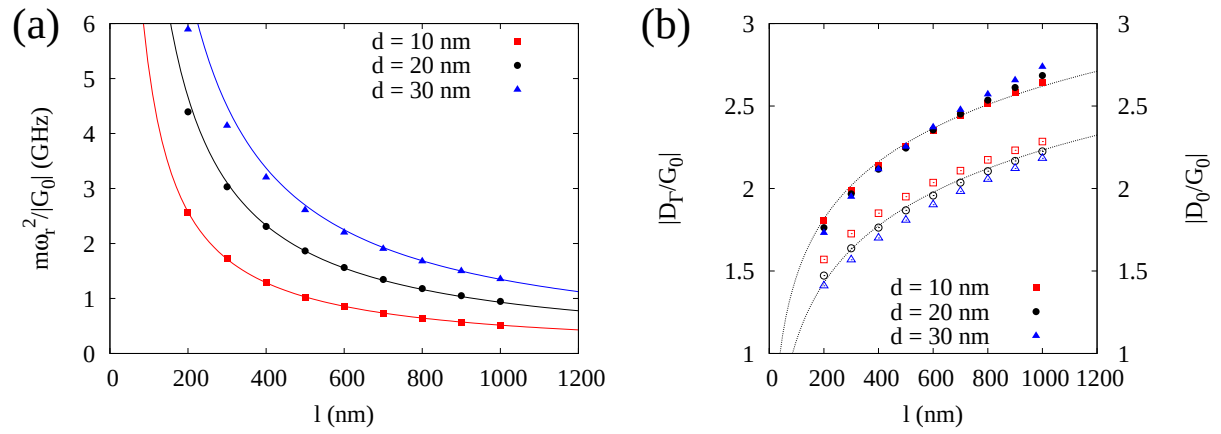

Figure 8.2: Values of the free parameters $m\omega_r^2$, D_Γ/G_0, and D_0/G_0 of the analytical calculations for a vortex in a permalloy square with edge length l and thickness d. (a) The strength $m\omega_r^2$ of the confining potential with respect to the length l for different thicknesses d divided by the length $|G_0|$ of the gyrovector. For small aspect ratios d/l the strength is well described by a $1/l$ power law.[36] The lines denote fits with $(41.7d + 98\text{ nm})\text{ GHz}/l$. Since $|G_0|$ is proportional to d, this fit describes a quadratic dependence of the energy on the thickness. (b) Values of the geometric prefactors for the damping D_Γ/G_0 (open symbols) and for the non-adiabatic spin torque D_0/G_0 (closed symbols) in dependence of l for different values of d. It can be clearly seen that both ratios are not the same as discussed in the analytical calculations in section 7.5. The dotted lines denote the logarithmic dependences on the sample size as found in equation (7.34). (Subfigure (b) is a reprint from the supporting material of reference [179].)

ξ is under strong debate.[105,121,170,172,185] Here a value of $\xi = \alpha = 0.01$ is used.[170,172] The model system is a square shaped thin-film element with $l = 200$ nm edge length and $d = 20$ nm thickness. This system size allows for a reasonable computation time.

The simulations start with the vortex in its groundstate. An alternating current with a spin-polarized current density $jP = 2.5 \cdot 10^{10}$ A/m^2 is applied in x-direction or an alternating field of $H = 250$ A/m is applied in y-direction. In a first step the system is simulated for at least 100 ns. In this time the transient states are damped out to about 0.15 % of their original amplitude. In a subsequent simulation the system is simulated for one period of the exciting force. During this simulation the magnetization is stored spatially resolved and the position of the core is extracted. From the trajectory one can obtain the maximum displacement from the center in x and y direction. The phase is given by the phase of the current or field at the time when the maximum displacement in x direction or y direction is reached.

Figures 8.3 and 8.4 show the numerically and analytically obtained amplitudes and the phases of the oscillation. In the current-driven oscillation an excellent accordance between analytical calculations and numerical simulations is found. In the field-driven case the amplitudes of the analytical solution are smaller than the amplitudes obtained from the micromagnetic simulations. These deviations are caused by the differences between the approximate magnetization depicted in figure 7.1 and the exact state. The phases between the maximum of the exciting magnetic field and the maximum deflection in x- and y-direction agree very well.

9 Oersted Field

In addition to the spin-torque effect the current acts on the magnetization via its Oersted field. In this section the Oersted field in a cube that is traversed by a current will be derived and its influence on the magnetization will be discussed.

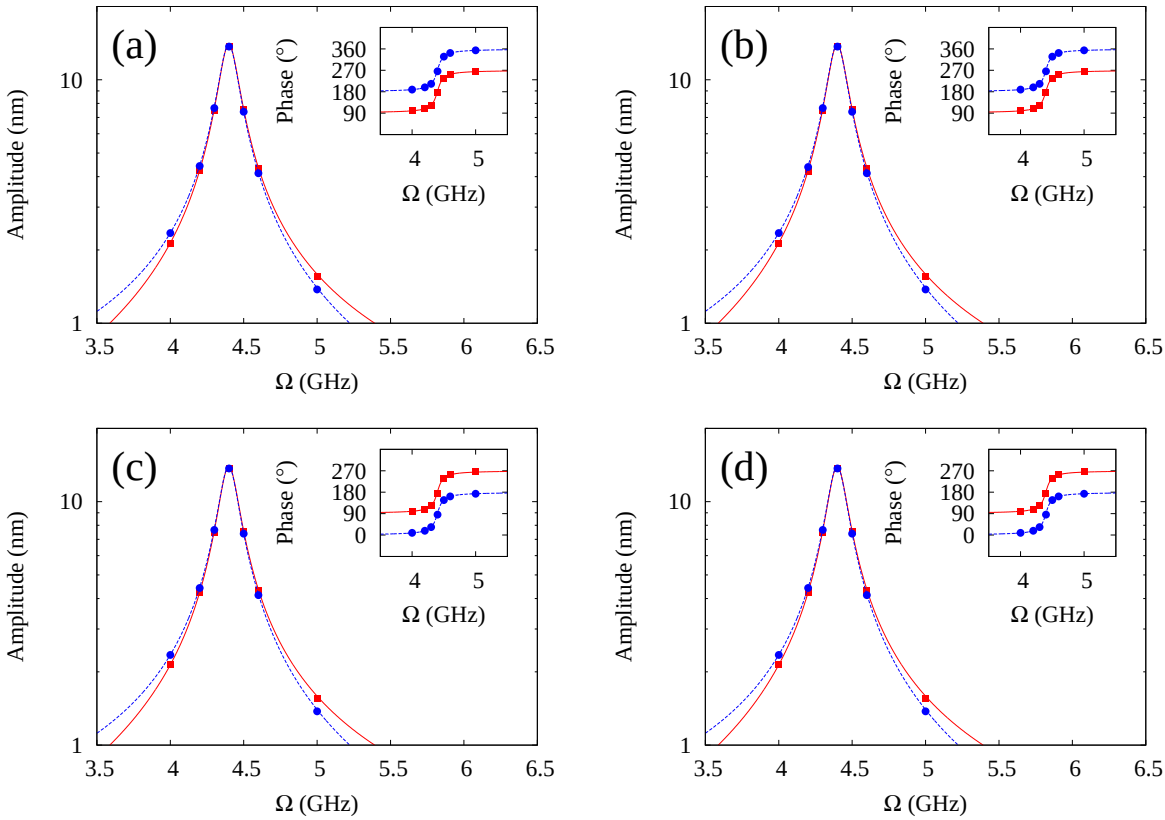

Figure 8.3: Amplitude of the current-driven vortex oscillation in x-direction (solid red line, squares) and y-direction (dashed blue line, discs) for a spin-polarized current density of $jP = 2.5 \cdot 10^{10}$ A/m^2 in x direction. The plots are for a vortex with (a) $c = 1$ and $p = 1$, (b) $c = -1$ and $p = 1$, (c) $c = 1$ and $p = -1$, and (d) $c = -1$ and $p = -1$. The insets show the phases between the maximum of the applied current and the core displacement in x-direction (solid red line, squares) and y-direction (dashed blue line, discs). The symbols denote numerical results while the lines are derived from the analytical expression in equation (7.72). (Subfigure (a) is a reprint from reference [178])

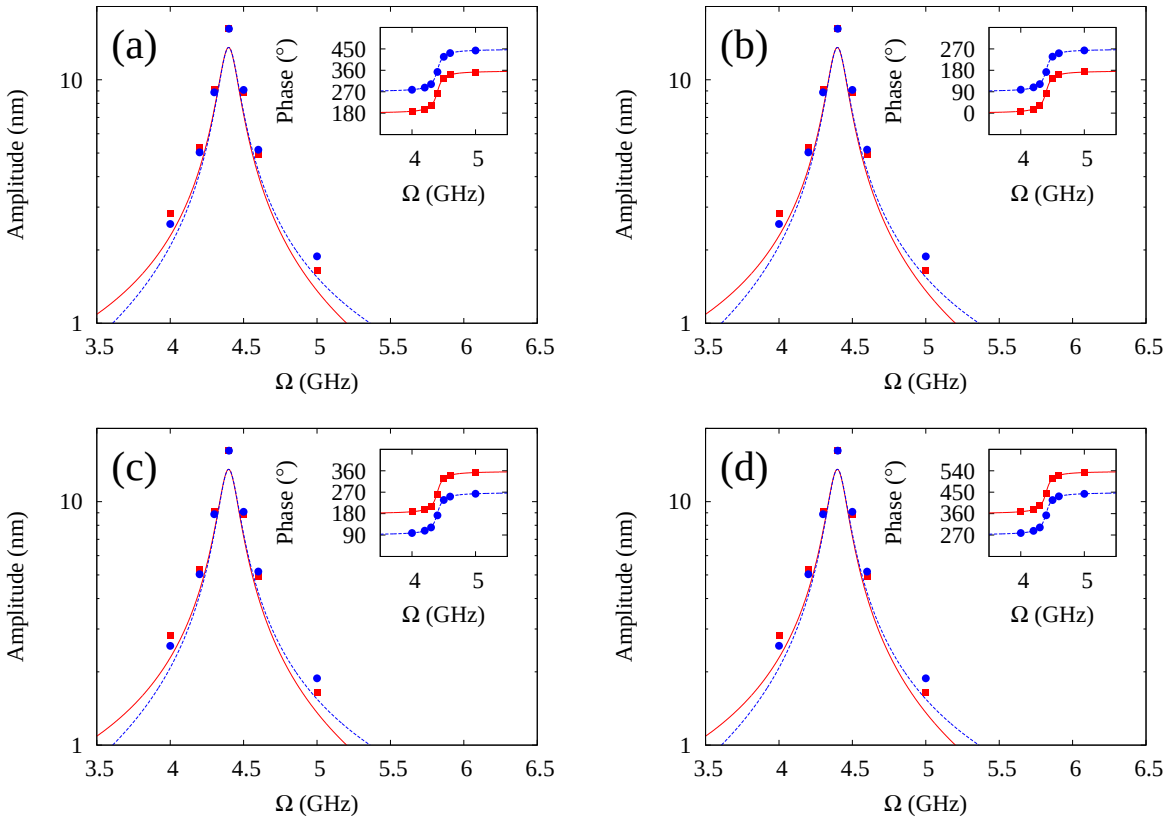

Figure 8.4: Amplitude of the field-driven vortex oscillation in x-direction (solid red line, squares) and y-direction (dashed blue line, discs) for a magnetic field of $H = 250$ A/m in y direction. The plots are for a vortex with (a) $c = 1$ and $p = 1$, (b) $c = -1$ and $p = 1$, (c) $c = 1$ and $p = -1$, and (d) $c = -1$ and $p = -1$. The insets show the phases between the maximum of the applied field and the core displacement in x-direction (solid red line, squares) and y-direction (dashed blue line, discs). The symbols denote numerical results while the lines are derived from the analytical expression in equation (7.72). (Subfigure (a) is a reprint from reference [178])

9.1 Oersted Field of a Homogeneous Current

The Oersted field at the position $\vec{r}$ depends on the current density j at each position $\vec{r}'$ within the sample volume V. It is given by the Biot-Savart law

$$\vec{H}(\vec{r}) = \frac{1}{4\pi} \int dV'\, j(\vec{r}') \times \frac{\vec{r} - \vec{r}'}{|\vec{r} - \vec{r}'|^3} \tag{9.1}$$

which reads explicitly

$$\vec{H}(\vec{r}) = \frac{1}{4\pi} \int dV' \, \frac{(j_z\vec{e}_y - j_y\vec{e}_z)(x - x') + (j_x\vec{e}_z - j_z\vec{e}_x)(y - y') + (j_y\vec{e}_x - j_x\vec{e}_y)(z - z')}{|\vec{r} - \vec{r}'|^3} \tag{9.2}$$

in the case of a homogeneous current density $\vec{j} = j_x\vec{e}_x + j_y\vec{e}_y + j_z\vec{e}_z$. For a cuboid with lateral edge lengths l_x, l_y, and l_z in x, y, and z direction the integral becomes

$$\vec{H}(\vec{r}) = \frac{1}{4\pi} \int\limits_{-\frac{l_x}{2}}^{\frac{l_x}{2}} dx' \int\limits_{-\frac{l_y}{2}}^{\frac{l_y}{2}} dy' \int\limits_{-\frac{l_z}{2}}^{\frac{l_z}{2}} dz' \, \frac{(j_z\vec{e}_y - j_y\vec{e}_z)(x - x') + (j_x\vec{e}_z - j_z\vec{e}_x)(y - y') + (j_y\vec{e}_x - j_x\vec{e}_y)(z - z')}{\sqrt{(x - x')^2 + (y - y')^2 + (z - z')^2}^3} \tag{9.3}$$

where the origin of the coordinate system is the midpoint of the cuboid. The components of the Oersted field

$$H_x(\vec{r}) = \frac{j_z}{4\pi} I(z, x, y, l_z, l_x, l_y) - \frac{j_y}{4\pi} I(y, x, z, l_y, l_x, l_z), \tag{9.4a}$$

$$H_y(\vec{r}) = \frac{j_x}{4\pi} I(x, y, z, l_x, l_y, l_z) - \frac{j_z}{4\pi} I(z, y, x, l_z, l_y, l_x), \text{ and} \tag{9.4b}$$

$$H_z(\vec{r}) = \frac{j_y}{4\pi} I(y, z, x, l_y, l_z, l_x) - \frac{j_x}{4\pi} I(x, z, y, l_x, l_z, l_y). \tag{9.4c}$$

are expressed with the aid of the integral

$$I(x, y, z, l_x, l_y, l_z) = \int\limits_{-\frac{l_x}{2}}^{\frac{l_x}{2}} dx' \int\limits_{-\frac{l_y}{2}}^{\frac{l_y}{2}} dy' \int\limits_{-\frac{l_z}{2}}^{\frac{l_z}{2}} dz' \, \frac{-(z - z')}{\sqrt{(x - x')^2 + (y - y')^2 + (z - z')^2}^3} \tag{9.5}$$

that is derived in equation (D.10) in appendix D.

Writing equations (9.4a), (9.4b), and (9.4c) in vector notation one finds

$$\vec{H}(\vec{r}) = \frac{1}{4\pi} \begin{pmatrix} 0 & I(y, x, -z, l_y, l_x, l_z) & I(z, x, y, l_z, l_x, l_y) \\ I(x, y, z, l_x, l_y, l_z) & 0 & I(z, y, -x, l_z, l_y, l_x) \\ I(x, z, -y, l_x, l_z, l_y) & I(y, z, x, l_y, l_z, l_x) & 0 \end{pmatrix} \vec{j}. \tag{9.6}$$

The tensor connecting the Oersted field and the current density is antisymmetric.

9.2 In-Plane Field

For a homogeneous current in x direction the in-plane field is shown in figure 9.1. Except for small parts at the boundaries of the sample the in-plane Oersted field is homogeneous with respect to the x and y position. The field is antisymmetric with respect to the z coordinate, that is it is positive at the bottom surface, negative at the top surface, and zero in between. Taking the average over the thickness the field vanishes and there will be no contribution of the Oersted field to the core displacement.

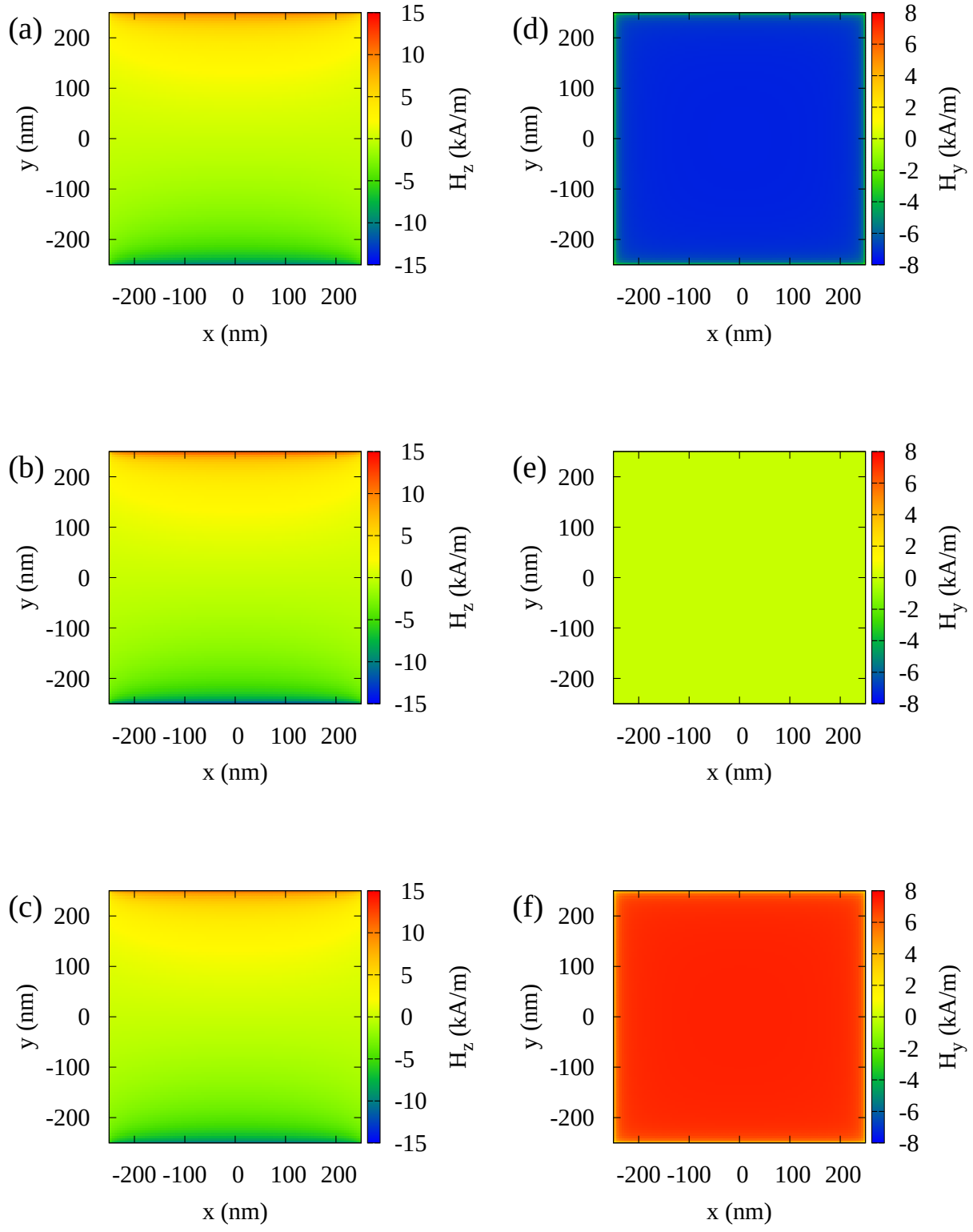

Figure 9.1: Oersted field of a homogeneous current in a sample with $l = 500$ nm and $d = 10$ nm. The current density is $j = 1.5 \cdot 10^{12}$ A/m^2 in x direction. Shown is (a)-(c) the out-of-plane field and (d)-(f) the in-plane field for (a) and (d) the upper boundary, (b) and (e) the center layer, and (c) and (f) the lower boundary of the film. The in-plane field is nearly independent of the x and y position. It has a maximum value of $H_y(x = 0, y = 0, z = \pm 5 \text{ nm}) = \mp 7365$ A/m which is slightly smaller than the value of $jd/2 = 7500$ A/m for an infinitely large film.

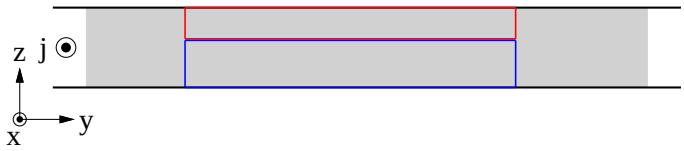

Figure 9.2: Scheme of the calculation of the in-plane Oersted field for an infinitely large film. The integration along the upper (red) contour contributes $(d/2 - z)j/2$ and along the lower (blue) contour contributes $-(d/2 + z)j/2$ to the Oersted field.

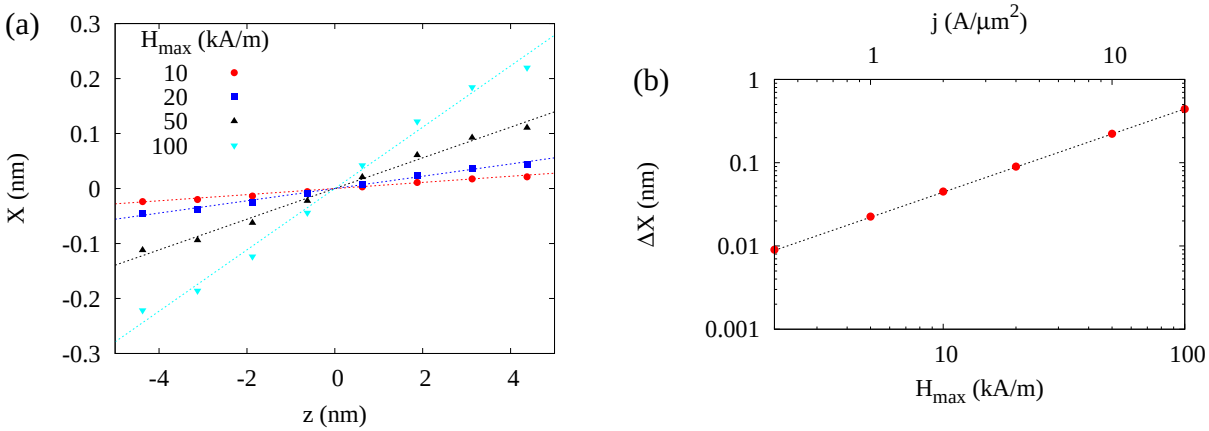

Figure 9.3: Positions of the vortex core in a square with $l = 500$ nm and $d = 10$ nm in the presence of a field of the form $H_y(z) = -zj$ as derived from Ampère's law. We get a maximum field at both surfaces. This field is given by $H_{\max} = dj/2$. (a) Positions of the vortex core in each slice of simulation cells in z direction. The lines are fits with the expression $X = zH_{\max}/(1800\ \text{kA/m})$, that is a linear dependence between X and z as well as between X and $H_{\max}$. (b) Difference ΔX between the core position at the topmost slice and the lowermost slice. The line is a linear fit.

However, it is possible that the Oersted field deforms the vortex core. For the approximation of an infinitely large film we can estimate the in-plane Oersted field inside the sample from Ampère's law $\vec{\nabla} \times \vec{H} = \vec{j}$ which yields $H_y(z) = -zj$ with the aid of Stokes' theorem (see figure 9.2). This is exactly the result that can be found from equation (9.4b) with the aid of the limiting case that is given in equation (D.20). At the surfaces of the film the field assumes its maximum of $H_{\max} = dj/2$

Simulations of a thin-film element with $l = 500$ nm and $d = 10$ nm using 1.25 nm cellsize in z direction including only the above in-plane field with j up to $2 \cdot 10^{13}$ A/m^2 showed that it is a reasonable approximation that the magnetization is independent of the z coordinate. Figure 9.3 shows the positions of the vortex core in each slice of simulation cells and the difference between the core position at the upper surface and the lower surface. Even for extremely large current densities there is only a small tilting of the vortex core.

For a current density that is not constant but z dependent the in-plane field is not exactly antisymmetric with respect to the z coordinate. Thus after averaging over the thickness we are left with an unbalanced in-plane field. As for the homogeneous current this field is not capable to distort the vortex core. Thus this field can be replaced by a homogeneous field in y direction that equals the average of the Oersted field over the thickness. This allows us to include the action of the in-plane Oersted field in the analytical calculations where a homogeneous in-plane field has been taken into account.

As a model system we use a current density that depends linearly on the z position in the sample. We write

$$j_x(z) = j_0 + \Delta j \frac{z}{d} \tag{9.7}$$

where j_0 is the average current density and Δj is the difference between the current densities at the upper and lower surfaces. The strength of the spin torque is calculated by averaging over the thickness. This yields

$$j_{\text{av}} = \frac{1}{d} \int_{-d/2}^{d/2} dz\, j(z) = \frac{1}{d} \int_{-d/2}^{d/2} dz\, \left(j_0 + \Delta j \frac{z}{d} \right) = j_0. \tag{9.8}$$

For the calculation of the unbalanced Oersted field we use the approximation for the infinitely large film. The strength of the unbalanced field is then given by

$$\begin{aligned} H_{\text{ub}} &= \frac{1}{d} \int_{-d/2}^{d/2} dz \left(\frac{1}{2} \int_{z}^{d/2} dz' \left(j_0 + \Delta j \frac{z'}{d} \right) - \frac{1}{2} \int_{-d/2}^{z} dz' \left(j_0 + \Delta j \frac{z'}{d} \right) \right) \\ &= \frac{1}{d} \int_{-d/2}^{d/2} dz\, \frac{1}{2} \left(j_0 \left(\frac{d}{2} - z \right) + \Delta j \frac{d^2 - 4z^2}{8d} - j_0 \left(\frac{d}{2} + z \right) - \Delta j \frac{4z^2 - d^2}{8d} \right) \\ &= \frac{1}{d} \int_{-d/2}^{d/2} dz \left(-j_0 z + \Delta j \frac{d^2 - 4z^2}{8d} \right) = \frac{1}{d} \Delta j \frac{3d^3 - d^3}{24d} = \frac{\Delta j\, d}{12}. \end{aligned} \tag{9.9}$$

The ratio between the unbalanced Oersted field and the current

$$\frac{H_{\text{ub}}}{j_{\text{av}}} = \frac{d}{12} \frac{\Delta j}{j_0} \tag{9.10}$$

depends on the ratio between Δj and j_0.

9.3 Inhomogeneous Current

In real samples we have to consider several mechanisms that lead to an inhomogeneous current flow and concomitantly to an unbalanced Oersted field. Here we will discuss four examples.

Contact Geometry

A first mechanism that leads to an inhomogeneous current flow is that to ensure a sufficient electric contact the sample and the contacts have to overlap each other so that there is an area where the contacts are on top of the sample. If the specific resistivity of the sample is large compared to the specific resistivity of the contacts the current tends to flow into the sample from its top surface.[186,187] Thus the way through the high-ohmic sample is shortest for a current flowing along the top surface. This leads to an inhomogeneous current flow with a higher current density in the upper part of the sample.

Temperature of the Sample

For high current densities Joule heating has to be taken into account. In experiments the magnetic sample has to be placed on a substrate. Theoretical considerations[188] as well as experimental results[114,189] show that a major part of the heat is dissipated through this substrate. Consequently there is a temperature gradient in the sample where the top surface is hotter than the bottom surface. Thus the specific resistivity varies. This results in an inhomogeneous current flow depending on the temperature coefficient of the specific resistivity of the sample material.

Reflection at the Surfaces

In thin films finite-size effects may become important. For thin-film elements with a thickness that is comparable with the mean free path of the conduction electrons, scattering at the surfaces becomes important. In the Fuchs-Sondheimer theory the surfaces of the film are described by a parameter p_s that denotes the probability that an electron is reflected specularly at the surface.[190] This theory was expanded by Mayadas and Shatzkes for polycrystalline films.[191] For a value of $p_s = 1$ the current is the same as for a bulk material. For $p_s < 1$ the current becomes smaller at the surfaces. If the value p_s is the same for both surfaces the suppression is symmetric and thus it does not lead to an unbalanced Oersted field. For experimental samples the bottom surface is a border between two solids, that are the sample and the substrate, while the upper surface is normally a boundary to a gas or vacuum. Thus the probability of specularly reflection is expected to be different for both surfaces leading to an asymmetric current flow and therefore to an unbalanced Oersted field.

Inhomogeneous Growth of the Sample

Finally the current flow can also be influenced by an inhomogeneous growth of the sample material and a concomitant inhomogeneity in the resistance.

9.4 Out-of-Plane Field

In contrast to the in-plane Oersted field that couples to the large domains of the magnetization pattern, the out-of-plane field couples only to the small vortex core where the magnetization points out-of-plane. In this section the interaction between the vortex core and the out-of-plane field will be derived. The energy of the vortex core in the out-of-plane field is given by

$$E_o(\vec{r}) = -\mu_0 M_s p V_c H_z(\vec{r}) \tag{9.11}$$

where

$$V_c = \left| \int dV \frac{M_z(\vec{r})}{M_s} \right| \tag{9.12}$$

is the effective volume of the vortex core and

$$H_z(\vec{r}) = -\frac{j_x}{4\pi} I(x, z, y, l_x, l_z, l_y) \tag{9.13}$$

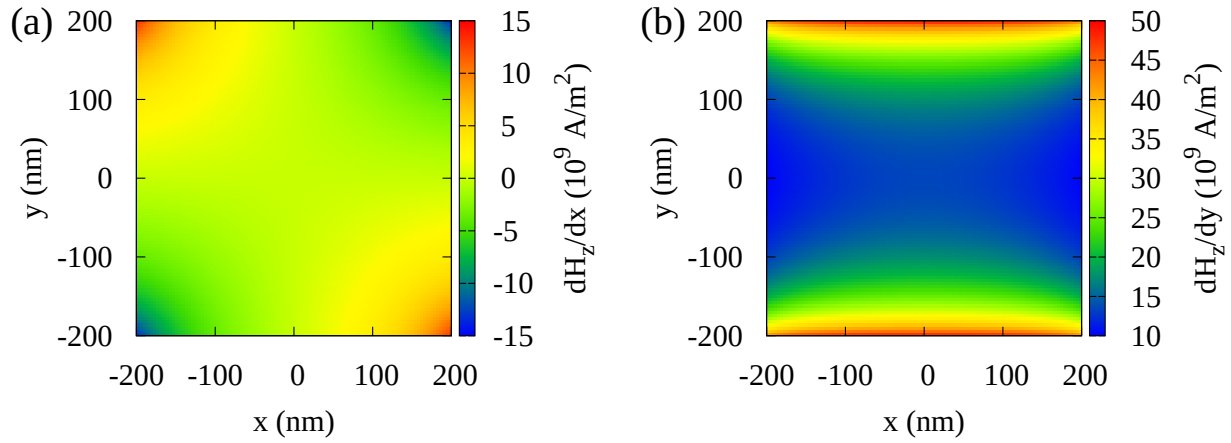

Figure 9.4: Derivative of the out-of-plane Oersted field in a sample with $l = 500$ nm and $d = 10$ nm. The plots show a section of the sample with the derivative in (a) x direction and (b) y direction. The current density is $j = 1.5 \cdot 10^{12}$ A/m^2 in x direction.

is the out-of-plane field. Here we restricted ourselves to a current in x direction. The force is then given by the spatial derivative of the energy

$$\vec{F}_o(\vec{r}) = \mu_0 M_s p V_c \vec{\nabla} H_z(\vec{r}). \tag{9.14}$$

The displacement of the vortex core with a static gradient field can be evaluated by setting the force on the core to zero. This yields

$$\mu_0 M_s p V_c \vec{\nabla} H_z(\vec{r}) - m\omega_r^2 \begin{pmatrix} X \\ Y \end{pmatrix} = 0. \tag{9.15}$$

Here the second term is the confining potential of the vortex. From this one can calculate the displacement as

$$\begin{pmatrix} X \\ Y \end{pmatrix} = \frac{\mu_0 M_s p V_c}{m\omega_r^2} \vec{\nabla} H_z(\vec{r}). \tag{9.16}$$

For the following quantitative considerations we assume that the magnetic field can be expressed by the gradient field $H(\vec{r}) = gy\vec{e}_z$. For the center of a film the gradient

$$g = \frac{\sqrt{2} d j_x}{\pi l} \tag{9.17}$$

of the field has been calculated in equation (D.28). For the center layer of a square with $l = 500$ nm and $d = 10$ nm the derivatives of the field are depicted in figure 9.4. For the center one gets $g = 13.5 \cdot 10^9$ A/m^2 in good agreement with equation (9.17). It becomes clear that the gradient changes only slightly in the vicinity of the center of the sample. Thus the out-of-plane field can be well described by a gradient field.

For our permalloy square with $l = 500$ nm and $d = 10$ nm the numerical simulations yield $V_c = 2600$ nm^3 and $m\omega_r^2 = 2.93 \cdot 10^{-4}$ kg/s^2. Simulations including a magnetic field of the form $H(\vec{r}) = gy\vec{e}_z$ with $g = 4 \cdot 10^{10}$ A/m^2 and $g = 4 \cdot 10^{11}$ A/m^2 yield displacements of the core of $Y = 0.37$ nm and $Y = 3.55$ nm, respectively. This is in perfect agreement with the $Y = 0.36$ nm and $Y = 3.57$ nm that can be calculated from equation (9.16).

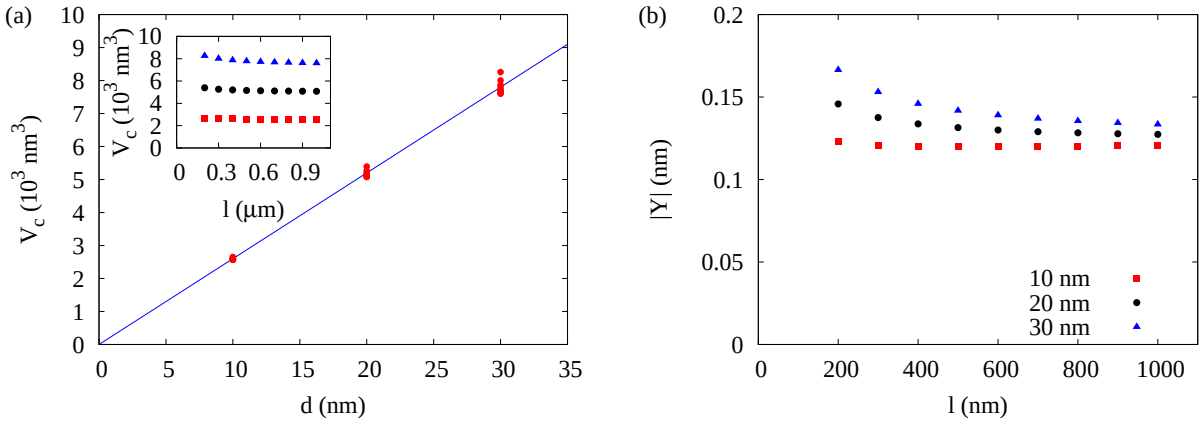

Figure 9.5: (a) Effective volume of the vortex core as defined in equation (9.12) determined from the numerically calculated groundstates in samples of different sizes. The volume is plotted in dependence of the thickness and the lateral extension (inset) of the sample. The different symbols in the inset denote data for different thicknesses and are the same as in (b). The blue line is the linear fit 260 nm^2 d. (b) Displacement of the vortex core due to the out-of-plane Oersted field in the vicinity of the center of the sample, that is $(x, y) = (0, 0)$, calculated from equation (9.18). The displacement is shown for $j_x = 1.5 \cdot 10^{12}$ A/m^2 in dependence of the lateral extension of the square. The symbols denote data for different thicknesses.

In the vicinity of the center of the sample, that is $(x, y) = (0, 0)$, we can calculate the displacement of the core for different sizes of the sample and arbitrary current densities. From equations (7.26), (9.17), and (9.16) one finds

$$|Y| = \frac{\gamma}{\sqrt{2}\pi^2 l} \frac{|G_0|}{m\omega_r^2} V_c |j_x|. \tag{9.18}$$

Values for $|G_0|/(m\omega_r^2)$ and V_c can be found from numerical calculations and are plotted in figure 8.2(a) and figure 9.5(a), respectively. The resultant core displacement for $j_x = 1.5 \cdot 10^{12}$ A/m^2 is shown in figure 9.5(b). This large current density has recently been reached in permalloy on a diamond substrate.[189] Even for this large current density the displacement is negligibly small.

In the region of the sample shown in figure 9.4 the maximum gradient is $5 \cdot 10^{10}$ A/m^2. For this value equation (9.16) yields a displacement of 0.45 nm. This is below available experimental resolutions[40, 74, 162, 164, 192] and can thus be neglected. Outside this section, that is closer to the boundary of the sample, the gradient becomes larger. However, if the vortex core approaches this region there is a strong interaction between the core and the boundary of the sample that revokes the applicability of the model of the rigid vortex core. Thus, the out-of-plane field can be neglected because there is only a small interaction with the vortex core. Only the displacement of the vortex core due to the in-plane component of the Oersted field has to be taken into account.

10 Distinction between Spin Torque and Oersted Field

There are several mechanisms that lead to an inhomogeneous current flow and concomitantly to an unbalanced in-plane Oersted field, as discussed in section 9.3. Equation (7.72) shows that the current and field induced forces on the vortex are of the same form. For experiments it is important to separate the Oersted-field and the spin-torque driven case. The results of this section have been published in references [178, 186].

There are two possibilities to determine the ratio of the Oersted field and the spin torque. On the one hand for non-resonant excitations the trajectory of the vortex core is elliptical as

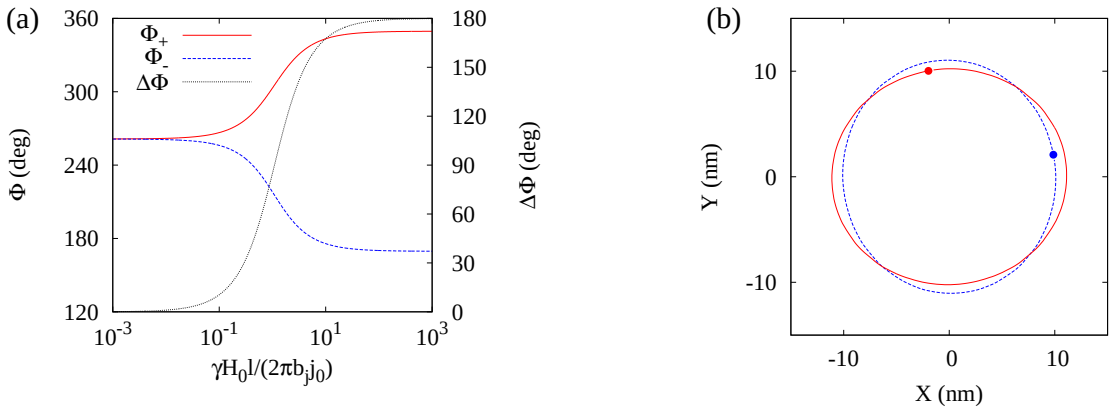

Figure 10.1: (a) Analytically calculated phase Φ between the maximum current or magnetic field and the x-deflection of the vortex core with $p = +1$ in a 200 nm $\times$ 200 nm $\times$ 20 nm permalloy square. The phases Φ_+ and Φ_- are the phases of vortices with chiralities $c = +1$ and $c = -1$, respectively. The dotted line denotes the phase difference $\Delta\Phi = \Phi_+ - \Phi_-$. The excitation frequency of $\Omega = 4.8$ GHz is above the resonance frequency of $\omega = 4.4$ GHz. (b) Section of the sample, with a vortex with $c = +1$, showing the simulated trajectories of the vortex core excited with i) (solid red line) a spin-polarized current density with an amplitude of $jP = 1.2 \cdot 10^{11}$ A/m^2 and ii) (dashed blue line) a magnetic field with an amplitude of $H = 1000$ A/m. Points denote the position of the vortex at maximum current (i) and magnetic field (ii), respectively. (Subfigure (b) is a reprint from reference [178].)

illustrated in figure 10.1(b). According to equation (7.72) the direction of the major axis of the ellipse is determined by the ratio of the Oersted field and the spin torque. The amplitude of the vortex motion decreases very fast when the excitation frequency deviates from resonance, that is for experimental observation very high current densities with frequencies close to resonance are needed for a reliable determination of the ratio. On the other hand the excitation mechanisms can be distinguished using the phase of the vortex deflection. As indicated by the dots in figure 10.1(b) the position of the vortex at maximum current depends on the ratio of the Oersted field and the spin torque, which can be determined from equation (7.72). The latter method is also applicable with excitations at resonance frequency.

In most experiments the measurement of the absolute phase is a challenging task. This problem can be overcome by a measurement of the phase difference between two vortices with different chiralities. As shown in figure 10.1(a) this phase difference vanishes for the fully spin-torque driven case. If the vortex is exclusively driven by the Oersted field the phase difference is 180°. In between we get a bijective function that allows for an unambiguous calculation of the ratio of the Oersted field and the spin torque from the phase difference.

Possible experimental realizations for the spin-torque driven and Oersted-field driven vortex dynamics are shown in figure 10.2. The vortex can either be placed between two contacts so that the current flows directly through the sample or the vortex can be placed on a strip line. In the former case the vortex is excited by spin torque and possibly by an Oersted field that is due to an inhomogeneous current flow. In the latter case the vortex is driven by an Oersted field only as long as the specific resistance of the strip line is small compared to the specific resistance of the sample. In this case only a very small percentage of the current flows through the sample.

Experimental results for both cases have been published in reference [186] and are shown in figure 10.3. In these experiments the position of the vortex core has been measured for different times by X-ray microscopy. From these positions it is possible to extract the phase and the amplitude of the gyration of the core. For the field-driven vortices the phases have an unknown offset. Thus the phases have been shifted by a constant value. This value is a fit parameter that is the same for both

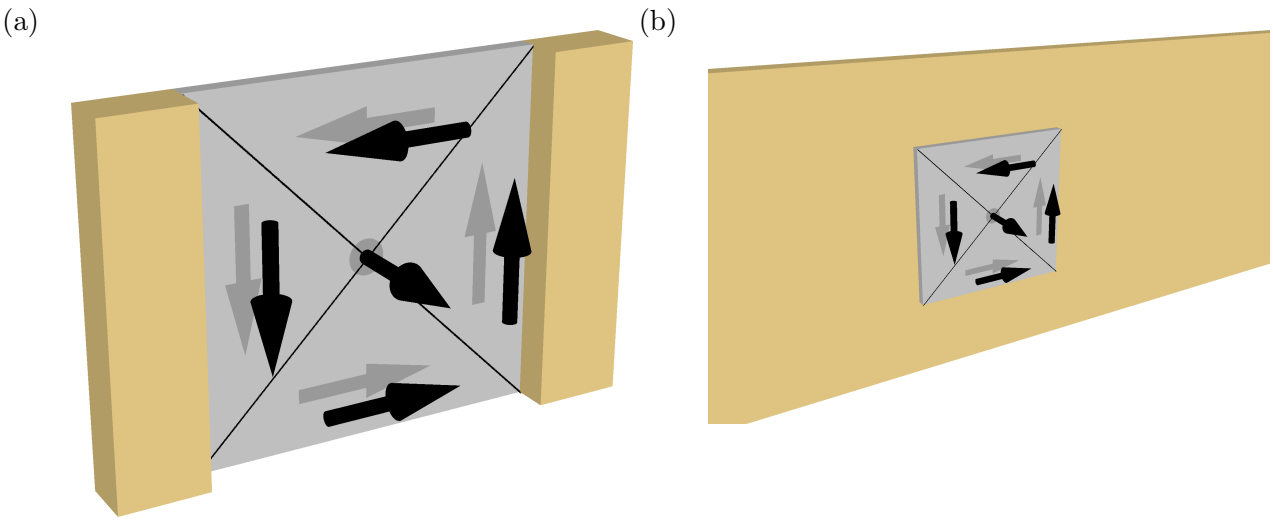

Figure 10.2: Two possible experimental realizations for the spin-torque driven and Oersted-field driven vortex dynamics. The vortex can be placed (a) between two contacts so that the current flows directly through the sample or (b) on a strip line so that the major part of the current flows through the strip line.

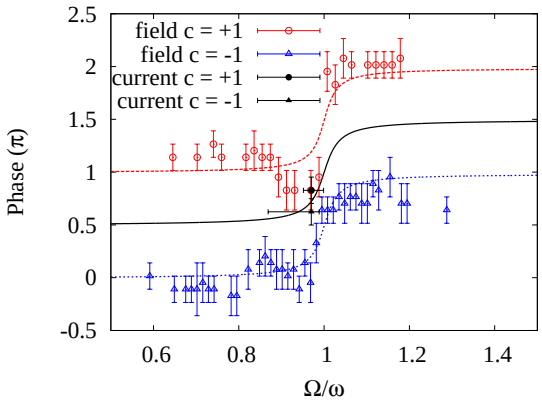

Figure 10.3: Experimentally obtained phases (points) of vortices with different chiralities that are excited by current or field. The lines are the analytical results. For the field-driven case a phase difference of 180 degrees between vortices of different chiralities can be seen. Between the two spin-torque driven vortices with different chiralities there is only a small phase splitting. The asymmetric error bars for the frequencies of the current-driven vortices include the case that both vortices have different free frequencies. (This figure is a reprint from reference [186].)

chiralities. Additional fit parameters are the free frequencies of the two vortices. For all vortices, that are the current and field driven, the value of $|D_\Gamma/G_0|$ is determined by extrapolation of the logarithmic curve in figure 8.2. α is assumed to be 0.01. As theoretically predicted the phases of the two field-driven vortices differ by 180 degrees.

The free frequency of the current-driven vortices can be derived from the phase of the gyration. The points are obtained by the assumption that the free frequency of both vortices is the same. The error bars for the frequency include an error of 30 % for $\Gamma/\omega = \alpha|D_\Gamma/G_0|$, the uncertainty of the phase, and the case that the free frequencies of both vortices are different. We find a phase difference of about 45 degrees. This difference can be due to an unbalanced Oersted field. For the experimental sample with $l = 2$ μm and $d = 20$ nm one finds that the force due to this field has to be about 40 % of the force due to the spin torque. This means that the Oersted field constitutes about 30 % of the total force. From equation (7.72) one finds that the unbalanced Oersted field is about $H_{\mathrm{ub}} \approx 30$ A/m for a current density of $j_{\mathrm{av}} = 1.2 \cdot 10^{11}$ A/m^2 with a spin polarization $P = 0.7$. With the model system that is used in equation (9.9) the difference between the current density at the upper and lower surface of the sample is approximated to be in the order of magnitude of $\Delta j \approx 10^{10}$ A/m^2.

11 Determination of the Non-Adiabatic Spin-Torque Parameter

Theoretically, several mechanisms have been proposed as the origin of the non-adiabatic spin torque, leading to different orders of magnitude for ξ.[24,149–152] Thus a precise measurement of the non-adiabatic spin torque is necessary to give insight into its microscopic origin. The determination of ξ is further important for a reliable prediction of the current-driven domain-wall velocity[24] which is important for applications as discussed in section 5. Currently measured values of ξ for permalloy differ by one order of magnitude,[105,121,170,172] thus the value of ξ is under strong debate. In these experiments the observed motion of a domain wall was compared with micromagnetic simulations to determine ξ. However, this analysis is highly susceptible to experimental uncertainties such as surface roughness and Oersted fields.

Due to its high symmetry and spatial confinement a vortex in a micro- or nanostructured magnetic thin-film element is a promising system for the investigation of the spin-torque effect. We have seen that vortices are displaced from their equilibrium position when excited by spin-polarized electric currents. From the last section we know that the spatial confinement of the vortex core within the film element yields an especially accessible system for measurements with scanning probe techniques. The experimental data that is shown in the last section was obtained using x-ray microscopy but it is also possible to use other techniques like x-ray photo emission electron microscopy or scanning electron microscopy with polarization analysis.

Here we will discuss a scheme which allows us to measure the contributions due to the adiabatic spin torque, the non-adiabatic spin torque, and the Oersted field separately. It bases upon the analytical calculations in section 7 and overcomes the two main difficulties that occur in an experiment. The first problem arises from an additional vortex displacement due to the Oersted field accompanying the current flow (see section 9).[186] This displacement is comparable in size to the displacement due to the non-adiabatic spin torque and both displacements point in the same direction.[178] Thus, the unknown contribution of the Oersted field has to be separated from the measured signal. The second problem is the exact determination of the displacement angle. Since the displacement due to the adiabatic spin torque is about one order of magnitude larger than the displacement due to the non-adiabatic spin torque, a small uncertainty in the direction of the current through the sample would cause large errors in the determination of ξ as shown in figure 11.1. To test the applicability of our analytical findings they are applied to vortex displacements obtained from three-dimensional micromagnetic simulations. The results that are shown in this section have been published in reference [179].

For the analytical calculations we start from the modified Thiele equation (7.46). We will investigate a square thin-film element with a current flowing in x direction as shown in figure 11.2(a). This current is laterally homogeneous. The Oersted field accompanying the current consists of an in-plane component and an out-of-plane component. In section 9.4 we have discussed that the out-of-plane component can be neglected as it causes a displacement of the vortex core that is below the experimental resolution. The in-plane field is negative at the top surface and positive at the bottom surface. As shown in section 9.2, for a realistic strength this field is not capable of significantly distorting the vortex. For a homogeneous current the average Oersted field vanishes and there will be no contribution of the Oersted field to the core displacement. However, such a contribution has been identified in experiment (see section 10) and it is attributed to vertical inhomogeneities of the current density leading to an unbalanced in-plane Oersted field after taking the average over the thickness (see equation (9.9)). We will approximate this unbalanced Oersted field by a homogeneous field H in y direction while its precise shape and strength turned out to be of minor importance for the vortex dynamics. However, the force due to the Oersted field depends on the vortex chirality.

A measurement of the nonadiabatic spin torque with a resonant excitation using an alternating current is not suitable, as small deviations of the exciting frequency from the resonance frequency cause strong deviations in the trajectory of the vortex. An excitation with a direct current causes

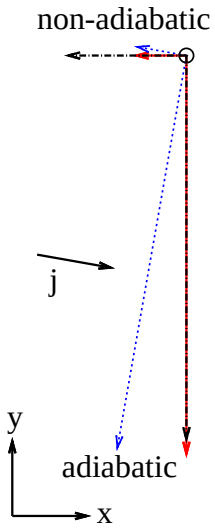

Figure 11.1: Scheme of the displacement of the vortex core from its equilibrium position (circle) due to the adiabatic and the smaller non-adiabatic spin torque for a polarization of $p = +1$. The solid red arrows denote the displacements for a homogeneous current that flows in exact x direction. In experiments the real direction of the current may be different. This can for example be due to rotations of the sample or imperfections in the alignment of the contacts. The dashed blue arrows denote the displacements due to a current that flows in the direction of the solid black arrow, that is rotated by 10 degrees. The black dashed-dotted arrows represents a projection of the displacements due to the rotated current on the coordinate axes as measured in experiments. By comparing the black arrows to the red arrows it becomes obvious that a small deviation in the direction of the current flow may cause a large error in the measurement of the non-adiabatic spin torque.

a displacement of the vortex core to a new steady-state position. An additional benefit is that a direct current allows for a measurement with a non-time-resolving technique. From equation (7.72) we get the new equilibrium position

$$\vec{R}_c^p(j) = -\frac{\omega}{\omega^2+\Gamma^2}\begin{pmatrix}\left|\frac{D_0}{G_0}\right|\xi\tilde{j}_x + \tilde{H}_y c\\ \tilde{j}_x p\end{pmatrix} = -\frac{|G_0|}{m\omega_r^2}\begin{pmatrix}\left|\frac{D_0}{G_0}\right|\xi\tilde{j}_x + \tilde{H}_y c\\ \tilde{j}_x p\end{pmatrix} \tag{11.1}$$

by setting $\Omega = 0$ and restricting ourselves to chiralities of $c = \pm 1$. For simplicity we neglect any dependence of b_j on ξ, that is $b_j = \mu_B P/(eM_s)$, in the remaining part of this section. This will not affect the final result that is independent of b_j.

From equation (11.1) it is obvious that an Oersted field has the same influence on the vortex as the non-adiabatic spin torque. Thus the presence of an Oersted field can disturb the measurement of ξ. In experiments we are faced with a small uncertainty of the direction of the current flow, for example due to a rotation or imperfections of the sample. As shown in figure 11.1 this yields a mixing of the displacement components, resulting from the adiabatic spin torque and the smaller non-adiabatic spin torque. This mixing causes a large error in the measurement of the displacement originating from the non-adiabatic spin torque.

From equation (11.1) we find that the sign of the displacement induced by the Oersted field depends on the chirality of the vortex, while the displacement due to the adiabatic spin torque is determined by the polarization.[50] The non-adiabatic spin torque causes a displacement that is independent of the vortex properties p and c. Vortices with different p and c values can be achieved by remagnetizing the sample. Comparing the displacement of three vortices with different polarizations and chiralities it is therefore possible to separate the contributions of all three forces to the displacement of the vortex. From equation (11.1) we find

$$2R_{\text{non-ad}} = 2\left|\frac{G_0\xi\tilde{j}}{m\omega_r^2}\frac{D_0}{G_0}\right| = \left|\vec{R}_c^p(j) - \vec{R}_{-c}^{-p}(-j)\right| \tag{11.2a}$$

$$2R_{\text{ad}} = 2\left|\frac{G_0\tilde{j}}{m\omega_r^2}\right| = \left|\vec{R}_c^p(j) - \vec{R}_c^{-p}(j)\right| \tag{11.2b}$$

$$2R_{\text{Oe}} = 2\left|\frac{G_0\tilde{H}}{m\omega_r^2}\right| = \left|\vec{R}_c^{-p}(j) - \vec{R}_{-c}^{-p}(j)\right|. \tag{11.2c}$$

These equations are schematically illustrated in figure 11.2. From equations (11.2a) and (11.2b)

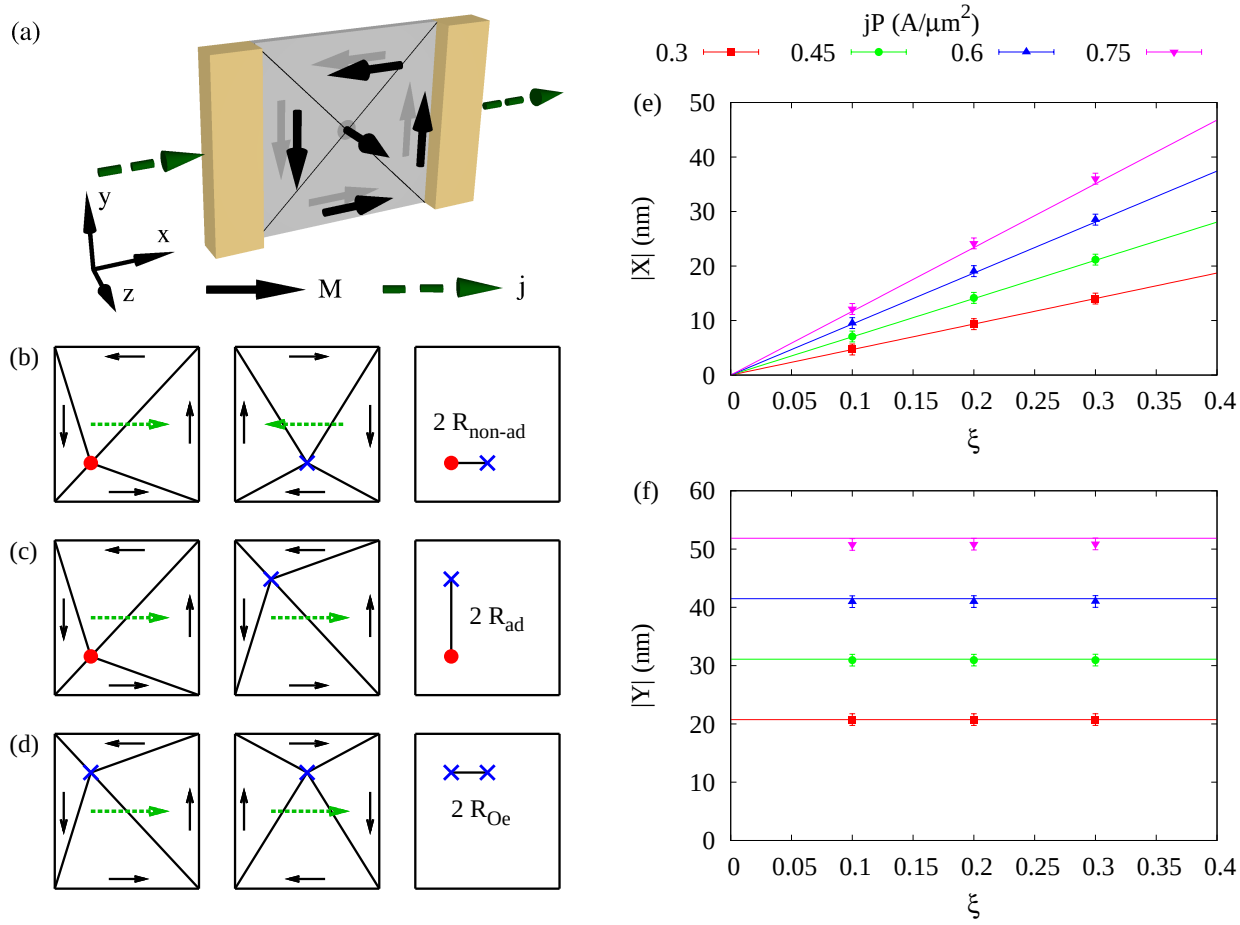

Figure 11.2: (a) Sketch of the sample, including current contacts, for the proposed experiment for the determination of ξ. (b)-(d) Scheme for the determination of the three different contributions to the vortex displacement according to equation (11.2). By measuring the distance between the positions of two different vortices it is possible to separate the displacements (b) due to the non-adiabatic spin torque, (c) the adiabatic spin torque, and (d) the Oersted field. Points and crosses denote cores with positive and negative polarization, respectively. The in-plane magnetization is denoted by the solid arrows. The dashed arrows denote the current direction. For the sake of illustration the displacements are exaggerated. (e) and (f) Numerically calculated displacement of the vortex core due to a direct spin-polarized current of density jP in the absence of an Oersted field. (e) The displacement parallel to the current is proportional to ξ. (f) The displacement perpendicular to the current is independent of ξ. The lines are fits with the linear model in equation (11.1). For large current densities small non-linear effects can be seen. (This figure is a reprint from reference [179].)

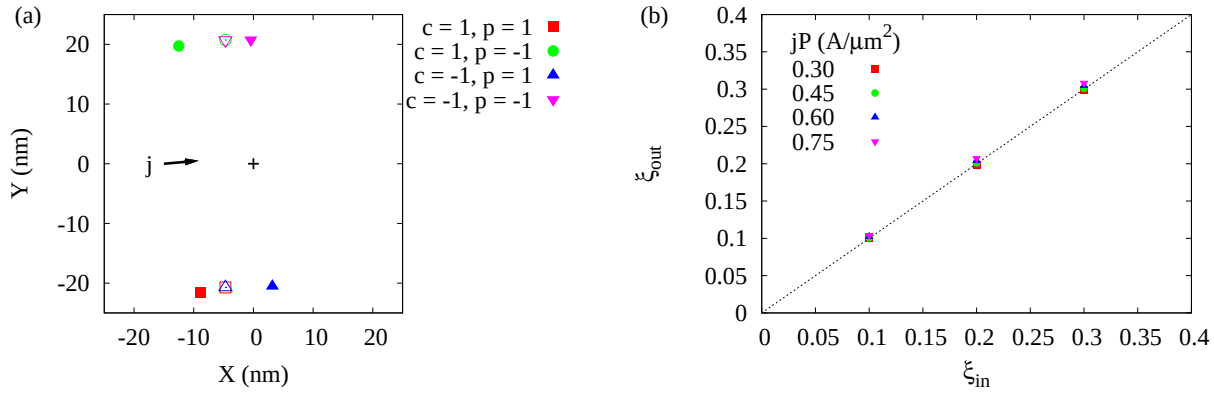

Figure 11.3: (a) Position of the vortex core displaced by a spin-polarized direct current of density $jP = 3 \cdot 10^{11}$ A/m with $\xi = 0.1$. The overlapping open symbols denote the positions for a current in exact x direction without Oersted field. The closed symbols denote the positions with an applied Oersted field and a rotation of the sample by 5 degrees around its midpoint (plus). For the latter case the direction of the current is denoted by the arrow. (b) Results for ξ_{out} derived from the positions of the vortex with applied Oersted field, exemplarily shown in (a), using equation (11.3) for different current densities. ξ_{in} is the value of the non-adiabaticity parameter that was used for the simulations. (This figure is a reprint from reference [179].)

it is possible to determine ξ as

$$\xi = \frac{2R_{\text{non-ad}}}{2R_{\text{ad}}} \left|\frac{G_0}{D_0}\right| = \frac{\left|\vec{R}_c^{\,p}(j) - \vec{R}_{-c}^{\,-p}(-j)\right|}{\left|\vec{R}_c^{\,p}(j) - \vec{R}_c^{\,-p}(j)\right|} \left|\frac{G_0}{D_0}\right|. \tag{11.3}$$

Since this equation is independent of the strength of the Oersted field, the angle of the sample, and the parameter D_Γ, it yields the sought measurement scheme. With this scheme a direct determination of ξ is accessible. Only one micromagnetic simulation for the determination of $|D_0/G_0|$ is necessary since $|D_0/G_0|$ is independent of ξ and j.

Micromagnetic simulations of the experimental setup allow us to determine the positions of the vortex core with a precise knowledge of the micromagnetic parameters of the system. The simulations therefore allow us to test the analytical results in equations (11.1) and (11.3). For the simulations the material parameters of permalloy, that are a saturation magnetization of $M_{\text{s}} = 8 \cdot 10^5$ A/m and an exchange constant of $A = 1.3 \cdot 10^{-11}$ J/m, are used. Since we are interested only in the steady final position of the vortex we used a Gilbert damping of $\alpha = 0.5$ to ensure a fast damping of the transient states to reduce computation time. As a sample system we considered a square thin-film element of length $l = 500$ nm and thickness $d = 10$ nm with a cell size of 2 nm in the lateral directions and 10 nm perpendicular to the film.

Figures 11.2 (e) and (f) show the displacement of the vortex core in simulations without Oersted field. As predicted by equation (11.1) the displacement in the direction of the current flow is proportional to ξ and the displacement perpendicular to the current flow is independent of ξ. From these simulations the value $|D_0/G_0| = 2.26$ is determined.

In experimental samples we are faced with an unbalanced Oersted field and possibly some uncertainty of the direction of the current flow. To mimic the unbalanced Oersted field in the simulations we applied an in-plane field perpendicular to the current. The strength of the field is proportional to the current density. We assume that a spin-polarized current density of $1 \cdot 10^9$ A/m^2 generates an unbalanced in-plane field of 1 A/m. For this field the ratio between the deflections due to the field and due to the current are in the regime found by experiments (see section 10). The uncertainty of the direction of the current flow was taken into account by rotating the sample by

5 degrees. Figure 11.3(a) shows the positions of the vortex core for both simulations. It becomes visible that the unbalanced Oersted field and the rotation of the sample strongly shift the core positions, complicating the determination of ξ.

To test the analytical model we compared the non-adiabatic spin-torque parameter ξ_{in} that was inserted into the simulations with the value ξ_{out} that was calculated from equation (11.3) using the core positions. Here it is worth noting that the value of the Oersted field and the angle of the sample are not needed for the calculation of ξ_{out}. The results are shown in figure 11.3(b). It can be seen that all the perturbations that are inserted in the simulations can be effectively excluded by the analytical calculations.

In experimental samples we are also faced with the anisotropic magneto resistance (AMR) effect that leads to inhomogeneous current paths, that is a higher current density in the vortex core. Simulations including these inhomogeneous current paths yield a small shift to lower values of ξ_{out}. This shift is up to 2 % for an AMR ratio of 10 %.[179]

Now we will discuss the experimental accuracy in the determination of ξ that can be achieved with the presented scheme. In experiments direct currents of densities up to $1.5 \cdot 10^{12}$ A/m^2 have been realized in permalloy on a diamond substrate.[189] Assuming a spin polarization of 0.5 we get a spin-polarized current density of $0.75 \cdot 10^{12}$ A/m^2, that is the maximum shown in figure 11.2. This yields values of up to $\tilde{j} = 55$ m/s.

The displacements of the vortex in the numerically investigated samples are small compared to the experimental resolutions available. A larger displacement of the vortex can be achieved by increasing the lateral size of the structure. For example simulations of a square thin-film element of length $l = 5000$ nm and thickness $d = 10$ nm yielded values of $|D_0/G_0| = 3.82$ and $|G_0|/(m\omega_r^2) = 1 \cdot 10^{-8}$ s. With these values equation (11.2b) yields $2R_{\text{ad}}$ =1100 nm. We assume that the core position can be measured with a resolution of $\delta(2R_{\text{non-ad}}) = 20$ nm. Equation (11.3) then yields that $\delta\xi = 0.005$ can be realized. This resolution ranges from 5 % to 50 % depending on the value of ξ.[105,121,170,172,185] The resolution can be further increased by using thin-film elements with still larger lateral sizes.

In conclusion this is a robust and direct measurement scheme for the non-adiabatic spin torque using the displacement of magnetic vortices. This scheme allows us to distinguish between the displacements of the vortex core due to the non-adiabatic spin torque, the adiabatic spin torque, and the Oersted field, independently of the exact direction of the current flow. We also found that an inhomogeneous current due to the AMR effect can be neglected. The scheme thus allows a precise measurement of the non-adiabatic spin-torque parameter ξ.

12 Application in Memory Devices

The high degeneracy of the groundstates of a vortex or an antivortex opens the possibility to use these magnetic structures as memory devices. Both vortex and antivortex have two possible out-of-plane orientations of their cores. These orientations, that are up or down, can be used to store a single bit.[193] Both states are separated by an energy barrier that is of the order of ten electron volt.[159] Thus the core orientation is stable against thermal fluctuations and can serve as a non-volatile memory device.

The polarization can be switched by a current or field that is applied in the film plane. This switching takes place independently of the initial state of the vortex core. Thus before a writing process a reading operation is needed to determine whether the core has to be switched or not.

It has been proposed to switch the core by a rotating current or field.[193,194] This kind of excitation excites only vortices or antivortices with one distinct polarization[62,64,65] and a preceding reading operation is not necessary. For a rotating current or field one needs two currents that are flowing directly through the sample or through a strip line. These currents need a phase difference of $\pi/2$ which is technically demanding for alternating currents with the high resonance frequencies of the vortex or the antivortex.

In this section it will be discussed how information can be stored using a magnetic vortex or antivortex. In this discussion we will put special attention on how the information can be stored and read out using one current only. As we will see the main advantage of these memory cells is that no reading operation is needed before the writing. The results that are presented here have been published slightly modified in references [77] and [78].

12.1 Vortex Random Access Memory

Here, a possible realization of a Vortex Random Access Memory (VRAM) is presented that stores the information in the handedness cp of the vortex. Since the chirality c is not affected by a switching of the polarization p of the vortex core, a switching of the core's orientation always changes the handedness. The values of $cp = +1$ and $cp = -1$ can be interpreted as the "zero" and the "one", respectively. One cell of the VRAM is depicted in figure 12.1(a). The injected current splits up in two parts. One part flows in x direction directly through the vortex. The other part flows through the strip line that is situated under the vortex. This allows for a collinear alignment of a current and a magnetic field that can be used for a handedness selective switching of the vortex core.

In the following analytical calculations we restrict ourselves to a vortex ($n = 1$) with chirality $c = \pm 1$. From equations (7.72) and (7.74) one can determine that the position of a harmonically excited core is given by

$$\begin{pmatrix} X \\ Y \end{pmatrix} = -\frac{e^{i\Omega t}}{\omega^2 + (i\Omega + \Gamma)^2} \begin{pmatrix} \tilde{j}_x - \tilde{H}_x cp & \left|\frac{D_0}{G_0}\right| \xi \tilde{j}_x p \\ -\left|\frac{D_0}{G_0}\right| \xi \tilde{j}_x p & \tilde{j}_x - \tilde{H}_x cp \end{pmatrix} \begin{pmatrix} \frac{\omega^2 i\Omega}{\omega^2+\Gamma^2} \\ \omega p + \frac{p\Gamma\omega i\Omega}{\omega^2+\Gamma^2} \end{pmatrix}. \tag{12.1}$$

For a weakly damped system ($\Gamma \ll \omega$) that is excited at resonance ($\Omega = \omega$) the radius

$$R(\tilde{j}_x, \tilde{H}_x, \Gamma, cp) = \sqrt{(\Re X)^2 + (\Re Y)^2} = \frac{1}{2\Gamma} \sqrt{\left(\tilde{j}_x - \tilde{H}_x cp\right)^2 + \frac{D_0^2}{G_0^2} \xi^2 \tilde{j}_x^2} \tag{12.2}$$

of the trajectory of the vortex core becomes time independent. Obviously the radius depends on the handedness cp of the vortex but not on the chirality c or the polarization p alone. For the case that the absolute values $|\tilde{H}_x|$ and $|\tilde{j}_x|$ are equal the difference between the radii for $cp = +1$ and $cp = -1$ has a maximum. The velocity of the vortex core is then given by

$$v_\pm(cp) = \frac{\omega|\tilde{j}|}{2\Gamma} \sqrt{(1 \mp cp)^2 + \frac{D_0^2}{G_0^2}\xi^2} = \left|\frac{G_0 \tilde{j}}{2\alpha D_\Gamma}\right| \sqrt{(1 \mp cp)^2 + \frac{D_0^2}{G_0^2}\xi^2} \tag{12.3}$$

where $v_+(cp)$ is the velocity for a parallel alignment of current and field and $v_-(cp)$ is the velocity for an antiparallel alignment. It depends on the handedness of the vortex and on the relative alignment of current and field whether the exciting forces amplify or attenuate each other. In the VRAM cell that is depicted in figure 12.1(a) a parallel alignment is achieved when both currents flow in the directions that are denoted by the dashed arrows. For an antiparallel alignment only one current direction has to be reversed.

Recent investigations found that the question whether the vortex core switches or not depends only on the velocity of the vortex core but does not depend on the source of the driving force, that is adiabatic spin torque, non-adiabatic spin torque, or magnetic field. There exist theories about the value of the critical velocities. For permalloy Guslienko et *al.*[63] found $v_{\text{crit}} = 320$ m/s while Yamada et *al.*[54] found $v_{\text{crit}} = 250$ m/s. For permalloy equation (12.3) yields that a spin-polarized current density in the order of $jP = 10^{11}$ A/m^2 is needed to reach this velocity when both forces amplify each other. For this approximation we used $\alpha = 0.01$ and $|D_\Gamma/G_0| \approx 2$ (see figure 8.2).

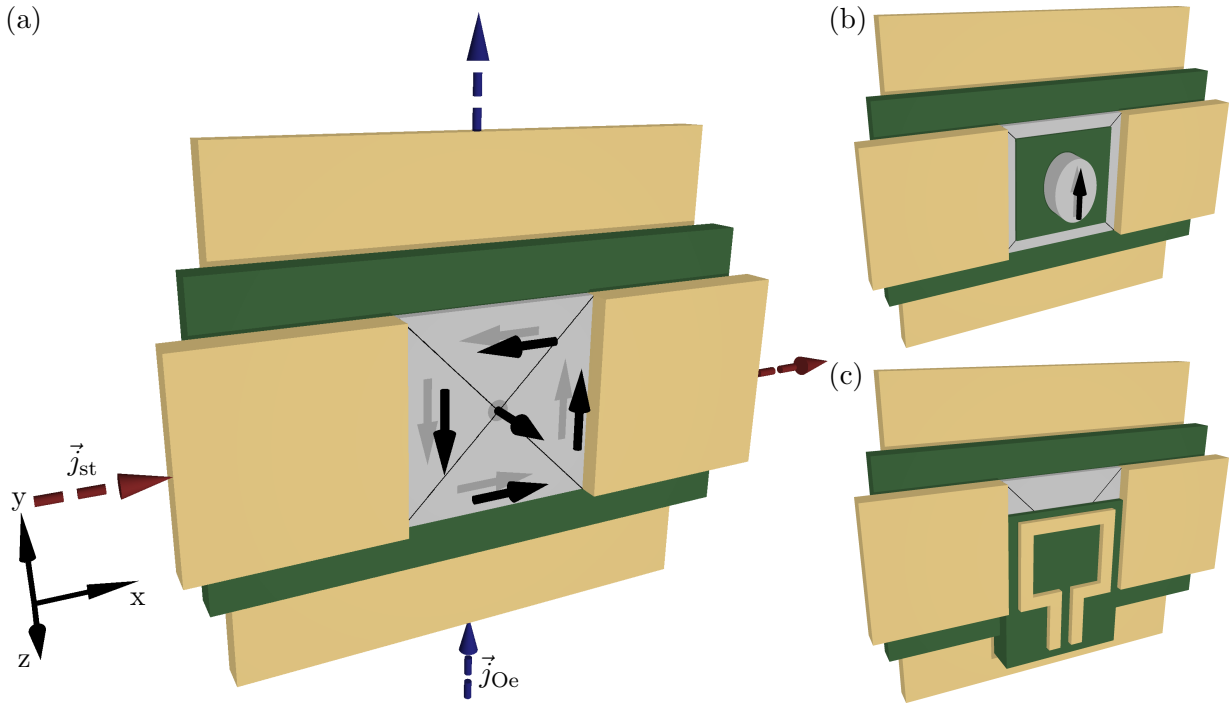

Figure 12.1: Scheme of a Vortex Random Access Memory. The ferromagnetic material is shown in grey. The strip line and the contacts (gold) are separated by an electrical insulator (green). (a) The vortex in the center can be excited via spin torque or Oersted field. A current that is injected along the red arrows flows directly through the vortex and excites it via spin torque. A current that is injected along the blue arrows generates an Oersted field that also excites the vortex. The current and the Oersted field are aligned parallel. They point in x direction. An antiparallel alignment can be achieved by reversing one current. (b) With an insulating and a magnetic layer placed on top of the magnetic film a spin valve is created. The resistivity of the spin valve depends on the magnetization in the part of the magnetic film that is below the second magnetic layer. This allows for a detection of the vortex dynamics. (c) An additional possibility to detect the vortex dynamics is an induction loop on the magnetic film. The voltage between both ends of the loop depends on the temporal variation of the magnetic flux through the loop, that is, on the magnetization dynamics in the film.

It is possible to choose the current density in such a way that

$$\frac{\omega|\tilde{j}|}{2\Gamma}\sqrt{4+\frac{D_0^2}{G_0^2}\xi^2} > v_{\mathrm{crit}} \quad \text{and} \quad \frac{\omega|\tilde{j}|}{2\Gamma}\left|\frac{D_0\xi}{G_0}\right| < v_{\mathrm{crit}}. \tag{12.4}$$

Then the critical velocity for switching can be reached only if the forces due to the current and due to the field amplify each other. This is the case if the current and field are aligned parallel and the initial handedness is $cp = -1$ or if the current and field are aligned antiparallel and the initial handedness is $cp = +1$. After the vortex core is switched we get an attenuation of the driving forces and the core cannot switch again because the critical velocity is not reached. Thus, for a parallel alignment the vortex always ends up in the $cp = +1$ state independently of the starting configuration. To get $cp = -1$ as the final state the current and field have to be aligned antiparallel. From these observations we get our sought writing procedure that allows us to write binary data to the vortex without the knowledge of its initial state.

For the read out of the stored information the currents generating the spin torque and the magnetic field have to be chosen so that the critical velocity cannot be reached regardless of the vortex state, that is the relation

$$\frac{\omega|\tilde{j}|}{2\Gamma}\sqrt{4+\frac{D_0^2}{G_0^2}\xi^2} < v_{\mathrm{crit}} \tag{12.5}$$

has to be fulfilled. Then the currents have no influence on the polarization nor on the chirality. For a current and field that are aligned parallel to each other the binary values "zero" and "one" correspond to a weak or strong gyration, respectively. There are several mechanisms to detect this gyration. Here we will discuss a spin valve or a coil on top of the sample.

The VRAM cell in figure 12.1 is a two dimensional system. Thus it is possible to place two additional layers on top of the system to get a spin valve as depicted in figure 12.1(b). A spin valve consists of two magnetic layers with one non-magnetic spacer in between. Here, the lowest layer is the film that contains the vortex. The resistance of a spin valve depends on the angle between the magnetization in both magnetic layers. It is lowest for a parallel alignment and highest for an antiparallel alignment. If the vortex core is displaced from its equilibrium position the resistance of the spin valve changes.[66,73] This allows for a detection of the vortex dynamics.

A second possibility is to detect the time dependent magnetic flux that is created by the vortex. The flux can be detected by placing an induction loop on top of the sample as depicted in figure 12.1(c). The voltage between both ends of the loop are proportional to the temporal derivative of the flux through the loop. Simulations show that the voltage lies in the range of some μV.[78]

Recent numerical investigations showed that switching with short current and field pulse may be faster than switching with alternating currents and fields.[58,59] The VRAM can be also operated with current and field pulses $\tilde{j}_x^p$ and $\tilde{H}_x^p$. As for the harmonic excitation we choose a collinear alignment of current and field. With a small damping ($\Gamma \ll \omega$) we get

$$\begin{pmatrix}\dot{X}\\ \dot{Y}\end{pmatrix} = \begin{pmatrix}-\Gamma & -np\omega\\ np\omega & -\Gamma\end{pmatrix}\begin{pmatrix}X\\ Y\end{pmatrix} + \begin{pmatrix}\tilde{H}_x^p cp - \tilde{j}_x^p\\ \left|\frac{D_0}{G_0}\right|\xi\tilde{j}_x^p p\end{pmatrix}. \tag{12.6}$$

In the last term, that is the driving force, the actions of the short current and field pulses amplify or attenuate each other depending on the handedness of the vortex.

12.2 Antivortex Random Access Memory

In the case of the VRAM we need one current that is split up into two branches. One branch flows directly through the sample and couples to the vortex via the spin-torque effect and the other branch generates the magnetic field. With an antivortex it is possible to build a memory

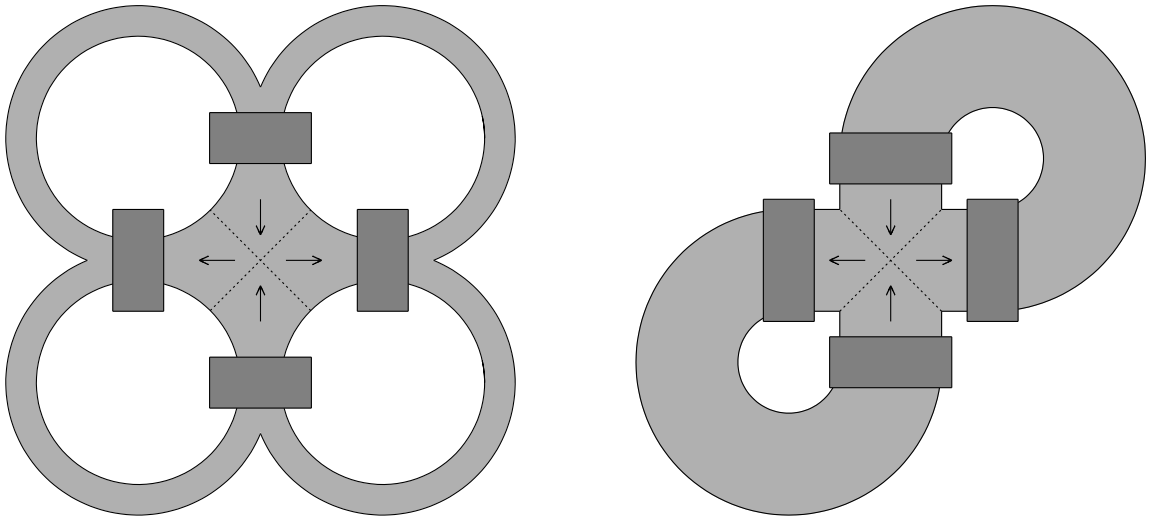

Figure 12.2: Scheme of two possible realizations of an Antivortex Random Access Memory. The nanostructured magnetic film is depicted in light gray while the darker gray denotes the electrical contacts that are placed on the top of the sample. The arrows denote the magnetization for a chirality of $c = 0$ and the dashed lines illustrate the domain walls. The rings ensure that the structure that is present in the center of the samples is an antivortex. Without these rings also a vortex state would be possible.

device where the current has not to be split up. The current flows directly through the sample and interacts with the magnetization via the spin torque. As the source for the field excitation serves the unbalanced Oersted field that accompanies the current. Two possible realizations of an Antivortex Random Access Memory are depicted in figure 12.2. The antivortex is located in the center of the structures and can be traversed by a current that is injected via the left and right or via the lower and upper contacts.

For an antivortex ($n = -1$) with chirality $c = 0$ or $c = 2$ equations (7.72) and (7.74) yield the displacements

$$\begin{pmatrix} X \\ Y \end{pmatrix} = -\frac{e^{i\Omega t}}{\omega^2 + (i\Omega + \Gamma)^2} \begin{pmatrix} \tilde{j}_x + \tilde{H}_y p \cos\left(\frac{\pi c}{2}\right) & -\left|\frac{D_0}{G_0}\right| \xi \tilde{j}_x p \\ \left|\frac{D_0}{G_0}\right| \xi \tilde{j}_x p & \tilde{j}_x + \tilde{H}_y p \cos\left(\frac{\pi c}{2}\right) \end{pmatrix} \begin{pmatrix} \frac{\omega^2 i\Omega}{\omega^2+\Gamma^2} \\ -\omega p - \frac{p\Gamma\omega i\Omega}{\omega^2+\Gamma^2} \end{pmatrix} \tag{12.7}$$

for a current between the left and right contacts and

$$\begin{pmatrix} X \\ Y \end{pmatrix} = -\frac{e^{i\Omega t}}{\omega^2 + (i\Omega + \Gamma)^2} \begin{pmatrix} -\left|\frac{D_0}{G_0}\right| \xi \tilde{j}_y p & -\tilde{j}_y - \tilde{H}_x p \cos\left(\frac{\pi c}{2}\right) \\ \tilde{j}_y + \tilde{H}_x p \cos\left(\frac{\pi c}{2}\right) & -\left|\frac{D_0}{G_0}\right| \xi \tilde{j}_y p \end{pmatrix} \begin{pmatrix} \frac{\omega^2 i\Omega}{\omega^2+\Gamma^2} \\ -\omega p - \frac{p\Gamma\omega i\Omega}{\omega^2+\Gamma^2} \end{pmatrix} \tag{12.8}$$

for a current between the lower and upper contacts.

The unbalanced Oersted field is proportional to the applied current density. It is possible to tailor the unbalanced Oersted field by adding a non-magnetic conducting layer on the top or the bottom of the sample. This layer has the same effect as a strip line. As for the VRAM we assume that $|\tilde{H}| = |\tilde{j}|$. In the following we express $\tilde{H}_y$ by $C_{\mathrm{Oe}}\tilde{j}_x$ and $\tilde{H}_x$ by $-C_{\mathrm{Oe}}\tilde{j}_y$ where $C_{\mathrm{Oe}} = +1$ denotes that the current density at the top surface is larger than the current at the lower surface. A value of $C_{\mathrm{Oe}} = -1$ describes the case where the current density at the lower surface is larger. We can use the displacements in equations (12.7) and (12.8) to derive the velocities

$$v_{\pm}\left(C_{\mathrm{Oe}} p \cos\left(\frac{\pi c}{2}\right)\right) = \frac{\omega|\tilde{j}|}{2\Gamma} \sqrt{\left(1 \mp C_{\mathrm{Oe}} p \cos\left(\frac{\pi c}{2}\right)\right)^2 + \frac{D_0^2}{G_0^2}\xi^2} \tag{12.9}$$

where $v_-\left(C_{\mathrm{Oe}}p\cos\left(\frac{\pi c}{2}\right)\right)$ is the velocity for a current in x direction and $v_+\left(C_{\mathrm{Oe}}p\cos\left(\frac{\pi c}{2}\right)\right)$ is the velocity for a current in y direction. As for the VRAM we used the case of a weakly damped system ($\Gamma \ll \omega$) that is excited at resonance ($\Omega = \omega$). The core velocities are the same as the velocities that have been calculated for the VRAM in equation (12.3) with the handedness cp replaced by $C_{\mathrm{Oe}}p\cos\left(\frac{\pi c}{2}\right)$. Similar to the handedness for the vortex the quantity $C_{\mathrm{Oe}}p\cos\left(\frac{\pi c}{2}\right)$ of the antivortex changes its sign when the core switches.

Thus, it is possible to operate the AVRAM in the same manner as the VRAM. We define $C_{\mathrm{Oe}}p\cos\left(\frac{\pi c}{2}\right) = -1$ and $C_{\mathrm{Oe}}p\cos\left(\frac{\pi c}{2}\right) = +1$ as the "zero" and the "one", respectively. For the writing process we need a current density that is chosen in accordance to equation (12.4). To write a "zero" the current has to be injected along the x direction and to write a "one" the current has to be injected along the y direction.

For the reading process we use a lower current density that fulfills equation (12.5) and is not able to switch the antivortex core. If the reading current is injected along the x direction the binary values "zero" and "one" correspond to a weak or strong gyration, respectively. This gyration can now be detected by a spin valve or by an induction loop as it has been discussed in the last section.

Part III
Dynamics of Domain Walls

Similar to magnetic vortices and antivortices, domain walls in magnetic nanowires can be excited by a magnetic field or a spin-polarized current. The resulting dynamics is discussed in this part. The discussion starts with analytical calculations describing the dynamics of transverse, Néel, and Bloch walls within the micromagnetic framework using some approximations. It is shown that the results for these walls can also be effectively used for a vortex wall. In a second and a third section these analytical results are applied to the dynamics of domain walls in pinning potentials. The second section deals with the dynamics of a wall that stays pinned. While the third section discusses when does the wall leave the potential due to the injection of a current pulse in the sample. In these investigations special attention is put on the influence of the pulse risetime. The last section discusses the mutual interaction of transverse domain walls.

13 Analytical Calculations

13.1 Generalization of the Thiele Equation

In 2008 Tretiakov et al. showed that in the absence of a current the Thiele equation can be generalized by the use of collective coordinates, which can also be non-spatial coordinates.[118,195] In the following a generalization of the Thiele equation including the spin-transfer torque will be derived. Here, the i-th collective coordinate will be denoted by C_i while $\vec{C}$ denotes a vector with all collective coordinates. In the generalized case the number of collective coordinates is not always three as in the special case of the Thiele equation (7.13). Thus the product with the gyro tensor in equation (7.11) cannot always be written as a crossproduct with a vector.

For the calculation of the generalized Thiele equation we express the temporal derivative of the magnetization

$$\frac{d\vec{M}(\vec{r},\vec{C})}{dt} = \sum_i \dot{C}_i \frac{\partial \vec{M}(\vec{r},\vec{C})}{\partial C_i} = \left(\dot{\vec{C}} \cdot \vec{\nabla}_C\right) \vec{M}(\vec{r},\vec{C}) \tag{13.1}$$

by the derivatives with respect to the collective coordinates. Here the i-th component of the vector $\vec{\nabla}_C$ is the derivative $\partial/\partial C_i$. As for the derivation of the Thiele equation we start with the implicit version of the Landau-Lifshitz-Gilbert equation

$$\frac{d\vec{M}}{dt} = -\gamma \vec{M} \times \vec{H} + \frac{\alpha}{M_s} \vec{M} \times \frac{d\vec{M}}{dt} - \frac{b_j}{M_s^2} \vec{M} \times \left(\vec{M} \times \left(\vec{j} \cdot \vec{\nabla}\right) \vec{M}\right) - \frac{\xi b_j}{M_s} \vec{M} \times \left(\vec{j} \cdot \vec{\nabla}\right) \vec{M} \tag{13.2}$$

that is derived in equation (3.2). We insert the time derivative that is calculated in equation (13.1) to get

$$\left(\dot{\vec{C}} \cdot \vec{\nabla}_C\right) \vec{M} = -\gamma \vec{M} \times \vec{H} + \frac{\alpha}{M_s} \vec{M} \times \left(\dot{\vec{C}} \cdot \vec{\nabla}_C\right) \vec{M} - \frac{b_j}{M_s^2} \vec{M} \times \left(\vec{M} \times \left(\vec{j} \cdot \vec{\nabla}\right) \vec{M}\right) - \frac{\xi b_j}{M_s} \vec{M} \times \left(\vec{j} \cdot \vec{\nabla}\right) \vec{M}. \tag{13.3}$$

On the right hand side of equation (13.3) all terms contain a cross product with the magnetization and are thus perpendicular to the magnetization. Thus, the term on the left-hand side is also perpendicular to the magnetization and can be rewritten by the use of equation (1.14). We get

$$\left(\dot{\vec{C}} \cdot \vec{\nabla}_C\right) \vec{M} = -\frac{1}{M_s^2} \vec{M} \times \left(\vec{M} \times \left(\dot{\vec{C}} \cdot \vec{\nabla}_C\right) \vec{M}\right). \tag{13.4}$$

With this expression equation (13.3) becomes

$$\begin{aligned} 0 = &\frac{1}{M_s^2}\vec{M}\times\left(\vec{M}\times\left(\dot{\vec{C}}\cdot\vec{\nabla}_C\right)\vec{M}\right) - \gamma\vec{M}\times\vec{H} + \frac{\alpha}{M_s}\vec{M}\times\left(\dot{\vec{C}}\cdot\vec{\nabla}_C\right)\vec{M} \\ &- \frac{b_j}{M_s^2}\vec{M}\times\left(\vec{M}\times\left(\vec{j}\cdot\vec{\nabla}\right)\vec{M}\right) - \frac{\xi b_j}{M_s}\vec{M}\times\left(\vec{j}\cdot\vec{\nabla}\right)\vec{M}. \end{aligned} \tag{13.5}$$

As for the Thiele equation the field equation

$$\begin{aligned} 0 = &\vec{H} - \frac{1}{\gamma M_s^2}\vec{M}\times\left(\dot{\vec{C}}\cdot\vec{\nabla}_C\right)\vec{M} - \frac{\alpha}{\gamma M_s}\left(\dot{\vec{C}}\cdot\vec{\nabla}_C\right)\vec{M} \\ &+ \frac{b_j}{\gamma M_s^2}\vec{M}\times\left(\vec{j}\cdot\vec{\nabla}\right)\vec{M} + \frac{\xi b_j}{\gamma M_s}\left(\vec{j}\cdot\vec{\nabla}\right)\vec{M} + \rho\vec{M} \end{aligned} \tag{13.6}$$

reproduces equation (13.5) after multiplication with $-\gamma$ and application of the cross product with $\vec{M}$ from the left. Again $\rho\vec{M}$ is a magnetic field in the direction of the magnetization that is arbitrary since the torque on the magnetization depends only on the cross product between the field an the magnetization. We will see that this field will vanish in the following considerations. The force on the magnetization pattern is given by

$$\vec{F}_i = -\frac{\partial E}{\partial C_i} = -\int dV \sum_k \frac{\delta E}{\delta \vec{M}_k(\vec{r})}\frac{\partial \vec{M}_k}{\partial C_i} = \mu_0 \int dV \sum_k \vec{H}_k \frac{\partial \vec{M}_k}{\partial C_i}. \tag{13.7}$$

From inserting equation (13.6) in equation (13.7) we find the i-th component of the force that is given by

$$\begin{aligned} 0 = &\underbrace{\int dV \sum_k \mu_0 \frac{\partial \vec{M}_k}{\partial C_i}\vec{H}_k}_{F_i} \\ &+ \sum_n \underbrace{\int dV \sum_{k,l,m} (-1)\frac{\mu_0 \epsilon_{klm}}{\gamma M_s^2}\frac{\partial \vec{M}_k}{\partial C_i}\vec{M}_l\frac{\partial \vec{M}_m}{\partial C_n}\dot{\vec{C}}_n}_{G_{in}} + \sum_n \underbrace{\int dV \sum_k (-1)\frac{\mu_0}{\gamma M_s}\frac{\partial \vec{M}_k}{\partial C_i}\frac{\partial \vec{M}_k}{\partial C_n}\alpha\dot{\vec{C}}_n}_{D_{in}} \\ &+ \sum_n \underbrace{\int dV \sum_{k,l,m} \frac{\mu_0 \epsilon_{klm}}{\gamma M_s^2}\frac{\partial \vec{M}_k}{\partial C_i}\vec{M}_l\frac{\partial \vec{M}_m}{\partial r_n}b_j\vec{j}_n}_{A_{in}} + \sum_n \underbrace{\int dV \sum_k \frac{\mu_0}{\gamma M_s}\frac{\partial \vec{M}_k}{\partial C_i}\frac{\partial \vec{M}_k}{\partial r_n}\xi b_j\vec{j}_n}_{N_{in}}. \end{aligned} \tag{13.8}$$

In vector notation this yields the generalized equation

$$0 = \vec{F} + G\dot{\vec{C}} + Ab_j\vec{j} + D\alpha\dot{\vec{C}} + N\xi b_j\vec{j}, \tag{13.9}$$

with the force

$$\vec{F}_i = \mu_0 \int dV \sum_k \frac{\partial \vec{M}_k}{\partial C_i}\vec{H}_k = -\frac{\partial E}{\partial C_i}, \tag{13.10}$$

the gyro tensor

$$G_{in} = \frac{\mu_0}{\gamma M_s^2}\int dV\, \vec{M}\cdot\left(\frac{\partial \vec{M}}{\partial C_i}\times\frac{\partial \vec{M}}{\partial C_n}\right), \tag{13.11}$$

the dissipation tensor

$$D_{in} = -\frac{\mu_0}{\gamma M_s}\int dV \frac{\partial \vec{M}}{\partial C_i}\cdot\frac{\partial \vec{M}}{\partial C_n}, \tag{13.12}$$

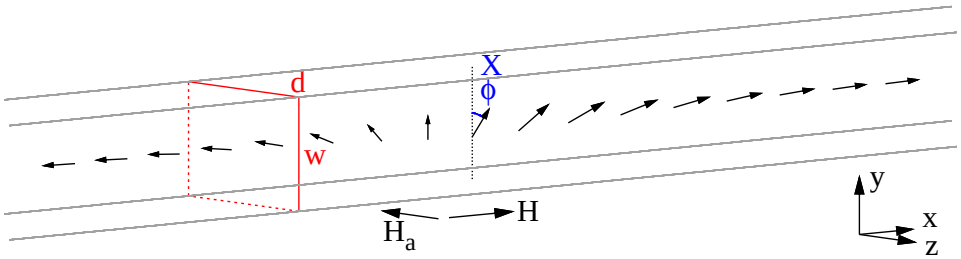

Figure 13.1: Parameterization of a tail-to-tail transverse wall in a wire with a rectangular cross section. The position of the maximum of the perpendicular magnetization, that is the center of the wall, is denoted by X. The value ϕ is the angle by which the magnetization is rotated around the wire axis. In this geometry the magnetic field H, that is used to move the domain wall, points in x direction. The anisotropy field H_a that forces the magnetization back in the xy plane points in $-z$ direction.

the tensor for the adiabatic spin torque

$$A_{in} = -\frac{\mu_0}{\gamma M_s^2} \int dV\, \vec{M} \cdot \left(\frac{\partial \vec{M}}{\partial C_i} \times \frac{\partial \vec{M}}{\partial \vec{r}_n} \right), \tag{13.13}$$

and the tensor for the non-adiabatic spin torque

$$N_{in} = \frac{\mu_0}{\gamma M_s} \int dV\, \frac{\partial \vec{M}}{\partial C_i} \cdot \frac{\partial \vec{M}}{\partial \vec{r}_n}. \tag{13.14}$$

For a vanishing current this is exactly the result that has been found by Tretiakov et al.[118,195] It is worth noting that equations (13.10), (13.12), and (13.14) contain scalar products only while equations (13.11) and (13.13) contain parallelepipedial products only. Both types of products are invariant under a rotation of the involved vectors. Thus a rotation of the magnetization and the magnetic field in the whole sample would not change equation (13.9).

13.2 Equation of Motion of the Transverse Wall

For the calculation of the equation of motion we restrict ourselves to a tail-to-tail transverse wall in which the magnetization is given by

$$\vec{M} = \frac{M_s}{\cosh\left(\frac{x-X}{\lambda}\right)} \begin{pmatrix} \sinh\left(\frac{x-X}{\lambda}\right) \\ \cos(\phi) \\ \sin(\phi) \end{pmatrix} \tag{13.15}$$

as derived in equations (5.5) and (5.6). Later on we will see that the results for the tail-to-tail transverse wall can easily be generalized to a head-to-head wall and even to other types of domain walls like Néel walls or Bloch walls. It has been shown that for a current and a magnetic field which are applied perpendicular to the wall the dynamics of the domain wall can be expressed by two collective coordinates that are parameters in equation (13.15).[105,129] These coordinates are the position of the wall X and the out-of-plane angle ϕ that is uniform in the system as depicted in figure 13.1.

The tensors in the generalized Thiele equation can be calculated by using the derivatives of the magnetization with respect to the collective coordinates. These derivatives are given by

$$\frac{\partial \vec{M}}{\partial X} = \frac{M_s}{\lambda \cosh^2\left(\frac{x-X}{\lambda}\right)} \begin{pmatrix} -1 \\ \sinh\left(\frac{x-X}{\lambda}\right)\cos(\phi) \\ \sinh\left(\frac{x-X}{\lambda}\right)\sin(\phi) \end{pmatrix} \tag{13.16}$$

and

$$\frac{\partial \vec{M}}{\partial \phi} = \frac{M_s}{\cosh\left(\frac{x-X}{\lambda}\right)} \begin{pmatrix} 0 \\ -\sin(\phi) \\ \cos(\phi) \end{pmatrix}. \tag{13.17}$$

For the current dependent part we also need

$$\frac{\partial \vec{M}}{\partial x} = -\frac{\partial \vec{M}}{\partial X} = \frac{M_s}{\lambda \cosh^2\left(\frac{x-X}{\lambda}\right)} \begin{pmatrix} 1 \\ -\sinh\left(\frac{x-X}{\lambda}\right)\cos(\phi) \\ -\sinh\left(\frac{x-X}{\lambda}\right)\sin(\phi) \end{pmatrix}. \tag{13.18}$$

Using these results we calculate the mixed products

$$\vec{M} \cdot \left(\frac{\partial \vec{M}}{\partial X} \times \frac{\partial \vec{M}}{\partial \phi} \right) = \frac{M_s^3}{\lambda \cosh^4\left(\frac{x-X}{\lambda}\right)} \begin{pmatrix} \sinh\left(\frac{x-X}{\lambda}\right) \\ \cos(\phi) \\ \sin(\phi) \end{pmatrix} \cdot \begin{pmatrix} \sinh\left(\frac{x-X}{\lambda}\right) \\ \cos(\phi) \\ \sin(\phi) \end{pmatrix} = \frac{M_s^3}{\lambda \cosh^2\left(\frac{x-X}{\lambda}\right)} \tag{13.19}$$

and

$$\vec{M} \cdot \left(\frac{\partial \vec{M}}{\partial \phi} \times \frac{\partial \vec{M}}{\partial x} \right) = \vec{M} \cdot \left(\frac{\partial \vec{M}}{\partial X} \times \frac{\partial \vec{M}}{\partial \phi} \right) = \frac{M_s^3}{\lambda \cosh^2\left(\frac{x-X}{\lambda}\right)}. \tag{13.20}$$

We also calculate the dot products

$$\frac{\partial \vec{M}}{\partial X} \cdot \frac{\partial \vec{M}}{\partial X} = \frac{M_s^2}{\lambda^2 \cosh^2\left(\frac{x-X}{\lambda}\right)} \tag{13.21}$$

and

$$\frac{\partial \vec{M}}{\partial \phi} \cdot \frac{\partial \vec{M}}{\partial \phi} = \frac{M_s^2}{\cosh^2\left(\frac{x-X}{\lambda}\right)}. \tag{13.22}$$

The dot product between two different derivatives, that is one derivative with respect to X and one derivative with respect to ϕ, vanishes. For the current dependent part the product

$$\frac{\partial \vec{M}}{\partial X} \cdot \frac{\partial \vec{M}}{\partial x} = -\frac{\partial \vec{M}}{\partial X} \cdot \frac{\partial \vec{M}}{\partial X} = -\frac{M_s^2}{\lambda^2 \cosh^2\left(\frac{x-X}{\lambda}\right)} \tag{13.23}$$

is also needed.

We assume that the energy of the system depends on X and on ϕ only. This leads to the expression

$$\vec{F} = -\begin{pmatrix} \frac{\partial E}{\partial X} \\ \frac{\partial E}{\partial \phi} \end{pmatrix} \tag{13.24}$$

for the force. Using the mixed products calculated above we can derive the gyro tensor

$$G = \begin{pmatrix} G_{XX} & G_{X\phi} \\ G_{\phi X} & G_{\phi\phi} \end{pmatrix} = \begin{pmatrix} 0 & \frac{2S\mu_0 M_s}{\gamma} \\ -\frac{2S\mu_0 M_s}{\gamma} & 0 \end{pmatrix} \tag{13.25}$$

and the tensor for the adiabatic spin-torque

$$A = \begin{pmatrix} A_{Xx} \\ A_{\phi x} \end{pmatrix} = \begin{pmatrix} 0 \\ -\frac{2S\mu_0 M_s}{\gamma} \end{pmatrix} \tag{13.26}$$

where S is the cross section of the wire. The dot products lead to the damping tensor

$$D = \begin{pmatrix} D_{XX} & D_{X\phi} \\ D_{\phi X} & D_{\phi\phi} \end{pmatrix} = \begin{pmatrix} -\frac{2S\mu_0 M_s}{\gamma\lambda} & 0 \\ 0 & -\frac{2S\mu_0 M_s \lambda}{\gamma} \end{pmatrix} \tag{13.27}$$

and the tensor for the non-adiabatic spin-torque

$$N = \begin{pmatrix} N_{Xx} \\ N_{\phi x} \end{pmatrix} = \begin{pmatrix} -\frac{2S\mu_0 M_s}{\gamma\lambda} \\ 0 \end{pmatrix}. \tag{13.28}$$

Inserting these results in the equation of motion for the collective coordinates we get

$$0 = -\begin{pmatrix} \frac{\partial E}{\partial X} \\ \frac{\partial E}{\partial \phi} \end{pmatrix} + \frac{2S\mu_0 M_s}{\gamma} \begin{pmatrix} -\frac{\alpha}{\lambda} & 1 \\ -1 & -\alpha\lambda \end{pmatrix} \begin{pmatrix} \dot{X} \\ \dot{\phi} \end{pmatrix} - \frac{2S\mu_0 M_s}{\gamma} \begin{pmatrix} \frac{\xi}{\lambda} \\ 1 \end{pmatrix} b_j j \tag{13.29}$$

which can be transformed to

$$\begin{pmatrix} \frac{\alpha}{\lambda} & -1 \\ 1 & \alpha\lambda \end{pmatrix} \begin{pmatrix} \dot{X} \\ \dot{\phi} \end{pmatrix} = -\frac{\gamma}{2S\mu_0 M_s} \begin{pmatrix} \frac{\partial E}{\partial X} \\ \frac{\partial E}{\partial \phi} \end{pmatrix} - \begin{pmatrix} \frac{\xi}{\lambda} \\ 1 \end{pmatrix} b_j j. \tag{13.30}$$

This form of the equation of motion is the same as found by Thomas et *al.*.[105] Both components contain time derivatives of X and ϕ. We can get two explicit equations with only one time derivative by a multiplication with

$$\begin{pmatrix} \frac{\alpha}{\lambda} & -1 \\ 1 & \alpha\lambda \end{pmatrix}^{-1} = \frac{1}{1+\alpha^2} \begin{pmatrix} \alpha\lambda & 1 \\ -1 & \frac{\alpha}{\lambda} \end{pmatrix} \tag{13.31}$$

that yields

$$\begin{pmatrix} \dot{X} \\ \dot{\phi} \end{pmatrix} = -\frac{\gamma'}{2S\mu_0 M_s} \begin{pmatrix} \alpha\lambda & 1 \\ -1 & \frac{\alpha}{\lambda} \end{pmatrix} \begin{pmatrix} \frac{\partial E}{\partial X} \\ \frac{\partial E}{\partial \phi} \end{pmatrix} - \begin{pmatrix} \alpha\lambda & 1 \\ -1 & \frac{\alpha}{\lambda} \end{pmatrix} \begin{pmatrix} \frac{\xi}{\lambda} \\ 1 \end{pmatrix} b'_j j \tag{13.32}$$

with $\gamma' = \gamma/(1+\alpha^2)$ and $b'_j = b_j/(1+\alpha^2)$. In component notation this is[129,196]

$$\dot{X} = -\frac{\gamma'\alpha\lambda}{2S\mu_0 M_s}\frac{\partial E}{\partial X} - \frac{\gamma'}{2S\mu_0 M_s}\frac{\partial E}{\partial \phi} - (1+\alpha\xi)b'_j j \text{ and} \tag{13.33a}$$

$$\dot{\phi} = \frac{\gamma'}{2S\mu_0 M_s}\frac{\partial E}{\partial X} - \frac{\gamma'\alpha}{2S\mu_0 M_s\lambda}\frac{\partial E}{\partial \phi} + \frac{\xi-\alpha}{\lambda} b'_j j. \tag{13.33b}$$

To calculate the derivatives of the energy we use the expression in equation (5.7) plus the Zeeman energy for an external field in the direction of the easy axis and a pinning potential. Since the collective coordinate ϕ is assumed to be constant in space we neglect the energy that depends on the spatial derivative of ϕ. The energy then reads

$$E = \int dV \left(A\left(\frac{\partial\theta}{\partial x}\right)^2 + K\sin^2(\theta) + K_\perp \sin^2(\theta)\sin^2(\phi) - \mu_0 M_s H_{\text{ext}}\cos(\theta)\right) + E_{\text{pin}}(X). \tag{13.34}$$

For the integration we use the expressions for $\cos(\theta)$ and $\sin(\theta)$ that have been calculated in equations (5.5) and (5.6). With the aid of the integrals in appendix F the energy then yields

$$E = 2S\frac{A}{\lambda} + 2SK\lambda + 2SK_\perp\lambda\sin^2(\phi) + 2S\mu_0 M_s H_{\text{ext}} X + E_{\text{pin}}(X). \tag{13.35}$$

The derivatives are

$$\frac{\partial E}{\partial X} = 2S\mu_0 M_s H_{\text{ext}} + \frac{dE_{\text{pin}}}{dX} \tag{13.36}$$

and

$$\frac{\partial E}{\partial \phi} = 2SK_\perp\lambda\sin(2\phi). \tag{13.37}$$

For small rotations the derivative in equation (13.37) can be linearized in ϕ. The equations of motion then read

$$\dot{X} = -\frac{\gamma'\alpha\lambda}{2S\mu_0 M_s}\left(2S\mu_0 M_s H_{\text{ext}} + \frac{dE_{\text{pin}}}{dX}\right) - \frac{2K_\perp\lambda\gamma'}{\mu_0 M_s}\phi - (1+\alpha\xi)b'_j j \text{ and} \tag{13.38a}$$

$$\dot{\phi} = \frac{\gamma'}{2S\mu_0 M_s}\left(2S\mu_0 M_s H_{\text{ext}} + \frac{dE_{\text{pin}}}{dX}\right) - \frac{2K_\perp\gamma'\alpha}{\mu_0 M_s}\phi + \frac{\xi-\alpha}{\lambda} b'_j j. \tag{13.38b}$$

Taking the time derivative of equation (13.38a) and replacing $\dot{\phi}$ by equation (13.38b) we get

$$\begin{aligned}\ddot{X} =& -\frac{\gamma'\alpha\lambda}{2S\mu_0 M_s}\frac{d}{dt}\left(2S\mu_0 M_s H_{\text{ext}} + \frac{dE_{\text{pin}}}{dX}\right) \\ & - \frac{2K_\perp\lambda\gamma'}{\mu_0 M_s}\left(\frac{\gamma'}{2S\mu_0 M_s}\left(2S\mu_0 M_s H_{\text{ext}} + \frac{dE_{\text{pin}}}{dX}\right) - \frac{2K_\perp\gamma'\alpha}{\mu_0 M_s}\phi + \frac{\xi-\alpha}{\lambda}b_j' j\right) - (1+\alpha\xi)b_j'\dot{j}\end{aligned} \tag{13.39}$$

From equation (13.38a) one can derive

$$-\frac{2K_\perp\gamma'\alpha}{\mu_0 M_s}\phi = \frac{\alpha\dot{X}}{\lambda} + \frac{\gamma'\alpha^2}{2S\mu_0 M_s}\left(2S\mu_0 M_s H_{\text{ext}} + \frac{dE_{\text{pin}}}{dX}\right) + \frac{\alpha(1+\alpha\xi)}{\lambda}b_j' j \tag{13.40}$$

leading to

$$\begin{aligned}\ddot{X} =& -\frac{2K_\perp\gamma'\alpha}{\mu_0 M_s}\dot{X} - \frac{\gamma'\alpha\lambda}{2S\mu_0 M_s}\frac{d}{dt}\frac{dE_{\text{pin}}}{dX} - \frac{K_\perp\lambda\gamma'\gamma}{S\mu_0^2 M_s^2}\frac{dE_{\text{pin}}}{dX} \\ & - \frac{2K_\perp\lambda\gamma'\gamma}{\mu_0 M_s}H_{\text{ext}} - \gamma'\alpha\lambda\dot{H}_{\text{ext}} - \frac{2K_\perp\gamma'\alpha}{\mu_0 M_s}\frac{\xi}{\alpha}b_j j - (1+\alpha\xi)b_j'\dot{j}.\end{aligned} \tag{13.41}$$

The freely moving domain wall ($E_{\text{pin}} \equiv 0$, $H_{\text{ext}} = 0$, and $j = 0$) needs the damping time

$$\tau_d = \frac{\mu_0 M_s}{2\gamma' K_\perp \alpha} \tag{13.42}$$

to slow down to $1/e$ of its initial velocity.

Equation (13.41) describes the motion of the domain wall as a composite particle. Since it has a non-vanishing kinetic energy a mass can be assigned to the particle. According to equation (13.35) the kinetic energy of the wall is given by the anisotropy energy $2SK_\perp\lambda\sin^2(\phi) \approx 2SK_\perp\lambda\phi^2$. From

$$\frac{1}{2}m\dot{X}^2 = 2K_\perp S\lambda\phi^2 = 2K_\perp S\lambda\left(\frac{\mu_0 M_s}{2\gamma' K_\perp\lambda}\right)^2\dot{X}^2 = \frac{1}{2}\frac{S\mu_0^2 M_s^2}{\gamma'^2 K_\perp\lambda}\dot{X}^2 \tag{13.43}$$

one can derive the mass

$$m = \frac{S\mu_0^2 M_s^2}{\gamma'^2 K_\perp\lambda} \tag{13.44}$$

of the domain wall. Here we used

$$\phi = -\frac{\mu_0 M_s}{2\gamma' K_\perp\lambda}\dot{X} \tag{13.45}$$

that can be derived for the free domain wall using equation (13.38a).

We express the derivative

$$\frac{d}{dt}\frac{dE_{\text{pin}}}{dX} = \dot{X}\frac{d^2 E_{\text{pin}}}{dX^2} \tag{13.46}$$

in equation (13.41) with the aid of the velocity and find

$$\ddot{X} = -\left(1 + \frac{\alpha^2\tau_d^2}{m}\frac{d^2 E_{\text{pin}}}{dX^2}\right)\frac{\dot{X}}{\tau_d} - \frac{1}{m'}\frac{dE_{\text{pin}}}{dX} - \frac{\lambda\gamma}{\alpha}\frac{H_{\text{ext}}}{\tau_d} - \gamma'\alpha\lambda\dot{H}_{\text{ext}} - \frac{\xi}{\alpha}\frac{b_j j}{\tau_d} - (1+\alpha\xi)b_j'\dot{j} \tag{13.47}$$

using the mass $m' = m/(1+\alpha^2)$ and the damping time τ_d of the domain wall. It is worth noting that the mass m that is derived from the kinetic energy is not the same as the mass m' that is given by the inertia in equation (13.47). A second interesting observation is that in a potential with non-vanishing curvature the damping, that is the first term in equation (13.47), is position dependent. However, the position dependent term is small for most systems.

The difference between m and m' are due to the fact that there are two different mechanisms involved in the motion of the domain wall. For the following consideration we focus on the tail-to-tail domain wall that is shown in figure 13.1 and assume that the influence of the pinning potential E_{pin} on the domain wall is mediated by a magnetic field, that is aligned parallel to the wire. According to the LLG equation (1.16) this field has two different effects on the magnetization in the wall. There is the damping, that is proportional to α and rotates the magnetization in the direction of the wire, and the gyration, that is a rotation of the magnetization around the wire axis. The first effect leads directly to a shift of the domain wall and will be called direct motion in the following. The second effect leads to a rotation of the wall, that is a change of ϕ. This rotation counteracts the anisotropy that forces the wall in the xy plane. Thus an anisotropy field emerges. This field points perpendicular to the wire as shown in figure 13.1. We now get a rotation of the magnetization around this anisotropy field, leading to an additional motion. This motion employing the anisotropy field is accompanied by the kinetic energy $2SK_\perp\lambda\phi^2$. In contrast the aforementioned direct motion has no kinetic energy since ϕ is left unchanged. This leads to the effect that for the pinned wall the kinetic energy is no longer proportional to $\dot{X}$.

13.3 Generalization to Other Wall Types

Since the parallelepipedial products and the scalar products are invariant under rotation, equation (13.47) is valid for every type of domain wall that can be obtained by a rotation of the magnetization in equation (13.15). Here we will not discuss a mirroring of the magnetization since these magnetization patterns can be accessed by replacing ϕ by $-\phi$ before the rotation. The rotation of the magnetization can be described by three rotations, described by the Euler angles. First we rotate the magnetization around the x axis. The second rotation is around the y axis while the final rotation is again around the x axis. The rotated magnetization $\vec{M}'$ is given by

$$\begin{aligned}
\frac{\vec{M}'}{M_s} &= \begin{pmatrix} 1 & 0 & 0 \\ 0 & \cos\psi_3 & -\sin\psi_3 \\ 0 & \sin\psi_3 & \cos\psi_3 \end{pmatrix} \begin{pmatrix} \cos\psi_2 & 0 & \sin\psi_2 \\ 0 & 1 & 0 \\ -\sin\psi_2 & 0 & \cos\psi_2 \end{pmatrix} \begin{pmatrix} 1 & 0 & 0 \\ 0 & \cos\psi_1 & -\sin\psi_1 \\ 0 & \sin\psi_1 & \cos\psi_1 \end{pmatrix} \begin{pmatrix} \tanh\left(\frac{x-X}{\lambda}\right) \\ \frac{\cos(\phi)}{\cosh\left(\frac{x-X}{\lambda}\right)} \\ \frac{\sin(\phi)}{\cosh\left(\frac{x-X}{\lambda}\right)} \end{pmatrix} \\
&= \begin{pmatrix} \cos\psi_2 & 0 & \sin\psi_2 \\ \sin\psi_2\sin\psi_3 & \cos\psi_3 & -\cos\psi_2\sin\psi_3 \\ -\sin\psi_2\cos\psi_3 & \sin\psi_3 & \cos\psi_2\cos\psi_3 \end{pmatrix} \begin{pmatrix} 1 & 0 & 0 \\ 0 & \cos\psi_1 & -\sin\psi_1 \\ 0 & \sin\psi_1 & \cos\psi_1 \end{pmatrix} \begin{pmatrix} \tanh\left(\frac{x-X}{\lambda}\right) \\ \frac{\cos(\phi)}{\cosh\left(\frac{x-X}{\lambda}\right)} \\ \frac{\sin(\phi)}{\cosh\left(\frac{x-X}{\lambda}\right)} \end{pmatrix} \\
&= \begin{pmatrix} \cos\psi_2 \\ \sin\psi_2\sin\psi_3 \\ -\sin\psi_2\cos\psi_3 \end{pmatrix} \tanh\left(\frac{x-X}{\lambda}\right) + \begin{pmatrix} \sin\psi_1\sin\psi_2 \\ \cos\psi_1\cos\psi_3 - \sin\psi_1\cos\psi_2\sin\psi_3 \\ \cos\psi_1\sin\psi_3 + \sin\psi_1\cos\psi_2\cos\psi_3 \end{pmatrix} \frac{\cos(\phi)}{\cosh\left(\frac{x-X}{\lambda}\right)} \\
&+ \begin{pmatrix} \cos\psi_1\sin\psi_2 \\ -\sin\psi_1\cos\psi_3 - \cos\psi_1\cos\psi_2\sin\psi_3 \\ -\sin\psi_1\sin\psi_3 + \cos\psi_1\cos\psi_2\cos\psi_3 \end{pmatrix} \frac{\sin(\phi)}{\cosh\left(\frac{x-X}{\lambda}\right)}
\end{aligned} \tag{13.48}$$

with the rotation angles ψ_1, ψ_2, and ψ_3 for the first, second, and third rotation, respectively. It is important that the external magnetic field and the easy and hard axes have to be rotated in the same way. As one can see, replacing ψ_1 by $\psi_1 + \pi$, ψ_2 by $2\pi - \psi_2$, and ψ_3 by $\psi_3 + \pi$ does not change equation (13.48) and $\vec{M}'$ does not change. Thus, the rotation angles are not unambiguously defined. For the special cases $\psi_2 = 0$ and $\psi_2 = \pi$ the matrix is only a function of $\psi_1 + \psi_3$ and $\psi_1 - \psi_3$, respectively.

In the following discussion we will restrict ourselves to the cases where all three rotation angles are integer multiples of $\pi/2$. Then for the groundstate of the wall, that is, for $\phi = 0$, the magnetization in the domains and at the center of the wall are aligned parallel or antiparallel to the axes of the coordinate system.

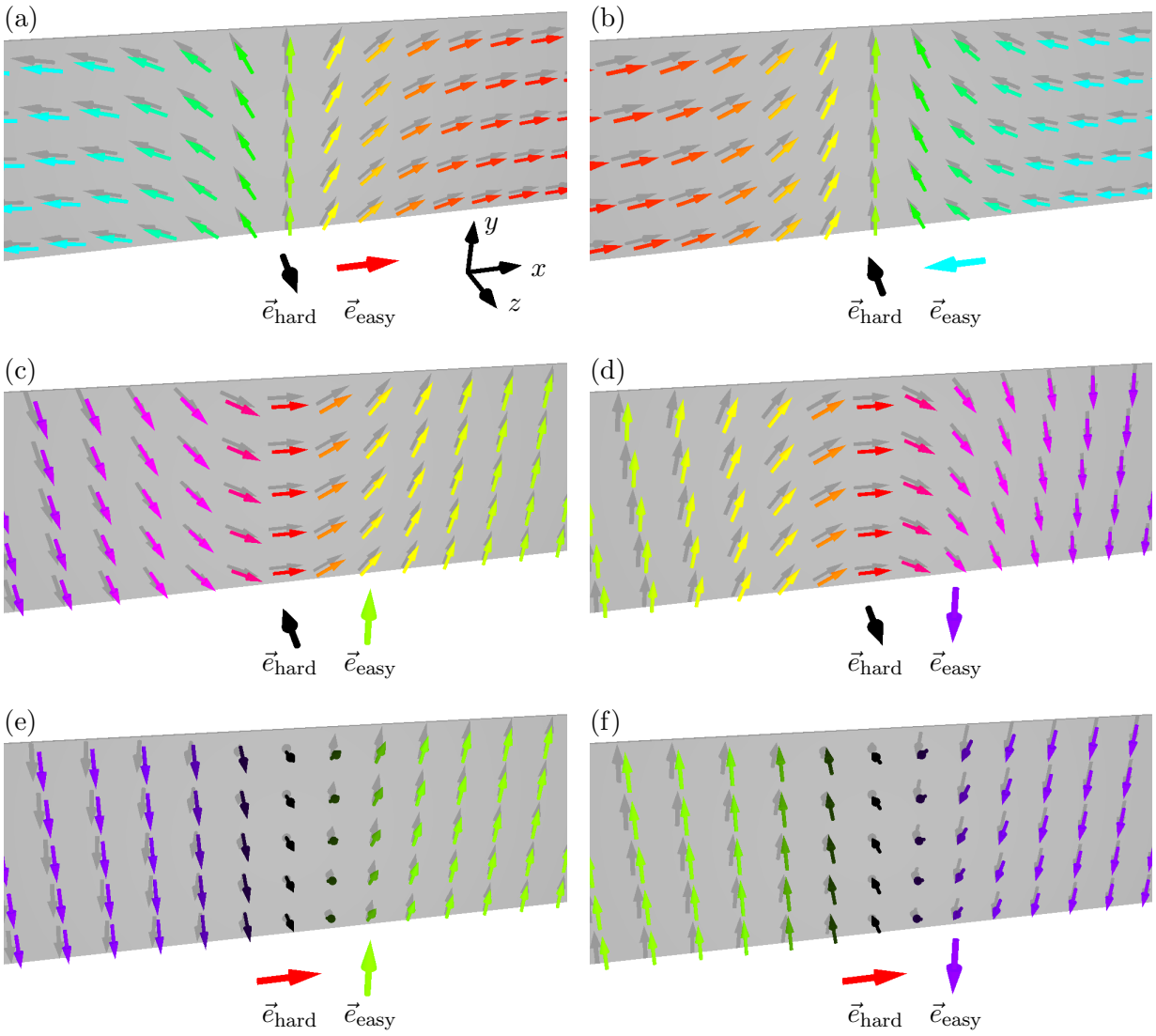

Figure 13.2: Examples of different types of domain walls that can be described by the equation of motion that is derived above. The color of the arrows denote the direction of the in-plane magnetization. A black arrow denotes a magnetization that points out-of-plane. The directions of the easy axis $\vec{e}_{\text{easy}}$ and the hard axis $\vec{e}_{\text{hard}}$ are denoted by the two arrows in the lower part of the figures. For a field-driven motion of the domain wall in $-x$ direction the external field has to point in the direction of the easy axis $\vec{e}_{\text{easy}}$. The shown domain walls are (a) a tail-to-tail transverse wall with $\psi_1 = 0$, $\psi_2 = 0$, and $\psi_3 = 0$, (b) a head-to-head transverse wall with $\psi_1 = 0$, $\psi_2 = \pi$, and $\psi_3 = 0$, (c) and (d) two Néel walls with (c) $\psi_1 = \pi/2$, $\psi_2 = \pi/2$, and $\psi_3 = \pi/2$ and (d) $\psi_1 = \pi/2$, $\psi_2 = \pi/2$, and $\psi_3 = -\pi/2$, and (e) and (f) two Bloch walls with (e) $\psi_1 = 0$, $\psi_2 = \pi/2$, and $\psi_3 = \pi/2$ and (f) $\psi_1 = 0$, $\psi_2 = \pi/2$, and $\psi_3 = -\pi/2$.

Depending on the angles ψ_1 and ψ_2, equation (13.48) describes different types of domain walls. The magnetization in the right domain is given by

$$\vec{M}'(x \to \infty) = M_s \begin{pmatrix} \cos\psi_2 \\ \sin\psi_2 \sin\psi_3 \\ -\sin\psi_2 \cos\psi_3 \end{pmatrix}. \tag{13.49}$$

Thus $\psi_2 = 0$ describes a tail-to-tail and $\psi_2 = \pi$ describes a head-to-head transverse wall. For a Néel wall and a Bloch wall the magnetization in the domains has to be parallel to the wall, that is, the magnetization of the domains have to be in the yz plane, which corresponds to $\psi_2 = \pi/2$. In the groundstate, the magnetization

$$\vec{M}'(x = X, \phi = 0) = M_s \begin{pmatrix} \sin\psi_1 \sin\psi_2 \\ \cos\psi_1 \cos\psi_3 - \sin\psi_1 \cos\psi_2 \sin\psi_3 \\ \cos\psi_1 \sin\psi_3 + \sin\psi_1 \cos\psi_2 \cos\psi_3 \end{pmatrix} \tag{13.50}$$

at the center of the wall allows us to distinguish between a Néel wall with $\psi_1 = \pm\pi/2$ where the magnetization is perpendicular to the wall and a Bloch wall with $\psi_1 = 0$ or $\psi_1 = \pi$ where the magnetization stays in the wall plane. Figure 13.2 shows some examples of magnetization configurations that can be obtained by the above rotation.

For a further generalization of the equation of motion we neglect the spatially dependent term of the damping, that is,

$$\frac{\alpha^2 \tau_d^2}{m} \frac{d^2 E_{\text{pin}}}{dX^2} \ll 1 \tag{13.51}$$

and write equation (13.47) in the form

$$\ddot{X} = -\frac{\dot{X}}{\tau_d} - \frac{1}{m'} \frac{dE_{\text{pin}}}{dX} + \frac{C_1}{\tau_d} H_{\text{ext}} + C_2 \dot{H}_{\text{ext}} + \frac{C_3}{\tau_d} j + C_4 \dot{j} \tag{13.52}$$

with the coefficients

$$C_1 = -\lambda\gamma/\alpha, \;\; C_2 = -\gamma'\alpha\lambda, \;\; C_3 = -b_j\xi/\alpha, \;\; \text{and} \;\; C_4 = -(1+\alpha\xi)b'_j \tag{13.53}$$

for the wall types given above. In the absence of a pinning potential ($E_{\text{pin}} \equiv 0$) the domain-wall velocity in equation (13.52) is given by

$$\dot{X}(t) = \int_{-\infty}^{t} dt' \; e^{-\frac{t-t'}{\tau_d}} \left(\frac{C_1}{\tau_d} H_{\text{ext}}(t') + C_2 \dot{H}_{\text{ext}}(t') + \frac{C_3}{\tau_d} j(t') + C_4 \dot{j}(t') \right) \tag{13.54}$$

as derived in appendix E. This equation describes a linear response of the velocity to the field H_{ext} and the current j as well as their time derivatives $\dot{H}_{\text{ext}}$ and $\dot{j}$. We now assume that the velocity of other domain-wall types like vortex walls is given by the same linear response but with coefficients that differ from those given in equations (13.42), (13.44), and (13.53).

For a field of the form $H_{\text{ext}}(t) = H_0\Theta(t)$ and a current of the form $j(t) = j_0\Theta(t)$ with the Heaviside step function $\Theta(t)$ the velocity for $t > 0$ is given by

$$\begin{aligned} \dot{X}(t) &= \int_{-\infty}^{t} dt' \; e^{-\frac{t-t'}{\tau_d}} \left(\frac{C_1}{\tau_d} H_0 \Theta(t') + C_2 H_0 \delta(t') + \frac{C_3}{\tau_d} j_0 \Theta(t') + C_4 j_0 \delta(t') \right) \\ &= \left(\frac{C_1}{\tau_d} H_0 + \frac{C_3}{\tau_d} j_0 \right) \int_{0}^{t} dt' \; e^{-\frac{t-t'}{\tau_d}} + (C_2 H_0 + C_4 j_0) \, e^{-\frac{t}{\tau_d}} \\ &= \underbrace{(C_1 H_0 + C_3 j_0)}_{v_f} \left(1 - e^{-\frac{t}{\tau_d}} \right) + \underbrace{(C_2 H_0 + C_4 j_0)}_{v_i} e^{-\frac{t}{\tau_d}}. \end{aligned} \tag{13.55}$$

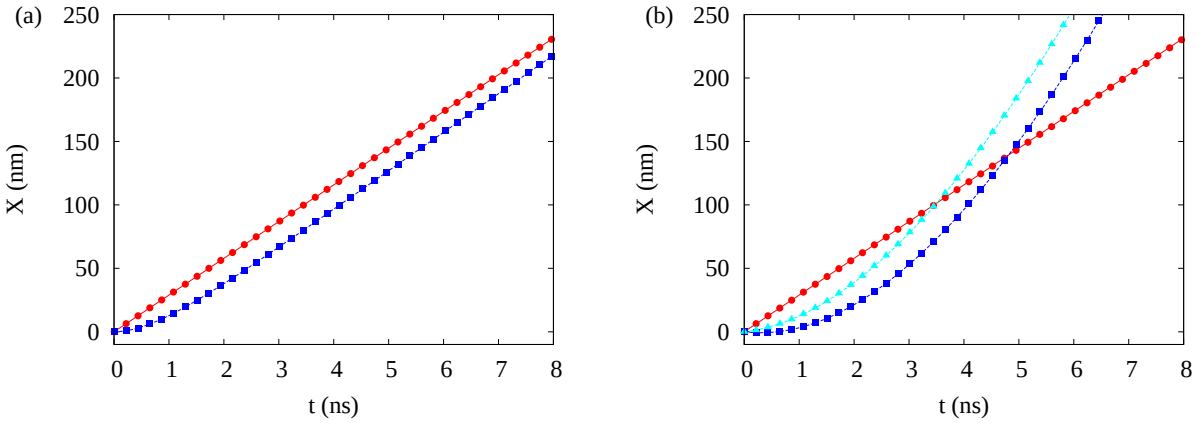

Figure 13.3: Simulated domain-wall positions of (a) a transverse wall in a wire with $w = 120$ nm width and $d = 10$ nm thickness and (b) two vortex walls in a wire with $w = 120$ nm width and $d = 20$ nm thickness. The symbols denote (a) the current-driven positions (discs) and the field-driven positions (squares) of the wall (b) the current-driven positions (discs) and the field-driven positions of the right-handed ($cp = +1$) (squares) and left-handed ($cp = -1$) (triangles) wall. The lines are analytical fits. The simulations start with the wall in its groundstate. Then the current or field is applied instantaneously at time $t = 0$. The position of the transverse wall is defined as the center of the wall. The positions of the vortex walls are defined as the positions of the vortex cores (see appendix C).

Here we can identify an initial velocity $v_i = C_2 H_0 + C_4 j_0$ when the field and current are switched on and a final velocity $v_f = C_1 H_0 + C_3 j_0$ that is reached an infinitely long time later. From the velocity it is possible to derive the position

$$X(t) = \int_0^t dt' \left(v_f \left(1 - e^{-\frac{t'}{\tau_d}} \right) + v_i e^{-\frac{t'}{\tau_d}} \right) = v_f t + (v_f - v_i)\tau_d \left(e^{-\frac{t}{\tau_d}} - 1 \right) \tag{13.56}$$

of the wall for $t > 0$.

Finally, this analytical expression is compared with numerical data. The simulated positions of a tail-to-tail transverse wall and tail-to-tail vortex walls with different handedness are shown in figure 13.3. The simulated wire has a width of $w = 120$ nm. The thickness is $d = 10$ nm for the transverse wall and $d = 20$ nm for the vortex walls. It can be seen that the expression in equation (13.56) fits the numerical data very well for all wall types. In the simulations the spin-polarized current density was $jP = -4 \cdot 10^{11}$ A/m^2. The applied fields were $H = -50$ A/m and $H = -500$ A/m for the transverse and the vortex walls, respectively. The non-adiabaticity parameter and the Gilbert damping are chosen as $\xi = \alpha = 0.01$.

The parameters for the field-driven walls are determined from the fits. For the transverse wall the fit yields the damping time $\tau_d = 0.8$ ns and the final velocity $v_f = 30$ m/s. For the vortex wall one finds $\tau_d = 8.2$ ns, $v_f = 135$ m/s, and $v_i = -5$ m/s for the right-handed ($cp = +1$) and $\tau_d = 8.1$ ns, $v_f = 134$ m/s, and $v_i = 4.8$ m/s for the left-handed ($cp = -1$) wall. Within the uncertainties of the fit both types of vortex walls have the same damping time. In the field-driven case their final velocities are the same and their initial velocities have the same absolute values but different signs. The wall with a right-handed vortex initially moves to the left while the left-handed vortex wall moves to the right. The final motion of both walls is to the right. This difference becomes clear in view of section 12 where it is found that the initial deflection of a field-driven vortex depends on the product cp.

In the current-driven case all initial and final velocities are $v_i = v_f = -b_j j = 29$ m/s as derived in section 3. Since the velocities are the same it is not possible to derive a damping time from this

fit because τ_d vanishes in equation (13.56).

14 Pinned Domain Walls

In section 13 we derived an equation of motion that describes the dynamics of a domain wall in the presence a confining potential E_p. In this section we will use equation (13.47) to describe the experimentally observed dynamics of a pinned domain wall. The results of this section have been published in references [187] and [197].

The experimental data for the dynamics of the pinned domain wall was obtained at an "infinity" shaped permalloy micostructure that is shown in figure 14.1. This structure is the same as the structure that has been discussed for an Antivortex Random Access Memory in section 12. Whether this structure contains an antivortex or a domain wall was found to depend on the lateral dimensions and on the thickness of the sample.[78, 187, 197] While large and thin samples contain a domain wall antivortices are present in smaller and thicker samples. The sample that is discussed here is made of a 20 nm-thick permalloy film and contacted by 20 nm-thick gold contacts. More details on the preparation of the sample can be found in reference [187]. At remanence two magnetic configurations of the sample can be observed. In one configuration, that is shown in figure 14.1(a), the magnetization in both rings curls in the same direction. In the second configuration the curling direction is different as shown in figure 14.1(c). The former configuration contains a domain wall in the center of the structure while the latter configuration has no domain wall. Here we focus on the configuration with a domain wall.

The domain wall is displaced by a current pulse that is injected via the two gold contacts. This current pulse interacts with the magnetization via the spin torque and via the unbalanced Oersted field. After the current is switched off there is no spin torque and Oersted present and the domain wall relaxes to its equilibrium position by a free damped oscillation. The equation of motion in the absence of a current can be derived from equation (13.47). It yields

$$\ddot{Y} = -\left(1 + \frac{\tau_d^2 \alpha^2}{m} \frac{\partial^2 E_p}{\partial Y^2}\right) \frac{\dot{Y}}{\tau_d} - \frac{1}{m'} \frac{\partial E_p}{\partial Y}. \tag{14.1}$$

For the small displacements during the free oscillation of the wall we use the harmonic pinning potential

$$E_p = \frac{m'}{2} \omega_r^2 Y^2. \tag{14.2}$$

where ω_r is the resonance frequency of the potential. With this potential the equation of motion becomes

$$\ddot{Y} = -2\Gamma \dot{Y} - \omega_r^2 Y \tag{14.3}$$

with the damping constant

$$\Gamma = \frac{1 + \frac{\tau_d^2 \alpha^2 \omega_r^2}{1+\alpha^2}}{2\tau_d}. \tag{14.4}$$

The solution of the equation of motion is

$$Y = A e^{-\Gamma(t-t_0)} \cos(\omega(t - t_0)) \tag{14.5}$$

with the free frequency $\omega = \sqrt{\omega_r^2 - \Gamma^2}$. We use this solution to fit the experimentally-obtained domain-wall positions that are shown in figure 14.1(e). The fit parameters are $A = 125$ nm, $t_0 = 1.85$ ns, $\Gamma = 554$ MHz, and $\omega = 3.6$ GHz. From the damping constant and the free frequency the resonance frequency $\omega_r = 3.64$ GHz can be derived. The damping time τ_d can be calculated with the aid of equation (14.4). It is given by

$$\tau_d = \frac{\Gamma(1+\alpha^2)}{\alpha^2 \omega_r^2} - \sqrt{\left(\frac{\Gamma(1+\alpha^2)}{\alpha^2 \omega_r^2}\right)^2 - \frac{1+\alpha^2}{\alpha^2 \omega_r^2}} \approx \frac{1}{2\Gamma} = 0.9 \text{ ns} \tag{14.6}$$

since the Gilbert damping α is smaller than about 0.01 for permalloy.

As shown in figure 14.1(a) the current pulse is injected in the sample so that the electrons move from the upper to the lower contact. For a spin-torque driven domain wall motion we would expect that the domain wall moves initially in the direction of the electron flow, that is downwards. As one can see from figure 14.1(e) the initial motion is upwards. Thus we can conclude that the domain-wall dynamics is mainly driven by the unbalanced Oersted field that accompanies the current. An additional indication that the wall is driven by a magnetic field is that a reversion of the magnetization in the sample reverses the displacement of the domain wall. This is not expected for a spin-torque driven displacement. The equation of motion is thus given by

$$\ddot{Y} = -\frac{\dot{Y}}{\tau_d} - \frac{1}{m'}\frac{\partial E_p}{\partial Y} - \frac{\gamma\lambda}{\alpha}\frac{H_{\text{ext}}}{\tau_d} - \gamma'\lambda\alpha\dot{H}_{\text{ext}} \tag{14.7}$$

using the fact that

$$\frac{\tau_d^2\alpha^2}{m}\frac{\partial^2 E_p}{\partial Y^2} = \tau_d^2\alpha^2\omega_r^2 \ll 1. \tag{14.8}$$

In the absence of a temporally varying external magnetic field equation (14.7) describes a damped harmonic oscillation of the domain wall.

With the knowledge of the pinning potential $E_p(Y)$ the full time evolution of the domain wall position is given by equation (14.7) and the position of the wall can be calculated by a time integration of this equation. The time integration is done numerically using the explicit Euler method and a Gilbert damping of $\alpha = 0.01$. Figure 14.2 shows a comparison between the numerically calculated wall positions and the experimental results for three different pulse lengths. As one can see numerical calculations using the harmonic potential in equation (14.2) and $\mu_0 H_{\text{ext}}\lambda = -6.0 \cdot 10^{-11}$ Tm does not describe the dynamics very well. For a better agreement the pinning potential has to be extended by non-harmonic terms. Since the sample is symmetric the confining potential has to be symmetric as well. Thus the term that is of third order in Y vanishes. The pinning potential expanded up to fourth order in Y thus reads

$$E_p = \frac{m'}{2}\omega_r^2 Y^2 + \frac{m'}{4}kY^4. \tag{14.9}$$

Numerical calculations using this potential, $\mu_0 H_{\text{ext}}\lambda = -7.5 \cdot 10^{-11}$ Tm, and $k = 4.5 \cdot 10^{32}$ $\text{s}^{-2}\text{m}^{-2}$ fit the measurements very well.

The width λ of the domain wall is directly connected to the exchange constant A and the anisotropy K in y direction. The anisotropy can be calculated as

$$K = \frac{A}{\lambda^2}. \tag{14.10}$$

If the anisotropy is given by the dipolar interaction alone, that is no crystalline anisotropy is present, as it is the case for permalloy, the sum of the three anisotropy constants is given by

$$K_x + K_y + K_z = 2K + K_\perp = \frac{1}{2}\mu_0 M_s^2. \tag{14.11}$$

From equations (14.10) and (14.11) we find the perpendicular anisotropy

$$K_\perp = \frac{1}{2}\mu_0 M_s^2 - 2\frac{A}{\lambda^2}. \tag{14.12}$$

Inserting this result in the definition of the damping time

$$\tau_d = \frac{\mu_0 M_s(1+\alpha^2)}{2\gamma K_\perp \alpha} \tag{14.13}$$

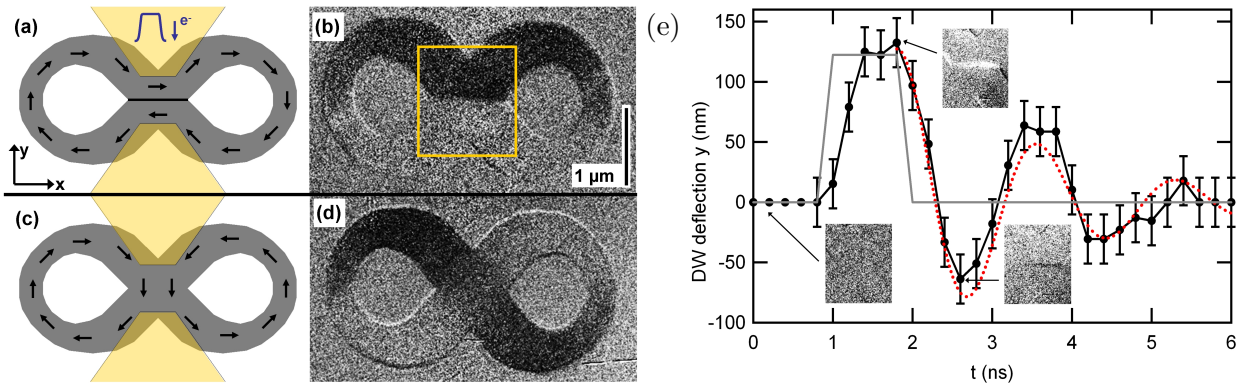

Figure 14.1: [(a) and (c)] Scheme of the experimental sample. The arrows show the magnetization in the infinity structure (gray). The gold areas depict the gold contacts. [(b) and (d)] Corresponding differential X-ray images. (e) Time evolution of the displacement of the domain wall from its equilibrium position. The black line is a guide to the eye while the dotted red curve is a fit using equation (14.5). The gray curve illustrates the current pulse. The insets show the differential X-ray images at different times. Shown is the area that is enclosed by the yellow rectangle in (b). (This figure is a reprint from reference [187].)

we end up with

$$\alpha = \frac{\gamma\tau_d(\mu_0 M_s^2 - 4A/\lambda^2)}{2\mu_0 M_s} - \sqrt{\left(\frac{\gamma\tau_d(\mu_0 M_s^2 - 4A/\lambda^2)}{2\mu_0 M_s}\right)^2 - 1}. \tag{14.14}$$

In addition to the material parameters this equation contains the damping time and the width of the domain wall. While the damping time has been determined from the domain-wall dynamics this is not possible for the domain-wall width. In equation (14.7) the domain-wall width λ occurs only in a product with the magnetic field that is generated by the current. Thus it is only possible to determine this product but it is not possible to determine the Oersted field or the domain-wall width from the dynamics that is driven by a current pulse. However, the wall width can be determined from the static magnetization. A fit of the magnetic contrast shown in figure 14.2(d) with the expression

$$M_x = M_s \cos(\theta) = M_s \tanh\left(\frac{y - Y}{\lambda}\right) \tag{14.15}$$

for the magnetization in x direction yields $\lambda = 24$ nm. With this result equation (14.14) yields a Gilbert damping of $\alpha = 0.007$.

With the knowledge of the Gilbert damping it is possible to calculate the mass of the domain wall. With the aid of equations (13.44) and (13.42) we derive the expression

$$m' = \frac{S\mu_0^2 M_s^2}{\gamma\gamma' K_\perp \lambda} = \frac{2S\mu_0 M_s \alpha \tau_d}{\gamma\lambda} \tag{14.16}$$

for the domain wall mass. With the crossection $S = 2 \cdot 10^{-14}$ m^2 and the damping time $\tau_d = 0.9$ ns from equation (14.6) one finds $m' = 4.8 \cdot 10^{-23}$ kg. Now all parameters of the non-harmonic potential in equation (14.9) are known. The resulting potential is shown in figure 14.2(e).

15 Depinning of Domain Walls

We have seen that in thin nanowires domain walls at low energies behave like quasi particles. These particles can be moved along the wire by an electrical current j or by an external magnetic field

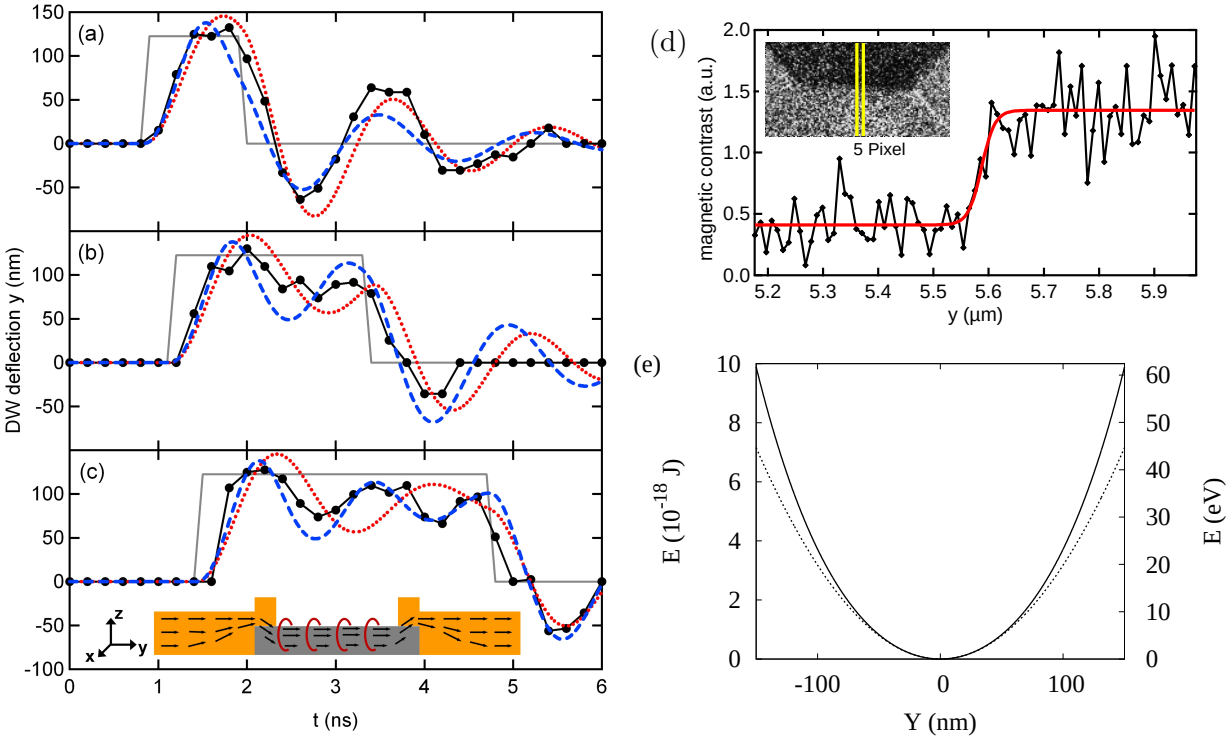

Figure 14.2: [(a)-(c)] Time evolution of the wall displacement for (a) a 1.1 ns (b) a 2.2 ns, and (c) a 3.3 ns current pulse. The black lines are guides to the eye and the gray lines illustrate the current pulse. The dotted red and dashed blue lines are the displacements that are calculated using equation (14.7) with a harmonic and an anharmonic potential, respectively. The inset in (c) illustrates how the unbalanced Oersted field (red) is generated from an inhomogeneous current flow (black arrows) in the sample (gray) due to an overlap of the contacts (gold). (d) The magnetic contrast (black line), that is proportional to the x component of the magnetization, is fitted with the analytic expression in equation (14.15) (red line) to determine the domain wall width. The magnetic contrast is averaged over the area that is depicted in the inset. (e) Harmonic (dashed line) and an anharmonic (solid line) potential of the domain wall that is derived from equation (14.9). (Subfigures (a)-(c) are reprints from reference [187]. Subfigure (d) is a reprint from reference [197].)

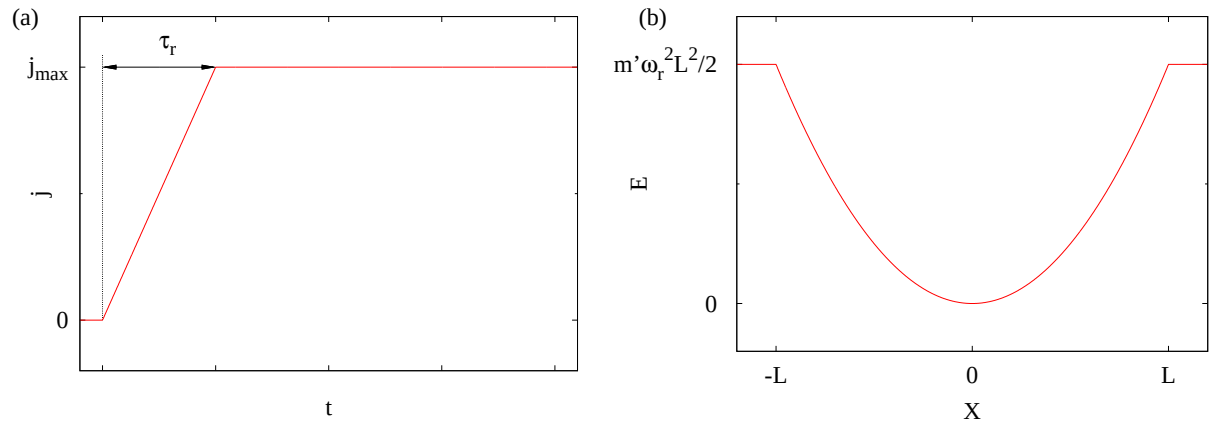

Figure 15.1: (a) Shape of the current pulse that is used for the analytic calculations. During the risetime τ_r the current density increases linearly from zero to the maximum current density $j_{\max}$. After the current density reaches $j_{\max}$ it remains constant. (b) For the investigation of the depinning of the domain wall the parabolic potential is assumed to have a finite length L.

H. In experiments it has been found that due to pinning of the domain wall at random pinning sites in the wire the motion of the wall is stochastic.[172,173] Thus, after the current pulse has been injected into the wire the wall displacement is non-deterministic. This effect can be overcome by periodically adding pinning potentials to the wire, for example notches or constrictions, so that the wall jumps deterministically from pinning center to pinning center. Thus, it is important to investigate the depinning process of a domain wall. Recently it has been shown that the displacement of a domain wall can be supported by special temporal shapes of the current.[105,111,113,174,198] These investigations aim at a resonant excitation of the domain wall. Usually the resonance peak of a domain wall is narrow. Thus, to get a reasonable impact of the resonant excitations it is important to excite the wall close to the resonance frequency. Due to the preparation process this resonance frequency may vary from pinning center to pinning center leading to a complication of simultaneous depinning of walls at different pinning centers.

It has been theoretically found that a fast varying current density exerts a higher force on a domain wall than a constant current density.[129,175] This leads to the assumption that a current pulse with a fast rising edge can also support the depinning of the domain wall, without the knowledge of the resonance frequency. In this section the depinning process of a domain wall is discussed in detail. The results of this section have been published in part in references [199] and [200].

15.1 Analytical Considerations

For primary analytical discussions the pinning potential is approximated by a harmonic potential

$$E_p = \frac{1}{2} m' \omega_r^2 X^2 \tag{15.1}$$

with its resonance frequency ω_r. The applied current pulse needs a rise time τ_r to get to its maximum current density $j_{\max}$. During this risetime the current density is assumed to increase linearly as depicted in figure 15.1(a). During the current pulse the domain wall should move away from the pinning center. Thus, we do not consider the trailing edge of the pulse for the depinning. Instead we shall assume that the current pulse has an infinite length.

Without an applied field the equation of motion of the domain wall becomes

$$\ddot{X}(t) = -\frac{\dot{X}(t)}{\tau_d} - \omega_r^2 X(t) + \frac{C_3}{\tau_d} j(t) + C_4 \dot{j}(t) = -\frac{\dot{X}(t)}{\tau_d} - \omega_r^2 X(t) + \ddot{X}_{\mathrm{sp}}(t). \tag{15.2}$$

with the acceleration

$$\ddot{X}_{\mathrm{sp}}(t) = \begin{cases} \frac{C_3}{\tau_d}\frac{t}{\tau_r} j_{\max} + \frac{C_4}{\tau_r} j_{\max} & 0 < t \leq \tau_r \\ \frac{C_3}{\tau_d} j_{\max} + 0 & t > \tau_r \end{cases} \tag{15.3}$$

due to the spin torque. The first term is due to the current while the second term is due to the time derivative of the current. Both terms are comparable in size when the risetime τ_r is in the order of magnitude of the damping time τ_d.

The solution of equation (15.2) is a linear response to the applied current. For the underdamped case where $2\tau_d\omega_r > 1$ the solution is calculated in equation (E.13) and given by

$$X(t) = \int_{-\infty}^{t} dt'\, e^{-\frac{t-t'}{2\tau_d}} \frac{\sin(\omega(t-t'))}{\omega} \ddot{X}_{\mathrm{sp}}(t) \tag{15.4}$$

with the frequency

$$\omega = \sqrt{\omega_r^2 - \frac{1}{4\tau_d^2}} \tag{15.5}$$

of the free oscillation of the wall. From equation (15.4) it becomes obvious that, beside the dependence on the maximum current density $j_{\max}$, the maximum displacement of the domain wall depends on the ratios of three different timescales, that are the risetime τ_r of the current pulse, the damping time τ_d of the domain wall, and the period $2\pi/\omega$ of free oscillation in the pinning potential.

For an infinitely long risetime the displacement of the domain wall inside the potential well is proportional to the current density. The expression

$$X_\infty(t) = \frac{4\tau_d C_3}{1 + 4\tau_d^2\omega^2} j(t) \tag{15.6}$$

is calculated in appendix E. When the risetime is reduced the domain wall performs an oscillatory motion as shown in figure 15.2. Details of the calculation of the domain wall positions can be found in appendix E. Due to this oscillation the maximum of the domain-wall displacement increases. Here it is worth noting that the final position

$$X(\infty) = \frac{4\tau_d C_3}{1 + 4\tau_d^2\omega^2} j_{\max} \tag{15.7}$$

is always independent of the risetime.

There are two reasons for the oscillation of the wall position. First there is an overshooting due to the rapid changes of the force due to temporal changes of the current density. This overshooting occurs when the time in which the current density changes, that is the risetime, is in the order of magnitude of the damping time. It is illustrated by the solid lines in figure 15.2. The second and more important reason is the non-vanishing force due to the time derivative of the current density. This force is present during the risetime of the current only and does not affect the final position of the wall. However, it can lead to strong displacements in the transient region as depicted by the dashed lines in figure 15.2.

To allow the domain wall to leave the potential we introduce a finite range L of the potential as depicted in figure 15.1(b). An analytical expression of this potential is given by

$$E_p = \begin{cases} \frac{1}{2} m\omega_r^2 X^2 & |X| \leq L \\ \frac{1}{2} m\omega_r^2 L^2 & |X| > L. \end{cases} \tag{15.8}$$

For the infinitely long risetime the domain wall is depinned if its maximum displacement

$$X_{\max}^{\infty} = \frac{4\tau_d C_3 j_{\max}}{1 + 4\tau_d^2\omega^2} \tag{15.9}$$

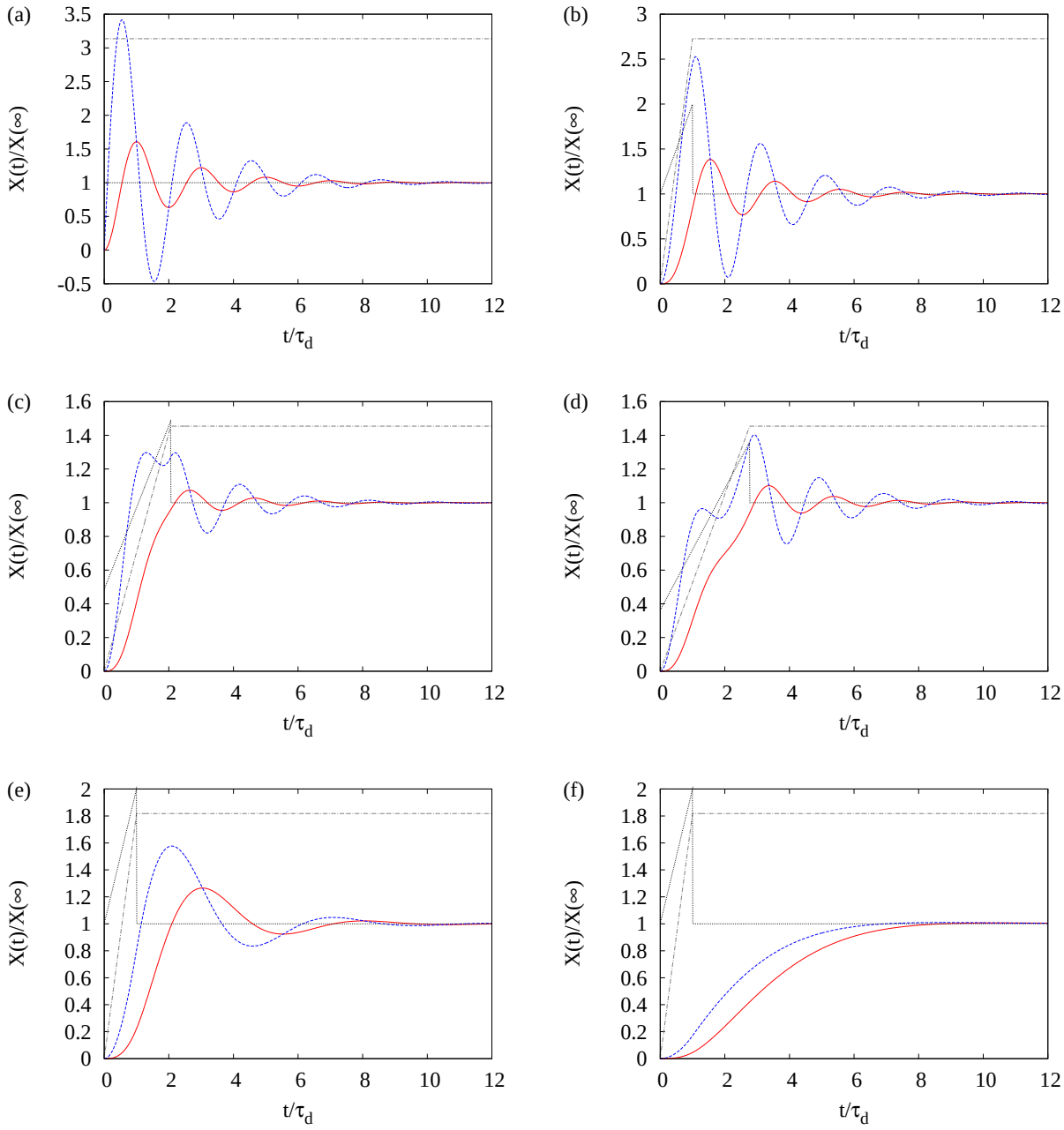

Figure 15.2: Domain wall position versus time. (a)-(d) The oscillation period of the potential is twice the damping time, that is $\omega\tau_d = \pi$. Shown are the positions for risetimes τ_r of (a) 0, (b) τ_d, (c) $2.06\tau_d$, and (d) $2.77\tau_d$. (e) and (f) The risetime is equal to the damping time while the oscillation period of the potential is (e) five times the damping time and (f) twenty times the damping time, that are $\omega\tau_d = 0.4\pi$ and $\omega\tau_d = 0.1\pi$, respectively. In all subfigures the solid red line shows the position of the wall that is calculated by neglecting the force due to the time derivative of the current density ($C_4 = 0$). The dashed blue line represents the position for $C_4 = C_3$ as it is the case for $\xi = \alpha$. For this case the time dependent equilibrium position is given by the dotted black line. The dashed-dotted grey line illustrates the shape of the current pulse. In all cases the final position $X(\infty)$ is the same as for an infinite risetime but it becomes visible that the maximum displacement can be strongly increased by using a shorter risetime of the current pulse.

exceeds the range of the potential. Beyond this point the potential exerts no force on the wall and the force due to the constant part of the current is able to move the wall away from the pinning center. The critical current density for the depinning of the domain wall is thus calculated by setting $|X^{\infty}_{\max}| = L$, which yields the critical current density

$$|j^{\infty}_{\mathrm{crit}}| = \frac{1 + 4\tau_d^2\omega^2}{4\tau_d|C_3|}L. \tag{15.10}$$

For a finite risetime the oscillation holds the possibility that the wall leaves and reenters the potential during the oscillatory motion. In such a case equation (15.4) and its solutions, as calculated in appendix E, are not valid since they are calculated for a potential with an infinite range. Then the position of the wall has to be calculated by a numerical integration of equation (15.2).

Due to the large oscillations one would expect a noticeable reduction of the critical current density for small risetimes. For $C_4 = C_3$ this reduction is depicted in figure 15.3. In this figure we are able to identify three different regimes:

1. For shallow potentials at about $\omega\tau_d < 0.8$ the oscillation period $2\pi/\omega$ is large compared to the damping time τ_d of the wall. Thus we are close to the critically damped system. In this case most of the transient states are damped out before the wall reaches its first reversal point. An according wall motion is depicted in figure 15.2(f).

2. For steeper potentials and short risetimes at about $\tau_r < 1.2\tau_d$ there is a strong force due to the time derivative of the current density that leads to a high acceleration of the wall and thus facilitates the depinning. This additional force is supported by the overshooting that occurs due to the rapid change in the force. According wall motions are depicted in figures 15.2(a) and (b).

3. In the remaining part we find a resonant behavior in which the maximum displacement of the wall depends on the ratio between the risetime of the pulse and the oscillation period of the potential. According wall motions are depicted in figures 15.2(c) and (d).

15.2 Comparison with Experimental Results

There is some experimental work that investigates the influence of the risetime on the domain wall dynamics.[124, 199, 200] In references [199] and [200] the depinning probability of a domain wall from a notch in a magnetic nanowire is measured for different risetimes, yielding a reduction of the current density that is needed to depin the wall. When the wall is driven by a current pulse with an extremely short risetime of about 100 ps, as in reference [124] a more effective domain-wall motion, compared to domain walls driven by a current pulse with a longer risetime, is observed.[98, 103, 124] Here, we shall put our attention on the data of reference [199]. In these experiments the length of the current pulse is not infinite as assumed in the theoretical investigations. Thus the trailing edge of the pulse has to be taken into account. The shape of the experimental current pulse is shown in figure 15.4(a).

For the experiments in reference [199] a curved wire with two electrodes was used. This wire is depicted in figure 15.5. The curvature of the wire is needed to create a domain wall. First a strong field is applied under an angle of $\varphi = 80°$. When this field is switched off the remanent state of the wire contains a wall in the curvature. The configuration of the wall, that is either head-to-head or tail-to-tail, depends on the sign of the field. This wall is then moved to the notch by a small field that is applied along the x direction. After the domain wall gets pinned a constant external field H_x is applied in x direction and a voltage pulse of $V_0 = -1$ V is injected into the wire. This voltage corresponds to a maximum current density of $|j| = 8.5 \cdot 10^{11}$ A/m^2 between the two leads. In the experiment the values of pulse risetime, pulse length, and external magnetic field were varied. Repetitive measurements were performed for each set of parameters to get the depinning

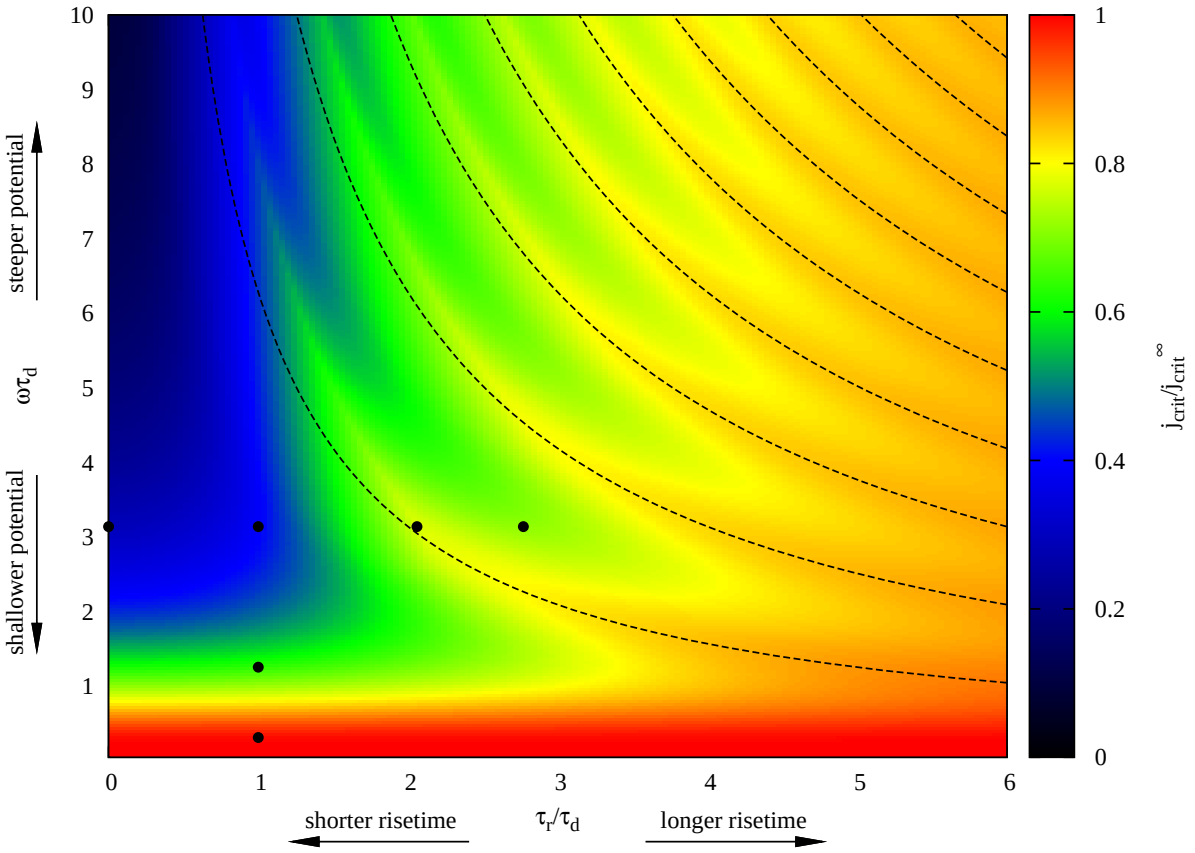

Figure 15.3: Reduction of the critical current density that is needed to depin the domain wall due to a pulse with a short risetime. Shown is the critical current density in units of the critical current density for an infinite risetime. The reduction is shown in dependence of the ratio τ_r/τ_d between the risetime and the damping time and $\omega\tau_d$ that is 2π times the ratio between the damping time and the oscillation period. The dashed black lines denote the positions where the risetime assumes an integer multiple of the oscillation period. The dots represent the parameters that are used in figure 15.2.

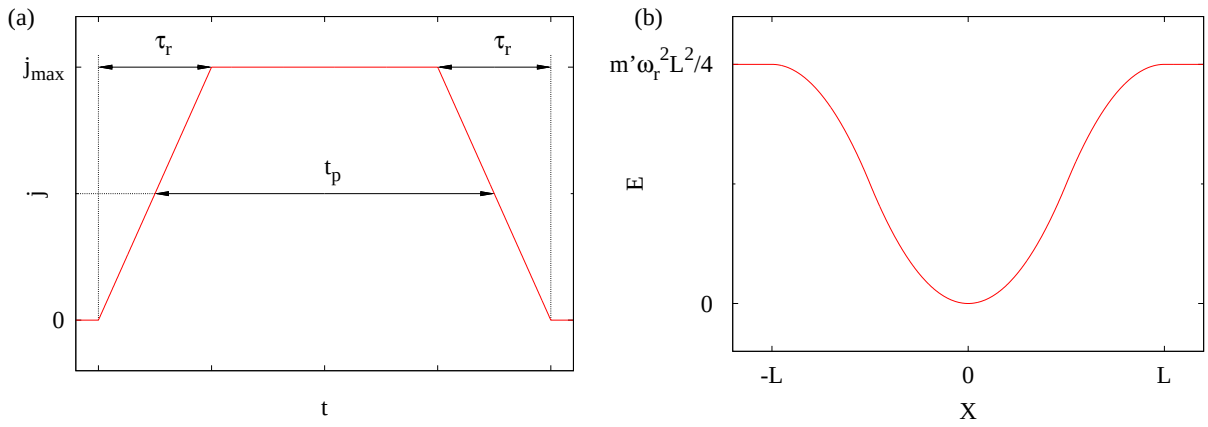

Figure 15.4: (a) Scheme of the current pulse that is used in the experiments. During the risetime τ_r the current density increases linearly from zero to the maximum current density $j_{\max}$. After the current density reaches $j_{\max}$ it remains constant until the length t_p of the pulse has been reached. Then the current density decreases linearly to zero during the time τ_r. (b) For the numerical solution the pinning potential is modeled by a piecewise sequence of quadratic functions as given in equation (15.11). The potential has a finite range L.

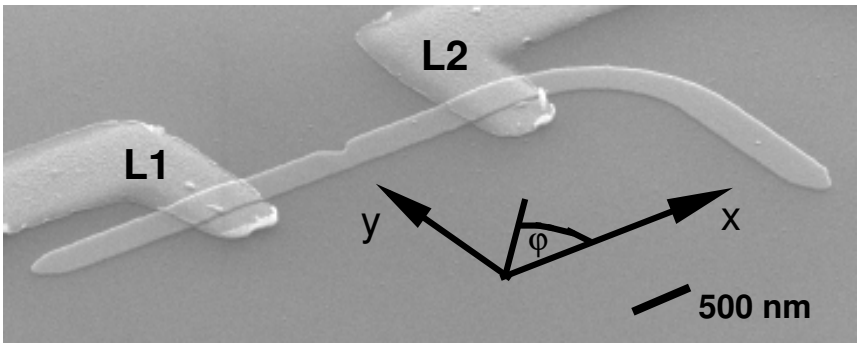

Figure 15.5: Scanning-electron micrograph of the permalloy wire that is used in reference [199]. The wire contains a notch to pin the domain wall. This notch is situated between two leads, that are labeled $L1$ and $L2$ and are used to inject a current pulse into the wire. The curvature allows for the creation of a domain wall in the wire. (This figure is a reprint from reference [199].)

probability of the wall. The results are depicted in figure 15.6. More details on the preparation process and the measurement setup can be found in the aforesaid reference.

In the above theoretical investigations the confining potential is modeled by a harmonic potential with a finite range which facilitates the according considerations. However, this potential is not continuously differentiable and thus the pinning force has a discontinuity. To overcome this deficiency we use the potential

$$E_p = \begin{cases} \frac{1}{2}m'\omega_r^2 X^2 & |X| \leq \frac{L}{2} \\ \frac{1}{4}m'\omega_r^2 L^2 - \frac{1}{2}m\omega_r^2(L-|X|)^2 & \frac{L}{2} < |X| \leq L \\ \frac{1}{4}m'\omega_r^2 L^2 & |X| > L \end{cases} \tag{15.11}$$

to compare the theoretical and experimental results. The new potential is depicted in figure 15.4(b). The action of this potential on the domain wall is described by the range L and the resonance frequency ω_r of the potential. Here, it is worth noting that the shape of the potential is an assumption that is used since the exact shape of the experimental potential is not known. However,

we will see that it is possible to get a good agreement between theory and experiment by using this potential.

The constant magnetic field deforms the pinning potential and thus facilitates the depinning of the wall. Analytically the wall motion is described by the equation

$$\ddot{X}(t) = -\frac{\dot{X}(t)}{\tau_d} - \frac{1}{m'}\frac{dE(X(t))}{dX} + \frac{C_1}{\tau_d}H_x + \frac{C_3}{\tau_d}j(t) + C_4\dot{j}(t), \tag{15.12}$$

where the term $C_2\dot{H}_x$ vanishes since the magnetic field is constant.

When the field is larger than a critical field the wall is depinned even without the injection of a current pulse. This critical field H_c can be found by setting $j \equiv 0$ and $\dot{X} \equiv 0$ in equation (15.12). One derives a critical field of

$$H_c = \frac{\tau_d \omega_r^2 L}{2C_1}. \tag{15.13}$$

For fields H_x that are smaller than this critical value, that is given by $|\mu_0 H_c| = 9$ mT in the considered experiments,[199] the initial position of the domain wall is given by

$$X(0) = \frac{1}{\omega_r^2}\frac{C_1}{\tau_d}H_x = \frac{L}{2}\frac{H_x}{H_c}, \tag{15.14}$$

which is chosen to be inside the pinning potential. When the current is injected the wall starts moving. Its momentary position can be derived by a numerical integration of equation (15.12) with the potential that is given in equation (15.11).

In addition to the uncertainty of the form of the potential we get six parameters that influence the motion of the domain wall. These parameters are the range L and the resonance frequency ω_r of the potential, the damping time τ_d of the wall, and the three remaining prefactors C_1, C_3, and C_4 in equation (15.12). Equation (15.13) allows us to derive C_1 from the experimentally measured value of H_c.

For the remaining parameters we are able to find some estimates. By measuring the depinning probability of a domain wall that is subjected to current pulses of different length Thomas et *al.* found a period of the domain-wall oscillation of about 4 ns which yields a resonance frequency of $\omega = 1.6$ GHz.[105] Even though these experiments are performed with a different geometry we shall assume that our resonance frequency is of the same order of magnitude. The damping time of a vortex domain wall can be estimated from figure 13.3 which yields about 8 ns. For the case $\xi = \alpha$[170,172] the free domain wall does not deform but moves with the velocity $\dot{X}(t) = b_j j(t)$ (see section 3). This is a solution of equation (15.12) for $E \equiv 0$, that is the free wall, and $C_3 = C_4 = b_j$.

Starting from these estimates we are able to find values that deliver a good agreement between theory and experiment. The lines in figure 15.6 are calculated using $L = 2$ μm, $\omega_r = 0.5$ GHz, $\tau_d = 8$ ns, $C_1 = \pm 0.28$ m^2/C and $C_3 = C_4 = -3.62 \cdot 10^{11}$ m^3/C. Here, the positive value of C_1 is used for the head-to-head and the negative value is for the tail-to-tail wall.

16 Interaction of Domain Walls

For a reliable description of the dynamics of a domain wall in an extended wire it is important to take the interaction with other walls into account. These walls can be situated in the same wire or in neighboring wires. If the two interacting domain walls have a sizable distance there is no exchange interaction and the interaction via the demagnetization energy can be expanded in a series of multipoles. For the interaction of two vortex walls it has been shown that the interaction can be well described by an interaction between two monopoles.[201,202] In this section we investigate the interaction of two transverse domain walls. For this investigation we also include the dipole-monopole, dipole-dipole, and quadrupole-monopole interaction.

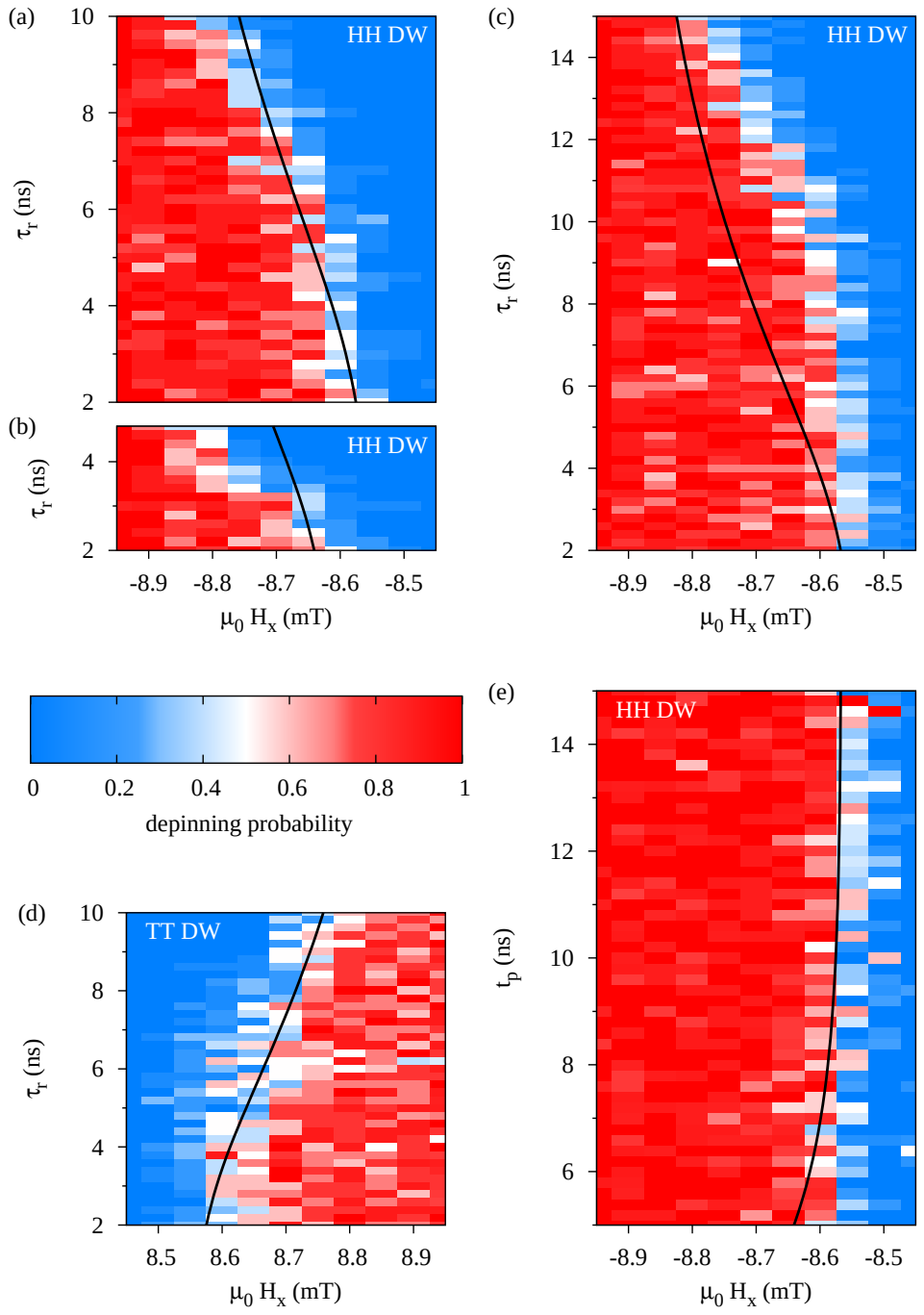

Figure 15.6: Experimentally measured depinning probability of the domain wall (color gradient) compared to the theoretically determined boundary of the depinning (black line). Shown are results for (a) to (c) and (e) a head-to-head domain wall (HH DW) and (d) a tail-to-tail domain wall (TT DW). In (a) to (d) the risetime of the pulse is varied while the pulse length is kept fixed at (b) 5 ns, (a) and (d) 10 ns, and (c) 15 ns. (e) shows results for a fixed risetime of 2 ns. Here the pulse length is changed. (The experimental data is taken from reference [199].)

The demagnetization energy of the whole sample is

$$E_D = \frac{\mu_0}{8\pi} \int \left(dV\ \rho_v(\vec{r}) + dA\ \sigma_s(\vec{r})\right) \int dV' \left(dV'\ \rho_v(\vec{r}') + dA'\ \sigma_s(\vec{r}')\right) \frac{1}{|\vec{r} - \vec{r}'|} \tag{16.1}$$

with the volume charges

$$\rho_v(\vec{r}) = -\vec{\nabla}\vec{M}(\vec{r}) \tag{16.2}$$

and surface charges

$$\sigma_s(\vec{r}) = \vec{M}(\vec{r})\vec{n}(\vec{r}) \tag{16.3}$$

where $\vec{n}(\vec{r})$ is the normal vector at the surface. These charges are depicted in figure 16.1. In the following we neglect all terms that are independent of the distance between the walls. The interaction energy of two walls then yields

$$E = \frac{\mu_0}{4\pi} \int \left(dV_1\ \rho_{v1}(\vec{r}_1) + dA_1\ \sigma_{s1}(\vec{r}_1)\right) \int \left(dV_2\ \rho_{v2}(\vec{r}_2) + dA_2\ \sigma_{s2}(\vec{r}_2)\right) \frac{1}{|\vec{R} + \vec{r}_2 - \vec{r}_1|} \tag{16.4}$$

where $\vec{r}_1$ and $\vec{r}_2$ are the position with respect to the center of the first and second domain wall, respectively. The distance vector $\vec{R}$ points from the center of the first wall to the center of the second wall. V_1 and V_2 are the volumes of the first and second domain wall, respectively. A_1 and A_2 represent the respective surfaces. In the following we assume that both walls are situated in nanowires that are aligned along the x direction. Then equation (16.4) can be written as

$$E = \frac{\mu_0}{4\pi} \int dV\ \rho_1(\vec{r}_1) \int dV'\ \rho_2(\vec{r}_2) \frac{1}{|\vec{R} + \vec{r}_2 - \vec{r}_1|} \tag{16.5}$$

with the charge density

$$\begin{aligned} \rho_i(\vec{r}) = &\frac{a_i M_s}{\lambda_i \cosh^2\left(\frac{x}{\lambda_i}\right)} \Theta\left(\frac{w_i}{2} - |y|\right) \Theta\left(\frac{d_i}{2} - |z|\right) \\ &+ \cos(\chi_i) M_s \frac{\delta\left(y - \frac{w_i}{2}\right) - \delta\left(y + \frac{w_i}{2}\right)}{\cosh\left(\frac{x}{\lambda_i}\right)} \Theta\left(\frac{d_i}{2} - |z|\right) \\ &+ \sin(\chi_i) M_s \frac{\delta\left(z - \frac{d_i}{2}\right) - \delta\left(z + \frac{d_i}{2}\right)}{\cosh\left(\frac{x}{\lambda_i}\right)} \Theta\left(\frac{w_i}{2} - |y|\right) \end{aligned} \tag{16.6}$$

that includes volume and surface charges. Here we used the analytical expressions for the magnetization that are given in equations (5.5) and (5.6). The surface integrals are translated to volume integrals with the aid of a δ-function. $\Theta(x)$ is the Heaviside step function. w_i and d_i denote the width and thickness of the wire in which the i-th domain wall is situated, respectively. The constant a_i and the angle $\chi_i = -a_i\phi_i$ describe the magnetization in the i-th domain wall as depicted in figure 16.2. The term that depends on a_i denotes the volume charges and the terms that depend on χ_i denote the surface charges. For a head-to-head wall the volume charges are positive and $a_i = +1$. For a tail-to-tail wall the volume charges are negative and $a_i = -1$. The angle χ_i describes the location of the surface charges. This location changes when the magnetization in the domain wall rotates around the wire axis.

For $|\vec{r}_1| \ll |\vec{R}|$ and $|\vec{r}_2| \ll |\vec{R}|$ we are able to expand the interaction in equation (16.5) in a

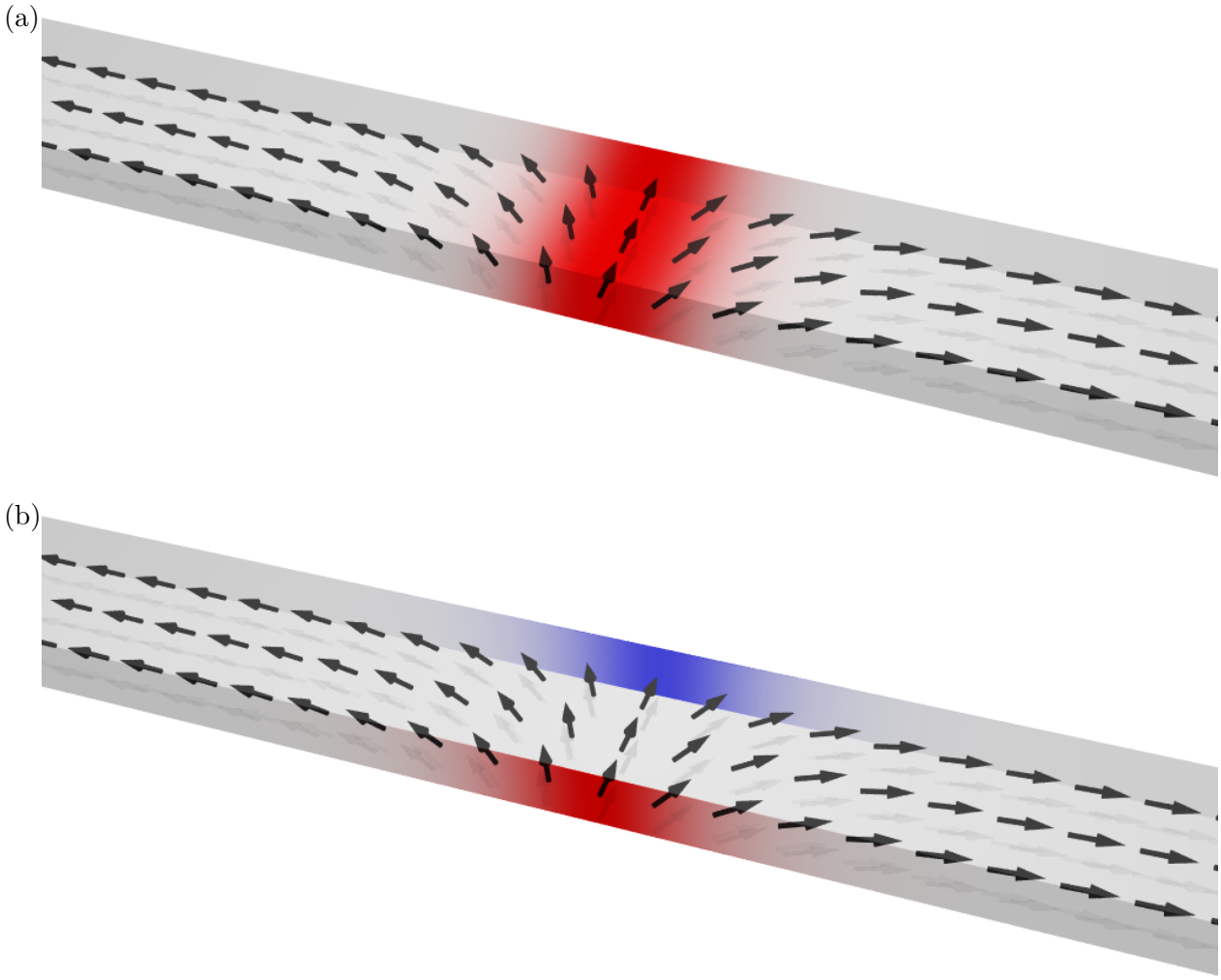

Figure 16.1: Scheme of (a) the volume and (b) the surface charges of a transverse wall in a wire with a rectangular crossection. The charges are given by a color gradient from red (negative charges) to blue (positive charges). The arrows denote the magnetization.

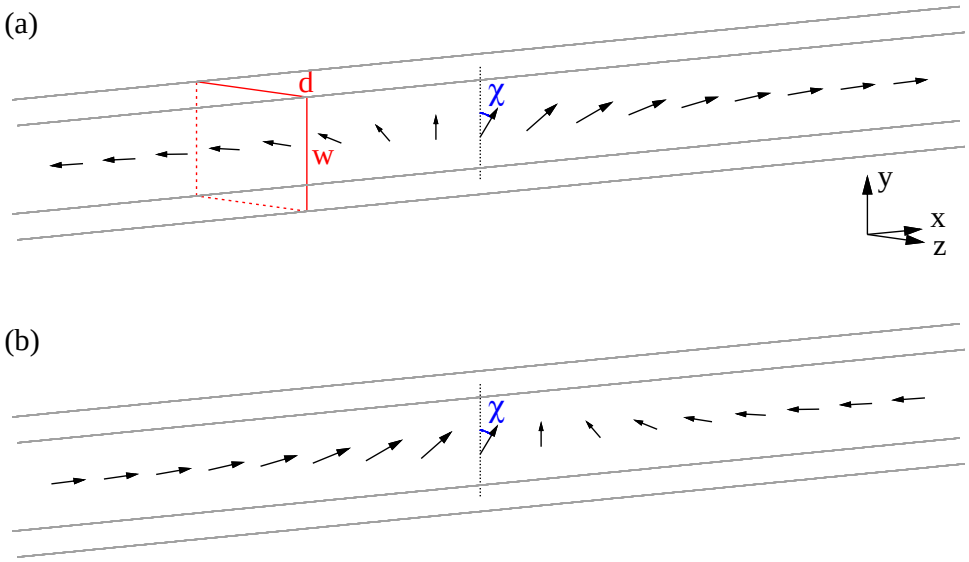

Figure 16.2: Scheme of the magnetization (arrows) of two transverse walls in a nanowire with width w and thickness d. The parameter a, that is the sign of the volume charges of the wall, distinguishes between (a) a tail-to-tail ($a = -1$) and (b) a head-to-head ($a = +1$) domain wall. The orientation of the perpendicular magnetization, that is important for the surface charges of the wall, is given by the angle χ.

series of multipoles. A Taylor series up to second order in $\vec{r}_1$ and $\vec{r}_2$ at $\vec{r}_1 = 0$ and $\vec{r}_2 = 0$ yields

$$
\begin{aligned}
E \approx\ & \frac{\mu_0}{4\pi|\vec{R}|} \underbrace{\int dV\ \rho_1(\vec{r}_1)}_{=q_1} \underbrace{\int dV'\ \rho_2(\vec{r}_2)}_{=q_2} \\
& + \frac{\mu_0}{4\pi|\vec{R}|^3} \underbrace{\int dV\ \vec{r}_1 \rho_1(\vec{r}_1)}_{=p_1} \underbrace{\int dV'\ \rho_2(\vec{r}_2)}_{=q_2} \vec{R} - \frac{\mu_0}{4\pi|\vec{R}|^3} \underbrace{\int dV\ \rho_1(\vec{r}_1)}_{=q_1} \underbrace{\int dV'\ \vec{r}_2 \rho_2(\vec{r}_2)}_{=p_2} \vec{R} \\
& + \frac{\mu_0}{4\pi|\vec{R}|^5} \vec{R} \left(\left(\underbrace{\int dV\ \vec{r}_1 \rho_1(\vec{r}_1)}_{=p_1} \underbrace{\int dV'\ \vec{r}_2 \rho_2(\vec{r}_2)}_{=p_2} \right) \mathbb{1} - 3 \left(\underbrace{\int dV\ \vec{r}_1 \rho_1(\vec{r}_1)}_{=p_1} \right) \otimes \left(\underbrace{\int dV'\ \vec{r}_2 \rho_2(\vec{r}_2)}_{=p_2} \right) \right) \vec{R} \\
& + \frac{\mu_0}{8\pi|\vec{R}|^5} \vec{R} \underbrace{\int dV\ (3\vec{r}_1 \otimes \vec{r}_1 - (\vec{r}_1\vec{r}_1)\mathbb{1})\, \rho_1(\vec{r}_1)}_{=Q_1} \underbrace{\int dV'\ \rho_2(\vec{r}_2)}_{=q_2} \vec{R} \\
& + \frac{\mu_0}{8\pi|\vec{R}|^5} \vec{R} \underbrace{\int dV\ \rho_1(\vec{r}_1)}_{=q_1} \underbrace{\int dV'\ (3\vec{r}_2 \otimes \vec{r}_2 - (\vec{r}_2\vec{r}_2)\mathbb{1})\, \rho_2(\vec{r}_2)}_{=Q_2} \vec{R},
\end{aligned}
\tag{16.7}
$$

where q_i, p_i, and Q_i are the monopole, dipole, and quadrupole moments of the i-th wall, respectively.

All terms in equation (16.6) are symmetric in x direction. The first and third terms are symmetric in y direction while the second term is antisymmetric. The third term is antisymmetric in z. In this direction the first and second terms are symmetric. Due to this symmetry some of the

terms in the multipole moments vanish. The monopole of the i-th wall is

$$q_i = \int d^3\vec{r}\,\rho_i(\vec{r}) = 2M_s a_i S_i. \tag{16.8}$$

Here, $S_i = w_i d_i$ is the crossection of the wire. The dipole and quadrupole moments are given by

$$\vec{p}_i = \int d^3\vec{r} \begin{pmatrix} x \\ y \\ z \end{pmatrix} \rho_i(\vec{r}) = M_s S_i \pi \lambda_i \begin{pmatrix} 0 \\ \cos(\chi_i) \\ \sin(\chi_i) \end{pmatrix} \tag{16.9}$$

and

$$\begin{aligned} Q_i &= \int d^3\vec{r} \begin{pmatrix} 2x^2 - y^2 - z^2 & 3xy & 3xz \\ 3xy & 2y^2 - x^2 - z^2 & 3yz \\ 3xz & 3yz & 2z^2 - x^2 - y^2 \end{pmatrix} \rho_i(\vec{r}) \\ &= M_s \frac{a_i S_i}{6} \begin{pmatrix} 2\pi^2\lambda_i^2 - w_i^2 - d_i^2 & 0 & 0 \\ 0 & 2w_i^2 - \pi^2\lambda_i^2 - d_i^2 & 0 \\ 0 & 0 & 2d_i^2 - \pi^2\lambda_i^2 - w_i^2 \end{pmatrix}. \end{aligned} \tag{16.10}$$

For details on the evaluation of the integrals see appendix F.

With these multipole moments we are able to expand the interaction energy in terms of $1/R$, with $R = |\vec{R}|$, according to the Taylor series in equation (16.7). The first order is given by the interaction between the two monopole terms. The according energy is

$$E_{qq} = \frac{\mu_0}{4\pi R} q_1 q_2 = \frac{\mu_0 M_s^2}{\pi R} a_1 a_2 S_1 S_2. \tag{16.11}$$

The second order is the interaction between the monopole of the first wall with the dipole of the second wall and vice versa. This reads

$$\begin{aligned} E_{pq} &= \frac{\mu_0}{4\pi R^3} \vec{R}\,(\vec{p}_1 q_2 - \vec{p}_2 q_1) \\ &= \frac{\mu_0 M_s^2}{2R^3} S_1 S_2 \left(\lambda_1 a_2 (R_y \cos(\chi_1) + R_z \sin(\chi_1)) - \lambda_2 a_1 (R_y \cos(\chi_2) + R_z \sin(\chi_2))\right). \end{aligned} \tag{16.12}$$

The next order consists of two terms, that are the dipole-dipole and quadrupole-monopole interactions. The dipole-dipole term is

$$\begin{aligned} E_{pp} &= \frac{\mu_0}{4\pi R^5} \left(\vec{p}_1\vec{p}_2 R^2 - 3(\vec{p}_1\vec{R})(\vec{p}_2\vec{R})\right) \\ &= \frac{\mu_0 M_s^2}{4R^5} \pi \lambda_1 \lambda_2 S_1 S_2 R^2 (\cos(\chi_1)\cos(\chi_2) + \sin(\chi_1)\sin(\chi_2)) \\ &- 3\frac{\mu_0 M_s^2}{4R^5} \pi \lambda_1 \lambda_2 S_1 S_2 (R_y \cos(\chi_1) + R_z \sin(\chi_1))(R_y \cos(\chi_2) + R_z \sin(\chi_2)) \\ &= \frac{\mu_0 M_s^2}{4R^5} \pi \lambda_1 \lambda_2 S_1 S_2 (R^2 - 3R_y^2) \cos(\chi_1)\cos(\chi_2) \\ &+ \frac{\mu_0 M_s^2}{4R^5} \pi \lambda_1 \lambda_2 S_1 S_2 (R^2 - 3R_z^2) \sin(\chi_1)\sin(\chi_2) \\ &- 3\frac{\mu_0 M_s^2}{4R^5} \pi \lambda_1 \lambda_2 S_1 S_2 R_y R_z (\cos(\chi_1)\sin(\chi_2) + \sin(\chi_1)\cos(\chi_2)). \end{aligned} \tag{16.13}$$

The energy of the quadrupole-monopole interaction can be calculated as

$$\begin{aligned} E_{Qq} &= \frac{\mu_0}{8\pi R^5} \left(\vec{R} Q_1 \vec{R} q_2 + \vec{R} Q_2 \vec{R} q_1\right) \\ &= \frac{\mu_0 M_s^2}{24\pi R^5} a_1 a_2 S_1 S_2 \left(\left(2\pi^2\lambda_1^2 - w_1^2 - d_1^2\right) R_x^2 + \left(2w_1^2 - \pi^2\lambda_1^2 - d_1^2\right) R_y^2 + \left(2d_1^2 - \pi^2\lambda_1^2 - w_1^2\right) R_z^2\right) \\ &+ \frac{\mu_0 M_s^2}{24\pi R^5} a_1 a_2 S_1 S_2 \left(\left(2\pi^2\lambda_2^2 - w_2^2 - d_2^2\right) R_x^2 + \left(2w_2^2 - \pi^2\lambda_2^2 - d_2^2\right) R_y^2 + \left(2d_2^2 - \pi^2\lambda_2^2 - w_2^2\right) R_z^2\right). \end{aligned} \tag{16.14}$$

In the following we assume for simplicity that both domain walls are in wires that have the same width w and thickness d. Since the width of the wall depends only on material parameters and the crossection of the wire, the width of both walls is the same. Then the energies reduce to

$$E_{qq} = \frac{\mu_0 M_s^2 S^2}{\pi R} a_1 a_2 \tag{16.15}$$

for the monopole-monopole interaction,

$$E_{pq} = \frac{\mu_0 M_s^2 S^2}{2R^3} \lambda a_1 a_2 \left(R_y \left(a_1 \cos(\chi_1) - a_2 \cos(\chi_2) \right) + R_z \left(a_1 \sin(\chi_1) - a_2 \sin(\chi_2) \right) \right) \tag{16.16}$$

for the dipole-monopole interaction,

$$\begin{aligned} E_{pp} = & \frac{\mu_0 M_s^2 S^2}{4R^5} \pi \lambda^2 (R^2 - 3R_y^2) \cos(\chi_1) \cos(\chi_2) \\ & + \frac{\mu_0 M_s^2 S^2}{4R^5} \pi \lambda^2 (R^2 - 3R_z^2) \sin(\chi_1) \sin(\chi_2) \\ & - 3 \frac{\mu_0 M_s^2 S^2}{4R^5} \pi \lambda^2 R_y R_z (\cos(\chi_1) \sin(\chi_2) + \sin(\chi_1) \cos(\chi_2)) \end{aligned} \tag{16.17}$$

for the dipole-dipole interaction, and

$$E_{Qq} = \frac{\mu_0 M_s^2 S^2}{12\pi R^5} \left(\left(2\pi^2 \lambda^2 - w^2 - d^2 \right) R_x^2 + \left(2w^2 - \pi^2 \lambda^2 - d^2 \right) R_y^2 + \left(2d^2 - \pi^2 \lambda^2 - w^2 \right) R_z^2 \right) a_1 a_2 \tag{16.18}$$

for the quadrupole-monopole interaction. The energies in equations (16.15) to (16.18) have to be added to the energy of the wall given in equation (13.35). Thus the interaction has an influence on the domain-wall dynamics given by equations (13.33a) and (13.33b).

The interaction energy should be invariant under a rotation of the sample by 180 degrees around the x axis with a renumbering of the walls and under an inversion of the magnetization. The rotation is equivalent to the substitutions

$$a_1 \to a_2, \;\; a_2 \to a_1, \;\; \chi_1 \to \chi_2 + \pi, \;\; \chi_2 \to \chi_1 + \pi, \;\; \text{and} \;\; R_x \to -R_x$$

here R_y and R_z remain the same because both the rotation and the renumbering changes their sign. The inversion of the magnetization is equivalent to the substitutions

$$a_1 \to -a_1, \;\; a_2 \to -a_2, \;\; \chi_1 \to \chi_1 + \pi, \;\; \text{and} \;\; \chi_2 \to \chi_2 + \pi.$$

Obviously, equations (16.15) to (16.18) are invariant under the above substitutions.

16.1 Domain Walls in the Same Wire

If both domain walls are in the same wire $R_y = R_z = 0$. Thus the dipole-monopole interaction vanishes. The remaining contributions to the interaction energy become

$$E_{qq} = \frac{\mu_0 M_s^2 S^2}{\pi R} a_1 a_2 \tag{16.19}$$

for the monopole-monopole interaction,

$$E_{pp} = \frac{\mu_0 M_s^2 S^2}{4R^3} \pi \lambda^2 \cos(\chi_1 - \chi_2) \tag{16.20}$$

for the dipole-dipole interaction, and

$$E_{Qq} = \frac{\mu_0 M_s^2 S^2}{12\pi R^3} \left(2\pi^2 \lambda^2 - w^2 - d^2 \right) a_1 a_2. \tag{16.21}$$

for the quadrupole-monopole interaction. Thus the interaction energy is

$$E_{\mathrm{WW}} = \frac{\mu_0 M_s^2 S^2 a_1 a_2}{\pi R} \left(1 + \frac{\pi^2 \lambda^2 (2 + 3 a_1 a_2 \cos(\chi_1 - \chi_2)) - w^2 - d^2}{12 R^2} \right) \tag{16.22}$$

where the term in brackets describes the deviation from the pure monopole model.

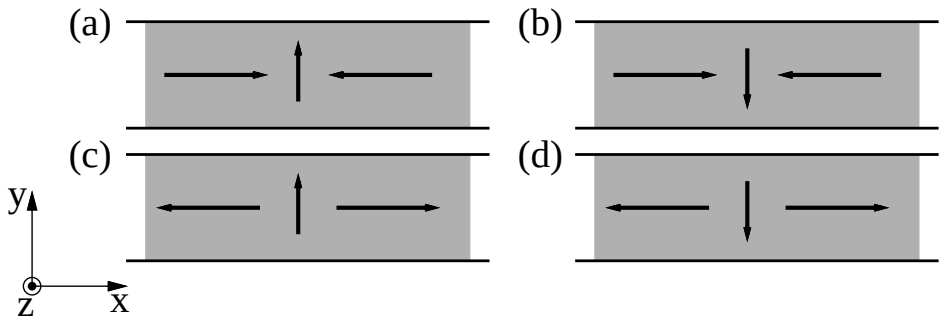

Figure 16.3: Schemes of the four different magnetic configurations of a domain wall with a magnetization that lies in the xy plane. The figure shows domain walls with (a) $a = +1$ and $\cos(\chi) = +1$, (b) $a = +1$ and $\cos(\chi) = -1$, (c) $a = -1$ and $\cos(\chi) = +1$, and (d) $a = -1$ and $\cos(\chi) = -1$.

16.2 Domain Walls in Neighboring Wires

For two domain walls that are located in neighboring wires with distance D in y direction the dipole-monopole interaction is finite. The maximum contribution of the dipole-monopole energy is obtained if $|\cos(\chi_1)| = |\cos(\chi_2)| = 1$. In this case the magnetization of both walls lies in the xy plane as depicted in figure 16.3. The interaction energy of two walls that have the smallest possible distance is calculated by setting $R_x = R_z = 0$ and $R_y = D$ in equations (16.15) to (16.18). With these assumptions for the angles and the distance the energies reduce to

$$E_{qq} = \frac{\mu_0 M_s^2 S^2}{\pi D} a_1 a_2 \tag{16.23}$$

for the monopole-monopole interaction,

$$E_{pq} = \frac{\mu_0 M_s^2 S^2}{2D^2} \lambda a_1 a_2 \left(a_1 c_1 - a_2 c_2\right) \tag{16.24}$$

for the dipole-monopole interaction,

$$E_{pp} = -\frac{\mu_0 M_s^2 S^2}{2D^3} \pi \lambda^2 c_1 c_2 = -\frac{\mu_0 M_s^2 S^2}{2D^3} \pi \lambda^2 a_1 a_2 \left(1 - \frac{\left(a_1 c_1 - a_2 c_2\right)^2}{2}\right) \tag{16.25}$$

for the dipole-dipole interaction, and

$$E_{Qq} = \frac{\mu_0 M_s^2 S^2}{12\pi D^3} \left(2w^2 - \pi^2 \lambda^2 - d^2\right) a_1 a_2 \tag{16.26}$$

for the quadrupole-monopole interaction. Here we used the abbreviations $c_1 = \cos(\chi_1)$ and $c_2 = \cos(\chi_2)$. The interaction energy is given by

$$E_{\mathrm{WW}} = \frac{\mu_0 M_s^2 S^2 a_1 a_2}{\pi D} \left(1 + \frac{\pi \lambda (a_1 c_1 - a_2 c_2)}{2D} + \frac{2w^2 - \pi^2 \lambda^2 \left(7 - 3(a_1 c_1 - a_2 c_2)^2\right) - d^2}{12 D^2}\right). \tag{16.27}$$

The term in brackets describes the deviation from the monopole model. A maximum attractive interaction is found for $a_1 a_2 = -1$ and $a_1 c_1 - a_2 c_2 = +2$. For $a_1 a_2 = -1$ and different values of $a_1 c_1 - a_2 c_2$ the interactions are depicted in figure 16.4.

For a comparison of the analytical expression in equation (16.27) with numerical calculations a system that consist of two parallel wires of length l and distance D is simulated. For these simulations wires with rectangular cross section with $w = 100$ nm and $d = 10$ nm are used. A sketch of the interactions in this system is shown in figure 16.5. The magnetization at the four wire

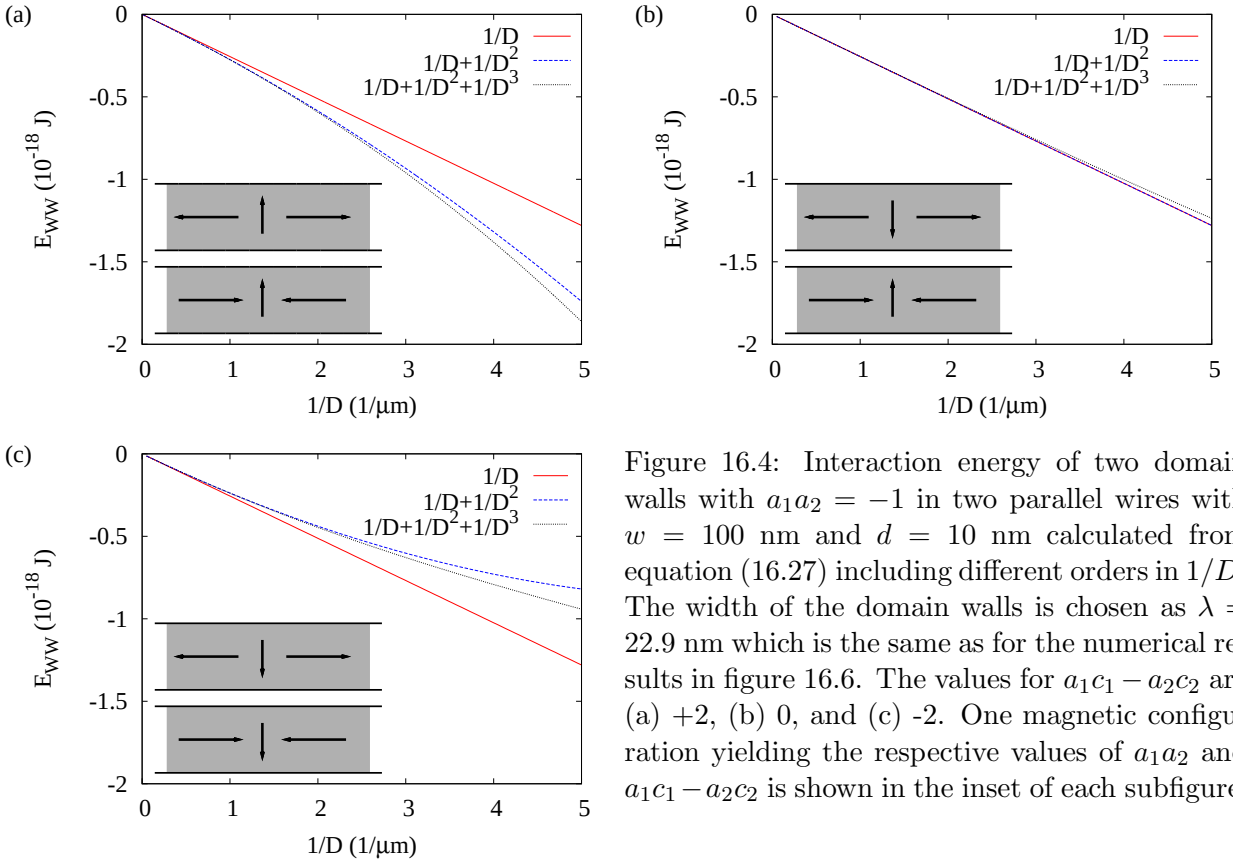

Figure 16.4: Interaction energy of two domain walls with $a_1 a_2 = -1$ in two parallel wires with $w = 100$ nm and $d = 10$ nm calculated from equation (16.27) including different orders in $1/D$. The width of the domain walls is chosen as $\lambda = 22.9$ nm which is the same as for the numerical results in figure 16.6. The values for $a_1 c_1 - a_2 c_2$ are (a) +2, (b) 0, and (c) -2. One magnetic configuration yielding the respective values of $a_1 a_2$ and $a_1 c_1 - a_2 c_2$ is shown in the inset of each subfigure.

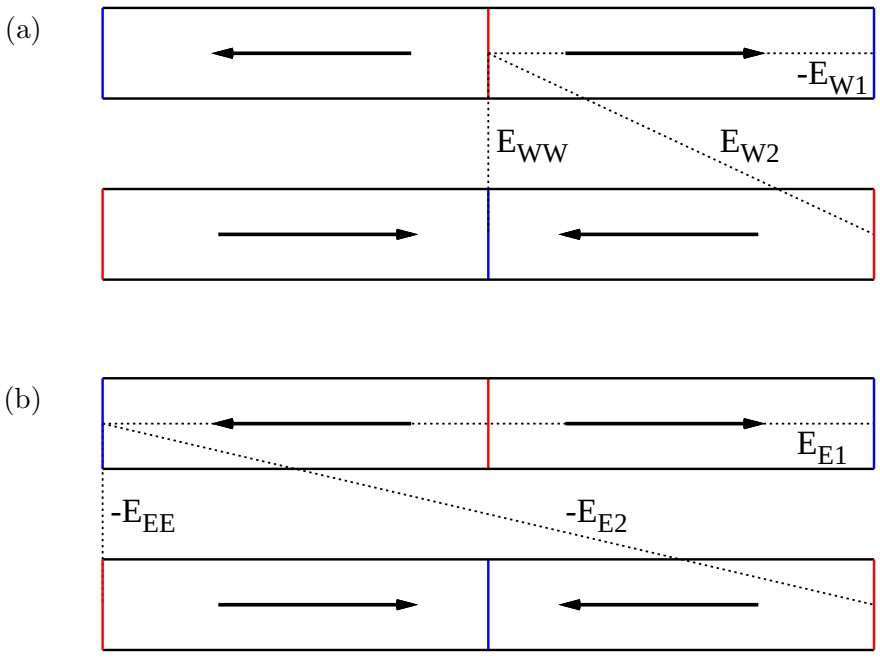

Figure 16.5: Scheme of the different interactions in the two wires. The color denotes positive magnetic charges (blue) and negative magnetic charges (red). The arrows denote the magnetization in the domains. (a) Interactions between the two domain walls and between the domain walls and the ends of the wire. (b) Interactions between the ends of the wires.

ends is kept constant in the direction of the wire. This ensures that no end domains are formed and the energy of the ends of the wire can be calculated analytically.

From the expression calculated in equation (5.5) one finds

$$m_\perp = M_s S \pi \lambda \tag{16.28}$$

for the magnetic moment $m_\perp$ perpendicular to the wire. In turn this allows for a calculation of λ from the numerically obtained value $m_\perp = 5.75 \cdot 10^{-17}$ Am^2. This leads to a width of the domain walls of $\lambda = 22.9$ nm.

The energy of this system is

$$\begin{aligned} E(l,D) = {} & 2E_{\mathrm{W}} + E_{\mathrm{WW}}(a_1, a_2, c_1, c_2, D) - 4E_{\mathrm{W1}}(l) + 4E_{\mathrm{W2}}(a_1 a_2, l, D) \\ & + 4E_{\mathrm{WE}} - 2E_{\mathrm{EE}}(a_1 a_2, D) + 2E_{\mathrm{E1}}(l) - 2E_{\mathrm{E2}}(a_1 a_2, l, D) \end{aligned} \tag{16.29}$$

here E_{W} is the self energy of one domain wall,

$$E_{\mathrm{WE}} = \frac{\mu_0 M_s^2}{8\pi} \int_{-w/2}^{w/2} dy \int_{-d/2}^{d/2} dz \int_{-w/2}^{w/2} dy' \int_{-d/2}^{d/2} dz' \frac{1}{\sqrt{(y-y')^2 + (z-z')^2}} \tag{16.30}$$

is the self energy of one of the four wire ends,

$$E_{\mathrm{EE}} = \frac{\mu_0 M_s^2}{4\pi} \int_{-w/2}^{w/2} dy \int_{-d/2}^{d/2} dz \int_{-w/2}^{w/2} dy' \int_{-d/2}^{d/2} dz' \frac{1}{\sqrt{(D+y-y')^2 + (z-z')^2}} \tag{16.31}$$

is the interaction energy of adjacent ends of different wires, and E_{WW} is the interaction energy between the two domain walls. The remaining terms are the interaction energies as depicted in figure 16.5. The expressions in equations (16.30) and (16.31) can be derived from equation (16.1) bearing in mind that the magnetization at the ends of the wires is kept constant as mentioned above. The integrals have been calculated by A. J. Newell et *al.*[203] Their result yields

$$\begin{aligned} F_{\mathrm{N}}(D) = {} & \int_{-w/2}^{w/2} dy \int_{-d/2}^{d/2} dz \int_{-w/2}^{w/2} dy' \int_{-d/2}^{d/2} dz' \frac{1}{\sqrt{(D+y-y')^2 + (z-z')^2}} \\ = {} & (D+w)d^2 \mathrm{arcsinh}\left(\frac{D+w}{d}\right) + (D-w)d^2 \mathrm{arcsinh}\left(\frac{D-w}{d}\right) - 2Dd^2 \mathrm{arcsinh}\left(\frac{D}{d}\right) \\ & + d(D+w)^2 \mathrm{arcsinh}\left(\frac{d}{|D+w|}\right) + d(D-w)^2 \mathrm{arcsinh}\left(\frac{d}{|D-w|}\right) - 2dD^2 \mathrm{arcsinh}\left(\frac{d}{|D|}\right) \\ & - \frac{\sqrt{(D+w)^2 + d^2}^3 + \sqrt{(D-w)^2 + d^2}^3 - 2\sqrt{D^2 + d^2}^3}{3} + \frac{|D+w|^3 + |D-w|^3 - 2|D|^3}{3}. \end{aligned} \tag{16.32}$$

Beside the sought interaction energy of the two domain walls the simulations also yield some additional energies that are due to a finite distance between the walls and the ends of the wires, a finite distance between two different ends, and the self energy of the ends. The self energy of the four wire ends and the interaction energy of adjacent ends of different wires can be calculated analytically since the magnetization at the ends of the wires is fixed. The remaining energies due to interactions with the ends of the wires decrease for longer wires. For an infinite length these interactions would vanish.

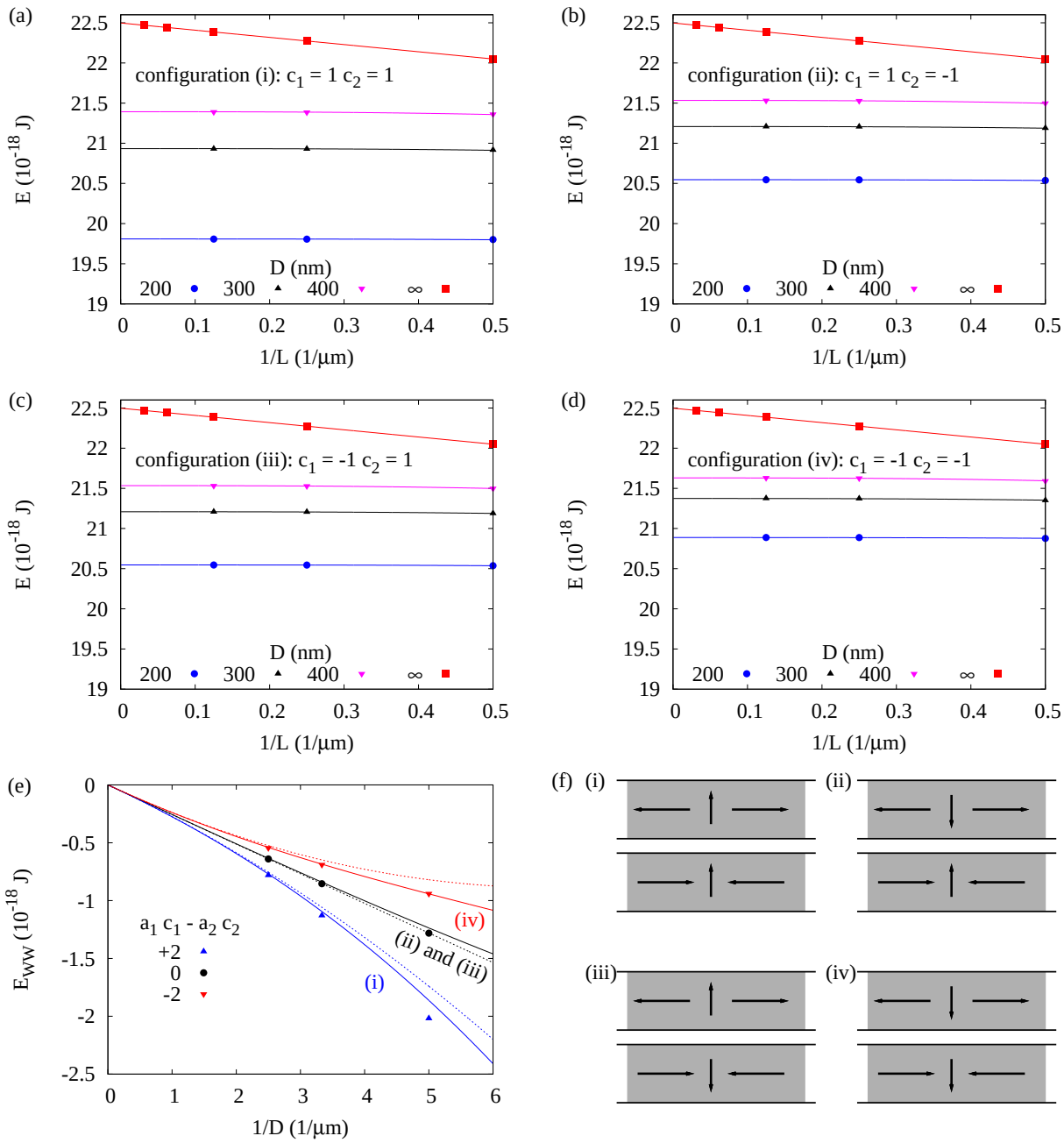

Figure 16.6: (a)-(d) Total energies of the systems shown in (f) as determined from micromagnetic simulations (dots) in dependence of the length L of the wires and their distance D. The lines are fits using equation (16.33). (e) Interaction energy of the two domain walls calculated from the fits of (a)-(d) using equation (16.34). The values found in (b) and (c) (both configurations have $a_1c_1 - a_2c_2 = 0$) are the same within the numerical accuracy. The solid (dashed) lines are the analytical results from equation (16.27) up to third (second) order in $1/D$. Here $w = 100$ nm, $d = 10$ nm, and $\lambda = 22.9$ nm has been used. The roman numbers denote the according magnetization configuration in (f). (f) Scheme of the magnetization of four different domain-wall configurations with attractive interaction.

It is not possible to simulate wires of infinite length. However, we are able to vary the length l while the distance D is kept constant. In the limit of long wires the l dependent energies can be expressed by a monopole-monopole interaction. For $a_1 = +1$, $a_2 = -1$ equation (16.29) becomes

$$\begin{aligned} E(l,D) = 2E_{\mathrm{W}} + E_{\mathrm{WW}}(c_1,c_2,D) - 4\underbrace{\frac{\mu_0 M_s^2 S^2}{\pi l}}_{E_{\mathrm{W1}}} + 4\underbrace{\frac{\mu_0 M_s^2 S^2}{\pi\sqrt{l^2+4D^2}}}_{E_{\mathrm{W2}}} \\ + 4\underbrace{\frac{\mu_0 M_s^2}{8\pi}F_N(0)}_{E_{\mathrm{WE}}} - 2\underbrace{\frac{\mu_0 M_s^2}{4\pi}F_N(D)}_{E_{\mathrm{EE}}} + 2\underbrace{\frac{\mu_0 M_s^2 S^2}{4\pi l}}_{E_{\mathrm{E1}}} - 2\underbrace{\frac{\mu_0 M_s^2 S^2}{4\pi\sqrt{l^2+D^2}}}_{E_{\mathrm{E2}}}. \end{aligned} \tag{16.33}$$

Here, we took into account that the monopoles of the ends of the i-th wire are given by $-M_s S a_i$.

Numerically calculated energies for $a_1 = +1$ and $a_2 = -1$, and different values of c_1, c_2, D, and l are depicted in figure 16.6. The energies are plotted versus the inverse wire length and fitted using equation (16.33) that is valid for long wires. From this fit we get one fit parameter that is given by the energy $E_{\mathrm{fit}}(c_1,c_2,D) = 2E_{\mathrm{W}} + E_{\mathrm{WW}}(c_1,c_2,D)$. For an infinite distance D of the wires the interaction energy E_{WW} certainly vanishes. This yields $E_{\mathrm{fit}}(c_1,c_2,\infty) = 2E_{\mathrm{W}}$. Thus the interaction energy of the domain walls is given by

$$E_{\mathrm{WW}}(c_1,c_2,D) = E_{\mathrm{fit}}(c_1,c_2,D) - E_{\mathrm{fit}}(c_1,c_2,\infty). \tag{16.34}$$

In figure 16.6(e) these energies are compared with the analytical result in equation (16.27) up to different orders in $1/D$. It can be clearly seen that the second order in $1/D$, that is the monopole-dipole interaction is important to reproduce the behavior of the numerical data. The third order in $1/D$ is also found to be not negligible. For the configurations (ii) and (iii) the monopole-dipole interaction vanishes (see equation (16.27)). Thus the respective dashed line in figure 16.6(e) correspond to the value of the monopole-monopole interaction only. The maximum interaction energy is found for $a_1c_1 - a_2c_2 = +2$ as predicted in equation (16.27). The contributions of the three different orders in $1/D$ to the interaction energies are plotted in figure 16.4. The interaction energies shown in figure 16.6(e) are of the same order of magnitude as the pinning potential in figure 14.2(e). This reveals that their interaction may have a sizable impact on the dynamics of the domain walls.

Part IV
Further Investigations and Conclusion

17 Further Investigations

In the subject area of the present work there are several topics that may be appealing for further investigations. Some of them are mentioned below.

Oersted Field

In section 9 it has been shown that the Oersted field that accompanies the current may have a strong impact on the dynamics of the magnetization. Thus it is important to take this field into account. In appendix D it is derived how the Oersted field can be calculated numerically for an arbitrary current density. The resulting convolution has the same runtime complexity as the calculation of the demagnetization field. Here, the next step would be to include the action of the inhomogeneous current that is mediated by the Oersted field.

Current Paths

For the calculation of the magnetization dynamics using equation (3.3) one needs the spatially resolved current density $\vec{j}$. In addition the current paths have a large influence on the aforementioned calculation of the Oersted field. In most parts of this work the current density was assumed to be homogeneous but in experiments there are several reasons that can lead to an inhomogeneous current density. Some of these reasons are discussed in section 9.3. Here, we will sketch how the current density can be calculated from the sample's geometry and its magnetization. Similar considerations can be found in references [144, 204].

For the calculation of the current density one starts from the continuity equation

$$\frac{\partial \rho}{\partial t} = -\vec{\nabla}\vec{j} \tag{17.1}$$

of the charge density. Following Ohm's law one can express the current density

$$\vec{j} = -\sigma\vec{\nabla}\Phi \tag{17.2}$$

by the electric potential Φ using the conductivity tensor σ, that may depend on the magnetization due to the anisotropic magnetoresistance (AMR). We now assume that the relaxation of the current paths happens on a short time scale compared to the dynamics of the magnetization. Then the charge Q in each simulation cell can be assumed to be constant. By inserting equation (17.2) in equation (17.1) and integrating over the volume V of a simulation cell one gets

$$\int dV \vec{\nabla}\sigma\vec{\nabla}\Phi = \int dV \frac{\partial \rho}{\partial t} = \frac{\partial Q}{\partial t} = 0 \tag{17.3}$$

for the stationary current. With the aid of the divergence theorem one finds

$$\int dS\ \vec{n}\sigma\vec{\nabla}\Phi = 0, \tag{17.4}$$

where S is the surface of the cell and $\vec{n}$ is its normal vector.

For the above calculations the conductivity tensor σ is needed. This tensor can be found by inverting the resistivity tensor ρ. Here, it shall be assumed that the resistivity consist of a material dependent isotropic part and an anisotropic part that is given by the AMR. The AMR effect leads to different resistivities for current that flow perpendicular ($\rho_\perp$) or parallel ($\rho_\parallel$) to the magnetization.

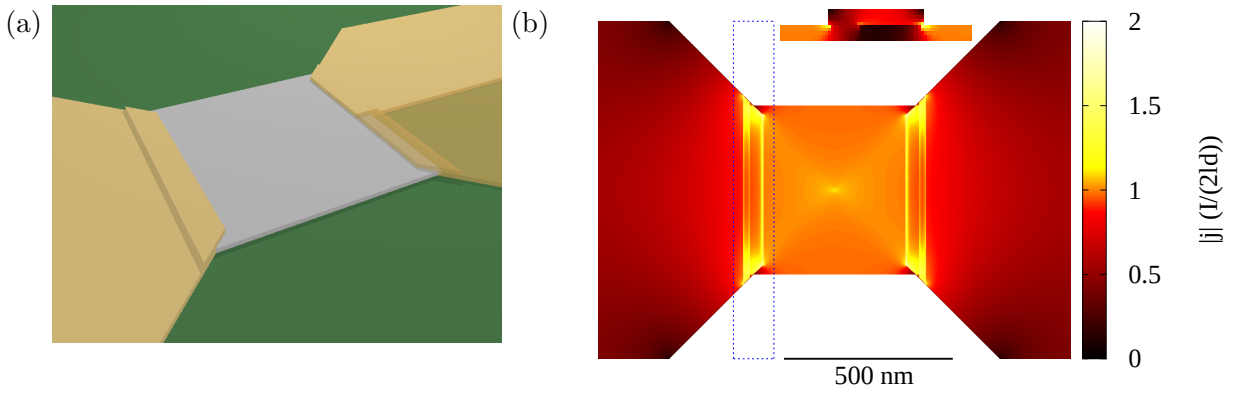

Figure 17.1: (a) Permalloy square and two gold contacts that have a finite overlap with the square. (b) Top view of the system shown in (a). The color denote the current density when a current I flows through the sample. The current density is averaged over the thickness. The inset shows a side view of the region encircled by the dashed blue line. (c) x component of the current density shown in (b).

One finds a resistivity of $\rho_\perp + (\rho_\parallel - \rho_\perp)\cos^2(\angle \vec{j}\vec{M})$ that scales with the square of the cosine of the angle between the current and the magnetization. In vector notation this reads

$$\rho = \rho_\perp \mathbb{1} + (\rho_\parallel - \rho_\perp) P_M \tag{17.5}$$

with the projection operator $P_M = \vec{m} \otimes \vec{m}$. Here, $\vec{m}$ is a unit vector that points in the direction of the magnetization. Taking into account that P_M is idempotent it can easily be verified that the inverse matrix reads

$$\sigma = \frac{1}{\rho_\perp}\mathbb{1} + \left(\frac{1}{\rho_\parallel} - \frac{1}{\rho_\perp}\right) P_M = \sigma_0 \mathbb{1} + \left(\frac{1}{\rho_\parallel} - \frac{1}{\rho_\perp}\right) \begin{pmatrix} m_x^2 - \frac{1}{3} & m_x m_y & m_x m_z \\ m_y m_x & m_y^2 - \frac{1}{3} & m_y m_z \\ m_z m_x & m_z m_y & m_z^2 - \frac{1}{3} \end{pmatrix} \tag{17.6}$$

with $\sigma_0 = (1/\rho_\parallel + 2/\rho_\perp)/3$.

From a discrete version of equation (17.4) where $\nabla\Phi$ is calculated using the potentials Φ at discrete grid points one gets a system of linear equations that allows for the calculation of the potential in each cell. From these potentials it is possible to calculate the current density using equation (17.2). When the system is discretized using a regular grid of cubic cells, as depicted in figure 6.2, there may also be non-conductive cells (see figure 17.1). For these cells equation (17.4) leads to arbitrary potentials. However, these potentials have no influence for the calculation of the current density using equation (17.2). Thus, non-conducting cells can be excluded from the resulting system of linear equations. It is also possible to exclude cells where the potential is given by the Dirichlet boundary conditions.

Figure 17.1 depicts the current density in a permalloy square with edge length $l = 500$ nm and thickness $d = 10$ nm between two gold contacts. The overlap between the contacts and the square is 30 nm. The AMR ratio of permalloy is assumed to be $2(\rho_\parallel - \rho_\perp)/(\rho_\parallel + \rho_\perp) = 5\%$ and the ratio between the specific conductivity of gold and permalloy is set to 8.8:1. The calculated volume of 1600 nm $\times$ 1000 nm $\times$ 20 nm is divided in 4 million cubic cells with an edge length of 2 nm leading to a system of 1.615 million linear equations for the calculation of the potential. Outside this

volume the current is assumed to be homogeneous. The linear system is solved using the iterative αGMRES algorithm, that bases on the generalized minimization of residuals (GMRES), and an SSOR preconditioner.[205–207]

The current density is now inserted in equation (3.3) to calculate the dynamics of the magnetization leading to a self consistent calculation. First self consistent calculations of the magnetization and current for the dynamics of magnetic vortices can be found in references [144, 204]. They showed that there is a sizable influence of the AMR on the current-driven displacement of a magnetic vortex. In these calculations the linear system is solved directly. Iterative methods like the aforementioned GMRES have two advantages. First the iterative solution makes use of the sparsity of the discretized version of equation (17.4). In addition it is possible to start the iteration with the potentials from the last time step. This leads to a drastic speed up of the calculations. This is due to the fact that σ has only a small variation in time and thus the potential for the last timestep yields a good approximation for the current timestep.

Finite Temperatures

The micromagnetic model used in the present work describes the magnetization dynamics at zero temperature. In contrast experimental data is obtained at finite temperatures. In many cases it is needed to take thermal effects into account to allow for a comparison of theoretical and experimental results. A prime example for a thermal effect is the diffuse transition between the two regimes, that are the domain wall is depinned or not depinned, in figure 15.6. From the analytical calculations one finds a sharp transition.

The temperature leads to fluctuations of the magnetic moments. For a sample that has a homogeneous temperature these fluctuations enter the equations of motion of the quasiparticles in two ways. On one hand there is a change of the saturation magnetization that influences parameters like the mass or damping time. On the other hand the quasiparticles perform a Brownian like stochastic motion. This motion is especially important for systems with a positive Lyapunov exponent where a small deviation in the initial conditions can lead to a strong difference in the dynamics. This is for example the case during the depinning of domain walls. Here, the fluctuations can facilitate or impede the depinning of the wall. For systems with a negative Lyapunov exponent, like a vortex that is excited by an alternating field or current, the fluctuations are rapidly damped out and the system returns to its stable trajectory in phase space. Here, the fluctuations are of minor importance compared to the change of the saturation magnetization.

For time dependent currents, like current pulses, the sample is not in thermal equilibrium due to the joule heating. Also for direct currents a temperature gradient may appear in the sample leading to an inhomogeneous resistivity as discussed in section 9.3. To take all three effects into account one needs to calculate the temperature at all positions inside the sample. For this calculation we start from the continuity equation

$$c\rho\frac{\partial T}{\partial t} = -\vec{\nabla}\vec{j}_Q + S \tag{17.7}$$

for the heat. Here, c is the specific heat and ρ is the density of the sample. This equation is similar to equation (17.1) but it contains a source term

$$S = -\vec{j}\vec{\nabla}\Phi = -\vec{\nabla}(\vec{j}\Phi) + \Phi\vec{\nabla}\vec{j} \tag{17.8}$$

that describes the Joule heating. The last term in equation (17.8) is zero since the divergence of the current vanishes. With the heat transfer

$$\vec{j}_Q = -\lambda\vec{\nabla}T, \tag{17.9}$$

with the thermal conductivity λ, equation (17.7) reads

$$c\rho\frac{\partial T}{\partial t} = \vec{\nabla}\lambda\vec{\nabla}T - \vec{\nabla}(\vec{j}\Phi). \tag{17.10}$$

For the static case $\partial T/\partial t = 0$ equation (17.10) has the same form as equation (17.4) and can be solved likewise. In the dynamic case the differential equation can be numerically integrated in time.

In the following we will examine the influence of the changing saturation magnetization on the magnetization dynamics. For this purpose we introduce the temperature dependent parameter $\eta(T) = M_s(T)/M_s(0) \leq 1$ that describes the decreasing saturation magnetization with increasing temperature. A good approximation for η is given by the solution of the equation $\eta = \tanh(\eta T_c/T)$.[208] Here T_c is the Curie temperature of the magnet. We will now investigate how the different quantities entering equation (3.3) scale with η. For this purpose equation (3.3) is written as

$$\begin{aligned}\frac{d(\eta\vec{M})}{d(t/\eta)} =& -\gamma'\eta\vec{M}\times\eta\vec{H}_{\text{eff}} - \frac{\gamma'\alpha}{\eta M_s}\eta\vec{M}\times\left(\eta\vec{M}\times\eta\vec{H}_{\text{eff}}\right)\\ &- \frac{(1+\xi\alpha)\mu_B}{e(1+\alpha^2)(1+\xi^2)(\eta M_s)^3}\eta\vec{M}\times\left(\eta\vec{M}\times(\eta^2P\vec{j}\vec{\nabla})\eta\vec{M}\right)\\ &- \frac{(\xi-\alpha)\mu_B}{e(1+\alpha^2)(1+\xi^2)(\eta M_s)^2}\eta\vec{M}\times(\eta^2P\vec{j}\vec{\nabla})\eta\vec{M}.\end{aligned} \tag{17.11}$$

Using the definition of η we replace $\eta\vec{M}$ by $\vec{M}(T)$ and ηM_s by $M_s(T)$.

In section 2 it has been found that the demagnetization field depends linearly on the magnetization. For the exchange field one finds a linear dependence on the ratio between the exchange constant A and the saturation magnetization. The temperature dependence of A is commonly described by $A(T) \propto M_s^2(T)$ which yields the same decrease for the exchange field as for the demagnetization field. For this reason the fields in equation (17.11) are replaced in the same way as the magnetization, that is $\eta\vec{H}_{\text{eff}}$ becomes $\vec{H}_{\text{eff}}(T)$.

From these considerations one finds that in the absence of a current the right hand side of equation (17.11) becomes independent of η. To get rid of η on the left hand side one needs to replace t/η by $t(T)$. Thus the magnetization needs a longer time to perform the same dynamics. This leads for example to a decrease of the resonance frequency of a magnetic vortex.

With the replacement of the spin-polarized current $\eta^2P\vec{j}$ by $P(T)\vec{j}(T)$ and under the assumption that the temperature dependence of the Gilbert damping parameter and the degree of non-adiabaticity are negligible equation (17.11) becomes independent of η. It then reads

$$\begin{aligned}\frac{d\vec{M}(T)}{dt(T)} =& -\gamma'\vec{M}(T)\times\vec{H}_{\text{eff}}(T) - \frac{\gamma'\alpha}{M_s(T)}\vec{M}(T)\times\left(\vec{M}(T)\times\vec{H}_{\text{eff}}(T)\right)\\ &- \frac{(1+\xi\alpha)\mu_B}{e(1+\alpha^2)(1+\xi^2)M_s^3(T)}\vec{M}(T)\times\left(\vec{M}(T)\times(P(T)\vec{j}(T)\vec{\nabla})\vec{M}(T)\right)\\ &- \frac{(\xi-\alpha)\mu_B}{e(1+\alpha^2)(1+\xi^2)M_s^2(T)}\vec{M}(T)\times(P(T)\vec{j}(T)\vec{\nabla})\vec{M}(T)\end{aligned} \tag{17.12}$$

with the resulting scalings $M_s(T) = \eta M_s(0)$, $\vec{H}_{\text{eff}}(T) = \eta\vec{H}_{\text{eff}}(0)$, $t(T) = t(0)/\eta$, and $P(T)\vec{j}(T) = \eta^2P(0)\vec{j}(0)$.

In reference [209] experimental measurements of vortices excited by alternating magnetic fields are compared with the analytical predictions from section 7. It is found that the experimental data is well described when the above scalings are applied. However, for a description of the depinning of domain walls, that is discussed in section 15, at finite temperatures it is inevitable to include the stochastic motion of the wall. This should for example be possible by describing the domain wall motion using a Fokker-Planck equation.

Non-Linearities

In equation (7.36) it has been assumed that the force due to the confining potential depends linearly on the displacement of the vortex or antivortex core. In equations (13.38a) and (13.38b) the force

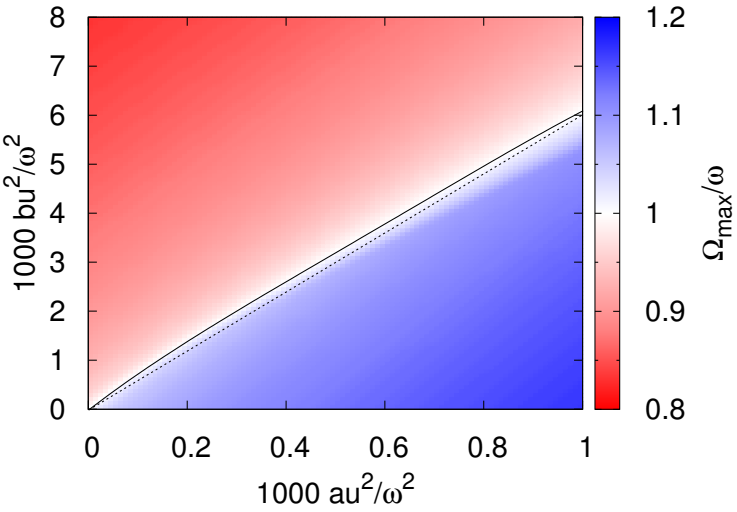

Figure 17.2: Ratio $\Omega_{\max}/\omega$ for which the steady state displacement of the vortex core reaches a maximum. The displacement is calculated by a numerical integration of equation (17.15) with $\Gamma/\omega = 0.02$ and different values of u^2a/ω^2 and u^2b/ω^2. The solid black line illustrate the values of a and b where the resonance is not shifted, that is $\Omega_{\max} = \omega$. A straight line with $b = 6a$ is denoted by the dashed line.

has been linearized with respect to the angle ϕ that describes the rotation of the wall around the wire axis. Both linearizations have been introduced to allow for an analytical solution of the equations of motion. Here the non-linear dynamics of a magnetic vortex will be shortly discussed.

For larger excitations the confining potential for the vortex and for the antivortex can be expanded up to fourth order. It then reads

$$E(X,Y) = m\omega_r^2(X^2+Y^2+a(X^2+Y^2)^2 - bX^2Y^2)/2, \tag{17.13}$$

where a and b describe the strength of the non-linear terms of the force. As the potential changes, the non-linearities influence the displacement of the vortex core in two ways. First the resonant displacement is changed due to a changing slope of the potential. A second and more important influence is the shift of the resonance frequency to lower or higher frequencies compared to the linear case. To calculate this shift one can derive the non-linear equation of motion[210]

$$\begin{pmatrix}\dot X\\ \dot Y\end{pmatrix} = -\Gamma\begin{pmatrix}X+2aX(X^2+Y^2)-bXY^2\\ Y+2aY(X^2+Y^2)-bX^2Y\end{pmatrix} + np\omega\begin{pmatrix}-Y-2aY(X^2+Y^2)+bX^2Y\\ X+2aX(X^2+Y^2)-bXY^2\end{pmatrix} + \begin{pmatrix}u\cos(\Omega t)\\ 0\end{pmatrix} \tag{17.14}$$

from the non-linear energy using equation (7.50). For simplicity we shall assume that there is only an excitation in x direction with a strength that is given by the velocity u. Equation (17.14) can be written in the form

$$\begin{pmatrix}\dot{\hat X}\\ \dot{\hat Y}\end{pmatrix} = -\hat\Gamma\begin{pmatrix}\hat X+2\hat a\hat X(\hat X^2+\hat Y^2)-\hat b\hat X\hat Y^2\\ \hat Y+2\hat a\hat Y(\hat X^2+\hat Y^2)-\hat b\hat X^2\hat Y\end{pmatrix} + np\begin{pmatrix}-\hat Y-2\hat a\hat Y(\hat X^2+\hat Y^2)+b\hat X^2\hat Y\\ \hat X+2\hat a\hat X(\hat X^2+\hat Y^2)-\hat b\hat X\hat Y^2\end{pmatrix} + \begin{pmatrix}\cos(\hat\Omega\hat t)\\ 0\end{pmatrix} \tag{17.15}$$

where the dimensionless positions $\hat X = \omega X/u$ and $\hat Y = \omega Y/u$ and the dimensionless time $\hat t = \omega t$ describe the position in phase space. The trajectory of the vortex core is determined by the four dimensionless parameters $\hat a = u^2a/\omega^2$, $\hat b = u^2b/\omega^2$, $\hat\Gamma = \Gamma/\omega$, and $\hat\Omega = \Omega/\omega$. Equation (17.15) can be integrated numerically. The according shift of the resonance frequency is depicted in figure 17.2 for $\hat\Gamma = 0.02$. This shift is in the order of the width of the resonance peak that is about $2\sqrt{3}\hat\Gamma \approx 0.07$. Thus, to obtain a large displacement of the vortex core the shift of the resonance frequency has to be taken into account.[210]

For constant fields and currents the velocity of a domain wall exhibiting a large angle ϕ has been calculated by Hayashi et al.[170] The limiting case for large excitations has also been derived by Mougin et al.[211] For time dependent excitations the equations of motion have to be solved numerically.

In view of the importance of vortex switching, which happens at large excitations, and fast domain-wall velocities, that coincide with a large angle, for possible future memory devices it is important to investigate the non-linear regimes of vortex and domain-wall dynamics in detail.

Dynamics of Interacting Domain Walls

In section 16 the interaction of domain walls is discussed. The analytical results are compared with static micromagnetic calculations. It has been found that for transverse domain walls the interaction is not negligible since the involved energy scales can have the same order of magnitude as pinning potentials. Transverse walls are present in small wires (see section 5), that are important for memory devices. Thus, a further investigation is needed. Here, the next step is the comparison of the analytical results with micromagnetic simulations of domain-wall dynamics.

18 Conclusion

In the present work the dynamics of the magnetization in micro and nanostructured materials excited by spin-polarized currents or magnetic fields is investigated. These investigations base on the micromagnetic model and include numerical simulations and analytical calculations. The latter base on models where the magnetization is described by a collective coordinates approach. As model systems skyrmions in thin-film elements and domain walls in nanowires are discussed.

The analytical calculations for the skyrmions in thin-film elements base on the Thiele equation that describes the motion of a magnetization pattern. The Thiele equation is valid for a magnetization that is shifted but undergoes no deformation. This equation is expanded to account for the deformation of the magnetization at the boundaries of the sample. From the calculation of the Zeeman energy it is found that in first order only skyrmions with a skyrmion number $n = \pm 1$, that are vortices ($n = 1$) and antivortices ($n = -1$), are excited by an external magnetic field. The spin-polarized current excites all kinds of skyrmion with non-vanishing n via the spin-transfer torque. For a harmonic confining potential an analytical expression for the current- and field-driven trajectory of a vortex or antivortex is derived. For harmonic excitations the vortex or antivortex moves on an elliptical orbit. The ratio between the semiaxes depends on the ratio between the exciting frequency and the resonance frequency of the vortex or antivortex. At resonance the trajectory becomes circular.

The free parameters of the analytical calculations, that are the resonance frequency, the damping constant, and a coupling constant for the non-adiabatic spin-transfer torque, are determined from numerical simulations. The geometry dependence of these parameters meets analytical predictions, that are the resonance frequency scales with the inverse of the lateral extension l of the film and the ratio between damping constant and resonance frequency scales logarithmically with l.

With these parameters it is possible to compare the analytically predicted trajectories with the results of the numerical simulations. Here special attention is put on the amplitude of the gyration and its phase with respect to the excitation. The comparison yields good accordance between the analytical and numerical results.

It is discussed how an inhomogeneous current flow is able to create an unbalanced Oersted field that is also able to excite the vortex or antivortex. A scheme is derived that allows for the numerical calculation of the Oersted field of arbitrary current densities.

For the analytical calculations it is argued that the unbalanced Oersted field has the same effect as a spatially homogeneous external field that lays in the film plane. Thus the analytical expression allows for a determination of the ratio between spin torque and Oersted field driven motion by spotting the phase of the gyration. For a field-driven vortex the phase changes by 180 degrees when the chirality of the vortex is changed. For a current-driven vortex no phase change is predicted. A comparison with measurements on field driven vortex gyrations shows the predicted phase shift. For vortices that are directly traversed by the current the experimental phase shift of 45 degrees reveals that in the experimentally investigated geometry about 30 percent of the force are due to the Oersted field while the remainder is due to the spin-transfer torque.

Basing on the aforementioned results a robust and direct measurement scheme for the non-adiabatic spin torque using the displacement of magnetic vortices is derived. This scheme allows us to distinguish between the displacements of the vortex core due to the non-adiabatic spin torque, the adiabatic spin torque, and the Oersted field, independently of the exact direction of the current flow. The scheme allows for a precise measurement of the non-adiabatic spin-torque parameter ξ that is currently under strong debate.

Beside providing the possibility to experimentally distinguish between the adiabatic spin torque, the non-adiabatic spin torque, and the Oersted field, the presented results allow for the construction of new magnetic memories.

In a vortex random access memory (VRAM) a bit is stored using the handedness of a vortex

in a thin-film element. The vortex is excited by a current that traverses the vortex and by a field that is created by a strip line that is situated below the film. The analytical calculations show that if the current and the field have a collinear alignment and are in phase their combined action on the vortex depends strongly on the handedness of the vortex. For one handedness the vortex exhibits a strong excitation while for the other handedness the actions are opposing each other and the gyration may be completely quenched. This can be used for a handedness dependent switching of the orientation of the vortex core, called polarization. Since the change of the polarization also changes the handedness, this effect allows for writing a single bit. The excitation by collinear currents and magnetic fields can also be used to read out the current state of the memory.

In contrast to the VRAM the antivortex random access memory (AVRAM) contains an antivortex. The utilization of an antivortex allows for a perpendicular alignment of the current and the field. Thus it is possible to use the Oersted field of the current eliminating the need of the strip line.

Both memories have the advantage that they need no reading operation before writing, as it would be the case for vortices that are switched by a current or a magnetic field alone. They also do not require a preceding slow erasing procedure of the present memory state as flash memories.

For the analytical description of the domain wall the Thiele equation is extended in a way that the collective coordinates describing the actual state of the magnetization can be non-spatial coordinates. This equation is then used to derive an equation of motion for a transverse domain wall. From this derivation one finds an analytical expression that connects the properties of the domain-wall quasiparticle, that are the mass and the damping time of the wall, with the microscopic parameters that enter the micromagnetic model.

A comparison with numerical simulations yields that this equation delivers a good description of the field and current-driven dynamics of the wall. Subsequently the equation of motion is extended to Bloch and Néel walls. For vortex walls the equation of motion can be used with effective coefficients that are obtained by fitting results of numerical simulations.

A comparison of the analytically calculated domain-wall dynamics with experiments shows that the equation of motion precisely describes oscillations of the wall in a restoring potential. From the experiment the potential of the confined DW is extracted. For the given experimental geometry, the results allow one to identify the current's Oersted field as the main source of excitation of the magnetization although the current flows directly through the sample. Using the analytical equation it is possible to derive the domain wall mass and the Gilbert damping parameter α from the experiment.

From the analytical calculations it is found that the force on a domain wall depends not only on the current and the magnetic field but also on their time derivatives. This is of special importance for the critical current density that is used to depin a domain wall as these dependencies are independent of the origin of pinning at material defects or artificial pinning sites. This result should allow for efficient displacements of domain walls by fast varying currents. For currents with risetimes that are smaller than the damping time of the wall a strong reduction of the critical current density is predicted. A comparison with experiments reveal that this reduction can indeed be observed.

When the domain walls are close together their interaction becomes important. The dynamics of interacting transverse domain walls can be calculated analytically by adding the interaction energy to the energy that is used in the aforementioned equation of motion of the wall. This interaction energy is calculated making use of a multipole expansion of the interaction energy up to third order. For domain walls that are situated in neighboring wires it is found that the main deficiency of the monopole model is the interaction of the monopole of the wall in the first wire with the dipole of the wall in the second wire and vice versa. The next order are the dipole-dipole and the quadrupole-monopole interactions. These interactions are found to be also of considerable size and non-negligible. If both walls are in the same wire the dipole-monopole interaction vanishes and the

first corrections are the dipole-dipole and the quadrupole-monopole interactions. The interaction energy of two domain walls in parallel wires is compared with micromagnetic simulations and shows a good agreement.

For the vortex or antivortex dynamics and for the domain-wall dynamics the analytical models, that where presented here, have proven to be valuable not only in the interpretation of available experimental or numerical results but also in predictions for new experiments and simulations.

Appendix

A Non-Adiabatic Spin Torque

In this section a microscopic description for the non-adiabatic spin torque will be derived following the calculations of Zhang and Li.[24] This section is taken from reference [196].

For our description we assume that the localized d-electrons and the itinerant s-electrons are coupled via the Heisenberg Hamiltonian

$$H_{\mathrm{sd}} = -J_{\mathrm{ex}}\vec{s}\vec{S} \tag{A.1}$$

where J_{ex} is the coupling constant. $\vec{s}$ and $\vec{S}$ denote the itinerant and localized electrons, respectively. The continuity equation for itinerant spins is

$$\frac{\partial\vec{s}}{\partial t} + \vec{\nabla}\hat{J} = \frac{i}{\hbar}[H_{\mathrm{sd}}, \vec{s}] + \frac{i}{\hbar}[H_{\mathrm{scat}}, \vec{s}] \tag{A.2}$$

with the divergence of the spin current $\vec{\nabla}\hat{J}$, the torque due to the sd-interaction $\frac{i}{\hbar}[H_{\mathrm{sd}}, \vec{s}]$, and the torque due to electron scattering of the itinerant electrons $\frac{i}{\hbar}[H_{\mathrm{scat}}, \vec{s}]$. In a semiclassical approximation we replace the operators with their expectation values. In the limit $\hbar \to 0$ the continuity equation becomes

$$\frac{\partial\langle\vec{s}\rangle}{\partial t} + \langle\vec{\nabla}\hat{J}\rangle = -J_{\mathrm{ex}}\langle\vec{S}\rangle \times \langle\vec{s}\rangle - \Gamma(\vec{s}) \tag{A.3}$$

where $\Gamma(\vec{s})$ expresses the damping of the non-adiabatic electrons. We express the localized spins with their magnetization $\vec{M} = -M_s\langle\vec{S}\rangle/S$ and the itinerant spins with their induced magnetization. The induced magnetization from the moving electrons

$$\vec{m} = \frac{m_0\vec{M}}{M_s} + \vec{\delta m} \tag{A.4}$$

is divided into the equilibrium magnetization m_0 which is parallel to $\vec{M}$ and the non-equilibrium magnetization $\vec{\delta m}$ perpendicular to $\vec{M}$. The damping Γ is assumed to be proportional to the non-equilibrium magnetization. The inverse coefficient τ_{sf} is the average time before a non-equilibrium spin flips. With these expressions the continuity equation becomes

$$\frac{\partial\vec{m}}{\partial t} + \vec{\nabla}J = -\frac{SJ_{\mathrm{ex}}}{M_s}\vec{m} \times \vec{M} - \frac{\vec{\delta m}}{\tau_{\mathrm{sf}}}. \tag{A.5}$$

We assume a linear response of $\vec{\delta m}$ to a change of the magnetization $\vec{M}$. The derivatives of $\vec{\delta m}$ are of second order in the changes of $\vec{M}$ and will be neglected (see reference [24]). Then equation (A.5) leads to

$$\frac{m_0}{M_s}\frac{\partial\vec{M}}{\partial t} - \frac{\mu_B P}{eM_s}(\vec{j}\vec{\nabla})\vec{M} = -\frac{SJ_{\mathrm{ex}}}{M_s}\vec{\delta m} \times \vec{M} - \frac{\vec{\delta m}}{\tau_{\mathrm{sf}}} \tag{A.6}$$

expressing the magnetic current J with the density of the electric current $\vec{j}$. Introducing the exchange relaxation time $\tau_{\mathrm{ex}} = 1/(J_{\mathrm{ex}}S)$ leads to

$$\frac{m_0}{M_s}\frac{\partial\vec{M}}{\partial t} - \frac{\mu_B P}{eM_s}(\vec{j}\vec{\nabla})\vec{M} = -\frac{1}{\tau_{\mathrm{ex}}M_s}\vec{\delta m} \times \vec{M} - \frac{\vec{\delta m}}{\tau_{\mathrm{sf}}}. \tag{A.7}$$

On the left-hand side we recognize two source terms while the right-hand side contains two dissipative terms with different relaxation times. Expressing the spin-flip relaxation time with the exchange relaxation time by introducing the ratio $\xi = \tau_{\mathrm{ex}}/\tau_{\mathrm{sf}}$ we write

$$-\tau_{\mathrm{ex}}\frac{m_0}{\xi M_s}\frac{\partial\vec{M}}{\partial t} + \tau_{\mathrm{ex}}\frac{\mu_B P}{\xi eM_s}(\vec{j}\vec{\nabla})\vec{M} - \frac{1}{\xi M_s}\vec{\delta m} \times \vec{M} = \vec{\delta m}. \tag{A.8}$$

This is an implicit equation in $\delta\vec{m}$. We now use the scheme that has been used to get the explicit equation (1.16). Multiplying both sides in a cross product with $\frac{1}{\xi M_s}\vec{M}$ from the left leads to

$$\tau_{\text{ex}}\frac{m_0}{\xi^2 M_s^2}\frac{\partial\vec{M}}{\partial t}\times\vec{M}-\tau_{\text{ex}}\frac{\mu_B P}{\xi^2 e M_s^2}((\vec{j}\vec{\nabla})\vec{M})\times\vec{M}-\frac{1}{\xi^2}\delta\vec{m}=-\frac{1}{\xi M_s}\delta\vec{m}\times\vec{M} \tag{A.9}$$

because $\delta\vec{m}$ has been defined to be perpendicular to $\vec{M}$. Inserting equation (A.9) in equation (A.8) yields

$$-\tau_{\text{ex}}\frac{m_0}{\xi M_s}\frac{\partial\vec{M}}{\partial t}+\tau_{\text{ex}}\frac{\mu_B P}{\xi e M_s}(\vec{j}\vec{\nabla})\vec{M}+\tau_{\text{ex}}\frac{m_0}{\xi^2 M_s^2}\frac{\partial\vec{M}}{\partial t}\times\vec{M}-\tau_{\text{ex}}\frac{\mu_B P}{\xi^2 e M_s^2}((\vec{j}\vec{\nabla})\vec{M})\times\vec{M}-\frac{1}{\xi^2}\delta\vec{m}=\delta\vec{m} \tag{A.10}$$

where the last term on the left-hand side can be brought to the right-hand side. Dividing by $(1+\xi^2)/\xi^2$ the equation becomes

$$\delta\vec{m}=\frac{\tau_{\text{ex}}}{1+\xi^2}\left(-\frac{\xi m_0}{M_s}\frac{\partial\vec{M}}{\partial t}+\frac{\xi\mu_B P}{eM_s}(\vec{j}\vec{\nabla})\vec{M}-\frac{m_0}{M_s^2}\vec{M}\times\frac{\partial\vec{M}}{\partial t}+\frac{\mu_B P}{eM_s^2}\vec{M}\times(\vec{j}\vec{\nabla})\vec{M}\right) \tag{A.11}$$

which is an explicit equation in $\delta\vec{m}$. From the Hamiltonian in equation (A.1) we derive the additional torque on the magnetization. It is given by

$$T=-\frac{1}{\tau_{\text{ex}}M_S}\vec{M}\times\delta\vec{m}. \tag{A.12}$$

Inserting the result from equation (A.11) the torque reads

$$T=\frac{1}{1+\xi^2}\left(\frac{\xi m_0}{M_s^2}\vec{M}\times\frac{\partial\vec{M}}{\partial t}-\frac{\xi\mu_B P}{eM_s^2}\vec{M}\times(\vec{j}\vec{\nabla})\vec{M}-\frac{m_0}{M_s}\frac{\partial\vec{M}}{\partial t}-\frac{\mu_B P}{eM_s^3}\vec{M}\times(\vec{M}\times(\vec{j}\vec{\nabla})\vec{M})\right). \tag{A.13}$$

Because m_0 is small compared to M_s ($m_0/M_s\approx 0.01$ see reference [24]) we will neglect terms proportional to m_0/M_s. The extended LLG equation then is

$$\frac{d\vec{M}}{dt}=-\gamma\vec{M}\times\left(\vec{H}_{\text{eff}}-\frac{\alpha}{\gamma M_s}\frac{d\vec{M}}{dt}\right)-\frac{\xi b_j}{M_s}\vec{M}\times(\vec{j}\vec{\nabla})\vec{M}-\frac{b_j}{M_s^2}\vec{M}\times(\vec{M}\times(\vec{j}\vec{\nabla})\vec{M}) \tag{A.14}$$

with $b_j=\frac{\mu_B P}{eM_s(1+\xi^2)}$.

B Solving the Equation of Motion of the Vortex

B.1 Variation of Constants Ansatz

In this section we calculate the solution for the differential equation

$$\begin{pmatrix} \dot{X} \\ \dot{Y} \end{pmatrix} = \begin{pmatrix} -\Gamma & -np\omega \\ np\omega & -\Gamma \end{pmatrix} \begin{pmatrix} X \\ Y \end{pmatrix} + \begin{pmatrix} Ae^{i\Omega t} \\ Be^{i\Omega t} \end{pmatrix}. \tag{B.1}$$

To get this solution we follow the variation of constants ansatz. A fundamental system $F(t)$ is a matrix that is chosen so that the homogeneous part of equation (B.1) is solved by

$$\begin{pmatrix} X \\ Y \end{pmatrix} = F(t)\vec{C} \tag{B.2}$$

with a constant vector $\vec{C}$ which depends on the starting conditions. Thus the equation

$$\dot{F}(t)\vec{C} = \begin{pmatrix} -\Gamma & -np\omega \\ np\omega & -\Gamma \end{pmatrix} F(t)\vec{C} \tag{B.3}$$

holds.

To solve the inhomogeneous equation (B.1) the vector $\vec{C}$ is replaced by a vector $\vec{C}(t)$ that depends on time. Inserting this ansatz in equation (B.1) we get

$$\dot{F}(t)\vec{C}(t) + F(t)\dot{\vec{C}}(t) = \begin{pmatrix} -\Gamma & -np\omega \\ np\omega & -\Gamma \end{pmatrix} F(t)\vec{C}(t) + \begin{pmatrix} Ae^{i\Omega t} \\ Be^{i\Omega t} \end{pmatrix}. \tag{B.4}$$

With the aid of equation (B.3) we get

$$F(t)\dot{\vec{C}}(t) = \begin{pmatrix} Ae^{i\Omega t} \\ Be^{i\Omega t} \end{pmatrix} \tag{B.5}$$

which can also be written as

$$\dot{\vec{C}}(t) = F^{-1}(t) \begin{pmatrix} Ae^{i\Omega t} \\ Be^{i\Omega t} \end{pmatrix}. \tag{B.6}$$

This equation can be integrated with respect to time to get the expression

$$\vec{C}(t) = \int_{-\infty}^{t} dt' \; F^{-1}(t') \begin{pmatrix} Ae^{i\Omega t'} \\ Be^{i\Omega t'} \end{pmatrix} \tag{B.7}$$

for $\vec{C}(t)$. This expression is inserted in equation (B.2) to find

$$\begin{pmatrix} X \\ Y \end{pmatrix} = F(t)\vec{C}(t) = F(t) \int_{-\infty}^{t} dt' \; F^{-1}(t') \begin{pmatrix} Ae^{i\Omega t'} \\ Be^{i\Omega t'} \end{pmatrix} \tag{B.8}$$

which solves the inhomogeneous equation (B.1).

B.2 Integration of the Inhomogeneities

A fundamental system of equation (B.1) is

$$F(t) = e^{-\Gamma t} \begin{pmatrix} inpe^{i\omega t} & -inpe^{-i\omega t} \\ e^{i\omega t} & e^{-i\omega t} \end{pmatrix} \tag{B.9}$$

with the inverse system

$$F^{-1}(t) = \frac{e^{\Gamma t}}{2}\begin{pmatrix} -inpe^{-i\omega t} & e^{-i\omega t} \\ inpe^{i\omega t} & e^{i\omega t} \end{pmatrix}. \tag{B.10}$$

With this fundamental system one can calculate the solution of the inhomogeneous equation using equation (B.8). One gets

$$\begin{aligned}
\begin{pmatrix} X \\ Y \end{pmatrix} &= F(t)\int_{-\infty}^{t} dt'\; F^{-1}(t')\begin{pmatrix} Ae^{i\Omega t'} \\ Be^{i\Omega t'} \end{pmatrix} \\
&= e^{-\Gamma t}\begin{pmatrix} inpe^{i\omega t} & -inpe^{-i\omega t} \\ e^{i\omega t} & e^{-i\omega t} \end{pmatrix}\int_{-\infty}^{t} dt'\; \frac{e^{\Gamma t'}}{2}\begin{pmatrix} -inpe^{-i\omega t'} & e^{-i\omega t'} \\ inpe^{i\omega t'} & e^{i\omega t'} \end{pmatrix}\begin{pmatrix} Ae^{i\Omega t'} \\ Be^{i\Omega t'} \end{pmatrix} \\
&= \frac{e^{-\Gamma t}}{2}\begin{pmatrix} inpe^{i\omega t} & -inpe^{-i\omega t} \\ e^{i\omega t} & e^{-i\omega t} \end{pmatrix}\int_{-\infty}^{t} dt'\; \begin{pmatrix} -inpe^{\Gamma t'-i\omega t'} & e^{\Gamma t'-i\omega t'} \\ inpe^{\Gamma t'+i\omega t'} & e^{\Gamma t'+i\omega t'} \end{pmatrix}\begin{pmatrix} Ae^{i\Omega t'} \\ Be^{i\Omega t'} \end{pmatrix} \\
&= \frac{e^{-\Gamma t}}{2}\begin{pmatrix} inpe^{i\omega t} & -inpe^{-i\omega t} \\ e^{i\omega t} & e^{-i\omega t} \end{pmatrix}\int_{-\infty}^{t} dt'\; \begin{pmatrix} -Ainpe^{\Gamma t'+i\Omega t'-i\omega t'} + Be^{\Gamma t'+i\Omega t'-i\omega t'} \\ Ainpe^{\Gamma t'+i\Omega t'+i\omega t'} + Be^{\Gamma t'+i\Omega t'+i\omega t'} \end{pmatrix}.
\end{aligned} \tag{B.11}$$

Carrying out the integration this leads to

$$\begin{pmatrix} X \\ Y \end{pmatrix} = \frac{e^{-\Gamma t}}{2}\begin{pmatrix} inpe^{i\omega t} & -inpe^{-i\omega t} \\ e^{i\omega t} & e^{-i\omega t} \end{pmatrix}\begin{pmatrix} \frac{-Ainpe^{\Gamma t+i\Omega t-i\omega t}+Be^{\Gamma t+i\Omega t-i\omega t}}{\Gamma+i\Omega-i\omega} \\ \frac{Ainpe^{\Gamma t+i\Omega t+i\omega t}+Be^{\Gamma t+i\Omega t+i\omega t}}{\Gamma+i\Omega+i\omega} \end{pmatrix}. \tag{B.12}$$

After evaluating the matrix product this yields

$$\begin{pmatrix} X \\ Y \end{pmatrix} = \frac{e^{-\Gamma t}}{2}\begin{pmatrix} inpe^{i\omega t}\frac{-Ainpe^{\Gamma t+i\Omega t-i\omega t}+Be^{\Gamma t+i\Omega t-i\omega t}}{\Gamma+i\Omega-i\omega} - inpe^{-i\omega t}\frac{Ainpe^{\Gamma t+i\Omega t+i\omega t}+Be^{\Gamma t+i\Omega t+i\omega t}}{\Gamma+i\Omega+i\omega} \\ e^{i\omega t}\frac{-Ainpe^{\Gamma t+i\Omega t-i\omega t}+Be^{\Gamma t+i\Omega t-i\omega t}}{\Gamma+i\Omega-i\omega} + e^{-i\omega t}\frac{Ainpe^{\Gamma t+i\Omega t+i\omega t}+Be^{\Gamma t+i\Omega t+i\omega t}}{\Gamma+i\Omega+i\omega} \end{pmatrix} \tag{B.13}$$

which can be simplified to

$$\begin{pmatrix} X \\ Y \end{pmatrix} = \frac{e^{i\Omega t}}{2}\begin{pmatrix} \frac{A}{\Gamma+i\Omega-i\omega} + \frac{A}{\Gamma+i\Omega+i\omega} + \frac{inpB}{\Gamma+i\Omega-i\omega} + \frac{-inpB}{\Gamma+i\Omega+i\omega} \\ \frac{-inpA}{\Gamma+i\Omega-i\omega} + \frac{inpA}{\Gamma+i\Omega+i\omega} + \frac{B}{\Gamma+i\Omega-i\omega} + \frac{B}{\Gamma+i\Omega+i\omega} \end{pmatrix}. \tag{B.14}$$

Writing the common denominator in front of the vector yields the form

$$\begin{pmatrix} X \\ Y \end{pmatrix} = \frac{e^{i\Omega t}}{\omega^2 + (i\Omega+\Gamma)^2}\begin{pmatrix} A(i\Omega+\Gamma) - Bnp\omega \\ Anp\omega + B(i\Omega+\Gamma) \end{pmatrix} \tag{B.15}$$

of the solution of equation (B.1).

C Determination of the Position of the Vortex Core

In the micromagnetic simulations of the vortex dynamics the position of the vortex core is defined as the position of the maximum out-of-plane magnetization. In these simulations a grid with a finite cell size is used. For the raw data the resolution for the maximum out-of-plane magnetization is given by the cell size of the simulation. This cell size is normally in the order of magnitude of some nanometer. The resolution for the position of the vortex core can be enhanced by interpolating the out-of-plane magnetization in the vortex core. There are different analytical approximations for the shape of the vortex core. Each of these approximations has its assets and its drawbacks.[70,184,212] Most of these functions do not fit the vortex well enough for our purpose. Their benefit is that they may give insight into the dependences of the shape of the vortex core on the geometry and the micromagnetic parameters of the sample. Here, we do not aim an analytical understanding. Thus, we use two functions that fit the center of the vortex core well but are not physically motivated. Since the vortex core is rotational symmetric we need a function of the form $f(r)$ where r is the distance from the center of the vortex core. In the following it will be discussed how to find the x position of the maximum out-of-plane magnetization. The y position can be found likewise. For the fit we will use the magnetization at the cell with the maximum value and its next neighbors. In the following calculations we define the center of the coordinate system to be at the cell with the maximum out-of-plane magnetization. Their next neighbors are at the positions $(\pm\Delta x, 0)$ where Δx is the cell size in x direction. Here the absolute values of the out-of-plane magnetizations are denoted by m_l, m_0, and m_r for the left neighbor, center, and right neighbor, respectively. With the center of the vortex core at (x_0, y_0) the magnetization at the three cells has to be fitted with the function $f((x-x_0)^2+y_0^2)$. Having a closer look at the out-of-plane magnetization in figure C.1 one finds that there are at least two promising functions for the interpolation. One function is a polynomial of second order, that is $1-pr^2$, and the other is a Gaussian function, that is e^{-gr^2}. Both functions deviate by terms that are of fourth and higher orders in r. The parameters p and g are determined from the fit.

C.1 Polynomial of Second Order

The polynomial of second order can be written as

$$1 - p\left((x-x_0)^2 + y_0^2\right) = (-p)x^2 + (2px_0)x + (1 - px_0^2 - py_0^2). \tag{C.1}$$

It is given by the Lagrange polynomial

$$\frac{x(x-\Delta x)}{2\Delta x^2}m_l - \frac{(x+\Delta x)(x-\Delta x)}{\Delta x^2}m_0 + \frac{x(x+\Delta x)}{2\Delta x^2}m_r = \underbrace{\frac{m_l - 2m_0 + m_r}{2\Delta x^2}}_{=-p}x^2 + \underbrace{\frac{m_r - m_l}{2\Delta x}}_{=2px_0}x + m_0. \tag{C.2}$$

From this we can calculate the position of the maximum out-of-plane magnetization

$$x_{\max} = x_0 = -\frac{1}{2}\frac{2px_0}{-p} = \frac{\Delta x}{2}\frac{m_l - m_r}{m_l - 2m_0 + m_r}. \tag{C.3}$$

C.2 Gaussian

The Gaussian function can be written as

$$e^{-g[(x-x_0)^2+y_0^2]} = e^{-gy_0^2}e^{-g(x-x_0)^2}. \tag{C.4}$$

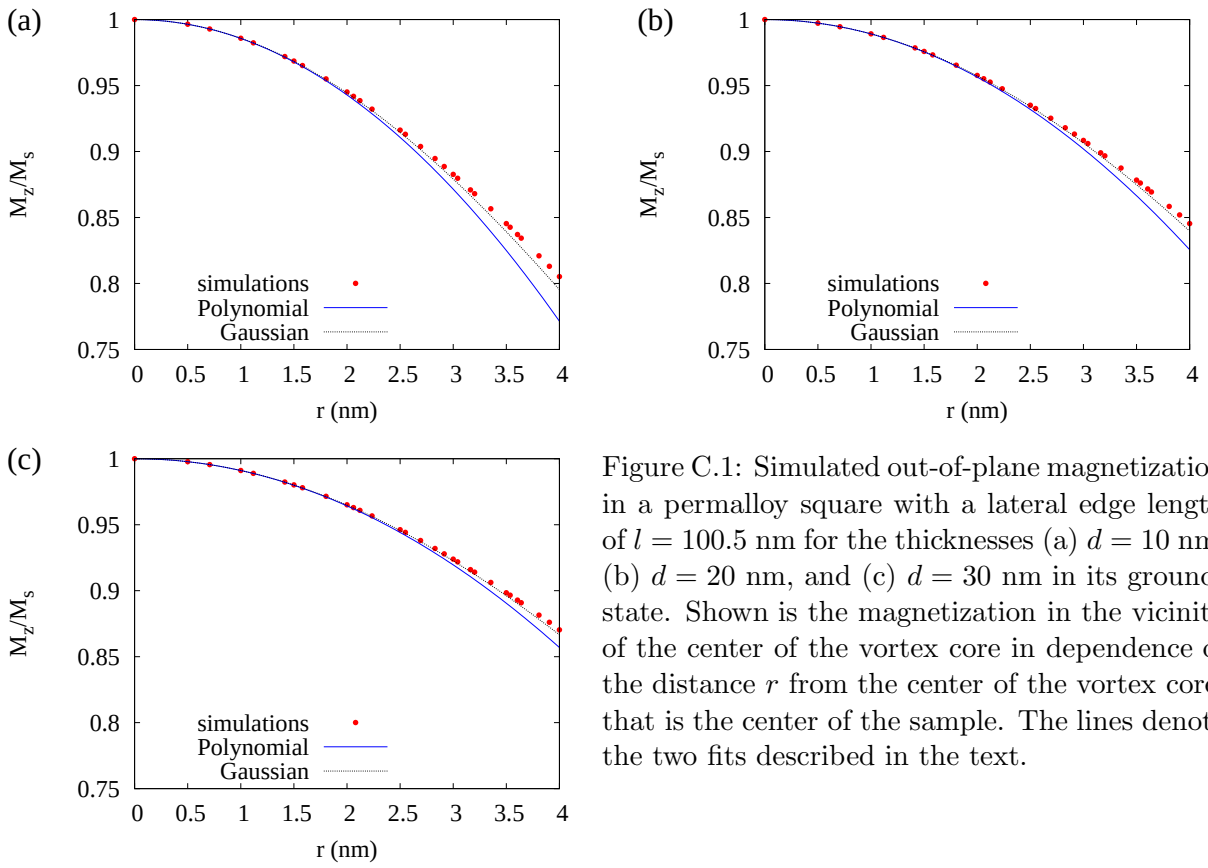

Figure C.1: Simulated out-of-plane magnetization in a permalloy square with a lateral edge length of $l = 100.5$ nm for the thicknesses (a) $d = 10$ nm, (b) $d = 20$ nm, and (c) $d = 30$ nm in its ground-state. Shown is the magnetization in the vicinity of the center of the vortex core in dependence of the distance r from the center of the vortex core, that is the center of the sample. The lines denote the two fits described in the text.

To calculate the parameter x_0 we evaluate the Gaussian at the three given points, that are the three cells, and get

$$e^{-gy_0^2}e^{-gx_0^2} = m_0 \tag{C.5a}$$
$$e^{-gy_0^2}e^{-g(\Delta x+x_0)^2} = m_l \tag{C.5b}$$
$$e^{-gy_0^2}e^{-g(\Delta x-x_0)^2} = m_r. \tag{C.5c}$$

This can be transformed to

$$-gx_0^2 = \ln(m_0) + gy_0^2 \tag{C.6a}$$
$$-g(\Delta x + x_0)^2 = \ln(m_l) + gy_0^2 \tag{C.6b}$$
$$-g(\Delta x - x_0)^2 = \ln(m_r) + gy_0^2. \tag{C.6c}$$

The parameter y_0 is eliminated by subtracting equation (C.6a) from equations (C.6b) and (C.6c). This yields

$$-g\Delta x^2 - 2g\Delta x x_0 = \ln\left(\frac{m_l}{m_0}\right) \tag{C.7a}$$
$$-g\Delta x^2 + 2g\Delta x x_0 = \ln\left(\frac{m_r}{m_0}\right). \tag{C.7b}$$

From the sum and difference of both equations we get

$$-2g\Delta x^2 = \ln\left(\frac{m_l m_r}{m_0^2}\right) \tag{C.8a}$$
$$-4g\Delta x x_0 = \ln\left(\frac{m_l}{m_r}\right). \tag{C.8b}$$

By dividing equation (C.8b) by equation (C.8a) we get

$$x_{\max} = x_0 = \frac{\Delta x}{2} \frac{\ln(m_l) - \ln(m_r)}{\ln(m_l) - 2\ln(m_0) + \ln(m_r)}. \tag{C.9}$$

Equation (C.9) and equation (C.3) differ only by the logarithmic functions. In the center of the vortex core the out-of-plane magnetization is close to one. Equation (C.9) can thus be rewritten as

$$x_{\max} = \frac{\Delta x}{2} \frac{\ln[1 + (m_l - 1)] - \ln[1 + (m_r - 1)]}{\ln[1 + (m_l - 1)] - 2\ln[1 + (m_0 - 1)] + \ln[1 + (m_r - 1)]} \approx \frac{\Delta x}{2} \frac{m_l - m_r}{m_l - 2m_0 + m_r} \tag{C.10}$$

since $\ln(1 + x) \approx x$ for $|x| \ll 1$. The resulting expression is identical to equation (C.3).

C.3 Accuracy

The above expressions for the position of the vortex core are exact if the out-of-plane magnetization follows exactly $f(r)$. As one can see from figure C.1 for larger r there are small deviations between the magnetization and the fit leading to uncertainties in the position of the core. An estimate for these uncertainties can be found by comparing the positions given in equation (C.3) and equation (C.9). Tests with material parameters of permalloy showed that the difference between the core positions determined from the Polynomial and the Gaussian fit depend on the size of the simulation cells. For 2 nm cell size, that is the size that is mostly used in the present work, the difference is about one hundredth of a nanometer. This value increases to about one tenth of a nanometer for 4 nm cell size.

D Integral of the Oersted Field

In section 9 we calculate the influence of an Oersted field. For these calculations we need to calculate the integral

$$I(x,y,z,l_x,l_y,l_z) = \int_{-l_x/2-x}^{l_x/2-x} dx' \int_{-l_y/2-y}^{l_y/2-y} dy' \int_{-l_z/2-z}^{l_z/2-z} dz' \, \frac{z'}{\sqrt{x'^2+y'^2+z'^2}^3}. \tag{D.1}$$

During the calculation of this integral we are faced with the problem that the integral of $1/\sqrt{x^2+y^2+z^2}$ with respect to x has the two different branches $\ln(\sqrt{x^2+y^2+z^2}+x)$ and $-\ln(\sqrt{x^2+y^2+z^2}-x)$ for $x>0$ and $x<0$, respectively.[203] To avoid any problems we ensure that all integrands are positive when the field is calculated inside the sample. The integral can be written as a sum of eight integrals of the form

$$\int_0^a dx' \int_0^b dy' \int_0^c dz' \, \frac{z'}{\sqrt{x'^2+y'^2+z'^2}^3}. \tag{D.2}$$

Splitting the integral in equation (D.1) in one integral for each octant one finds

$$\begin{aligned}
&I(x,y,z,l_x,l_y,l_z)\\
&= \int_0^{l_x/2-x}\int_0^{l_y/2-y}\int_0^{l_z/2-z} dx'\,dy'\,dz' \, \frac{z'}{\sqrt{x'^2+y'^2+z'^2}^3} \quad + \quad \int_0^{l_x/2-x}\int_0^{l_y/2-y}\int_{-l_z/2-z}^{0} dx'\,dy'\,dz' \, \frac{z'}{\sqrt{x'^2+y'^2+z'^2}^3}\\
&+ \int_0^{l_x/2-x}\int_{-l_y/2-y}^{0}\int_0^{l_z/2-z} dx'\,dy'\,dz' \, \frac{z'}{\sqrt{x'^2+y'^2+z'^2}^3} \quad + \quad \int_0^{l_x/2-x}\int_{-l_y/2-y}^{0}\int_{-l_z/2-z}^{0} dx'\,dy'\,dz' \, \frac{z'}{\sqrt{x'^2+y'^2+z'^2}^3}\\
&+ \int_{-l_x/2-x}^{0}\int_0^{l_y/2-y}\int_0^{l_z/2-z} dx'\,dy'\,dz' \, \frac{z'}{\sqrt{x'^2+y'^2+z'^2}^3} \quad + \quad \int_{-l_x/2-x}^{0}\int_0^{l_y/2-y}\int_{-l_z/2-z}^{0} dx'\,dy'\,dz' \, \frac{z'}{\sqrt{x'^2+y'^2+z'^2}^3}\\
&+ \int_{-l_x/2-x}^{0}\int_{-l_y/2-y}^{0}\int_0^{l_z/2-z} dx'\,dy'\,dz' \, \frac{z'}{\sqrt{x'^2+y'^2+z'^2}^3} \quad + \quad \int_{-l_x/2-x}^{0}\int_{-l_y/2-y}^{0}\int_{-l_z/2-z}^{0} dx'\,dy'\,dz' \, \frac{z'}{\sqrt{x'^2+y'^2+z'^2}^3}.
\end{aligned} \tag{D.3}$$

This can be rewritten to match the form in equation (D.2). The integrals then read

$$\begin{aligned}
&I(x,y,z,l_x,l_y,l_z)\\
&= \int_0^{l_x/2-x}\int_0^{l_y/2-y}\int_0^{l_z/2-z} dx'\,dy'\,dz' \, \frac{z'}{\sqrt{x'^2+y'^2+z'^2}^3} \quad - \quad \int_0^{l_x/2-x}\int_0^{l_y/2-y}\int_0^{l_z/2+z} dx'\,dy'\,dz' \, \frac{z'}{\sqrt{x'^2+y'^2+z'^2}^3}\\
&+ \int_0^{l_x/2-x}\int_0^{l_y/2+y}\int_0^{l_z/2-z} dx'\,dy'\,dz' \, \frac{z'}{\sqrt{x'^2+y'^2+z'^2}^3} \quad - \quad \int_0^{l_x/2-x}\int_0^{l_y/2+y}\int_0^{l_z/2+z} dx'\,dy'\,dz' \, \frac{z'}{\sqrt{x'^2+y'^2+z'^2}^3}\\
&+ \int_0^{l_x/2+x}\int_0^{l_y/2-y}\int_0^{l_z/2-z} dx'\,dy'\,dz' \, \frac{z'}{\sqrt{x'^2+y'^2+z'^2}^3} \quad - \quad \int_0^{l_x/2+x}\int_0^{l_y/2-y}\int_0^{l_z/2+z} dx'\,dy'\,dz' \, \frac{z'}{\sqrt{x'^2+y'^2+z'^2}^3}\\
&+ \int_0^{l_x/2+x}\int_0^{l_y/2+y}\int_0^{l_z/2-z} dx'\,dy'\,dz' \, \frac{z'}{\sqrt{x'^2+y'^2+z'^2}^3} \quad - \quad \int_0^{l_x/2+x}\int_0^{l_y/2+y}\int_0^{l_z/2+z} dx'\,dy'\,dz' \, \frac{z'}{\sqrt{x'^2+y'^2+z'^2}^3}.
\end{aligned} \tag{D.4}$$

This can be written as

$$\begin{aligned} I(x,y,z,l_x,l_y,l_z) = & F_1\left(\frac{l_x}{2}-x,\frac{l_y}{2}-y,\frac{l_z}{2}-z\right) - F_1\left(\frac{l_x}{2}-x,\frac{l_y}{2}-y,\frac{l_z}{2}+z\right) \\ & + F_1\left(\frac{l_x}{2}-x,\frac{l_y}{2}+y,\frac{l_z}{2}-z\right) - F_1\left(\frac{l_x}{2}-x,\frac{l_y}{2}+y,\frac{l_z}{2}+z\right) \\ & + F_1\left(\frac{l_x}{2}+x,\frac{l_y}{2}-y,\frac{l_z}{2}-z\right) - F_1\left(\frac{l_x}{2}+x,\frac{l_y}{2}-y,\frac{l_z}{2}+z\right) \\ & + F_1\left(\frac{l_x}{2}+x,\frac{l_y}{2}+y,\frac{l_z}{2}-z\right) - F_1\left(\frac{l_x}{2}+x,\frac{l_y}{2}+y,\frac{l_z}{2}+z\right). \end{aligned} \tag{D.5}$$

Here F_1 is the function

$$F_1(a,b,c) = \int_0^a dx' \int_0^b dy' \int_0^c dz' \, \frac{z'}{\sqrt{x'^2+y'^2+z'^2}^3} \tag{D.6a}$$

$$\begin{aligned} &= [F(a,b,c) - F(0,b,c)] - [F(a,0,c) - F(0,0,c)] \\ &- [F(a,b,0) - F(0,b,0)] + [F(a,0,0) - F(0,0,0)] \end{aligned} \tag{D.6b}$$

with[213]

$$\begin{aligned} F(x',y',z') &= \int dx' \int dy' \int dz' \, \frac{z'}{\sqrt{x'^2+y'^2+z'^2}^3} \\ &= -\int dx' \int dy' \, \frac{1}{\sqrt{x'^2+y'^2+z'^2}} \\ &= -\int dx' \left(\ln\left(y'+\sqrt{x'^2+y'^2+z'^2}\right) + \frac{x'^2}{x'^2+z'^2}\right) \\ &= z' \arctan\left(\frac{x'y'}{z'\sqrt{x'^2+y'^2+z'^2}}\right) \\ &- y' \ln\left(x'+\sqrt{x'^2+y'^2+z'^2}\right) - x' \ln\left(y'+\sqrt{x'^2+y'^2+z'^2}\right). \end{aligned} \tag{D.7}$$

The constant of the y integration is chosen as to simplify the x integration. F_1 can now be calculated as

$$\begin{aligned} F_1(a,b,c) =& c \arctan\left(\frac{ab}{c\sqrt{a^2+b^2+c^2}}\right) \\ &+ b\left(\ln\left(\sqrt{b^2+c^2}\right) - \ln\left(a+\sqrt{a^2+b^2+c^2}\right) + \ln\left(a+\sqrt{a^2+b^2}\right) - \ln\left(|b|\right)\right) \\ &+ a\left(\ln\left(\sqrt{a^2+c^2}\right) - \ln\left(b+\sqrt{a^2+b^2+c^2}\right) + \ln\left(b+\sqrt{a^2+b^2}\right) - \ln\left(|a|\right)\right) \\ =& c \arctan\left(\frac{ab}{c\sqrt{a^2+b^2+c^2}}\right) + b \operatorname{arctanh}\left(\frac{a}{\sqrt{a^2+b^2}}\right) + a \operatorname{arctanh}\left(\frac{b}{\sqrt{a^2+b^2}}\right) \\ &- b \operatorname{arctanh}\left(\frac{a}{\sqrt{a^2+b^2+c^2}}\right) - a \operatorname{arctanh}\left(\frac{b}{\sqrt{a^2+b^2+c^2}}\right) \end{aligned} \tag{D.8}$$

For $x'=0$, $y'=0$, or $z'=0$ the value of $F(x',y',z')$ has been replaced by the according limit. This ensures that $F_1(a,b,c)$ goes to zero for $a \to 0$, $b \to 0$, or $c \to 0$. From equation (D.5) it becomes obvious that the integral is symmetric in x and y and antisymmetric in z.

For the calculation of the Oersted field outside the sample some of the boundaries of the integrations in equation (D.4) become negative. In such cases we have to change the sign of the boundary to ensure that all boundaries have the same sign. For the x and y integrations such a sign

change changes the sign of the integral. A change of the sign of the boundary for the z integration leaves the value of the integral unchanged. By comparing equations (D.4) and (D.6a) one finds that the function $F_1(a,b,c)$ should have the same symmetry as the integral to be valid outside the sample. Equation (D.8) reveals that the symmetry is indeed the same. Thus equation (D.5) is also valid outside the sample.

Since $F_1(a,b,c)$ is symmetric in c and antisymmetric in a and b equation (D.5) can be written as

$$\begin{aligned}
I(x,y,z,l_x,l_y,l_z) = {} & F_1\left(x-\frac{l_x}{2},y-\frac{l_y}{2},z-\frac{l_z}{2}\right) - F_1\left(x+\frac{l_x}{2},y-\frac{l_y}{2},z-\frac{l_z}{2}\right) \\
& + F_1\left(x+\frac{l_x}{2},y+\frac{l_y}{2},z-\frac{l_z}{2}\right) - F_1\left(x-\frac{l_x}{2},y+\frac{l_y}{2},z-\frac{l_z}{2}\right) \\
& - F_1\left(x-\frac{l_x}{2},y-\frac{l_y}{2},z+\frac{l_z}{2}\right) + F_1\left(x+\frac{l_x}{2},y-\frac{l_y}{2},z+\frac{l_z}{2}\right) \\
& - F_1\left(x+\frac{l_x}{2},y+\frac{l_y}{2},z+\frac{l_z}{2}\right) + F_1\left(x-\frac{l_x}{2},y+\frac{l_y}{2},z+\frac{l_z}{2}\right)
\end{aligned} \tag{D.9a}$$

$$\begin{aligned}
= {} & F_1\left(x-\frac{l_x}{2},y-\frac{l_y}{2},z-\frac{l_z}{2}\right) - F_1\left(x-\frac{l_x}{2},y+\frac{l_y}{2},z-\frac{l_z}{2}\right) \\
& + F_1\left(x+\frac{l_x}{2},y+\frac{l_y}{2},z-\frac{l_z}{2}\right) - F_1\left(x+\frac{l_x}{2},y-\frac{l_y}{2},z-\frac{l_z}{2}\right) \\
& - F_1\left(x-\frac{l_x}{2},y-\frac{l_y}{2},z+\frac{l_z}{2}\right) + F_1\left(x-\frac{l_x}{2},y+\frac{l_y}{2},z+\frac{l_z}{2}\right) \\
& - F_1\left(x+\frac{l_x}{2},y+\frac{l_y}{2},z+\frac{l_z}{2}\right) + F_1\left(x+\frac{l_x}{2},y-\frac{l_y}{2},z+\frac{l_z}{2}\right)
\end{aligned} \tag{D.9b}$$

independently of the values of x, y, z, l_x, l_y, and l_z. A closer look at equations (D.9a), (D.9b), and (D.5) reveals that the summation cancels out all terms in F_1 that are independent of a, b or c. This allows for a simplification of the expression in equation (D.5) that reads

$$\begin{aligned}
I(x,y,z,l_x,l_y,l_z) = {} & F\left(x-\frac{l_x}{2},y-\frac{l_y}{2},z-\frac{l_z}{2}\right) - F\left(x+\frac{l_x}{2},y-\frac{l_y}{2},z-\frac{l_z}{2}\right) \\
& + F\left(x+\frac{l_x}{2},y+\frac{l_y}{2},z-\frac{l_z}{2}\right) - F\left(x-\frac{l_x}{2},y+\frac{l_y}{2},z-\frac{l_z}{2}\right) \\
& - F\left(x-\frac{l_x}{2},y-\frac{l_y}{2},z+\frac{l_z}{2}\right) + F\left(x+\frac{l_x}{2},y-\frac{l_y}{2},z+\frac{l_z}{2}\right) \\
& - F\left(x+\frac{l_x}{2},y+\frac{l_y}{2},z+\frac{l_z}{2}\right) + F\left(x-\frac{l_x}{2},y+\frac{l_y}{2},z+\frac{l_z}{2}\right).
\end{aligned} \tag{D.10}$$

Here it is worth noting that $F(a,b,c)$ does not show the symmetry of $F_1(a,b,c)$ with respect to a and b.

D.1 Spatial Derivatives

For the calculation of the spacial derivatives of $I(x, y, z, l_x, l_y, l_z)$ we need to calculate the derivatives of $F(a, b, c)$ with respect to the three parameters. The derivative with respect to a yields

$$\begin{aligned}\frac{dF}{da}(a,b,c) =& \frac{c\left(-\frac{a^2 b}{c\sqrt{a^2+b^2+c^2}^3}+\frac{b}{c\sqrt{a^2+b^2+c^2}}\right)}{1+\frac{a^2b^2}{c^2(a^2+b^2+c^2)}} - \frac{b\left(1+\frac{a}{\sqrt{a^2+b^2+c^2}}\right)}{a+\sqrt{a^2+b^2+c^2}} \\ & - \ln\left(b+\sqrt{a^2+b^2+c^2}\right) - \frac{a^2}{b\sqrt{a^2+b^2+c^2}+a^2+b^2+c^2} \\ =& -\ln\left(b+\sqrt{a^2+b^2+c^2}\right) - \frac{a^2}{a^2+c^2}\end{aligned} \tag{D.11}$$

and the derivative with respect to c reads

$$\begin{aligned}\frac{dF}{dc}(a,b,c) =& \arctan\left(\frac{ab}{c\sqrt{a^2+b^2+c^2}}\right) + \frac{c\left(-\frac{ab}{\sqrt{a^2+b^2+c^2}^3}-\frac{ab}{c^2\sqrt{a^2+b^2+c^2}}\right)}{1+\frac{a^2b^2}{c^2(a^2+b^2+c^2)}} \\ & - \frac{bc}{a\sqrt{a^2+b^2+c^2}+a^2+b^2+c^2} - \frac{ac}{b\sqrt{a^2+b^2+c^2}+a^2+b^2+c^2} \\ =& \arctan\left(\frac{ab}{c\sqrt{a^2+b^2+c^2}}\right) - \frac{ac}{a^2+c^2} - \frac{bc}{b^2+c^2}.\end{aligned} \tag{D.12}$$

For the remaining derivative we find

$$\frac{dF}{db}(a,b,c) = \frac{dF}{db}(b,a,c) \tag{D.13}$$

using the expression $F(a, b, c) = F(b, a, c)$.

The spatial derivatives of the integral then read

$$\begin{aligned}\frac{dI}{dx}(x,y,z,l_x,l_y,l_z) =& F_a\left(x-\frac{l_x}{2},y-\frac{l_y}{2},z-\frac{l_z}{2}\right) - F_a\left(x+\frac{l_x}{2},y-\frac{l_y}{2},z-\frac{l_z}{2}\right) \\ & + F_a\left(x+\frac{l_x}{2},y+\frac{l_y}{2},z-\frac{l_z}{2}\right) - F_a\left(x-\frac{l_x}{2},y+\frac{l_y}{2},z-\frac{l_z}{2}\right) \\ & - F_a\left(x-\frac{l_x}{2},y-\frac{l_y}{2},z+\frac{l_z}{2}\right) + F_a\left(x+\frac{l_x}{2},y-\frac{l_y}{2},z+\frac{l_z}{2}\right) \\ & - F_a\left(x+\frac{l_x}{2},y+\frac{l_y}{2},z+\frac{l_z}{2}\right) + F_a\left(x-\frac{l_x}{2},y+\frac{l_y}{2},z+\frac{l_z}{2}\right),\end{aligned} \tag{D.14}$$

$$\begin{aligned}\frac{dI}{dy}(x,y,z,l_x,l_y,l_z) =& F_a\left(y-\frac{l_y}{2},x-\frac{l_x}{2},z-\frac{l_z}{2}\right) - F_a\left(y+\frac{l_y}{2},x-\frac{l_x}{2},z-\frac{l_z}{2}\right) \\ & + F_a\left(y+\frac{l_y}{2},x+\frac{l_x}{2},z-\frac{l_z}{2}\right) - F_a\left(y-\frac{l_y}{2},x+\frac{l_x}{2},z-\frac{l_z}{2}\right) \\ & - F_a\left(y-\frac{l_y}{2},x-\frac{l_x}{2},z+\frac{l_z}{2}\right) + F_a\left(y+\frac{l_y}{2},x-\frac{l_x}{2},z+\frac{l_z}{2}\right) \\ & - F_a\left(y+\frac{l_y}{2},x+\frac{l_x}{2},z+\frac{l_z}{2}\right) + F_a\left(y-\frac{l_y}{2},x+\frac{l_x}{2},z+\frac{l_z}{2}\right),\end{aligned} \tag{D.15}$$

and

$$\begin{aligned}\frac{dI}{dz}(x,y,z,l_x,l_y,l_z) = &F_c\left(x-\frac{l_x}{2},y-\frac{l_y}{2},z-\frac{l_z}{2}\right) - F_c\left(x+\frac{l_x}{2},y-\frac{l_y}{2},z-\frac{l_z}{2}\right)\\ &+ F_c\left(x+\frac{l_x}{2},y+\frac{l_y}{2},z-\frac{l_z}{2}\right) - F_c\left(x-\frac{l_x}{2},y+\frac{l_y}{2},z-\frac{l_z}{2}\right)\\ &- F_c\left(x-\frac{l_x}{2},y-\frac{l_y}{2},z+\frac{l_z}{2}\right) + F_c\left(x+\frac{l_x}{2},y-\frac{l_y}{2},z+\frac{l_z}{2}\right)\\ &- F_c\left(x+\frac{l_x}{2},y+\frac{l_y}{2},z+\frac{l_z}{2}\right) + F_c\left(x-\frac{l_x}{2},y+\frac{l_y}{2},z+\frac{l_z}{2}\right)\end{aligned} \tag{D.16}$$

with

$$F_a(a,b,c) = -\ln\left(b+\sqrt{a^2+b^2+c^2}\right) \tag{D.17}$$

and

$$F_c(a,b,c) = \arctan\left(\frac{ab}{c\sqrt{a^2+b^2+c^2}}\right). \tag{D.18}$$

As for the integral the summation cancels out all terms that do not depend on all three parameters.

D.2 Limiting Cases

Now we will calculate some approximations for special systems. These approximations are useful for an analytical consideration of the current's Oersted field. They also allow for a comparison of the field that is calculated here with known solutions.

For the limiting case of an infinitely large film, that is $l_x = l_y = \infty$, the expression for the in-plane field can be simplified. The integral can be calculated using equation (D.10). Due to the translational invariance of the infinitely large film the integral does not depend on x and y. This yields

$$\begin{aligned}\lim_{l\to\infty} I(x,y,z,l,l,l_z) &= \lim_{l\to\infty} I(0,0,z,l,l,l_z)\\ &= \lim_{l\to\infty}\left[F\left(-\frac{l}{2},-\frac{l}{2},z-\frac{l_z}{2}\right) - F\left(-\frac{l}{2},-\frac{l}{2},z+\frac{l_z}{2}\right)\right]\\ &- \lim_{l\to\infty}\left[F\left(-\frac{l}{2},\frac{l}{2},z-\frac{l_z}{2}\right) - F\left(-\frac{l}{2},\frac{l}{2},z+\frac{l_z}{2}\right)\right]\\ &- \lim_{l\to\infty}\left[F\left(\frac{l}{2},-\frac{l}{2},z-\frac{l_z}{2}\right) - F\left(\frac{l}{2},-\frac{l}{2},z+\frac{l_z}{2}\right)\right]\\ &+ \lim_{l\to\infty}\left[F\left(\frac{l}{2},\frac{l}{2},z-\frac{l_z}{2}\right) - F\left(\frac{l}{2},\frac{l}{2},z+\frac{l_z}{2}\right)\right].\end{aligned} \tag{D.19}$$

For large l the logarithms in each bracket in equation (D.19) cancel out and the integral becomes

$$\lim_{l\to\infty} I(x,y,z,l,l,l_z) = 2\pi\left(\left|z-\frac{l_z}{2}\right| - \left|z+\frac{l_z}{2}\right|\right). \tag{D.20}$$

This allows for a calculation of the in-plane field

$$\vec{H}(x,y,z) = \frac{j_x\vec{e}_y - j_y\vec{e}_x}{2}\left(\left|z-\frac{l_z}{2}\right| - \left|z+\frac{l_z}{2}\right|\right) \tag{D.21}$$

using equations (9.4a) and (9.4b). This is the known solution for an infinite film.

For an infinitely long wire ($l_x = \infty$) with a rectangular crossection $l_y \times l_z$ one finds

$$\begin{aligned}\lim_{l\to\infty} I(x,y,z,l,l_y,l_z) &= \lim_{l\to\infty} I(0,y,z,l,l_y,l_z)\\ &= \lim_{l\to\infty}\left[F\left(-\frac{l}{2},y-\frac{l_y}{2},z-\frac{l_z}{2}\right)-F\left(-\frac{l}{2},y-\frac{l_y}{2},z+\frac{l_z}{2}\right)\right]\\ &- \lim_{l\to\infty}\left[F\left(-\frac{l}{2},y+\frac{l_y}{2},z-\frac{l_z}{2}\right)-F\left(-\frac{l}{2},y+\frac{l_y}{2},z+\frac{l_z}{2}\right)\right]\\ &- \lim_{l\to\infty}\left[F\left(\frac{l}{2},y-\frac{l_y}{2},z-\frac{l_z}{2}\right)-F\left(\frac{l}{2},y-\frac{l_y}{2},z+\frac{l_z}{2}\right)\right]\\ &+ \lim_{l\to\infty}\left[F\left(\frac{l}{2},y+\frac{l_y}{2},z-\frac{l_z}{2}\right)-F\left(\frac{l}{2},y+\frac{l_y}{2},z+\frac{l_z}{2}\right)\right].\end{aligned} \tag{D.22}$$

The limit can be expressed as

$$\begin{aligned}\lim_{l\to\infty} I(x,y,z,l,l_y,l_z) =&(2z+l_z)\left[\arctan\left(\frac{2y-l_y}{2z+l_z}\right)-\arctan\left(\frac{2y+l_y}{2z+l_z}\right)\right]\\ &-(2z-l_z)\left[\arctan\left(\frac{2y-l_y}{2z-l_z}\right)-\arctan\left(\frac{2y+l_y}{2z-l_z}\right)\right]\\ &-\frac{1}{2}(2y+l_y)\ln\left(\frac{(2y+l_y)^2+(2z+l_z)^2}{(2y+l_y)^2+(2z-l_z)^2}\right)\\ &+\frac{1}{2}(2y-l_y)\ln\left(\frac{(2y-l_y)^2+(2z+l_z)^2}{(2y-l_y)^2+(2z-l_z)^2}\right).\end{aligned} \tag{D.23}$$

At a large distance from the wire, that is $l_y \ll \sqrt{y^2+z^2}$ and $l_z \ll \sqrt{y^2+z^2}$, we can expand equation (D.23) in $l_y/\sqrt{y^2+z^2}$ and $l_z/\sqrt{y^2+z^2}$. Equation (D.23) is antisymmetric in l_y and l_z thus the first non-vanishing term is linear in l_x and l_y. A series up to second order reads

$$\lim_{l\to\infty} I(x,y,z,l,l_y,l_z) \approx -\frac{2zl_yl_z}{y^2+z^2}. \tag{D.24}$$

With the wire's crossection $S = l_yl_z$ and with aid of equations (9.4b) and (9.4c) the Oersted field can be calculated as

$$\vec{H}(x,y,z) \approx \frac{(y\vec{e}_z - z\vec{e}_y)Sj_x}{2\pi(y^2+z^2)} \tag{D.25}$$

as one would expect for an infinitely large wire with circular crossection. Since we calculated the field far away from the wire the shape of the crossection of the wire becomes unimportant.

In the vicinity of the center of the sample ($(x,y) = (0,0)$) the integral $I(x,z,y,l_x,l_z,l_y)$ can be approximated by a Taylor series up to second order in x/l_x and y/l_y. Due to the aforementioned symmetry conditions of I the only non-vanishing term is linear in y. The approximation then reads

$$\begin{aligned}I(x,z,y,l_x,l_z,l_y) &\approx \frac{dI}{dy}(0,z,0,l_x,l_z,l_y)y\\ &= 4\left(\arctan\left(\frac{l_x(2z-l_z)}{l_y\sqrt{l_x^2+l_y^2+(2z-l_z)^2}}\right)-\arctan\left(\frac{l_x(2z+l_z)}{l_y\sqrt{l_x^2+l_y^2+(2z+l_z)^2}}\right)\right)y.\end{aligned} \tag{D.26}$$

In thin squares, that is $l_x = l_y = l$ and $|2z| \le l_z = d \ll l$, one gets

$$I(x,z,y,l_x,l_z,l_y) \approx 4\left(\frac{2z-d}{\sqrt{2}l}-\frac{2z+d}{\sqrt{2}l}\right)y = -\frac{8d}{\sqrt{2}l}y. \tag{D.27}$$

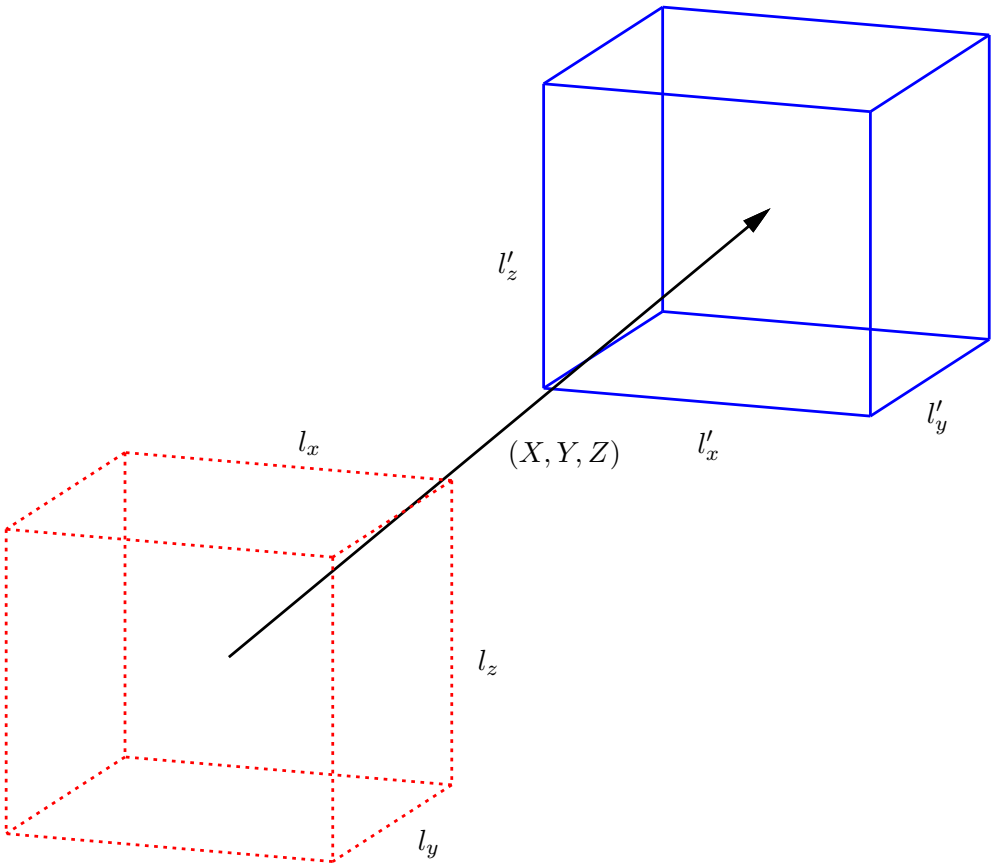

Figure D.1: Scheme of two cells that are involved in the calculation of the Oersted field. The first cell (dashed red lines) is traversed by a homogeneous current with density $\vec{j}$. This current generates an Oersted field $\vec{H}$ in the second cell (solid blue lines). The arrow denotes a vector that points from the center of the first cell to the center of the second cell.

Wit equation (9.4c) this allows us to approximate the out-of-plane field

$$H_z(x, y, z) \approx \frac{\sqrt{2}d(yj_x - xj_y)}{\pi l}. \tag{D.28}$$

It can be seen that in a sizeable distance from the boundaries of the square the out-of-plane field is given by a gradient field. Its gradient depend only on the current density and the aspect ratio of the sample.

D.3 Numerical Calculations for Arbitrary Samples and Currents

In numerical calculations samples of arbitrary shape with inhomogeneous current densities can be divided in cubic cells as depicted in figure 6.2. In each cell the current and magnetization is assumed to be homogeneous. The Oersted field in a distinct cell can then be calculated by the summation of the fields that are generated by the currents in each cell. To determined the influence of the field on the magnetization we need to average over the volume of the cell. To calculate the average field in a cell with size $l'_x \times l'_y \times l'_z$ that is generated by a cell with size $l_x \times l_y \times l_z$ (see figure D.1) we

replace the integral I in equation (9.6) by

$$
\begin{aligned}
I_2(X,Y,Z,l_x,l_y,l_z,l'_x,l'_y,l'_z) &= \frac{1}{l'_x l'_y l'_z}\int\limits_{X-l'_x/2}^{X+l'_x/2} dx \int\limits_{Y-l'_y/2}^{Y+l'_y/2} dy \int\limits_{Z-l'_z/2}^{Z+l'_z/2} dz\, I(x,y,z,l_x,l_y,l_z) \\
&= \frac{1}{l'_x l'_y l'_z}\int\limits_{X-l'_x/2}^{X+l'_x/2} dx \int\limits_{Y-l'_y/2}^{Y+l'_y/2} dy \int\limits_{Z-l'_z/2}^{Z+l'_z/2} dz \int\limits_{-l_x/2-x}^{l_x/2-x} dx' \int\limits_{-l_y/2-y}^{l_y/2-y} dy' \int\limits_{-l_z/2-z}^{l_z/2-z} dz' \,\frac{z'}{\sqrt{x'^2+y'^2+z'^2}^3} \\
&= -\frac{1}{l'_x l'_y l'_z}\int\limits_{X-l'_x/2}^{X+l'_x/2} dx \int\limits_{Y-l'_y/2}^{Y+l'_y/2} dy \int\limits_{Z-l'_z/2}^{Z+l'_z/2} dz \int\limits_{x-l_x/2}^{x+l_x/2} dx' \int\limits_{y-l_y/2}^{y+l_y/2} dy' \int\limits_{z-l_z/2}^{z+l_z/2} dz' \,\frac{z'}{\sqrt{x'^2+y'^2+z'^2}^3} \\
&= -\sum_{i,j,k}\sum_{o,p,q}\frac{ijkopq}{l'_x l'_y l'_z} G_1\left(X+i\frac{l_x}{2}+o\frac{l'_x}{2}, Y+j\frac{l_y}{2}+p\frac{l'_y}{2}, Z+k\frac{l_z}{2}+q\frac{l'_z}{2}\right)
\end{aligned}
\tag{D.29}
$$

where i, j, k, o, p, and q assume values of -1 and 1. G_1 is given by the integral

$$
\begin{aligned}
G_1(X,Y,Z) &= \int\limits_0^Z dz \int\limits_0^Y dy \int\limits_0^X dx \int\limits_0^x dx' \int\limits_0^y dy' \int\limits_0^z dz' \,\frac{z'}{\sqrt{x'^2+y'^2+z'^2}^3} = \int\limits_0^Z dz \int\limits_0^Y dy \int\limits_0^X dx\, F_1(x,y,z) \\
&= G(X,Y,Z) - G(0,Y,Z) - G(X,0,Z) + G(0,0,Z).
\end{aligned}
\tag{D.30}
$$

G is the function[213]

$$
\begin{aligned}
G(x,y,z) &= \int dz \int dy \int dx\, F_1(x,y,z) \\
&= \int dz \int dy \left(\frac{yR}{2} + xz\arctan\left(\frac{xy}{zR}\right) - xy\,\mathrm{arctanh}\left(\frac{x}{R}\right) + \frac{z^2-x^2}{2}\mathrm{arctanh}\left(\frac{y}{R}\right)\right. \\
&\left. -\frac{yR'}{2} + xy\,\mathrm{arctanh}\left(\frac{x}{R'}\right) + \frac{x^2}{2}\mathrm{arctanh}\left(\frac{y}{R'}\right)\right) \\
&= \int dz \left(\frac{\left(x^2+y^2-2z^2\right)R}{6} + xyz\arctan\left(\frac{xy}{zR}\right) - \frac{x\left(y^2-z^2\right)}{2}\mathrm{arctanh}\left(\frac{x}{R}\right)\right. \\
&\left. -\frac{y\left(x^2-z^2\right)}{2}\mathrm{arctanh}\left(\frac{y}{R}\right) - \frac{R'^3}{6} + \frac{xy^2}{2}\mathrm{arctanh}\left(\frac{x}{R'}\right) + \frac{yx^2}{2}\mathrm{arctanh}\left(\frac{y}{R'}\right)\right) \\
&= \frac{\left(3x^2z+3y^2z-2z^3\right)R}{24} + \frac{xyz^2}{2}\arctan\left(\frac{xy}{zR}\right) \\
&+ \frac{xy^3}{6}\arctan\left(\frac{xz}{yR}\right) + \frac{x^3y}{6}\arctan\left(\frac{yz}{xR}\right) + \frac{x^4-6x^2y^2+y^4}{24}\mathrm{arctanh}\left(\frac{z}{R}\right) \\
&- \frac{3xy^2z-xz^3}{6}\mathrm{arctanh}\left(\frac{x}{R}\right) - \frac{3x^2yz-yz^3}{6}\mathrm{arctanh}\left(\frac{y}{R}\right) \\
&- \frac{zR'^3}{6} + \frac{xy^2z}{2}\mathrm{arctanh}\left(\frac{x}{R'}\right) + \frac{x^2yz}{2}\mathrm{arctanh}\left(\frac{y}{R'}\right)
\end{aligned}
\tag{D.31}
$$

with $R=\sqrt{x^2+y^2+z^2}$ and $R'=\sqrt{x^2+y^2}$. Here, we took into account that $G(x,y,0)=0$.

G is symmetric in x and y and antisymmetric in z. Making use of this symmetry equation (D.29)

can be written as

$$I_2(X,Y,Z,l_x,l_y,l_z,l'_x,l'_y,l'_z) = -\sum_{i,j,k}\sum_{o,p,q}\frac{kopq}{l'_x l'_y l'_z} G_1\left(iX+\frac{l_x}{2}+o\frac{l'_x}{2}, jY+\frac{l_y}{2}+p\frac{l'_y}{2}, kZ+\frac{l_z}{2}+q\frac{l'_z}{2}\right). \tag{D.32}$$

From this equation one finds a symmetry of I_2 in X and Y as well as an antisymmetry in Z.

For numerical calculations equation (D.29) can be optimized. We find that all terms in G_1 that are constant or linear in x, y, or z cancel out in the summation leading to I_2. G_1 can thus be replaced by

$$\begin{aligned} G'_1(x,y,z) = {} & \frac{(3x^2+3y^2-2z^2)zR}{24} + \frac{\pi z}{4}|xyz| + \frac{x^4-6x^2y^2+y^4}{24}\ln(z+R) \\ & + \frac{xy}{6}\left((y^2-3z^2)\arctan\left(\frac{xz}{yR}\right)+(x^2-3z^2)\arctan\left(\frac{yz}{xR}\right)\right) \\ & + \frac{z}{6}\left(x(z^2-3y^2)\ln(x+R)+y(z^2-3x^2)\ln(y+R)\right). \end{aligned} \tag{D.33}$$

Here the equality

$$\frac{\pi}{2}|xyz| - xyz\arctan\left(\frac{xy}{zR}\right) = xyz\arctan\left(\frac{zR}{xy}\right) = xyz\left(\arctan\left(\frac{xz}{yR}\right)+\arctan\left(\frac{yz}{xR}\right)\right) \tag{D.34}$$

has been used. If all cells have the same size, that is $l'_x = l_x$, $l'_y = l_y$, and $l'_z = l'_z$, the integral can be written as

$$I_2(X,Y,Z,l_x,l_y,l_z) = \sum_{\eta,\mu,\nu}\frac{(2-3|\eta|)(2-3|\mu|)(2-3|\nu|)}{l_x l_y l_z} G'_1\left(X+\eta l_x, Y+\mu l_y, Z+\nu l_z\right) \tag{D.35}$$

where η, μ, and ν assume values of -1, 0, and 1. This expression depends only on the distance between the cells. Thus, the field can be written as the convolution

$$\vec{H}(\vec{r}_\chi) = \sum_\zeta K(\vec{r}_\chi - \vec{r}_\zeta)\vec{j}(\vec{r}_\zeta) \tag{D.36}$$

with

$$K_{yx}(\vec{r}) = -K_{xy}(\vec{r}) = \frac{I_2(x,y,z,l_x,l_y,l_z)}{4\pi} \tag{D.37a}$$

$$K_{zy}(\vec{r}) = -K_{yz}(\vec{r}) = \frac{I_2(y,z,x,l_y,l_z,l_x)}{4\pi} \tag{D.37b}$$

$$K_{xz}(\vec{r}) = -K_{zx}(\vec{r}) = \frac{I_2(z,x,y,l_z,l_x,l_y)}{4\pi} \tag{D.37c}$$

$$K_{xx}(\vec{r}) = K_{yy}(\vec{r}) = K_{zz}(\vec{r}) = 0. \tag{D.37d}$$

Here the sum over ζ is over all cells and $\vec{r}_\chi$ and $\vec{r}_\zeta$ denote the position of the cells.

E Solving the Equation of Motion of the Domain Wall

In this section the solution of equation (13.52) is derived for two special cases. The first case is the absence of a potential and the second case is the presence of a harmonic confining potential.

E.1 Without a Potential

In the absence of a potential equation (13.52) becomes

$$\ddot{X}(t) = -\frac{\dot{X}(t)}{\tau_d} + \frac{C_1}{\tau_d} H_{\text{ext}}(t) + C_2 \dot{H}_{\text{ext}}(t) + \frac{C_3}{\tau_d} j(t) + C_4 \dot{j}(t). \tag{E.1}$$

Its solution can be derived using the variation of constants ansatz which is introduced in section B. The homogeneous equation

$$\ddot{X}(t) = -\frac{\dot{X}(t)}{\tau_d} \tag{E.2}$$

has the solution

$$\dot{X}(t) = C e^{-\frac{t}{\tau_d}} \tag{E.3}$$

with a constant C that depends on the starting condition. For the solution of the inhomogeneous equation we replace C by a variable $C(t)$ that depends on time. Equation (E.1) then reads

$$\dot{C}(t) e^{-\frac{t}{\tau_d}} = \frac{C_1}{\tau_d} H_{\text{ext}}(t) + C_2 \dot{H}_{\text{ext}}(t) + \frac{C_3}{\tau_d} j(t) + C_4 \dot{j}(t). \tag{E.4}$$

The exponential function on the left-hand side can be brought to the right-hand side. After an integration the equation reads

$$C(t) = \int_{-\infty}^{t} dt' \; e^{\frac{t'}{\tau_d}} \left(\frac{C_1}{\tau_d} H_{\text{ext}}(t') + C_2 \dot{H}_{\text{ext}}(t') + \frac{C_3}{\tau_d} j(t') + C_4 \dot{j}(t') \right). \tag{E.5}$$

By inserting this result in equation (E.3) we get the expression

$$\dot{X}(t) = \int_{-\infty}^{t} dt' \; e^{-\frac{t-t'}{\tau_d}} \left(\frac{C_1}{\tau_d} H_{\text{ext}}(t') + C_2 \dot{H}_{\text{ext}}(t') + \frac{C_3}{\tau_d} j(t') + C_4 \dot{j}(t') \right) \tag{E.6}$$

for the velocity of the domain wall.

E.2 With a Harmonic Confining Potential

For a harmonic confining potential

$$E_{\text{pin}} = \frac{m'}{2} \omega_r^2 X^2 \tag{E.7}$$

with the resonance frequency ω_r equation (13.52) becomes

$$\ddot{X}(t) = -\frac{\dot{X}(t)}{\tau_d} - \omega_r^2 X(t) + \frac{C_1}{\tau_d} H_{\text{ext}}(t) + C_2 \dot{H}_{\text{ext}}(t) + \frac{C_3}{\tau_d} j(t) + C_4 \dot{j}(t). \tag{E.8}$$

This is a differential equation of second order in time. Introducing $v = \dot{X}$ this equation can be written as the system

$$\begin{pmatrix} \dot{v}(t) \\ \dot{X}(t) \end{pmatrix} = \begin{pmatrix} -\frac{1}{\tau_d} & -\omega_r^2 \\ 1 & 0 \end{pmatrix} \begin{pmatrix} v(t) \\ X(t) \end{pmatrix} + \begin{pmatrix} \frac{C_1}{\tau_d} H_{\text{ext}}(t) + C_2 \dot{H}_{\text{ext}}(t) + \frac{C_3}{\tau_d} j(t) + C_4 \dot{j}(t) \\ 0 \end{pmatrix} \tag{E.9}$$

of two differential equations of first order. This equation is solved using the variation of constants ansatz which is introduced in section B. For the underdamped system, that is $\omega_r^2 > 1/(2\tau_d)^2$, one finds the fundamental system

$$e^{-\frac{t}{2\tau_d}} \begin{pmatrix} (-\frac{1}{2\tau_d} + i\omega)e^{i\omega t} & (-\frac{1}{2\tau_d} - i\omega)e^{-i\omega t} \\ e^{i\omega t} & e^{-i\omega t} \end{pmatrix} \tag{E.10}$$

and its inverse

$$\frac{e^{\frac{t}{2\tau_d}}}{2i\omega} \begin{pmatrix} e^{-i\omega t} & -(-\frac{1}{2\tau_d} - i\omega)e^{-i\omega t} \\ -e^{i\omega t} & (-\frac{1}{2\tau_d} + i\omega)e^{i\omega t} \end{pmatrix}, \tag{E.11}$$

with the free frequency

$$\omega = \sqrt{\omega_r^2 - \frac{1}{(2\tau_d)^2}}. \tag{E.12}$$

From this system we are able to calculate the solution

$$X(t) = \int_{-\infty}^{t} dt'\, e^{-\frac{t-t'}{2\tau_d}} \frac{\sin(\omega(t-t'))}{\omega} \left(\frac{C_1}{\tau_d} H_{\text{ext}}(t') + C_2 \dot{H}_{\text{ext}}(t') + \frac{C_3}{\tau_d} j(t') + C_4 \dot{j}(t') \right). \tag{E.13}$$

In the following we restrict ourselves to a current-driven excitation, that is $H \equiv 0$. The current starts at $t = 0$. During the risetime τ_r the current density increases linearly to $j_{\max}$. Subsequently the current density remains constant. The position of the wall is calculated from equation (E.13). Before the current density reaches its maximum the position of the wall is given by

$$X(t) = \int_{0}^{t} dt'\, e^{-\frac{t-t'}{2\tau_d}} \frac{\sin(\omega(t-t'))}{\omega} \left(\frac{C_3 j_{\max} t'}{\tau_d \tau_r} + \frac{C_4 j_{\max}}{\tau_r} \right) = \left(F_r(t,t) - F_r(t,0)\right) j_{\max} \tag{E.14}$$

with

$$\begin{aligned} F_r(t,t') = {} & \frac{\sin(\omega(t-t')) + 2\tau_d\omega\cos(\omega(t-t'))}{1+4\tau_d^2\omega^2} \frac{2(t'C_3 + \tau_d C_4)}{\tau_r \omega} e^{-\frac{t-t'}{2\tau_d}} \\ & - \frac{2\left(1-4\tau_d^2\omega^2\right)\sin(\omega(t-t')) + 8\tau_d\omega\cos(\omega(t-t'))}{\left(1+4\tau_d^2\omega^2\right)^2} \frac{2\tau_d C_3}{\tau_r\omega} e^{-\frac{t-t'}{2\tau_d}}. \end{aligned} \tag{E.15}$$

During the constant part of the current density the position of the wall is given by

$$\begin{aligned} X(t) &= \int_{0}^{\tau_r} dt'\, e^{-\frac{t-t'}{2\tau_d}} \frac{\sin(\omega(t-t'))}{\omega} \left(\frac{C_3 j_{\max} t'}{\tau_d \tau_r} + \frac{C_4 j_{\max}}{\tau_r} \right) + \int_{\tau_r}^{t} dt'\, e^{-\frac{t-t'}{2\tau_d}} \frac{\sin(\omega(t-t'))}{\omega} \frac{C_3 j_{\max}}{\tau_d} \\ &= \left(F_r(t,\tau_r) - F_r(t,0) + F_c(t,t) - F_c(t,\tau_r)\right) j_{\max} \end{aligned} \tag{E.16}$$

where

$$F_c(t,t') = \frac{\sin(\omega(t-t')) + 2\tau_d\omega\cos(\omega(t-t'))}{1+4\tau_d^2\omega^2} \frac{2C_3}{\omega} e^{-\frac{t-t'}{2\tau_d}}. \tag{E.17}$$

In the remaining part we discuss the two limiting cases of large risetime ($\tau_r \gg \tau_d$) and vanishing risetime ($\tau_r = 0$). For $\tau_r \gg \tau_d$ we use a series expression up to zeroth order in τ_d/τ_r. From this expansion one finds

$$F_r(t,t') = \frac{\sin(\omega(t-t')) + 2\tau_d\omega\cos(\omega(t-t'))}{1+4\tau_d^2\omega^2} \frac{2C_3}{\omega} e^{-\frac{t-t'}{2\tau_d}} \frac{t'}{\tau_r} \tag{E.18}$$

and

$$F_c(t,t') = \frac{\sin(\omega(t-t')) + 2\tau_d\omega\cos(\omega(t-t'))}{1+4\tau_d^2\omega^2}\frac{2C_3}{\omega}e^{-\frac{t-t'}{2\tau_d}}. \tag{E.19}$$

This yields the wall position

$$X(t) = \begin{cases} \frac{4\tau_d C_3 j_{\max}}{1+4\tau_d^2\omega^2}\frac{t}{\tau_r} & t \le \tau_r \\ \frac{4\tau_d C_3 j_{\max}}{1+4\tau_d^2\omega^2} & t > \tau_r. \end{cases} \tag{E.20}$$

It can be easily seen that the maximum displacement is given by

$$X_{\max}^{\infty} = \frac{4\tau_d C_3 j_{\max}}{1+4\tau_d^2\omega^2}. \tag{E.21}$$

For an intermediate region of τ_r a closer look at equation (E.16) reveals that the displacement during the constant part of the current can be written as the sum

$$X(t) = \underbrace{\left(F_r(t,\tau_r) - F_r(t,0) - F_c(t,\tau_r)\right) j_{\max}}_{\text{oscillating}} + X_{\max}^{\infty} \tag{E.22}$$

of an oscillating part of the form

$$A\sin(\omega t + \phi_0)e^{-\frac{t}{2\tau_d}} \tag{E.23}$$

and a new equilibrium position. Due to its exponential decrease the oscillating part assumes its maximum during the first period of its oscillation. Thus the global maximum of the displacement is reached for $t_{\max} \le \tau_r + 2\pi/\omega$.

For a risetime of $\tau_r = 0$ it is important to take into account that $\lim_{\tau_r\to 0}(F_r(t,\tau_r) - F_r(t,0)) \neq 0$. From l'Hopital's rule we find

$$\lim_{\tau_r\to 0}(F_r(t,\tau_r) - F_r(t,0)) = \frac{\sin(\omega t)C_4}{\omega}e^{-\frac{t}{2\tau_d}} \tag{E.24}$$

which yields

$$\begin{aligned} X(t) &= \left(\frac{\sin(\omega t)C_4}{\omega}e^{-\frac{t}{2\tau_d}} + \frac{4\tau_d C_3}{1+4\tau_d^2\omega^2} - \frac{\sin(\omega t) + 2\tau_d\omega\cos(\omega t)}{1+4\tau_d^2\omega^2}\frac{2C_3}{\omega}e^{-\frac{t}{2\tau_d}}\right) j_{\max} \\ &= \left(1 + \frac{\left(C_4 + 4\tau_d^2\omega^2 C_4 - 2C_3\right)\sin(\omega t) - 4\tau_d\omega C_3\cos(\omega t)}{4\tau_d\omega C_3}e^{-\frac{t}{2\tau_d}}\right) X_{\max}^{\infty}. \end{aligned} \tag{E.25}$$

The new equilibrium position of the wall is the same as for very large risetimes but due to the additional damped oscillation the maximum displacement of the wall is larger than in the case where $\tau_r \gg \tau_d$.

F Integrals of the Domain Wall Dynamics

In the analytical description of the domain wall dynamics one is faced with a number of integrals that are calculated in the following. Here we use the abbreviation $x' = x/\lambda$ and $X' = X/\lambda$. The integrals

$$\int_{-\infty}^{\infty} dx \frac{1}{\cosh\left(\frac{x-X}{\lambda}\right)} = \lambda \int_{-\infty}^{\infty} dx' \frac{1}{\cosh(x'-X')} = \pi\lambda \tag{F.1}$$

and

$$\int_{-\infty}^{\infty} dx \frac{1}{\cosh^2\left(\frac{x-X}{\lambda}\right)} = \lambda \int_{-\infty}^{\infty} dx' \frac{1}{\cosh^2(x'-X')} = 2\lambda \tag{F.2}$$

are needed for the calculation of the multipole moments in section 16. The latter one is also needed to calculate the anisotropy energy in equation (13.35). For the calculation of this energy we also need the value of the integral

$$\begin{aligned}
\int_{-\infty}^{\infty} dx \tanh\left(\frac{x-X}{\lambda}\right) &= \lambda \lim_{a\to\infty} \int_{-a}^{a} dx' \tanh(x'-X') \\
&= \lambda \lim_{a\to\infty} \left(\ln(\cosh(a-X')) - \ln(\cosh(-a-X'))\right) \\
&= \lambda \lim_{a\to\infty} \ln\left(\frac{e^{a-X'}+e^{-a+X'}}{e^{a+X'}+e^{-a-X'}}\right) \\
&= \lambda \lim_{a\to\infty} \left(\ln\left(e^{-2X'}\right) + \ln\left(\frac{1+e^{-2a+2X'}}{1+e^{-2a-2X'}}\right)\right) \\
&= -\lambda \lim_{a\to\infty} \left(2X' + O\left(e^{-2a}\right)\right) = -2X
\end{aligned} \tag{F.3}$$

that is interpreted in the manner of Cauchy's principal value. Here $O\left(e^{-2a}\right)$ is a function that is at least of linear order in e^{-2a}. By applying the same method we are also able to calculate[213]

$$\begin{aligned}
&\int_{-\infty}^{\infty} dx \frac{x^2}{\cosh^2\left(\frac{x}{\lambda}\right)} = \lambda^3 \lim_{a\to\infty} \int_{-a}^{a} dx' \frac{x'^2}{\cosh^2(x')} \\
=&\lambda^3 \lim_{a\to\infty} \left(\mathrm{Li}_2\left(-e^{-2a}\right) - \mathrm{Li}_2\left(-e^{2a}\right) - 2a\ln\left(e^{2a}+1\right) - 2a\ln\left(e^{-2a}+1\right) + 2a^2\tanh(a)\right)
\end{aligned} \tag{F.4}$$

with the second polylogarithm function $\mathrm{Li}_2(x)$ defined by

$$\frac{\partial}{\partial x}\mathrm{Li}_2(x) = -\frac{\ln(1-x)}{x} \quad \text{and} \quad \mathrm{Li}_2(0) = 0. \tag{F.5}$$

For the calculation of the limit, equation (F.4) can be expressed as a series in e^{-2a}. Using equation (F.5) one finds

$$\mathrm{Li}_2\left(-e^{-2a}\right) = O\left(e^{-2a}\right). \tag{F.6}$$

There is also a series expansion for the other polylogarithm function in equation (F.4). This expression reads[213]

$$\mathrm{Li}_2\left(-e^{2a}\right) = -\frac{1}{2}\ln^2\left(-e^{-2a}\right) + i\pi\ln\left(-e^{-2a}\right) + \frac{\pi^2}{3} + O\left(e^{-2a}\right). \tag{F.7}$$

For the logarithms we find

$$\ln\left(e^{-2a}+1\right) = O\left(e^{-2a}\right) \tag{F.8}$$

and

$$\ln\left(e^{2a}+1\right) = 2a + \ln\left(e^{-2a}+1\right) = 2a + O\left(e^{-2a}\right). \tag{F.9}$$

Finally the hyperbolic tangent is expressed by

$$\tanh(a) = 1 + O\left(e^{-2a}\right). \tag{F.10}$$

Using these expressions and

$$\ln\left(-e^{-2a}\right) = -2a + i\pi \tag{F.11}$$

equation (F.4) can be written as

$$\begin{aligned}\int_{-\infty}^{\infty} dx \frac{x^2}{\cosh^2\left(\frac{x}{\lambda}\right)} =& \lambda^3 \lim_{a\to\infty} \left(\frac{1}{2}\left(-2a + i\pi\right)^2 - i\pi\left(-2a + i\pi\right) - \frac{\pi^2}{3} - 4a^2 + 2a^2\right) \\ =& \lambda^3 \lim_{a\to\infty} \left(2a^2 - 2ai\pi - \frac{\pi^2}{2} + 2ai\pi + \pi^2 - \frac{\pi^2}{3} - 2a^2\right) = \frac{\pi^2\lambda^3}{6}.\end{aligned} \tag{F.12}$$

Acknowledgment

There are many people without whom this work would not have been possible. I thank

- Professor Dr. Daniela Pfannkuche, for giving me the opportunity of a PhD position in her group and for many fruitful discussions,
- my second supervisor Professor Dr. Ulrich Merkt, who was always interested in my research and spend much time in reading my publications prior to submission,
- Professor Dr. Wolfgang Hansen for agreeing to be the second referee of the disputation,
- Professor Dr. Rembert Duine for acting as an external referee for my dissertation.

I thank all my colleagues from the research groups "Quantum Theory of Condensed Matter" and "Nanostructure Physics", from the graduate class "Functional Metal-Semiconductor Hybrid Systems", from the collaborative research center "Magnetismus vom Einzelatom zur Nanostruktur", and from the Cluster of Excellence "Nano-Spintronics". In particular I thank

- Dr. Stellan Bohlens for many helpful discussions about the analytical calculation of vortex dynamics and the calculation of the current paths,
- Dr. André Drews for our inspiring cooperation, for being my never ending source of simulation data, and for our nice times on several conferences in Bad Honnef,
- Dr. Massoud Najafi for our extremely fruitful discussions that were able to start at the verification of micromagnetic simulations and end at a measurement scheme for the non-adiabatic spin torque,
- Privatdozent Dr. Guido Meier without whom the intensive collaboration between theory and experiment would not have been possible,
- Dr. Lars Bocklage for performing many of the experiments that are compared with the theoretical results in this work, especially the difficult measurements that confirm the influence of the risetime,
- Dr. Bernd Güde for sharing his expertise in memory devices,
- Dr. Markus Bolte for the long and inspiring cooperation,
- Michael Martens for fruitful discussions about micromagnetic simulations and vortex dynamics,
- Thomas Kamionka for his patience in explaining the measurement setups to me,
- Dr. Robert Frömter for fruitful discussions about the difficulties in the measurement of the non-adiabatic spin torque,
- Gunnar Selke for sharing his ideas on how to speed up the numerical calculations, especially the calculations of the current paths,
- Claas Abert with whom I discussed the analytical expressions of the Oersted field and their simplification,
- Privatdozent Dr. Alexander Chudnovskiy for interesting discussions,
- Gesche Nahrwold for our discussions about current-induced depinning of domain walls,
- Bodo Krause-Kyora, who manages our simulation cluster that made the presented simulations possible,
- Dr. Katrin Buth for all her work for our graduate class,
- Holger Niehus for many relaxing discussions, especially at late office times when he was learning for his exams and I was writing this thesis,

- Eva-Maria Richter, Dr. Dirk-Sören Lühmann, and Dr. Frank Deuretzbacher for the nice and relaxing atmosphere in our office.

Furthermore I thank

- Professor Dr. Oleg Tchernyshyov, who gave me the opportunity for a great two month visit to his group at the Johns Hopkins University,
- Professor Dr. Hans Fangohr, Dr. Matteo Franchin, and Maximilian Albert for many interesting discussions on several conferences and on their visits to Hamburg,
- my family for continuous encouragement,
- the Deutsche Forschungsgemeinschaft, the Free and Hanseatic City of Hamburg, and the Forschungs- und Wissenschaftsstiftung Hamburg for funding.

References

[1] M. R. Williams, *A History of Computing Technology*. IEEE Computer Society Press 2nd edition (1997).

[2] P. E. Ceruzzi, *A History of Modern Computing*. MIT Press 2nd edition (2003).

[3] G. Binasch, P. Grünberg, F. Saurenbach, and W. Zinn, *Enhanced magnetoresistance in layered magnetic structures with antiferromagnetic interlayer exchange*. Phys. Rev. B **39**, 4828–4830 (1989).

[4] M. N. Baibich, J. M. Broto, A. Fert, F. N. Van Dau, F. Petroff, P. Etienne, G. Creuzet, A. Friederich, and J. Chazelas, *Giant Magnetoresistance of (001)Fe/(001)Cr Magnetic Superlattices*. Phys. Rev. Lett. **61**, 2472–2475 (1988).

[5] M. Julliere, *Tunneling between ferromagnetic films*. Phys. Lett. A **54**, 225 - 226 (1975).

[6] S. S. P. Parkin, C. Kaiser, A. Panchula, P. M. Rice, B. Hughes, M. Samant, and S.-H. Yang, *Giant tunnelling magnetoresistance at room temperature with MgO (100) tunnel barriers*. Nature Mater. **3**, 862 (2004).

[7] S. Yuasa, T. Nagahama, A. Fukushima, Y. Suzuki, and K. Ando, *Giant room-temperature magnetoresistance in single-crystal Fe/MgO/Fe magnetic tunnel junctions*. Nature Mater. **3**, 868 (2004).

[8] S. Ikeda, J. Hayakawa, Y. Ashizawa, Y. M. Lee, K. Miura, H. Hasegawa, M. Tsunoda, F. Matsukura, and H. Ohno, *Tunnel magnetoresistance of 604% at 300 K by suppression of Ta diffusion in CoFeB/MgO/CoFeB pseudo-spin-valves annealed at high temperature*. Appl. Phys. Lett. **93**, 082508 (2008).

[9] R. White, R. Newt, and R. Pease, *Patterned media: a viable route to 50 Gbit/in^2 and up for magnetic recording?*. IEEE Trans. Mag. **33**, 990 -995 (1997).

[10] H. J. Richter, A. Y. Dobin, R. T. Lynch, D. Weller, R. M. Brockie, O. Heinonen, K. Z. Gao, J. Xue, R. J. M. v. d. Veerdonk, P. Asselin, and M. F. Erden, *Recording potential of bit-patterned media*. Appl. Phys. Lett. **88**, 222512 (2006).

[11] H. Richter, A. Dobin, O. Heinonen, K. Gao, R. Veerdonk, R. Lynch, J. Xue, D. Weller, P. Asselin, M. Erden, and R. Brockie, *Recording on Bit-Patterned Media at Densities of 1 Tb/in^2 and Beyond*. IEEE Trans. Mag. **42**, 2255 -2260 (2006).

[12] A. Kikitsu, Y. Kamata, M. Sakurai, and K. Naito, *Recent Progress of Patterned Media*. IEEE Trans. Mag. **43**, 3685 -3688 (2007).

[13] A. Kikitsu, *Prospects for bit patterned media for high-density magnetic recording*. J. Magn. Magn. Mat. **321**, 526 - 530 (2009).

[14] A. Moser, O. Hellwig, D. Kercher, and E. Dobisz, *Off-track margin in bit patterned media*. Appl. Phys. Lett. **91**, 162502 (2007).

[15] Y. Tang, K. Moon, and H. J. Lee, *Write Synchronization in Bit-Patterned Media*. IEEE Trans. Mag. **45**, 822 -827 (2009).

[16] R. Victora and X. Shen, *Composite media for perpendicular magnetic recording*. IEEE Trans. Mag. **41**, 537 - 542 (2005).

[17] A. Kikitsu, T. Kai, T. Nagase, and J.-I. Akiyama, *A concept of exchange-coupled recording medium for heat-assisted magnetic recording*. J. Appl. Phys. **97**, 10P701 (2005).

[18] J. Åkerman, *Toward a Universal Memory*. Science **308**, 508-510 (2005).

[19] L. Berger, *Low-field magnetoresistance and domain drag in ferromagnets*. J. Appl. Phys. **49**, 2156 (1978).

[20] L. Berger, *Exchange interaction between ferromagnetic domain wall and electric current in very thin metallic films*. J. Appl. Phys. **55**, 1954 (1984).

[21] L. Berger, *Emission of spin waves by a magnetic multilayer traversed by a current*. Phys. Rev. B **54**, 9353 (1996).

[22] J. C. Slonczewski, *Current-driven excitation of magnetic multilayers*. J. Magn. Magn. Mat. **159**, L1 (1996).

[23] Y. B. Bazaliy, B. A. Jones, and S.-C. Zhang, *Modification of the Landau-Lifshitz equation in the presence of a spin-polarized current in colossal- and giant-magnetoresistive materials*. Phys. Rev. B **57**, R3213 (1998).

[24] S. Zhang and Z. Li, *Roles of Nonequilibrium Conduction Electrons on the Magnetization Dynamics of Ferromagnets*. Phys. Rev. Lett. **93**, 127204 (2004).

[25] K. Bussmann, G. A. Prinz, S.-F. Cheng, and D. Wang, *Switching of vertical giant magnetoresistance devices by current through the device*. Appl. Phys. Lett. **75**, 2476-2478 (1999).

[26] E. B. Myers, D. C. Ralph, J. A. Katine, R. N. Louie, and R. A. Buhrman, *Current-Induced Switching of Domains in Magnetic Multilayer Devices*. Science **285**, 867 (1999).

[27] J. A. Katine, F. J. Albert, R. A. Buhrman, E. B. Myers, and D. C. Ralph, *Current-Driven Magnetization Reversal and Spin-Wave Excitations in Co /Cu /Co Pillars*. Phys. Rev. Lett. **84**, 3149 (2000).

[28] B. E. Argyle, E. Terrenzio, and J. C. Slonczewski, *Magnetic Vortex Dynamics Using the Optical Cotton-Mouton Effect*. Phys. Rev. Lett. **53**, 190 (1984).

[29] R. Allenspach, *Ultrathin films: magnetism on the microscopic scale*. J. Magn. Magn. Mat. **129**, 160 - 185 (1994).

[30] A. Aharoni, *Demagnetizing factors for rectangular ferromagnetic prisms*. J. Appl. Phys. **83**, 3432 (1998).

[31] T. Shinjo, T. Okuno, R. Hassdorf, K. Shigeto, and T. Ono, *Magnetic Vortex Core Observation in Circular Dots of Permalloy*. Science **289**, 930 (2000).

[32] K. Y. Guslienko, V. Novosad, Y. Otani, H. Shima, and K. Fukamichi, *Field evolution of magnetic vortex state in ferromagnetic disks*. Appl. Phys. Lett. **78**, 3848 (2001).

[33] K. Y. Guslienko, V. Novosad, Y. Otani, H. Shima, and K. Fukamichi, *Magnetization reversal due to vortex nucleation, displacement, and annihilation in submicron ferromagnetic dot arrays*. Phys. Rev. B **65**, 024414 (2001).

[34] A. Wachowiak, J. Wiebe, M. Bode, O. Pietzsch, M. Morgenstern, and R. Wiesendanger, *Direct Observation of Internal Spin Structure of Magnetic Vortex Cores*. Science **298**, 577 (2002).

[35] H. Koo, C. Krafft, and R. D. Gomez, *Current-controlled bi-stable domain configurations in $Ni_{81}Fe_{19}$ elements: An approach to magnetic memory devices*. Appl. Phys. Lett. **81**, 862 (2002).

[36] K. Y. Guslienko, B. A. Ivanov, V. Novosad, Y. Otani, H. Shima, and K. Fukamichi, *Eigenfrequencies of vortex state excitations in magnetic submicron-size disks*. J. Appl. Phys. **91**, 8037 (2002).

[37] K. Shigeto, T. Okuno, K. Mibu, T. Shinjo, and T. Ono, *Magnetic force microscopy observation of antivortex core with perpendicular magnetization in patterned thin film of permalloy*. Appl. Phys. Lett. **80**, 4190 (2002).

[38] A. Thiaville, J. M. García, R. Dittrich, J. Miltat, and T. Schrefl, *Micromagnetic study of Bloch-point-mediated vortex core reversal*. Phys. Rev. B **67**, 094410 (2003).

[39] J. P. Park, P. Eames, D. M. Engebretson, J. Berezovsky, and P. A. Crowell, *Imaging of spin dynamics in closure domain and vortex structures*. Phys. Rev. B **67**, 020403 (2003).

[40] S.-B. Choe, Y. Acremann, A. Scholl, A. Bauer, A. Doran, J. Stohr, and H. A. Padmore, *Vortex Core-Driven Magnetization Dynamics*. Science **304**, 420 (2004).

[41] M. Steiner and J. Nitta, *Control of magnetization states in microstructured permalloy rings*. Appl. Phys. Lett. **84**, 939 (2004).

[42] I. N. Krivorotov, N. C. Emley, J. C. Sankey, S. I. Kiselev, D. C. Ralph, and R. A. Buhrman, *Time-Domain Measurements of Nanomagnet Dynamics Driven by Spin-Transfer Torques*. Science **307**, 228 (2005).

[43] R. D. McMichael and M. D. Stiles, *Magnetic normal modes of nanoelements*. J. Appl. Phys. **97**, 10J901 (2005).

[44] K. Y. Guslienko, W. Scholz, R. W. Chantrell, and V. Novosad, *Vortex-state oscillations in soft magnetic cylindrical dots*. Phys. Rev. B **71**, 144407 (2005).

[45] D. D. Sheka, J. P. Zagorodny, J.-G. Caputo, Y. Gaididei, and F. G. Mertens, *Vortex motion in a finite-size easy-plane ferromagnet and application to a nanodot*. Phys. Rev. B **71**, 134420 (2005).

[46] T. Taniuchi, M. Oshima, H. Akinaga, and K. Ono, *Vortex-chirality control in mesoscopic disk magnets observed by photoelectron emission microscopy*. J. Appl. Phys. **97**, 10J904 (2005).

[47] B. Van Waeyenberge, A. Puzic, H. Stoll, K. W. Chou, T. Tyliszczak, R. Hertel, M. Fähnle, H. Brückl, K. Rott, G. Reiss, I. Neudecker, D. Weiss, C. H. Back, and G. Schütz, *Magnetic vortex core reversal by excitation with short bursts of an alternating field*. Nature **444**, 461 (2006).

[48] K. Y. Guslienko, *Low-frequency vortex dynamic susceptibility and relaxation in mesoscopic ferromagnetic dots*. Appl. Phys. Lett. **89**, 022510 (2006).

[49] K. Y. Guslienko, X. F. Han, D. J. Keavney, R. Divan, and S. D. Bader, *Magnetic Vortex Core Dynamics in Cylindrical Ferromagnetic Dots*. Phys. Rev. Lett. **96**, 067205 (2006).

[50] J. Shibata, Y. Nakatani, G. Tatara, H. Kohno, and Y. Otani, *Current-induced magnetic vortex motion by spin-transfer torque*. Phys. Rev. B **73**, 020403 (2006).

[51] R. Hertel and C. M. Schneider, *Exchange Explosions: Magnetization Dynamics during Vortex-Antivortex Annihilation*. Phys. Rev. Lett. **97**, 177202 (2006).

[52] M. Bolte, G. Meier, and C. Bayer, *Spin-wave eigenmodes of Landau domain patterns*. Phys. Rev. B **73**, 052406 (2006).

[53] Y. Liu, S. Gliga, R. Hertel, and C. M. Schneider, *Current-induced magnetic vortex core switching in a Permalloy nanodisk*. Appl. Phys. Lett. **91**, 112501 (2007).

[54] K. Yamada, S. Kasai, Y. Nakatani, K. Kobayashi, H. Kohno, A. Thiaville, and T. Ono, *Electrical switching of the vortex core in a magnetic disk*. Nature Mater. **6**, 270 (2007).

[55] V. S. Pribiag, I. N. Krivorotov, G. D. Fuchs, P. M. Braganca, O. Ozatay, J. C. Sankey, D. C. Ralph, and R. A. Buhrman, *Magnetic vortex oscillator driven by d.c. spin-polarized current*. Nature Phys. **3**, 498 (2007).

[56] F. Giesen, J. Podbielski, B. Botters, and D. Grundler, *Vortex circulation control in large arrays of asymmetric magnetic rings*. Phys. Rev. B **75**, 184428 (2007).

[57] S.-K. Kim, Y.-S. Choi, K.-S. Lee, K. Y. Guslienko, and D.-E. Jeong, *Electric-current-driven vortex-core reversal in soft magnetic nanodots*. Appl. Phys. Lett. **91**, 082506 (2007).

[58] R. Hertel, S. Gliga, M. Fähnle, and C. M. Schneider, *Ultrafast Nanomagnetic Toggle Switching of Vortex Cores*. Phys. Rev. Lett. **98**, 117201 (2007).

[59] K.-S. Lee, K. Y. Guslienko, J.-Y. Lee, and S.-K. Kim, *Ultrafast vortex-core reversal dynamics in ferromagnetic nanodots*. Phys. Rev. B **76**, 174410 (2007).

[60] J.-G. Caputo, Y. Gaididei, F. G. Mertens, and D. D. Sheka, *Vortex Polarity Switching by a Spin-Polarized Current*. Phys. Rev. Lett. **98**, 056604 (2007).

[61] K.-S. Lee and S.-K. Kim, *Gyrotropic linear and nonlinear motions of a magnetic vortex in soft magnetic nanodots*. Appl. Phys. Lett. **91**, 132511 (2007).

[62] K.-S. Lee, S.-K. Kim, Y.-S. Yu, Y.-S. Choi, K. Y. Guslienko, H. Jung, and P. Fischer, *Universal Criterion and Phase Diagram for Switching a Magnetic Vortex Core in Soft Magnetic Nanodots*. Phys. Rev. Lett. **101**, 267206 (2008).

[63] K. Y. Guslienko, K.-S. Lee, and S.-K. Kim, *Dynamic Origin of Vortex Core Switching in Soft Magnetic Nanodots*. Phys. Rev. Lett. **100**, 027203 (2008).

[64] K.-S. Lee, Y.-S. Yu, Y.-S. Choi, D.-E. Jeong, and S.-K. Kim, *Oppositely rotating eigenmodes of spin-polarized current-driven vortex gyrotropic motions in elliptical nanodots*. Appl. Phys. Lett. **92**, 192513 (2008).

[65] K.-S. Lee and S.-K. Kim, *Two circular-rotational eigenmodes and their giant resonance asymmetry in vortex gyrotropic motions in soft magnetic nanodots*. Phys. Rev. B **78**, 014405 (2008).

[66] S. Kasai, K. Nakano, K. Kondou, N. Ohshima, K. Kobayashi, and T. Ono, *Three-Terminal Device Based on the Current-Induced Magnetic Vortex Dynamics with the Magnetic Tunnel Junction*. Appl. Phys. Express **1**, 091302 (2008).

[67] S. Kasai, P. Fischer, M.-Y. Im, K. Yamada, Y. Nakatani, K. Kobayashi, H. Kohno, and T. Ono, *Probing the Spin Polarization of Current by Soft X-Ray Imaging of Current-Induced Magnetic Vortex Dynamics*. Phys. Rev. Lett. **101**, 237203 (2008).

[68] R. Moriya, L. Thomas, M. Hayashi, Y. B. Bazaliy, C. Rettner, and S. S. P. Parkin, *Probing vortex-core dynamics using current-induced resonant excitation of a trapped domain wall*. Nature Phys. **4**, 368 (2008).

[69] A. B. Butenko, A. A. Leonov, A. N. Bogdanov, and U. K. Rößler, *Theory of vortex states in magnetic nanodisks with induced Dzyaloshinskii-Moriya interactions*. Phys. Rev. B **80**, 134410 (2009).

[70] Y. Gaididei, V. P. Kravchuk, and D. D. Sheka, *Magnetic vortex dynamics induced by an electrical current*. Int. J. Quantum Chem. **110**, 83 (2010).

[71] C. Moutafis, S. Komineas, and J. A. C. Bland, *Dynamics and switching processes for magnetic bubbles in nanoelements*. Phys. Rev. B **79**, 224429 (2009).

[72] A. Bisig, J. Rhensius, M. Kammerer, M. Curcic, H. Stoll, G. Schütz, B. Van Waeyenberge, K. W. Chou, T. Tyliszczak, L. J. Heyderman, S. Krzyk, A. von Bieren, and M. Kläui, *Direct imaging of current induced magnetic vortex gyration in an asymmetric potential well*. Appl. Phys. Lett. **96**, 152506 (2010).

[73] K. Nakano, D. Chiba, K. Sekiguchi, S. Kasai, N. Ohshima, K. Kobayashi, and T. Ono, *Electrical Detection of Vortex Core Polarity in Ferromagnetic Disk*. Appl. Phys. Express **3**, 053001 (2010).

[74] S.-H. Chung, D. Pierce, and J. Unguris, *Simultaneous measurement of magnetic vortex polarity and chirality using scanning electron microscopy with polarization analysis (SEMPA)*. Ultramicroscopy **110**, 177 (2010).

[75] F. Garcia, H. Westfahl, J. Schoenmaker, E. J. Carvalho, A. D. Santos, M. Pojar, A. C. Seabra, R. Belkhou, A. Bendounan, E. R. P. Novais, and A. P. Guimarães, *Tailoring magnetic vortices in nanostructures*. Appl. Phys. Lett. **97**, 022501 (2010).

[76] S. Hankemeier, A. Kobs, R. Frömter, and H. P. Oepen, *Controlling the properties of vortex domain walls via magnetic seeding fields*. Phys. Rev. B **82**, 064414 (2010).

[77] S. Bohlens, B. Krüger, A. Drews, M. Bolte, G. Meier, and D. Pfannkuche, *Current controlled random-access memory based on magnetic vortex handedness*. Appl. Phys. Lett. **93**, 142508 (2008).

[78] A. Drews, B. Krüger, G. Meier, S. Bohlens, L. Bocklage, T. Matsuyama, and M. Bolte, *Current- and field-driven magnetic antivortices for nonvolatile data storage*. Appl. Phys. Lett. **94**, 062504 (2009).

[79] S. S. P. Parkin, M. Hayashi, and L. Thomas, *Magnetic Domain-Wall Racetrack Memory*. Science **320**, 190 (2008).

[80] D. A. Allwood, G. Xiong, M. D. Cooke, C. C. Faulkner, D. Atkinson, N. Vernier, and R. P. Cowburn, *Submicrometer Ferromagnetic NOT Gate and Shift Register*. Science **296**, 2003 (2002).

[81] D. A. Allwood, G. Xiong, C. C. Faulkner, D. Atkinson, D. Petit, and R. P. Cowburn, *Magnetic Domain-Wall Logic*. Science **309**, 1688 (2005).

[82] D. Bouzidi and H. Suhl, *Motion of a Bloch domain wall*. Phys. Rev. Lett. **65**, 2587 (1990).

[83] T. Ono, H. Miyajima, K. Shigeto, K. Mibu, N. Hosoito, and T. Shinjo, *Propagation of a Magnetic Domain Wall in a Submicrometer Magnetic Wire*. Science **284**, 468 (1999).

[84] M. Redjdal, J. Giusti, M. F. Ruane, and F. B. Humphrey, *Thickness dependent wall mobility in thin Permalloy films*. J. Appl. Phys. **91**, 7547 (2002).

[85] M. Kläui, C. A. F. Vaz, J. A. C. Bland, W. Wernsdorfer, G. Faini, E. Cambril, and L. J. Heyderman, *Domain wall motion induced by spin polarized currents in ferromagnetic ring structures*. Appl. Phys. Lett. **83**, 105 (2003).

[86] J. Grollier, P. Boulenc, V. Cros, A. Hamzić, A. Vaurès, A. Fert, and G. Faini, *Switching a spin valve back and forth by current-induced domain wall motion*. Appl. Phys. Lett. **83**, 509 (2003).

[87] Y. Nakatani, A. Thiaville, and J. Miltat, *Faster magnetic walls in rough wires*. Nature Mater. **2**, 521 (2003).

[88] A. Yamaguchi, T. Ono, S. Nasu, K. Miyake, K. Mibu, and T. Shinjo, *Real-Space Observation of Current-Driven Domain Wall Motion in Submicron Magnetic Wires*. Phys. Rev. Lett. **92**, 077205 (2004).

[89] A. Yamaguchi, T. Ono, S. Nasu, K. Miyake, K. Mibu, and T. Shinjo, *Erratum: Real-Space Observation of Current-Driven Domain Wall Motion in Submicron Magnetic Wires [Phys. Rev. Lett. 92, 077205 (2004)]*. Phys. Rev. Lett. **96**, 179904 (2006).

[90] M. Kläui, C. A. F. Vaz, J. A. C. Bland, L. J. Heyderman, F. Nolting, A. Pavlovska, E. Bauer, S. Cherifi, S. Heun, and A. Locatelli, *Head-to-head domain-wall phase diagram in mesoscopic ring magnets*. Appl. Phys. Lett. **85**, 5637 (2004).

[91] A. Yamaguchi, S. Nasu, H. Tanigawa, T. Ono, K. Miyake, K. Mibu, and T. Shinjo, *Effect of Joule heating in current-driven domain wall motion*. Appl. Phys. Lett. **86**, 012511 (2005).

[92] G. Tatara and H. Kohno, *Theory of Current-Driven Domain Wall Motion: Spin Transfer versus Momentum Transfer*. Phys. Rev. Lett. **92**, 086601 (2004).

[93] Z. Li and S. Zhang, *Domain-wall dynamics driven by adiabatic spin-transfer torques*. Phys. Rev. B **70**, 024417 (2004).

[94] M. Yamanouchi, D. Chiba, F. Matsukura, and H. Ohno, *Current-induced domain-wall switching in a ferromagnetic semiconductor structure*. Nature **428**, 539 (2004).

[95] E. Saitoh, H. Miyajima, T. Yamaoka, and G. Tatara, *Current-induced resonance and mass determination of a single magnetic domain wall*. Nature **432**, 203 (2004).

[96] G. Tatara, N. Vernier, and J. Ferré, *Universality of thermally assisted magnetic domain-wall motion under spin torque*. Appl. Phys. Lett. **86**, 252509 (2005).

[97] G. Tatara, E. Saitoh, M. Ichimura, and H. Kohno, *Domain-wall displacement triggered by an ac current below threshold*. Appl. Phys. Lett. **86**, 232504 (2005).

[98] M. Kläui, P.-O. Jubert, R. Allenspach, A. Bischof, J. A. C. Bland, G. Faini, U. Rüdiger, C. A. F. Vaz, L. Vila, and C. Vouille, *Direct Observation of Domain-Wall Configurations Transformed by Spin Currents*. Phys. Rev. Lett. **95**, 026601 (2005).

[99] M. Kläui, C. A. F. Vaz, J. A. C. Bland, W. Wernsdorfer, G. Faini, E. Cambril, L. J. Heyderman, F. Nolting, and U. Rüdiger, *Controlled and Reproducible Domain Wall Displacement by Current Pulses Injected into Ferromagnetic Ring Structures*. Phys. Rev. Lett. **94**, 106601 (2005).

[100] J. He, Z. Li, and S. Zhang, *Current-driven domain-wall depinning*. J. Appl. Phys. **98**, 016108 (2005).

[101] Z. Li, J. He, and S. Zhang, *Effects of spin current on ferromagnets (invited).* J. Appl. Phys. **99**, 08Q702 (2006).

[102] J. He, Z. Li, and S. Zhang, *Current-driven vortex domain wall dynamics by micromagnetic simulations.* Phys. Rev. B **73**, 184408 (2006).

[103] M. Kläui, M. Laufenberg, L. Heyne, D. Backes, U. Rüdiger, C. A. F. Vaz, J. A. C. Bland, L. J. Heyderman, S. Cherifi, A. Locatelli, T. O. Mentes, and L. Aballe, *Current-induced vortex nucleation and annihilation in vortex domain walls.* Appl. Phys. Lett. **88**, 232507 (2006).

[104] M. H. Park, Y. K. Hong, B. C. Choi, M. J. Donahue, H. Han, and S. H. Gee, *Vortex head-to-head domain walls and their formation in onion-state ring elements.* Phys. Rev. B **73**, 094424 (2006).

[105] L. Thomas, M. Hayashi, X. Jiang, R. Moriya, C. Rettner, and S. S. P. Parkin, *Oscillatory dependence of current-driven magnetic domain wall motion on current pulse length.* Nature **443**, 197 (2006).

[106] V. K. Dugaev, V. R. Vieira, P. D. Sacramento, J. Barnaś, M. A. N. Araújo, and J. Berakdar, *Current-induced motion of a domain wall in a magnetic nanowire.* Phys. Rev. B **74**, 054403 (2006).

[107] G. Meier, M. Bolte, U. Merkt, B. Krüger, and D. Pfannkuche, *Current-induced domain-wall motion in permalloy semi rings.* J. Magn. Magn. Mat. **316**, e966 (2007).

[108] T. Jourdan, F. Lançon, and A. Marty, *Pinning of magnetic domain walls to structural defects in thin layers within a Heisenberg-type model.* Phys. Rev. B **75**, 094422 (2007).

[109] M. Hara, T. Kimura, and Y. Otani, *Controlled depinning of domain walls in a ferromagnetic ring circuit.* Appl. Phys. Lett. **90**, 242504 (2007).

[110] P. Vavassori, V. Metlushko, and B. Ilic, *Domain wall displacement by current pulses injection in submicrometer Permalloy square ring structures.* Appl. Phys. Lett. **91**, 093114 (2007).

[111] L. Thomas, M. Hayashi, X. Jiang, R. Moriya, C. Rettner, and S. Parkin, *Resonant Amplification of Magnetic Domain-Wall Motion by a Train of Current Pulses.* Science **315**, 1553 (2007).

[112] M. Hayashi, L. Thomas, C. Rettner, R. Moriya, Y. B. Bazaliy, and S. S. P. Parkin, *Current Driven Domain Wall Velocities Exceeding the Spin Angular Momentum Transfer Rate in Permalloy Nanowires.* Phys. Rev. Lett. **98**, 037204 (2007).

[113] D. Bedau, M. Kläui, S. Krzyk, U. Rüdiger, G. Faini, and L. Vila, *Detection of Current-Induced Resonance of Geometrically Confined Domain Walls.* Phys. Rev. Lett. **99**, 146601 (2007).

[114] F. Junginger, M. Kläui, D. Backes, U. Rüdiger, T. Kasama, R. E. Dunin-Borkowski, L. J. Heyderman, C. A. F. Vaz, and J. A. C. Bland, *Spin torque and heating effects in current-induced domain wall motion probed by transmission electron microscopy.* Appl. Phys. Lett. **90**, 132506 (2007).

[115] D. Backes, C. Schieback, M. Kläui, F. Junginger, H. Ehrke, P. Nielaba, U. Rüdiger, L. J. Heyderman, C. S. Chen, T. Kasama, R. E. Dunin-Borkowski, C. A. F. Vaz, and J. A. C. Bland, *Transverse domain walls in nanoconstrictions.* Appl. Phys. Lett. **91**, 112502 (2007).

[116] E.-M. Hempe, M. Kläui, T. Kasama, D. Backes, F. Junginger, S. Krzyk, L. J. Heyderman, R. Dunin-Borkowski, and U. Rüdiger, *Domain walls, domain wall transformations and structural changes in permalloy nanowires when subjected to current pulses.* Phys. Stat. Sol. (a) **204**, 3922 (2007).

[117] R. A. Duine, A. S. Núñez, and A. H. MacDonald, *Thermally Assisted Current-Driven Domain-Wall Motion*. Phys. Rev. Lett. **98**, 056605 (2007).

[118] D. J. Clarke, O. A. Tretiakov, G.-W. Chern, Y. B. Bazaliy, and O. Tchernyshyov, *Dynamics of a vortex domain wall in a magnetic nanostrip: Application of the collective-coordinate approach*. Phys. Rev. B **78**, 134412 (2008).

[119] M. Kläui, *Head-to-head domain walls in magnetic nanostructures*. J. Phys. **20**, 313001 (2008).

[120] M. Hayashi, L. Thomas, R. Moriya, C. Rettner, and S. S. P. Parkin, *Current-Controlled Magnetic Domain-Wall Nanowire Shift Register*. Science **320**, 209 (2008).

[121] L. Heyne, M. Kläui, D. Backes, T. A. Moore, S. Krzyk, U. Rüdiger, L. J. Heyderman, A. F. Rodríguez, F. Nolting, T. O. Mentes, M. A. Niño, A. Locatelli, K. Kirsch, and R. Mattheis, *Relationship between Nonadiabaticity and Damping in Permalloy Studied by Current Induced Spin Structure Transformations*. Phys. Rev. Lett. **100**, 066603 (2008).

[122] Y. Tserkovnyak, A. Brataas, and G. E. Bauer, *Theory of current-driven magnetization dynamics in inhomogeneous ferromagnets*. J. Magn. Magn. Mat. **320**, 1282 (2008).

[123] T. A. Moore, M. Kläui, L. Heyne, P. Möhrke, D. Backes, J. Rhensius, U. Rüdiger, L. J. Heyderman, J.-U. Thiele, G. Woltersdorf, C. H. Back, A. Fraile Rodríguez, F. Nolting, T. O. Mentes, M. A. Niño, A. Locatelli, A. Potenza, H. Marchetto, S. Cavill, and S. S. Dhesi, *Scaling of spin relaxation and angular momentum dissipation in permalloy nanowires*. Phys. Rev. B **80**, 132403 (2009).

[124] L. Heyne, J. Rhensius, A. Bisig, S. Krzyk, P. Punke, M. Kläui, L. J. Heyderman, L. L. Guyader, and F. Nolting, *Direct observation of high velocity current induced domain wall motion*. Appl. Phys. Lett. **96**, 032504 (2010).

[125] L. San Emeterio Alvarez, K.-Y. Wang, S. Lepadatu, S. Landi, S. J. Bending, and C. H. Marrows, *Spin-Transfer-Torque-Assisted Domain-Wall Creep in a Co/Pt Multilayer Wire*. Phys. Rev. Lett. **104**, 137205 (2010).

[126] C. Burrowes, A. P. Mihai, D. Ravelosona, J.-V. Kim, C. Chappert, L. Vila, A. Marty, Y. Samson, F. Garcia-Sanchez, L. D. Buda-Prejbeanu, I. Tudosa, E. E. Fullerton, and J.-P. Attane, *Non-adiabatic spin-torques in narrow magnetic domain walls*. Nature Phys. **6**, 17 (2010).

[127] L. Landau and E. Lifshitz, *On the Theory of the Dispersion of Magnetic Permeability in Ferromagnetic Bodies*. Phys. Zeitsch. Sow. **8**, 153 (1935).

[128] L. Landau and E. Lifshitz, *On the Theory of the Dispersion of Magnetic Permeability in Ferromagnetic Bodies*. Ukrainian Journal of Physics **53**, 14 (2008).

[129] B. Krüger, D. Pfannkuche, M. Bolte, G. Meier, and U. Merkt, *Current-driven domain-wall dynamics in curved ferromagnetic nanowires*. Phys. Rev. B **75**, 054421 (2007).

[130] M. Najafi, B. Krüger, S. Bohlens, G. Selke, B. Güde, M. Bolte, and D. P. F. Möller, *The micromagnetic modeling and simulation kit M^3S for the simulation of the dynamic response of ferromagnets to electric currents*. In H. Vakilzadian, R. Huntsinger, T. Ericsen, and R. Crosbie editors, 2008 Grand Challenges in Modeling & Simulation Conference (GCMS), pages 427-434 (2008).

[131] M. Najafi, G. Selke, B. Krüger, B. Güde, B. Krause-Kyora, M. Bolte, G. Meier, and D. P. F. Möller, *A Case Study for the Parallelization of a Complex MATLAB Program with Respect to Maintainability*. In J. S. Gauthier editor, 2008 Huntsville Simulation Conference HSC'08, pages 309-315 (2008).

[132] The MicroMagnum software by G. Selke, C. Abert, T. Gerhardt, and A. Drews. Currently the program can be obtained at http://micromagnum.informatik.uni-hamburg.de.

[133] T. Fischbacher, M. Franchin, G. Bordignon, and H. Fangohr, *A Systematic Approach to Multiphysics Extensions of Finite-Element-Based Micromagnetic Simulations: Nmag*. IEEE Trans. Mag. **43**, 2896 -2898 (2007).

[134] A. Vansteenkiste and B. Van de Wiele, *MuMax: A new high-performance micromagnetic simulation tool*. J. Magn. Magn. Mat. **323**, 2585 - 2591 (2011).

[135] A. Vanhaverbeke, A. Bischof, and R. Allenspach, *Control of Domain Wall Polarity by Current Pulses*. Phys. Rev. Lett. **101**, 107202 (2008).

[136] The LLG Micromagnetics Simulator by M. R. Scheinfein. Currently the program can be obtained at http://llgmicro.home.mindspring.com.

[137] The MicroMagus software by D. V. Berkov and N. L. Gorn. Currently the program can be obtained at http://www.micromagus.de.

[138] The M^3 software by C. K. A. Mewes and T. Mewes. Currently the program can be obtained at http://bama.ua.edu/˜tmewes/Mcube/Mcube.shtml.

[139] **OOMMF User's Guide, Version 1.0** M.J. Donahue and D.G. Porter Interagency Report **NISTIR 6376**, National Institute of Standards and Technology, Gaithersburg, MD (Sept 1999) (http://math.nist.gov/oommf/).

[140] T. L. Gilbert, *A Lagrangian Formulation of the Gyromagnetic Equation of the Magnetization Field*. Phys. Rev. **100**, 1243 (1955).

[141] J. P. Nibarger, R. Lopusnik, and T. J. Silva, *Damping as a function of pulsed field amplitude and bias field in thin film Permalloy*. Appl. Phys. Lett. **82**, 2112 (2003).

[142] M. L. Schneider, T. Gerrits, A. B. Kos, and T. J. Silva, *Gyromagnetic damping and the role of spin-wave generation in pulsed inductive microwave magnetometry*. Appl. Phys. Lett. **87**, 072509 (2005).

[143] Z. Liu, F. Giesen, X. Zhu, R. D. Sydora, and M. R. Freeman, *Spin Wave Dynamics and the Determination of Intrinsic Damping in Locally Excited Permalloy Thin Films*. Phys. Rev. Lett. **98**, 087201 (2007).

[144] S. Bohlens, *Interplay of Inhomogeneous Currents and Magnetization Textures*. PhD thesis Universtät Hamburg (2010).

[145] J. D. Jackson, *Classical electrodynamics*. Wiley 2nd edition (1975).

[146] W. Rave and A. Hubert, *Magnetic ground state of a thin-film element*. IEEE Trans. Mag. **36**, 3886 -3899 (2000).

[147] P.-O. Jubert, J.-C. Toussaint, O. Fruchart, C. Meyer, and Y. Samson, *Flux-closure-domain states and demagnetizing energy determination in sub-micron size magnetic dots*. Europhys. Lett. **63**, 132 (2003).

[148] A. Hubert and R. Schäfer, *Magnetic Domains the Analysis of Magnetic Microstructures*. Springer 3rd edition (2009).

[149] H. Kohno, G. Tatara, and J. Shibata, *Microscopic Calculation of Spin Torques in Disordered Ferromagnets*. J. Phys. Soc. Jap. **75**, 113706 (2006).

[150] Y. Tserkovnyak, H. J. Skadsem, A. Brataas, and G. E. W. Bauer, *Current-induced magnetization dynamics in disordered itinerant ferromagnets*. Phys. Rev. B **74**, 144405 (2006).

[151] R. A. Duine, A. S. Núñez, J. Sinova, and A. H. MacDonald, *Functional Keldysh theory of spin torques*. Phys. Rev. B **75**, 214420 (2007).

[152] G. Tatara, H. Kohno, J. Shibata, Y. Lemaho, and K.-J. Lee, *Spin Torque and Force due to Current for General Spin Textures*. J. Phys. Soc. Jap. **76**, 054707 (2007).

[153] A. Thiaville, Y. Nakatani, J. Miltat, and Y. Suzuki, *Micromagnetic understanding of current-driven domain wall motion in patterned nanowires*. Europhys. Lett. **69**, 990 (2005).

[154] C. Ziethen, O. Schmidt, G. Fecher, C. Schneider, G. Schönhense, R. Frömter, M. Seider, K. Grzelakowski, M. Merkel, D. Funnemann, W. Swiech, H. Gundlach, and J. Kirschner, *Fast elemental mapping and magnetic imaging with high lateral resolution using a novel photoemission microscope*. Journal of Electron Spectroscopy and Related Phenomena **88-91**, 983 - 989 (1998).

[155] K. Perzlmaier, M. Buess, C. H. Back, V. E. Demidov, B. Hillebrands, and S. O. Demokritov, *Spin-Wave Eigenmodes of Permalloy Squares with a Closure Domain Structure*. Phys. Rev. Lett. **94**, 057202 (2005).

[156] B. Krüger, A. Drews, M. Bolte, U. Merkt, D. Pfannkuche, and G. Meier, *Vortices and antivortices as harmonic oscillators*. J. Appl. Phys. **103**, 07A501 (2008).

[157] A. Drews, B. Krüger, M. Bolte, and G. Meier, *Current- and field-driven magnetic antivortices*. Phys. Rev. B **77**, 094413 (2008).

[158] A. A. Belavin and A. M. Polyakov, *Metastable states of two-dimensional isotropic ferromagnets*. JETP Lett. **22**, 245 (1975).

[159] O. A. Tretiakov and O. Tchernyshyov, *Vortices in thin ferromagnetic films and the skyrmion number*. Phys. Rev. B **75**, 012408 (2007).

[160] T. Senthil, A. Vishwanath, L. Balents, S. Sachdev, and M. P. A. Fisher, *Deconfined Quantum Critical Points*. Science **303**, 1490-1494 (2004).

[161] S. Kasai, Y. Nakatani, K. Kobayashi, H. Kohno, and T. Ono, *Current-Driven Resonant Excitation of Magnetic Vortices*. Phys. Rev. Lett. **97**, 107204 (2006).

[162] H. Stoll, A. Puzic, B. van Waeyenberge, P. Fischer, J. Raabe, M. Buess, T. Haug, R. Höllinger, C. Back, D. Weiss, and G. Denbeaux, *High-resolution imaging of fast magnetization dynamics in magnetic nanostructures*. Appl. Phys. Lett. **84**, 3328 (2004).

[163] J. Raabe, C. Quitmann, C. H. Back, F. Nolting, S. Johnson, and C. Buehler, *Quantitative Analysis of Magnetic Excitations in Landau Flux-Closure Structures Using Synchrotron-Radiation Microscopy*. Phys. Rev. Lett. **94**, 217204 (2005).

[164] M. R. Scheinfein, J. Unguris, M. H. Kelley, D. T. Pierce, and R. J. Celotta, *Scanning electron microscopy with polarization analysis (SEMPA)*. Review of Scientific Instruments **61**, 2501 (1990).

[165] R. McMichael and M. Donahue, *Head to head domain wall structures in thin magnetic strips*. IEEE Trans. Mag. **33**, 4167 -4169 (1997).

[166] Y. Nakatani, A. Thiaville, and J. Miltat, *Head-to-head domain walls in soft nano-strips: a refined phase diagram*. J. Magn. Magn. Mat. **290-291**, 750 - 753 (2005).

[167] W. C. Uhlig, M. J. Donahue, D. T. Pierce, and J. Unguris, *Direct imaging of current-driven domain walls in ferromagnetic nanostripes*. J. Appl. Phys. **105**, 103902 (2009).

[168] N. L. Schryer and L. R. Walker, *The motion of 180° domain walls in uniform dc magnetic fields*. J. Appl. Phys. **45**, 5406 (1974).

[169] M. Tsoi, R. E. Fontana, and S. S. P. Parkin, *Magnetic domain wall motion triggered by an electric current*. Appl. Phys. Lett. **83**, 2617 (2003).

[170] M. Hayashi, L. Thomas, Y. B. Bazaliy, C. Rettner, R. Moriya, X. Jiang, and S. S. P. Parkin, *Influence of Current on Field-Driven Domain Wall Motion in Permalloy Nanowires from Time Resolved Measurements of Anisotropic Magnetoresistance*. Phys. Rev. Lett. **96**, 197207 (2006).

[171] A. Kunz, *Field induced domain wall collisions in thin magnetic nanowires*. Appl. Phys. Lett. **94**, 132502 (2009).

[172] G. Meier, M. Bolte, R. Eiselt, B. Krüger, D.-H. Kim, and P. Fischer, *Direct Imaging of Stochastic Domain-Wall Motion Driven by Nanosecond Current Pulses*. Phys. Rev. Lett. **98**, 187202 (2007).

[173] S. Yang and J. L. Erskine, *Spin-transfer-torque-driven domin-wall dynamics in Permalloy nanowires*. Phys. Rev. B **75**, 220403 (2007).

[174] G. Nahrwold, L. Bocklage, J. M. Scholtyssek, T. Matsuyama, B. Krüger, U. Merkt, and G. Meier, *Current-induced domain-wall depinning in curved Permalloy nanowires*. J. Appl. Phys. **105**, 07D511 (2009).

[175] T. Suzuki, S. Fukami, N. Ohshima, K. Nagahara, and N. Ishiwata, *Analysis of current-driven domain wall motion from pinning sites in nanostrips with perpendicular magnetic anisotropy*. J. Appl. Phys. **103**, 113913 (2008).

[176] E. Feldtkeller, *Mikromagnetisch stetige und unstetige Magnetisierungskonfigurationen*. Z. Angew. Phys. **19**, 530 (1965).

[177] H. Niedoba and M. Labrune, *Magnetization reversal via bloch points nucleation in nanowires and dots: a micromagnetic study*. Eur. Phys. J. B **47**, 467-478 (2005).

[178] B. Krüger, A. Drews, M. Bolte, U. Merkt, D. Pfannkuche, and G. Meier, *Harmonic oscillator model for current- and field-driven magnetic vortices*. Phys. Rev. B **76**, 224426 (2007).

[179] B. Krüger, M. Najafi, S. Bohlens, R. Frömter, D. P. F. Möller, and D. Pfannkuche, *Proposal of a Robust Measurement Scheme for the Nonadiabatic Spin Torque Using the Displacement of Magnetic Vortices*. Phys. Rev. Lett. **104**, 077201 (2010).

[180] M. Najafi, B. Krüger, S. Bohlens, M. Franchin, H. Fangohr, A. Vanhaverbeke, R. Allenspach, M. Bolte, U. Merkt, D. Pfannkuche, D. P. F. Möller, and G. Meier, *Proposal for a standard problem for micromagnetic simulations including spin-transfer torque*. J. Appl. Phys. **105**, 113914 (2009).

[181] A. A. Thiele, *Steady-State Motion of Magnetic Domains*. Phys. Rev. Lett. **30**, 230 (1973).

[182] A. A. Thiele, *Applications of the gyrocoupling vector and dissipation dyadic in the dynamics of magnetic domains*. J. Appl. Phys. **45**, 377 (1974).

[183] D. L. Huber, *Dynamics of spin vortices in two-dimensional planar magnets*. Phys. Rev. B **26**, 3758 (1982).

[184] N. A. Usov and S. E. Peschany, *Magnetization curling in a fine cylindrical particle*. J. Magn. Magn. Mat. **118**, L290 (1993).

[185] L. Heyne, J. Rhensius, D. Ilgaz, A. Bisig, U. Rüdiger, M. Kläui, L. Joly, F. Nolting, L. J. Heyderman, J. U. Thiele, and F. Kronast, *Direct Determination of Large Spin-Torque Nonadiabaticity in Vortex Core Dynamics*. Phys. Rev. Lett. **105**, 187203 (2010).

[186] M. Bolte, G. Meier, B. Krüger, A. Drews, R. Eiselt, L. Bocklage, S. Bohlens, T. Tyliszczak, A. Vansteenkiste, B. Van Waeyenberge, K. W. Chou, A. Puzic, and H. Stoll, *Time-Resolved X-Ray Microscopy of Spin-Torque-Induced Magnetic Vortex Gyration*. Phys. Rev. Lett. **100**, 176601 (2008).

[187] L. Bocklage, B. Krüger, R. Eiselt, M. Bolte, P. Fischer, and G. Meier, *Time-resolved imaging of current-induced domain-wall oscillations*. Phys. Rev. B **78**, 180405 (2008).

[188] C.-Y. You, I. M. Sung, and B.-K. Joe, *Analytic expression for the temperature of the current-heated nanowire for the current-induced domain wall motion*. Appl. Phys. Lett. **89**, 222513 (2006).

[189] S. Hankemeier, K. Sachse, Y. Stark, R. Frömter, and H. P. Oepen, *Ultrahigh current densities in Permalloy nanowires on diamond*. Appl. Phys. Lett. **92**, 242503 (2008).

[190] E. H. Sondheimer, *The mean free path of electrons in metals*. Advances in Physics **1**, 1 (1952).

[191] A. F. Mayadas and M. Shatzkes, *Electrical-Resistivity Model for Polycrystalline Films: the Case of Arbitrary Reflection at External Surfaces*. Phys. Rev. B **1**, 1382 (1970).

[192] D. Zhu, M. Guizar-Sicairos, B. Wu, A. Scherz, Y. Acremann, T. Tyliszczak, P. Fischer, N. Friedenberger, K. Ollefs, M. Farle, J. R. Fienup, and J. Stöhr, *High-Resolution X-Ray Lensless Imaging by Differential Holographic Encoding*. Phys. Rev. Lett. **105**, 043901 (2010).

[193] S.-K. Kim, K.-S. Lee, Y.-S. Yu, and Y.-S. Choi, *Reliable low-power control of ultrafast vortex-core switching with the selectivity in an array of vortex states by in-plane circular-rotational magnetic fields and spin-polarized currents*. Appl. Phys. Lett. **92**, 022509 (2008).

[194] M. Curcic, B. Van Waeyenberge, A. Vansteenkiste, M. Weigand, V. Sackmann, H. Stoll, M. Fähnle, T. Tyliszczak, G. Woltersdorf, C. H. Back, and G. Schütz, *Polarization Selective Magnetic Vortex Dynamics and Core Reversal in Rotating Magnetic Fields*. Phys. Rev. Lett. **101**, 197204 (2008).

[195] O. A. Tretiakov, D. Clarke, G.-W. Chern, Y. B. Bazaliy, and O. Tchernyshyov, *Dynamics of Domain Walls in Magnetic Nanostrips*. Phys. Rev. Lett. **100**, 127204 (2008).

[196] B. Krüger, *Current-Induced Domain-Wall Dynamics in Ferromagnetic Nanowires*. Diploma thesis Universtät Hamburg (2006).

[197] L. Bocklage, B. Krüger, P. Fischer, and G. Meier, *Analytical modeling and x-ray imaging of oscillations of a single magnetic domain wall*. Phys. Rev. B **81**, 054404 (2010).

[198] E. Martinez, L. Lopez-Diaz, O. Alejos, and L. Torres, *Resonant domain wall depinning induced by oscillating spin-polarized currents in thin ferromagnetic strips*. Phys. Rev. B **77**, 144417 (2008).

[199] L. Bocklage, B. Krüger, T. Matsuyama, M. Bolte, U. Merkt, D. Pfannkuche, and G. Meier, *Dependence of Magnetic Domain-Wall Motion on a Fast Changing Current*. Phys. Rev. Lett. **103**, 197204 (2009).

[200] H. H. Langner, L. Bocklage, B. Krüger, T. Matsuyama, and G. Meier, *Magnetic domain-wall depinning with reduced current density by short pulse rise time*. Appl. Phys. Lett. **97**, 242503 (2010).

[201] T. J. Hayward, M. T. Bryan, P. W. Fry, P. M. Fundi, M. R. J. Gibbs, D. A. Allwood, M.-Y. Im, and P. Fischer, *Direct imaging of domain-wall interactions in $Ni80Fe20$ planar nanowires*. Phys. Rev. B **81**, 020410 (2010).

[202] T. J. Hayward, M. T. Bryan, P. W. Fry, P. M. Fundi, M. R. J. Gibbs, M.-Y. Im, P. Fischer, and D. A. Allwood, *Pinning induced by inter-domain wall interactions in planar magnetic nanowires*. Appl. Phys. Lett. **96**, 052502 (2010).

[203] A. J. Newell, W. Williams, and D. Dunlop, *A Generalization of the Demagnetizing Tensor for Nonuniform Magnetization*. J. Geophys. Res. **98**, 9551 (1993).

[204] S. Bohlens, *Interplay of Inhomogeneous Currents and Magnetization Textures*. Verlag Dr. Hut (2011).

[205] A. Baker, E. Jessup, and T. Kolev, *A simple strategy for varying the restart parameter in GMRES(m)*. J. of Comp. and Appl. Math. **230**, 751 - 761 (2009).

[206] Y. Saad, *Iterative methods for sparse linear systems*. Society for Industrial and Applied Mathematics 2nd edition (2003).

[207] Y. Saad and M. H. Schultz, *GMRES: A Generalized Minimal Residual Algorithm for Solving Nonsymmetric Linear Systems*. J. on Scien. and Stat. Comp. **7**, 856-869 (1986).

[208] C. Kittel, *Introduction to Solid State Physics*. Wiley 18th edition (2005).

[209] T. Kamionka, M. Martens, A. Drews, B. Krüger, O. Albrecht, and G. Meier, *Influence of temperature on the gyrotropic eigenmode of magnetic vortices*. Phys. Rev. B **83**, 224424 (2011).

[210] A. Drews, B. Krüger, G. Selke, T. Kamionka, A. Vogel, M. Martens, U. Merkt, D. Möller, and G. Meier, *Nonlinear magnetic vortex gyration*, (submitted).

[211] A. Mougin, M. Cormier, J. P. Adam, P. J. Metaxas, and J. Ferré, *Domain wall mobility, stability and Walker breakdown in magnetic nanowires*. Europhys. Lett. **78**, 57007 (2007).

[212] E. Feldtkeller and H. Thomas, *Struktur und Energie von Blochlinien in dünnen ferromagnetischen Schichten*. Zeitschrift für Physik B Condensed Matter **4**, 8 (1965).

[213] This expression has been calculated using Mathematica 7 from Wolfram Research.